New Physics at the Neutrino Oscillation Frontier

WANG, TSE-CHUN

WANG, TSE-CHUN (2018) *New Physics at the Neutrino Oscillation Frontier*, Durham theses, Durham University. Available at Durham E-Theses Online: http://etheses.dur.ac.uk/12549/

New Physics at the Neutrino Oscillation Frontier

TseChun Wang

A Thesis presented for the degree of
Doctor of Philosophy

Institute for Particle Physics Phenomenology
Department of Physics
University of Durham
England

April 2018

Dedicated to

my parents

New Physics at Neutrino Oscillation Frontier

TseChun Wang

Submitted for the degree of Doctor of Philosophy
April 2018

Abstract

The discovery of neutrino oscillations implies that neutrinos are massive, and therefore is a concrete evidence that the standard model (SM), which forbids the mass of neutrinos, is not complete. As a consequence, completing the knowledge of neutrino oscillations extends our understanding of new physics. We are entering the age of precision measurement of neutrino oscillations, with the preparation for the upcoming Long Baseline experiments (LBL) — Deep Underground Neutrino Experiment (DUNE) and Tokai to Hyper-Kamiokande (T2HK). In this thesis, we firstly study how DUNE, T2HK and the combination solve the remaining problems of the standard neutrino oscillation — octant and mass ordering degeneracy problems, if CP violates, and what the value of CP phase δ is. In the following, we study how Littlest Seesaw Models (LS) can be tested by DUNE, T2HK together with short- and medium-baseline reactor experiments, after fitting these models with the current global results. In the next half of this thesis, we extend our discussion to allow external interactions — nonstandard interactions (NSIs) in matter for DUNE. After reviewing current studies on the precision of NSI-parameter measurement, we discuss the exclusion ability of DUNE to the SM prediction over the possible scenarios. Considering NSIs are flavour-dependent, we demonstrate the possible correlations between or among NSI effects under flavour symmetries A_4 and Z_2. Based on these correlations, we present how DUNE can test flavour symmetries A_4 and Z_2 through NSIs. Our results show the experimental properties of DUNE and T2HK, and how they perform for the theory of flavour symmetry.

Declaration

The work in this thesis is based on research carried out at Institute for Particle Physics Phenomenology, Department of Physics, Durham University, England. No part of this thesis has been submitted elsewhere for any other degree or qualification and it is all my own work unless referenced to the contrary in the text. In this thesis, Chs. 3-7 are published in “Sensitivities and synergies of DUNE and T2HK,” P. Ballet, S. F. King, S. Pascoli, N. W. Prouse, and T. Wang, Phys. Rev. D 96, no. 3, 033003 (2017) doi:10.1103/PhysRevD.96.033003 [arXiv:1612.07275 [hep-ph]]. In this work, I did the analysis of the physics capacity of the official designs for both experiments; in addition, I also contributed to understanding of the capacity of alternative designs in order to find the optimal synergy scenario. Chs.8 and 9 are published in “Precision neutrino experiments vs the Littlest Seesaw,” P. Ballet, S. F. King, S. Pascoli, N. W. Prouse, and T. Wang, JHEP 1703, 110 (2017) doi:10.1007/JHEP03(2017)110 [arXiv:1612.01999 [hep-ph]]. In this work, I was engaged in the work of verifying the application Wilks’ theory for the CSDN model and in the task of solving the problem of the proper use of the priors, and did the cross-check on the results for future LBL experiments to test littlest seesaw models. Sec. 10.1 and Chs. 12 and 13 are released in “Neutrino non-standard interactions as a portal to test flavour symmetries,” TseChun Wang and Ye-Ling Zhou, arXiv:1801.05656 [hep-ph]. In this work, my main contributions are operator counting, and the analysis of the physics capacity of DUNE for testing the flavour symmetry A_4 and Z_2; further, all textures, sum rules have been double-checked by me. I was also included in the analysis of UV completion models. All content of these works are presented in this thesis.

April 5, 2018

Acknowledgements

This thesis would not be finished without the help from so many people. First of all, I sincerely say thank you to my supervisor Prof. Silvia Pascoli not only for guiding me through the whole landscape of this thesis, but also for kindly and friendly giving me advice and suggestions for my research and also for the way to treat myself and the other people. I also want to thank Dr. Peter Bellet. He cares me so much, such that we have private talks. He kindly and friendly reflected where I can improve myself, gave me lots of tips, thoughts, and ways to handle my research. Prof. Steve King is also an important person for my PhD. I thank him for helpful discussions on the works about the synergy of DUNE and T2HK and littlest seesaw models. I thank Dr. Ye-Ling Zhou; he kindly gave me lots of helps when I was gaining the knowledge of effective field theory and the concept of NSIs and flavour symmetry. I thank Dr. Nick Prouse for so many technique helps, and he is such a nice friend with a great patience. I would like to show appreciation to my parents for great financial supports, and thank all my families as they are my spiritual pillar. I also thank invisible and elusive for the financial support to attend schools, workshops, conferences, and science exchange programs. Finally, I thank my friends — BS Chen, Listen Chen, Peter Hwang, Chih-Wei Lee, Tung-Wei Huang, Yu-Wei Lin, Tsung-Han Lee, Shu-Wei Wang, Dr. Jessica Turner, Kari Cheng, Yoshimi Hung, Jiunn Wang, Inge Chen, Yoshing Yang, Hungying Chen, Xavier Huang, Hsiang-Wei Hsiao, Ching-Tien Chen, Pen-Yuan Hsing, Pin-Chu Chen, Anna Chen, Matheus Hostert, Andres Oliver, and Anderw Cheek.

Contents

List of Figures

List of Tables

Chapter 1

Introduction

In the middle of 1960s, the discrepancy in the flux of solar neutrinos between the prediction and the measurement. We call this discrepancy 'solar neutrino problem'. Now we know that this is because neutrinos can changes the flavour while travelling, and call this phenomenon 'the neutrino oscillation' [1]. This fact, however, conflicts the standard model (SM) prediction that neutrinos are massless, because massless particles do not evolve their physics properties according to the special relativity.

The framework of neutrino masses and mixing for explaining neutrino oscillations — the first direct experimental evidence for physics beyond the Standard Model (SM) — is now firmly established [1]. All three mixing angles (θ_{12}, θ_{13}, θ_{23}) together with the size of the two mass-squared differences (Δm^2_{21}, Δm^2_{31}) have been measured, with experimental efforts now focused on determining the final few unknowns: the ordering and scale of the neutrino masses; the value of the Dirac CP phase δ; and a precision measurement of the angle θ_{23} including, if non-maximal ($\theta_{23} \neq 45^\circ$ or $\sin^2\theta_{23} \neq 1/2$), its octant ($\theta_{23} >$ or $< 45^\circ$). Although there is some as yet inconclusive evidence for δ in the third or fourth quadrant, as well as for normal ordering (NO) and non-maximal atmospheric mixing, we rely on the next generation of oscillation experiments to set these issues to rest [2].

With the intention of building on the progress of the oscillation programme, the international community has conceived a range of future facilities with the potential to explore the final unknowns in the standard oscillation paradigm, and to hunt for tensions in the data which might indicate that a richer extension of the SM is required. Depending on the distance between the neutrino source and detector, there are three major strands in the future experimental neutrino oscillation programme: short-baseline experiments such as those comprising the SBN programme [3], intermediate baseline reactor facilities, RENO-50 and JUNO [4–6], and long-baseline experiments such as LBNF-DUNE and T2HK [7–12]. In this thesis we focus on these latter two proposals for novel long-baseline facilities: Long-Baseline Neutrino Facility-Deep Underground Neutrino Experiment (LBNF-DUNE, referred to subsequently as DUNE) and Tokai to Hyper-Kamiokande (T2HK). DUNE is the flag-ship long baseline experiment of the Fermilab neutrino programme [11, 12]. It consists of a new beam sourced at Fermilab and a detector complex at the Sanford Underground Research Facility (SURF) in South Dakota separated by a distance of 1300 km. T2HK [10] in contrast was conceived with a smaller baseline of 295 km and a different detector technology. Building on the successes of Kamiokande and Super-Kamiokande [13], Hyper-Kamiokande will employ Water Čerenkov technology at a significantly larger scale, with fiducial volumes on the order of hundreds of kilotonnes. Recently, as the designs for DUNE and T2HK have matured, both collaborations have considered significant alterations to the benchmark proposals in Refs. [10] and [12, 14].

The origin of neutrino masses and mixing remains unknown with many possible models considered viable (for reviews see e.g. [15, 16]). A large proportion of these models are based on the classic seesaw mechanism[1], involving heavy right-handed Majorana neutrinos [17], providing both a mechanism for generating the neutrino masses and a natural explanation for their smallness. However, in order to make predictions that can be probed experimentally, seesaw models require additional assumptions or constraints [18]. To accommodate the three distinct light neutrino masses which drive the oscillation phenomenon, the seesaw mechanism requires at least two right-handed neutrinos [19], such as the Littlest Seesaw model. In order to reduce the number of free parameters still further to the smallest number possible, and hence increase predictivity, various approaches to the two right-handed neutrino

---

[1] The seesaw mechanism is the theoretical model that explains the smallness of neutrino mass by the suppression by the mass of heavy particles. More details can see in Ch. 2.2.1.

seesaw model have been suggested[2], such as postulating one [20] or two [21] texture zeroes in the Dirac mass matrix in the flavour basis (i.e. the basis of diagonal charged lepton and right-handed neutrino masses).[3] The minimal two right-handed neutrino model with the normal ordering which can accommodate the known data of neutrino mixing involves a Dirac mass matrix with one texture zero and a characteristic form known as the Littlest Seesaw model [23]. The precision measurements of mixing angles and mass-square splittings examine the properties of the models at the higher energy, e.g. the couplings between the right-handed and active neutrinos, which can be naturally imposed by the flavour symmetry.

The flavour symmetry is motivated by the measured values of mixing angles, $\sin^2\theta_{12} \sim 1/3$ and $\sin^2\theta_{23} \sim 1/2$. In the framework of flavour symmetries, it is assumed that an underlying discrete flavour symmetry $G_{\rm f}$ exists at some high energy scale. It unifies the three flavours together. After the flavour symmetry is broken at lower energy, special flavour structures arise. In more detail, this process can be done in two ways — direct and indirect approaches. Accordingly, there are two classes of model. Direct models are based on A_4 or S_4 family symmetry. In this class of models, the lepton sector preserves some generators for the observed flavour symmetry, which is as a part of the symmetry. The second class — indirect models — is based on any flavour symmetry $G_{\rm f}$ that is completely broken in the neutrino sector, while the observed neutrino symmetry in neutrino flavour basis emerges as an accidental symmetry that is an indirect effect of $G_{\rm f}$, *e.g.* CSDN [15], etc. In most direct models, the flavour symmetry is assumed to be the tetrahedral group A_4 [24] or the hexahedron group S_4 [25]. These models naturally predict $\sin^2\theta_{12} = 1/3$, $\sin^2\theta_{23} = 1/2$ but $\sin^2\theta_{13} = 0$ [26–28], i.e., the so-called tri-bimaximal (TBM) mixing [29]. One important feature of flavour models is the existence of some slightly-preserved residual symmetries at low energy (for some reviews, see

---

[2] In seesaw models with two right-handed neutrinos, including those discussed in this thesis, a hierarchical spectrum of left-handed neutrino masses is obtained where the lightest left-handed neutrino is massless.

[3] Such two texture zero models are now phenomenologically excluded [22] for the case of a normal neutrino mass hierarchy.

e.g. [30]). The most-commonly used residual symmetries are a Z_3 and a Z_2, where charged leptons and neutrinos transform as

$$\begin{aligned} Z_3: \quad & e \to e\,, && \mu \to e^{-i2\pi/3}\mu\,, && \tau \to e^{i2\pi/3}\tau\,, \\ Z_2: \quad & \nu_e \to \frac{1}{3}(-\nu_e + 2\nu_\mu + 2\nu_\tau)\,, && \nu_\mu \to \frac{1}{3}(-\nu_\mu + 2\nu_\tau + 2\nu_e)\,, \\ & \nu_\tau \to \frac{1}{3}(-\nu_\tau + 2\nu_e + 2\nu_\mu)\,. \end{aligned} \tag{1.0.1}$$

The charged lepton and neutrino mass terms are invariant under the transformations, respectively. Both Z_3 and Z_2 are subgroups of A_4 and S_4. However, the predicted vanishing θ_{13} is not in agreement with data. It suggests small corrections to the mixing, and the residual symmetries should be slightly broken. Imposing flavour symmetries does not only predict the flavour mixing measured by neutrino oscillation experiments, but also contributes to other flavour-dependent phenomenological signatures, such as the charged lepton flavour violation (CLFV), nonstandard interactions,... etc.

Neutrino nonstandard interactions (NSIs) provide a model-independent framework of studying new physics in neutrino oscillation experiments (for some reviews, see [31]). These interactions are flavour-dependent, and are collected in a matrix $\epsilon_{\alpha\beta}$, where $\alpha, \beta = e,\ \mu,\ \tau$. They are usually considered as effective descriptions of contributions from higher dimensional operators mediated by heavy mediators [32–34], although they may also be induced by light mediators with very weak couplings [35]. Depending on where they occur in neutrino oscillation, these new interactions are taken as the NSIs at source, detector or during propagation. There are no experimental hints for NSIs at the source and the detector with the high precision [31,36]. The precision of current global fit results for matter effect NSIs is not as good as those of other experiments like CLFV... etc, and allows the size of NSIs to be from a few to tens of percentages of the weak interactions at 90% C.L. [39]. Due to precision upgrades and because of nonnegligible matter effects, the testability of NSIs in DUNE and T2HK (as well as its alternative T2HKK), and the influences on measurements of mass ordering and CP violation have caught a great attention, e.g., in [37,38].

Neutrino oscillation data can be described in the standard language — mixing angles and mass-squared splittings; extending the language to include NSI effects is maybe necessary. Moreover, words in this language are maybe spelt by the theory of flavour. We summarise the above perspective in the flow chart Fig. 1.1. In the lower part of this figure, we present that the neutrino oscillation can be directly explained by mixing angles and mass-squared splittings; the block with the dashed boundary presents that NSIs are maybe included to describe neutrino oscillation data. Therefore, the oscillation data can measure the oscillation parameters, and further tell us if NSIs exist. Then we move our focus on the upper layer — the connection of flavour symmetry to oscillation parameters (left) and NSIs (right). The left part demonstrates that the flavour symmetry model, which predicts the true values of oscillation parameters, can be tested by oscillation data through the measurement of mixing angles and mass-squared differences. On the other hand, the other part shows that the flavour symmetry also predicts the relations of NSIs with different flavour dependence; similarly, neutrino data can provide the extra information of flavour symmetry through the measurement or detection of NSI effects.

In this thesis, we study connections between or among blocks in Fig. 1.1 in details for understanding the physics potentials of future LBLs for solving current problems and for studying varieties of new physics, which are introduced in the previous paragraphs. For the first half of this thesis, we follow with the left part of Fig. 1.1. After reviewing the current understanding of the neutrino oscillation phenomenology in Ch. 4, we discuss how DUNE and T2HK can solve the current problems in the standard oscillation (unknown if CP violates or conserves, undetermined mass ordering and octant degeneracies) in Ch. 5, and extend the discussion to the precision of δ measurement in Ch. 6. In Ch. 7, we investigate the impact of alternative designs for DUNE and T2HK on the sensitivity for if CP violates maximally or conserves and the mass ordering sensitivity, and δ measurement. In the following, based on the knowledge of previous results in Chs. 5 and 6, we study how littlest seesaw models can be tested by DUNE, T2HK and short- and medium-baseline experiments in Ch. 9 as a benchmark study, after the overview of the current status of the littlest seesaw model in Ch. 8. In the next half of this thesis, we extend our discussion to nonstandard interactions in matter (matter NSI effects) for DUNE. With the knowledge of effective field theory, we present the possible operators with dimension ≤ 8 causing NSIs, and we also argue that sizeable NSIs in matter are allowed in Ch. 10. Then, we review current works on the precision on paramters for matter NSI effects for DUNE, and study how this experiment can exclude the SM prediction — no NSIs occur — if matter NSI effects enter ν oscillations in Ch. 11. In this chapter we focus on the lower three blocks in Fig. 1.1. In Ch. 12, we predict the correlations between or among NSIs in matter of different flavour dependence under A_4 flavour symmetry and its residual symmetry Z_2, as studying the connection between the blocks for NSIs and the flavour symmetry theory. Finally, based on the properties predicted in Ch. 12, taking the point of view of phenomenology, we generally studying the application of these correlations in DUNE — testing A_4 and Z_2 symmetries in NSIs in Ch. 13, covering all blocks in Fig. 1.1. Before any discussion, we introduce how neutrinos are predicted by the SM and the extension due to the neutrino oscillation in Ch. 2, and in Ch. 3 we describe details and the treatments of the experiments that are discussed in this thesis.

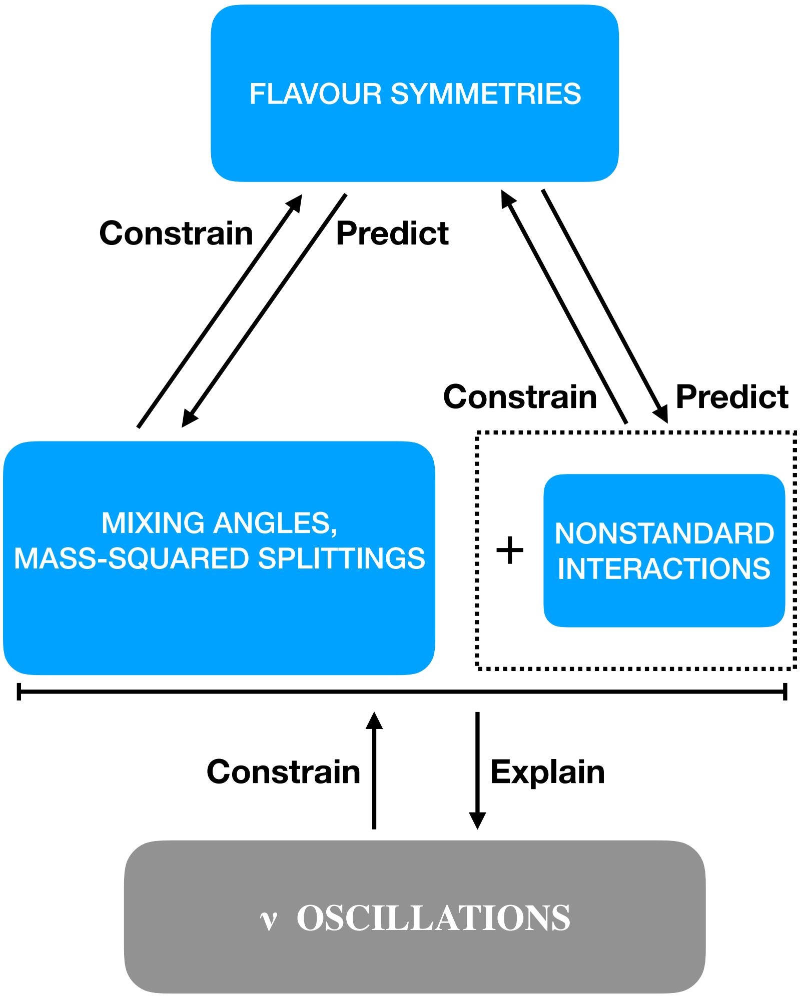

Figure 1.1: A summary of the perspective taken in this thesis.

Chapter 2

Neutrinos in and beyond the SM

We have found four fundamental forces — electromagnetic, weak, strong and gravity forces. In the framework of quantum field theory and in the gauge theory, we describe electromagnetic, weak and strong interactions of elementary particles, based on the local symmetry $\mathrm{SU}(3)_C \times \mathrm{SU}(2)_L \times \mathrm{U}(1)_Y$, where the subscripts C, L, and Y denote color, left-handed charity and weak hypercharge, respectively. The number of generators for different symmetries equals the number of gauge bosons of the corresponding force — 8 gluons for the strong force, three vector bosons $W^{\pm}$ and Z for the weak interaction, and the photon γ for the electromagnetic force. In the SM, there are four types of fermions — u- and d- like quarks, charged leptons, neutrinos. Quarks participate in all three SM forces, while charged leptons do not interact by the strong force. Neutrinos only enter the weak interaction. The scalar boson Higgs, which is proposed in the SM for breaking $\mathrm{SU}(2)_L \times \mathrm{U}(1)_Y$ to $\mathrm{U}(1)_Q$, introduces mass of particles by its coupling with them. Despite the success of the Higgs mechanism in the SM in describing the masses of SM charged fermions and gauge bosons, neutrinos are predicted to be massless under the SM. As a consequence, the discovery of neutrino oscillations, which implies that neutrinos are not massless, is considered as an evidence that the SM is not a complete theory, and therefore this evidence is seen as a hint of new physics

In the first section of this chapter, we review neutrino interactions under the SM and the masslessness of neutrino according to the SM Higgs mechanism. Then, we briefly introduce the most general framework to describe neutrino mass and study the 2-neutrino mixing case in order to understand the neutrino oscillation. Finally, we summarise the current understanding of neutrino oscillations.

2.1 Neutrino interactions in the SM

The electroweak SM Lagrangian is the most general renormalizable Lagrangian preserving the local symmetry $\mathrm{SU}(2)_L \times \mathrm{U}(1)_Y$. We write this Lagrangian in terms of the fermion fields for three generations, the boson fields, and a Higgs doublet,

$$\begin{aligned}\mathcal{L} = {} & i\textstyle\sum_{\alpha=e,\mu,\tau} \overline{L'_\alpha} \not{D} L'_\alpha + i\textstyle\sum_{\alpha=1,2,3} \overline{Q'_\alpha} \not{D} Q'_\alpha \\ & + \textstyle\sum_{\alpha=e,\mu,\tau} i\overline{E'_{\alpha R}} \not{D} E'_{\alpha R} + \textstyle\sum_{\alpha=d,s,b} i\overline{D'_{\alpha R}} \not{D} D'_{\alpha R} + \textstyle\sum_{\alpha=u,c,t} i\overline{U'_{\alpha R}} \not{D} U'_{\alpha R} \\ & -\tfrac{1}{4}\underline{A}_{\mu\nu}\underline{A}^{\mu\nu} - \tfrac{1}{4}B_{\mu\nu}B^{\mu\nu} \\ & + (D_\mu H)^\dagger (D^\mu H) - \mu^2 H^\dagger H - \lambda \left(H^\dagger H\right)^2 \\ & - \textstyle\sum_{\alpha=e,\mu,\tau} \left(Y'^{l}_{\alpha\beta} \overline{L'_\alpha} H E'_{\beta R} + Y'^{l*}_{\alpha\beta} \overline{E'_{\beta R}} H^\dagger L'_\alpha\right) \\ & - \textstyle\sum_{\alpha=1,2,3} \textstyle\sum_{\beta=d,s,b} \left(Y'^{D}_{\alpha\beta} \overline{Q'}_\alpha H D'_{\beta R} + Y'^{D*}_{\alpha\beta} \overline{D'_{\beta R}} H^\dagger Q'_\alpha\right) \\ & - \textstyle\sum_{\alpha=1,2,3} \textstyle\sum_{\beta=u,c,t} \left(Y'^{U}_{\alpha\beta} \overline{Q'_\alpha} \widetilde{H} U'_{\beta R} + Y'^{U*}_{\alpha\beta} \overline{U'_{\beta R}} \widetilde{H}^\dagger Q'_\alpha\right),\end{aligned} \tag{2.1.1}$$

where the covariant derivative $\not{D} \equiv D_\mu \gamma^\mu = (\partial_\mu + ig\underline{A}_\mu \cdot \underline{I} + ig' B_\mu \frac{Y}{2})\gamma^\mu$ and $\underline{A}^\mu = (A_1^\mu, A_2^\mu, A_3^\mu)$ and $\underline{I} \equiv (I_1, I_2, I_3)$, which are the generators for $\mathrm{SU}(2)_L$. In the two-dimensional representation, $I_a = \tau_a/2$, where τ_1, τ_2, and τ_3 are three Pauli matrices. Three components of $\underline{I}$ satisfy the condition $[I_a, I_b] = i\varepsilon_{abc} I_c$, where ε_{abc} is the totally antisymmetric tensor with three indices having $\varepsilon_{123} = 1$. A_1^μ, A_2^μ, and A_3^μ are three gauge bosons for $\mathrm{SU}(2)_L$, while B^μ is the gauge boson associated with the generator Y of the group $\mathrm{U}(1)_Y$. The expressions for $\underline{A}^{\mu\nu}$ and $B^{\mu\nu}$ are:

$$A_a^{\mu\nu} = \partial^\mu A_a^\nu - \partial^\nu A_a^\mu - g\sum_{b,c=1}^{3} \varepsilon_{abc} A_b^\mu A_c^\nu, \tag{2.1.2}$$

$$B^{\mu\nu} = \partial^\mu B^\nu - \partial^\nu B^\mu. \tag{2.1.3}$$

The SM fermions are described to be the lepton doublets L'_α, the quark doublets Q'_α, the lepton singlets $E'_{\alpha R}$, and the quark singlets $U'_{\alpha R}$, $D'_{\alpha R}$, where the subscripts L and R refer to left and right charity, respectively, and the other subscript α denotes the flavour and generation for leptons and quarks respectively. The primes are used for showing the fields do not have the definite masses, but are the linear combinations of the fields with definite masses. $Y'^{l}_{\alpha\beta}$, $Y'^{D}_{\alpha\beta}$, and $Y'^{U}_{\alpha\beta}$ are the Yukawa couplings of leptons, d-like quarks and u-like quarks, to Higgs boson respectively. The Higgs doublet is $H(x) = \left(h^+(x)\ h^0(x)\right)^T$, where $h^+(x)$ is a charged complex scalar field and $h^0(x)$ is a neutral complex scalar field. $\widetilde{H}$ is defined $\widetilde{H} \equiv i\tau_2 H^*$.

The first two lines in Eq. (2.1.1) are the kinetic terms and the gauge couplings for SM fermions. The third line is the kinetic and self-coupling terms for the gauge bosons. The fourth line is the kinetic term and the potential for the SM Higgs. The final three lines are the Higgs-fermion Yukawa couplings that generate the SM fermion masses and the quark mixing. The values of the weak isospin, hypercharge, and electric charge of the fermion doublets and singlets are presented in Tab. 2.1.

As we can see in Tab. 2.1, the charge Q of neutrinos is 0, and implies that neutrinos are not involved in the electric interaction, though they participate in the weak interaction. In this section, we firstly study the interaction of neutrinos in the SM, before describing the SM prediction that neutrinos are massless.

	I	I_3	Y	Q
lepton doublet $L \equiv (\nu_{eL}\ e_L)^{\mathrm{T}}$	1/2	$(1/2,\ -1/2)^{\mathrm{T}}$	−1	$(0,\ -1)^{\mathrm{T}}$
lepton singlet e_R	0	0	−2	−1
quark doublet $Q \equiv (u_L\ d_L)^T$	1/2	$(1/2,\ -1/2)^{\mathrm{T}}$	1/3	$(2/3,\ -1/3)^{\mathrm{T}}$
quark singlet u_R	0	0	4/3	2/3
quark singlet d_R	0	0	−2/3	−1/3
Higgs doublet $H \equiv (h^+\ h^0)^{\mathrm{T}}$	1/2	$(1/2,\ -1/2)^{\mathrm{T}}$	1	$(1,\ 0)^{\mathrm{T}}$

Table 2.1: The eigenvalues of the weak isospin I, of the third component I_3, of the hypercharge Y, and of the charge $Q = I_3 + Y/2$ of the fermion doublets of the 1st generation and singlets of the 1st family of the SM.

2.1.1 Neutrinos in weak interactions

To simplify our discussion, we focus on the one-generation case, where the mixing of fermions never occurs. Giving the charge of lepton doublet and singlet shown in

Tab. 2.1 in Eq. (2.1.1), we can write the SM Lagrangian for $\mathrm{SU}(2)_L \times \mathrm{U}(1)_Y$,

$$\begin{aligned}\mathcal{L}_I = &-\tfrac{1}{2}\overline{L}_L \left(g\underline{\not{A}} \cdot \underline{\tau} - g'\not{B}\right) L_L - \tfrac{1}{2}\overline{Q}_L \left(g\underline{\not{A}} \cdot \underline{\tau} + \tfrac{1}{3}g'\not{B}\right) Q_L \\ &+g'\bar{e}_R\not{B}e_R - \tfrac{2}{3}g'\bar{u}_R\not{B}u_R + \tfrac{1}{3}g'\bar{d}_R\not{B}d_R.\end{aligned} \tag{2.1.4}$$

We extract the leptonic part in Eq. (2.1.4), which is the first and the third term,

$$\mathcal{L}_{I,L} = -\tfrac{1}{2}\left(\bar{\nu}_{eL}\ \bar{e}_L\right)\begin{pmatrix} g\not{A}_3 - g'\not{B} & g\left(\not{A}_1 - i\not{A}_2\right) \\ g\left(\not{A}_1 + i\not{A}_2\right) & -g\not{A}_3 - g'\not{B}\end{pmatrix}\begin{pmatrix}\nu_{eL} \\ e_L\end{pmatrix} + g'\bar{e}_R\not{B}e_R. \tag{2.1.5}$$

Eq. (2.1.5) is separated into two parts, the neutral-current (NC) terms Eq. (2.1.6) and the charged-current (CC) terms Eq. (2.1.7),

$$\mathcal{L}_{I,L}^{(NC)} = -\tfrac{1}{2}\left\{\bar{\nu}_{eL}\left(g\not{A}_1 - g'\not{B}\right)\nu_{eL} - \bar{e}_L\left(g\not{A}_3 + g'\not{B}\right)e_L - 2g'\bar{e}_R\not{B}e_R\right\}, \tag{2.1.6}$$

$$\mathcal{L}_{I,L}^{(CC)} = -\frac{g}{2}\left\{\bar{\nu}_{eL}\left(\not{A}_1 - i\not{A}_2\right)e_L + \bar{e}_L\left(\not{A}_1 + i\not{A}_2\right)\nu_{eL}\right\}. \tag{2.1.7}$$

CC and NC interactions

We define a field $W^\mu \equiv \frac{A_1^\mu - iA_2^\mu}{\sqrt{2}}$ that annihilates W^+ bosons and creates W^- bosons, and the charged current of lepton, $j_{W,l}^\mu = \bar{\nu}_e\gamma^\mu(1-\gamma^5)e = 2\bar{\nu}_{eL}\gamma^\mu e_L$. As a result, we obtain

$$\mathcal{L}_{I,l}^{(CC)} = -\frac{g}{2\sqrt{2}}j_{W,l}^\mu W_\mu + \text{H.c.}. \tag{2.1.8}$$

By expressing the electromagnetic field A^μ as a linear combination of A_3^μ and B^μ, the Lagrangian for the quantum electric dynamics can be obtained as a part of Eq. (2.1.6). This combination is described with the Weinberg angle θ_W,

$$\begin{aligned}A^\mu &= \sin\theta_W A_3^\mu + \cos\theta_W B^\mu, \\ Z^\mu &= \cos\theta_W A_3^\mu - \sin\theta_W B^\mu,\end{aligned} \tag{2.1.9}$$

where Z^μ is a vector boson field for weak interactions. The neutral-current Lagrangian can be written as

$$\mathcal{L}_{I,L}^{(NC)} = \mathcal{L}_{I,L}^{(Z)} + \mathcal{L}_{I,L}^{(\gamma)} = -ej_{\gamma,l}^\mu A_\mu - \frac{g}{2\cos\theta_W}j_{Z,l}^\mu Z_\mu, \tag{2.1.10}$$

where two currents for leptons are defined $j_{\gamma,l}^\mu = -\bar{e}\gamma^\mu e$ and

$$j_{Z,l}^\mu = 2g_L^\mu\bar{\nu}_{eL}\gamma^\mu\nu_{eL} + 2g_L^l\bar{e}_L\gamma^\mu e_L + 2g_R^l\bar{e}_R\gamma^\mu e_R. \tag{2.1.11}$$

The couplings for a fermion field f in Eq. (2.1.11) are the combination of I_3^f and the electric charge q_L^f or g_R^f,

$$g_L^f = I_3^f - q_f \sin^2\theta_W, \tag{2.1.12}$$

$$g_R^f = -q_f \sin^2\theta_W, \tag{2.1.13}$$

where q_f is the electric charge Q for the fermion f. Among g, g' and e, there are conditions,

$$e = g\sin\theta_W = g'\cos\theta_W,\ \tan\theta_W = \frac{g'}{g}. \tag{2.1.14}$$

From the above, we know that the neutrino interactions in the SM are via mediating a $W^\pm$ or Z boson. Exchanging $W^\pm$ and Z bosons are the CC and NC interactions respectively. The π decay $\pi^- \to \mu^-\bar{\nu}_\mu$ and the μ^- decay $\mu^- \to e^-\nu_\mu\bar{\nu}_e$ produce the neutrino beam in DUNE and T2HK, and are explained by the CC interaction, in which a charged lepton of the same flavour is involved. In the detector, neutrinos interact with quarks (or nucleus) and electrons of the target of detector via the CC or NC interaction.

The above discussion is based on the assumption of 1-generation fermions. Extending to the 3-flavour case, the CC interaction is flavour dependent; as a result, interactions of this kind can be used to label the flavour of neutrinos. NC interactions, in which neutrinos of all flavours interact with nucleus, quarks, or electrons, are therefore blind to the neutrino flavour.

Lower-energy approximation

We know the masses of $W^\pm$ and Z boson are about 80 and 91 GeV respectively. When their kinetic energy is low enough in comparison to the mass, only the mass contributes to their propagator.

Under this approximation, we write the CC and NC Lagrangian as

$$\mathcal{L}_{\text{eff}}^{(CC)} = -\frac{G_{\text{F}}}{\sqrt{2}} j_{W\mu}^\dagger j_W^\mu, \tag{2.1.15}$$

$$\mathcal{L}_{\text{eff}}^{(NC)} = -\frac{G_{\text{F}}}{\sqrt{2}} j_Z^\mu j_{Z\mu}, \tag{2.1.16}$$

where the Fermi constant,

$$\frac{G_{\rm F}}{\sqrt{2}} = \frac{\pi}{2\sin^2\theta_W m_W^2} = \frac{\pi\alpha}{2\sin^2\cos^2\theta_W m_Z^2}, \tag{2.1.17}$$

with the fine-structure constant $\alpha \equiv e^2/4\pi$. Two currents j_W^μ and j_Z^μ are defined, $j_W^\mu \equiv j_{W,l}^\mu + j_{W,q}^\mu$ and $j_Z^\mu \equiv j_{Z,l}^\mu + j_{Z,q}^\mu$, where $j_{W,q}^\mu \equiv \bar{u}\gamma^\mu\left(1-\gamma^5\right)d = 2\overline{u_L}\gamma^\mu d_L$ and $j_{Z,q}^\mu \equiv 2g_L^U\overline{u_L}\gamma^\mu u_L + 2g_R^U\overline{u_R}\gamma^\mu u_R + 2g_L^D\overline{d_L}\gamma^\mu d_L + 2g_R^D\overline{d_R}\gamma^\mu d_R$ with $g_L^U = \frac{1}{2} - \frac{2}{3}\sin\theta_W$, $g_R^U = -\frac{2}{3}\sin\theta_W$, and $g_L^D = -\frac{1}{2} + \frac{2}{3}\sin\theta_W$, $g_R^U = \frac{1}{3}\sin\theta_W$. This approximation can be used for neutrino with energy, which is far below the energy scale of $W^\pm$ and Z mass. As the peak energy for DUNE and T2HK are around 3 and 0.6 GeV, this approximation is appropriate to our discussion in this thesis.

In this approximation, the expression of the cross section for neutrino-electron elastic scattering in terms of incoming neutrino energy E_ν and the kinetic energy of recoil electron T_e is given

$$\begin{aligned}\sigma(E_\nu, T_e^{\rm th}) = {} & \tfrac{\sigma_0}{m_e}\Big[(g_1^2+g_2^2)(T_e^{\rm max} - T_e^{\rm th}) \\ & - \left(g_2^2 + g_1 g_2\tfrac{m_e}{2E_\nu}\right)\left(\tfrac{T_e^{\rm max2} - T_e^{\rm th2}}{E_\nu}\right) + \tfrac{1}{3}g_2^2\left(\tfrac{T_e^{\rm max3} - T_e^{\rm th3}}{E_\nu^2}\right)\Big],\end{aligned} \tag{2.1.18}$$

where $T_e^{\rm max} = T_e^{\rm max}(E_\nu) \equiv \frac{2E_\nu^2}{m_e + 2E_\nu}$, corresponding to the motion of neutrinos in the forward direction, and the threshold energy $T_e^{\rm th}$ depends on the property of the detector. $\sigma_0 \equiv \frac{2G_{\rm F}^2 m_e^2}{\pi}$ is approximately 88.06×10^{-46} cm^2. The coefficients g_1 and g_2 depend on the flavour of incoming neutrinos. For ν_e and $\bar{\nu}_e$, we have

$$g_1^{(\nu_e)} = g_2^{(\bar{\nu}_e)} = 1 + \frac{g_V^l + g_A^l}{2} = 1 + g_L^l = \frac{1}{2} + \sin^2\theta_W, \tag{2.1.19}$$

$$g_2^{(\nu_e)} = g_1^{(\bar{\nu}_e)} = \frac{g_V^l - g_A^l}{2} = g_L^l = \sin^2\theta_W. \tag{2.1.20}$$

And, for the other two flavours, we have

$$g_1^{(\nu_{\mu,\tau})} = g_2^{(\bar{\nu}_{\mu,\tau})} = \frac{g_V^l + g_A^l}{2} = g_L^l = -\frac{1}{2} + \sin^2\theta_W, \tag{2.1.21}$$

$$g_2^{(\nu_{\mu,\tau})} = g_1^{(\bar{\nu}_{\mu,\tau})} = \frac{g_V^l - g_A^l}{2} = g_L^l = \sin^2\theta_W. \tag{2.1.22}$$

The high-energy part of the cross-section with $T_e^{\rm th} = 0$ corresponds to the values given in Tab. 2.2, and is given

$$\sigma(E_\nu, T_e^{\rm th} = 0) \simeq \sigma_0\frac{E_\nu}{m_e}\left(g_1^2 + \frac{1}{3}g_2^2\right), \text{ for } E_\nu \gg m_e, \tag{2.1.23}$$

which are proportional to E_ν in the laboratory frame.

Process	Total cross-section
$\nu_e + e^-$	$(G_\mathrm{F}^2 s/4\pi)\left[\left(1+2\sin^2\theta_W\right)^2+\frac{4}{3}\sin^4\theta_W\right]$
$\bar{\nu}_e + e^-$	$(G_\mathrm{F}^2 s/4\pi)\left[\frac{1}{3}\left(1+2\sin^2\theta_W\right)^2+4\sin^4\theta_W\right]$
$\nu_{\mu,\tau} + e^-$	$(G_\mathrm{F}^2 s/4\pi)\left[\left(1-2\sin^2\theta_W\right)^2+\frac{4}{3}\sin^4\theta_W\right]$
$\bar{\nu}_{\mu,\tau} + e^-$	$(G_\mathrm{F}^2 s/4\pi)\left[\frac{1}{3}\left(1-2\sin^2\theta_W\right)^2+4\sin^4\theta_W\right]$

Table 2.2: The total neutrino-electron elastic scattering cross sections for $\sqrt{s} \gg m_e$ for different flavours of neutrinos, with the unites of 10^{-46} cm^2, where the variable s is defined $s = 2m_e E_\nu$.

Neutrino interactions in matter

In addition to neutrino production and detection, their interactions in the earth during propagation can be also predicted by the SM. The interactions are CC or NC interactions, and the effective Hamiltonian for CC interactions is written

$$\mathcal{H}_\mathrm{eff}^{(\mathrm{CC})} = \frac{G_\mathrm{F}}{\sqrt{2}}\left[\bar{\nu}_e(x)\gamma^\rho\left(1-\gamma^5\right)e(x)\right]\left[\bar{e}(x)\gamma_\rho\left(1-\gamma^5\right)\nu_e(x)\right], \tag{2.1.24}$$

and that for NC interactions is

$$\mathcal{H}_\mathrm{eff}^{(\mathrm{NC})}(x) = \frac{G_\mathrm{F}}{\sqrt{2}}\sum_{\alpha=e,\mu,\tau}\left[\bar{\nu}_\alpha(x)\gamma^\rho(1-\gamma^5)\nu_\alpha(x)\right]\sum_{\mathrm{f}=e,u,d}\left[\bar{\mathrm{f}}(x)\gamma_\rho\left(g_V^\mathrm{f}-g_A^\mathrm{f}\gamma^5\right)\mathrm{f}(x)\right], \tag{2.1.25}$$

where two coefficients are defined $g_V^\mathrm{f} \equiv g_L^\mathrm{f} + g_R^\mathrm{f}$ and $g_A^\mathrm{f} \equiv g_L^\mathrm{f} - g_R^\mathrm{f}$. It is important to note that only electron-flavour neutrinos participate in CC interactions in matter. Therefore, only neutrinos of e flavour can be affected by CC interactions in matter. After doing the Fierz transformation, the average of the effective Hamiltonian over the electron background in the rest frame of the medium is given by

$$\overline{\mathcal{H}_\mathrm{eff}^{(\mathrm{CC})}}(x) = \frac{G_\mathrm{F}}{\sqrt{2}V}\int d^3p_e f(E_e,T)\bar{\nu}_e(x)\frac{\not{p}_e}{E_e}\left(1-\gamma^2\right)\nu_e(x), \tag{2.1.26}$$

where $f(E_e, T)$ is the statistical distribution of the electron energy E_e, which depends on the temperature T of the electron background, and is normalized by

$$\int d^3p_e f(E_e,T) = N_e V, \tag{2.1.27}$$

where N_e is the electron density in matter and N_eV is the total number of electrons. The integral over d^3p_e in Eq. (2.1.26) becomes

$$\int d^3p_e f(E_e, T)\frac{\not{p}_e}{E_e} = N_e V \gamma^0. \tag{2.1.28}$$

The effective Hamiltonian is therefore,

$$\overline{\mathcal{H}_{\text{eff}}^{(\text{CC})}}(x) = V_{CC}\bar{\nu}_{eL}(x)\gamma^0\nu_{eL}(x), \tag{2.1.29}$$

where the average potential for CC interaction with electron background in the earth is

$$V_{CC} = \sqrt{2}G_{\text{F}}N_e. \tag{2.1.30}$$

Due to the cancellation of the NC interactions with electrons and that with protons in matter, the NC interactions in matter is considered only with the neutrons. The same process can be applied for NC interactions, and the average potential is given

$$V_{NC} = -\frac{\sqrt{2}}{2}G_{\text{F}}N_n, \tag{2.1.31}$$

where N_n is the neutron density of the medium. In Sec. 2.2.2, we will introduce how neutrinos oscillate in matter. And we will see the NC interaction does not affect to neutrino oscillations, but the CC interaction does.

2.1.2 Massless Neutrino

Explaining how neutrinos are massless under the SM, we introduce the Higgs mechanism, which provides mass terms for massive fields in the SM Lagrangian, and preserves the local symmetry $\text{SU}(2)_L \times \text{U}(1)_Y$. Though in this subsection we focus on the mass for leptons, the same process applies for the other massive SM particles. The Lagrangian for the Higgs mechanism in Eq. (2.1.1) is

$$\mathcal{L}_{\text{Higgs}} = (D_\mu H)^\dagger (D^\mu H) - \mu^2 H^\dagger H - \lambda \left(H^\dagger H\right)^2. \tag{2.1.32}$$

We focus on the potential

$$V(H) = \mu^2 H^\dagger H + \lambda(H^\dagger H)^2. \tag{2.1.33}$$

In order to have bound from below, the coefficient λ of the quartic self-coupling of the Higgs fields must be positive, $\lambda > 0$. However, the mass-like coefficient μ^2 can be positive or negative. Once μ^2 is negative, realized is the spontaneous breaking of the symmetry $\mathrm{SU}(2)_L \times \mathrm{U}(1)_Y \to \mathrm{U}(1)_Q$, where $\mathrm{U}(1)_Q$ is the gauge symmetry group of electromagnetic interactions. We define

$$v \equiv \sqrt{-\frac{\mu^2}{\lambda}}. \tag{2.1.34}$$

Then, we can rewrite the Higgs potential Eq. (2.1.33),

$$V(H) = \lambda \left(H^\dagger H - \frac{v^2}{2} \right)^2 . \tag{2.1.35}$$

The minimum for this potential is therefore for,

$$H^\dagger H = \frac{v^2}{2}. \tag{2.1.36}$$

In the text below Eq. (2.1.1), we know two components of H are charged and neutral in electric charge. Because the vacuum is thought to be electrically neutral, the vacuum expectation value (VEV) is entirely contributed by h^0, then

$$\langle H \rangle = \frac{1}{\sqrt{2}} \begin{pmatrix} 0 \\ v \end{pmatrix} . \tag{2.1.37}$$

This is obvious that $I_i \langle H \rangle \neq 0$, where $i = 3$, and $Y \langle H \rangle \neq 0$, but $Q\langle H \rangle = \left(I_3 + \frac{Y}{2} \right) \langle H \rangle = 0$. This implies that when Higgs boson locates at the minimum Eq. (2.1.36), $\mathrm{SU}(2)_L \times \mathrm{U}(1)_Y$ breaks to $\mathrm{U}(1)_Q$. And the excitation state of the scalar doublet H around this minimum is

$$H(x) = \frac{1}{\sqrt{2}} \begin{pmatrix} 0 \\ v + h(x) \end{pmatrix} . \tag{2.1.38}$$

The mass of field in the SM is give with v. Implementing Eq. (2.1.36) into Eq. (2.1.1), the mass for leptons gives

$$\mathcal{L}_{h,l} = - \left(\frac{v+h}{\sqrt{2}} \right) \overline{E_L} Y^l E_R + \text{H.c.}, \tag{2.1.39}$$

where $E_L = V_L^{l\dagger} E'_L \equiv (e_L \; \mu_L \; \tau_L)$, $E_R = V_R^{l\dagger} E'_R \equiv (e_R \; \mu_R \; \tau_R)$, with V_L and V_R, diagonalising the matrix Y^l, $V_L^{l\dagger} Y'^l V_R^l = Y^l = y^l_\alpha \delta_{\alpha\beta}$ $(\alpha, \beta = e, \mu, \tau)$. We write Eq. (2.1.39)

$$\mathcal{L}_{h,l} = - \sum_{\alpha=e,\mu,\tau} \frac{y^l_\alpha v}{\sqrt{2}} \overline{E_\alpha} E_\alpha - \sum_{\alpha=e,\mu,\tau} \frac{y^l_\alpha}{\sqrt{2}} \overline{E_\alpha} E_\alpha h, \tag{2.1.40}$$

where $E_\alpha \equiv E_{\alpha L} + E_{\alpha R}$ $(\alpha = e, \mu, \tau)$ are the fields of the charged leptons with definite masses:

$$E_e \equiv e, \; E_\mu \equiv \mu, \; E_\tau \equiv \tau. \tag{2.1.41}$$

From the above, we find that in the only mass term for leptons Eq. (2.1.39), the SM neutrinos are massless, unless we introduce a chargeless particle of the SM, associated the Yukawa coupling of the SM neutrino and the SM Higgs boson. On the other hand, the masses for the charged leptons are give $m_\alpha = \frac{y^l_\alpha v}{\sqrt{2}}$.

2.2 Massive Neutrino

We have observed the change of the neutrino flavour as oscillations, which implies neutrinos have masses. However, from the previous section, we reach the conclusion that neutrinos are massless under the SM. As a result, the neutrino oscillation is taken as a concrete hint that the SM is not complete. The game of understanding the ultimate theory of the neutrino oscillation begins for the theoretical, phenomenological, and experimental scholars. In this section, we firstly go through the general way to extend the SM for massive neutrinos, before giving the brief introduction to neutrino oscillations.

2.2.1 Mass of Neutrino

This is unknown if SM neutrinos are Dirac or Majorana fermions, which affect how we extend the SM Lagrangian for the mass term for neutrinos. Except for neutrinos, we know that the SM fermions are Dirac particles. From Eq. (2.1.39), we know the Dirac mass term for neutrinos need the right-handed neutrino. On the other hand, the Majorana spinor satisfies the condition

$$\Psi = \Psi^C \equiv \mathcal{C}\overline{\Psi}^T, \tag{2.2.42}$$

where Ψ is a spinor, and $\mathcal{C}$ is the charge conjugation matrix, which can be expressed in terms of γ matrix $\mathcal{C} = i\gamma^2\gamma^0$.

The general way for the extension is the Dirac-Majorana neutrino mass term,

$$\mathcal{L}^{\mathrm{D+M}}_{\mathrm{mass}} = \mathcal{L}^{\mathrm{D}}_{\mathrm{mass}} + \mathcal{L}^{\mathrm{L}}_{\mathrm{mass}} + \mathcal{L}^{\mathrm{R}}_{\mathrm{mass}}, \tag{2.2.43}$$

where the Dirac mass term

$$\mathcal{L}^{\mathrm{D}}_{\mathrm{mass}} = -m_D \bar{\nu}_R \nu_L + \mathrm{H.c.}, \tag{2.2.44}$$

the Majorana mass term for left-handed neutrinos,

$$\mathcal{L}^{\mathrm{L}}_{\mathrm{mass}} = \frac{1}{2} m_L \nu_L^T \mathcal{C}^\dagger \nu_L + \mathrm{H.c.}, \tag{2.2.45}$$

and the Majorana mass term for right-handed neutrinos,

$$\mathcal{L}^{\mathrm{R}}_{\mathrm{mass}} = \frac{1}{2} m_R \nu_R^T \mathcal{C}^\dagger \nu_R + \mathrm{H.c.}. \tag{2.2.46}$$

Eqs. (2.2.44) and (2.2.46) are allowed, but ν_R needs to be a singlet of $\mathrm{SU}(3)_C \times \mathrm{SU}(2)_L \times \mathrm{U}(1)_Y$. However, the Majorana mass term for ν_L is not allowed by the symmetries of the SM because it is not invariant under the $\mathrm{SU}(2)_L \times \mathrm{U}(1)_Y$ transformation. In addition, Majorana mass term for ν_L breaks the lepton number. The lepton number is a global U(1) symmetry. The transformation of left-handed neutrinos under this symmetry is

$$\nu_L \to \mathrm{e}^{i\phi} \nu_L. \tag{2.2.47}$$

Therefore, Eq. (2.2.45) after the transformation becomes

$$\mathcal{L}^{\mathrm{L}}_{\mathrm{mass}} \to \frac{1}{2} \mathrm{e}^{2i\phi} m_L \nu_L^T \mathcal{C}^\dagger \nu_L + \mathrm{H.c.}. \tag{2.2.48}$$

Eq. (2.2.48) shows that lepton number does not conserve. The event with lepton-number breaking (*e.g.* neutrinoless double β decay, etc) is predicted, and can be used to confirm the Majorana property of neutrinos Eq. (2.2.42).

Smallness of ν mass

Some special limits can describe the smallness of neutrino masses in the framework Eq. (2.2.43). To understand this we study the 2-neutrino case by defining

$$N_L = \begin{pmatrix} \nu_L \\ \nu_R^C \end{pmatrix} = \begin{pmatrix} \nu_L \\ \mathcal{C} \bar{\nu}_R^T \end{pmatrix}, \tag{2.2.49}$$

and the Dirac-Majorana mass term is therefore

$$\mathcal{L}^{\mathrm{D+M}}_{\mathrm{mass}} = \frac{1}{2} N_L^T \mathcal{C}^\dagger M N_L + \mathrm{H.c.}, \tag{2.2.50}$$

with the symmetric mass matrix

$$M = \begin{pmatrix} m_L & m_D \\ m_D & m_R \end{pmatrix}. \tag{2.2.51}$$

The eigenvalues of M are

$$m_{2,1} = \frac{1}{2}\left[m_L + m_R \pm \sqrt{\left(m_L - m_R\right)^2 + 4m_D^2}\right]. \tag{2.2.52}$$

The Seesaw mechanism is when $m_D \ll m_R$ and $m_L = 0$. Under this limit,

$$m_1 \simeq \frac{m_D^2}{m_R},\ m_2 \simeq m_R. \tag{2.2.53}$$

Therefore, $\nu_2 \simeq m_R$ is heavy, but ν_1 is very light, due to the suppression by the ratio m_D/m_R.

We note that the Seesaw mechanism is a case of Weinberg operator, with which the Majorana mass $m \propto \frac{m_{\mathrm{D}}^2}{\mathcal{M}}$ is obtained, where $\mathcal{M}$ is a heavy mass characteristic of the symmetry-breaking scale of the high-energy unified theory.

$$\mathcal{L}^{\mathrm{D+M}} = -y^\nu \left(\bar{\nu}_R \widetilde{H}^\dagger L_L + \overline{L}_L \widetilde{H} \nu_R\right) + \frac{1}{2} m_R \left(\nu_R^{\mathrm{T}} \mathcal{C}^\dagger \nu_R + \nu_R^\dagger \mathcal{C} \nu_R^*\right), \tag{2.2.54}$$

where y^ν is a Yukawa coupling, and therefore

$$m_D = \frac{y^\nu v}{\sqrt{2}}. \tag{2.2.55}$$

Assuming the mass m_R is very heavy, the field ν_R can be integrated out at the SM electroweak energy scale by considering its static limit in which the kinetic term is neglected and the equation of motion is

$$0 \simeq \frac{\partial \mathcal{L}^{\mathrm{D+M}}}{\partial \nu_R} = m_R \nu_R^T \mathcal{C}^\dagger - y^\nu \overline{L}_L \widetilde{H}. \tag{2.2.56}$$

Eq. (2.2.54) can be therefore rewritten in the form,

$$\mathcal{L}_5^{\mathrm{D+M}} \simeq -\frac{\left(y^\nu\right)^2}{2m_R}\left[\left(L_L^T \tau_2 H\right) \mathcal{C}^\dagger \left(H^T \tau_2 L_L\right) - \left(\overline{L}_L \tau_2 H^*\right) \mathcal{C} \left(H^\dagger \tau_2 \overline{L}_L^T\right)\right]. \tag{2.2.57}$$

Below the electroweak symmetry-breaking, we can write,

$$\mathcal{L}_5^{\mathrm{D+M}} \simeq \frac{m_{\mathrm{D}}^2}{m_R}\left(\nu_{1L}^T \mathcal{C}^\dagger \nu_{1L} + \nu_{1L}^\dagger \mathcal{C} \nu_{1L}^*\right). \tag{2.2.58}$$

And, we get the Majorana mass term,

$$m_1 \simeq \frac{m_{\rm D}^2}{m_R}. \tag{2.2.59}$$

This is not the only way to get the Majorana mass term for neutrinos. For example, the type-II Seesaw mechanism, in which the left-handed Majorana mass m_L is small but nonzero, predicts that the mass m_L is generated by the new vacuum expectation value (VEV) of a Higgs triplet. This model predicts the Majorana mass for active neutrinos

$$m_L = g_v \frac{m_{\rm D}^2}{\mathcal{M}}, \tag{2.2.60}$$

where g_v is a numerical coefficient and $\mathcal{M}$ is a high-energy scale of new physics beyond the SM.

Mixing two models Eqs. (2.2.59) and (2.2.60) together, we have the mass term,

$$m_1 \simeq \left| g\frac{m_{\rm D}^2}{\mathcal{M}} - \frac{m_{\rm D}^2}{m_R} \right|, \; m_2 \simeq m_R. \tag{2.2.61}$$

When saying the 'type-II Seesaw', we consider the limit that $|m_L| \gg m_{\rm D}^2/m_R$; on the other hand, the 'type-I Seesaw' is when $|m_L| \ll m_{\rm D}^2/m_R$.

2.2.2 Two-neutrino mixing

Two-neutrino mixing is an approximation that only two massive neutrinos contribute the oscillation. In the case of two-neutrino mixing, we consider ν_α, ν_β, where (α, β) can be (e, μ), (e, τ), (μ, τ), or any linear combinations of pure flavour states for neutrinos; and we focus on the simple case that neutrinos travel in vacuum. for which the Hamiltonian is $\mathcal{H}_0$. The massive neutrino states $|\nu_k\rangle$ are eigenstates of the Hamiltonian,

$$\mathcal{H}_0|\nu_k\rangle = E_k|\nu_k\rangle, \tag{2.2.62}$$

with energy eigenvalues

$$E_k = \sqrt{\vec{p}^2 + m_k^2}. \tag{2.2.63}$$

The Schrodinger equation $i\frac{d}{dt}|\nu_k(t)\rangle = \mathcal{H}_0|\nu_k(t)\rangle$ implies that the massive neutrino states evolve in time as plane wavs:

$$|\nu_k(t)\rangle = {\rm e}^{-iE_k t}|\nu_k\rangle. \tag{2.2.64}$$

Two flavour neutrino states ν_α and ν_β are linear superpositions of two mass eigenstates ν_1 and ν_2 with the coefficients given by the elements of the two-neutrino effective mixing matrix

$$U_{2\times 2} = \begin{pmatrix} \cos\theta & \sin\theta \\ -\sin\theta & \cos\theta \end{pmatrix}, \tag{2.2.65}$$

where θ is the mixing angle, with a value in the interval $0 \leq \theta \leq \pi/2$. Therefore, we can write the flavour eigenstate in the form,

$$|\nu_{\mathrm{f}}\rangle = \sum_{k=1,2} U^*_{2\times 2,\mathrm{f}k} |\nu_k\rangle, \ (\mathrm{f} = \alpha, \ \beta). \tag{2.2.66}$$

And, both mass eigenstates $(\nu_k, \ \nu_j)$ and flavour eigenstates $(\nu_\alpha, \ \nu_\beta)$ satisfy the orthonormal condition:

$$\langle \nu_k | \nu_j \rangle = \delta_{k,j}, \tag{2.2.67}$$

and

$$\langle \nu_\alpha | \nu_\beta \rangle = \delta_{\alpha,\beta}. \tag{2.2.68}$$

Neutrinos are produced and detected in the eigenstates of flavour, but are propagated in vacuum in terms of mass state.

We consider the case that the neutrino of energy E is generated in the flavour state ν_α at the time 0, but detected in the state ν_β at the time t, $P(\nu_\alpha \to \nu_\beta, t)$.

$$|\nu_\alpha(t)\rangle = \sum_k U^*_{2\times 2,\alpha k} \mathrm{e}^{-iE_k t} |\nu_k\rangle, \tag{2.2.69}$$

where $|\nu_a(t=0)\rangle = |\nu_\alpha\rangle$. Implementing Eq. (2.2.66) into Eq. (2.2.69),

$$|\nu_\alpha(t)\rangle = \sum_{\mathrm{f}=\alpha,\beta} \left(\sum_k U^*_{2\times 2,\alpha k} \mathrm{e}^{-iE_k t} U_{2\times 2,\mathrm{f}k} \right) |\nu_{\mathrm{f}}\rangle. \tag{2.2.70}$$

The amplitude for the probability $P(\nu_\alpha \to \nu_\beta, t)$ as a function of time is given

$$A_{\alpha\beta}(t) \equiv \langle \nu_\beta | \nu_\alpha(t) \rangle = \sum_k U^*_{2\times 2,\alpha k} U_{2\times 2,\beta k} \mathrm{e}^{-iE_k t}. \tag{2.2.71}$$

The probability $P_{\nu_\alpha \to \nu_\beta}(t)$ is given

$$P(\nu_\alpha \to \nu_\beta, t) = |A_{\alpha\beta}(t)|^2 = \sum_{k,j} U^*_{2\times 2,\alpha k} U_{2\times 2,\beta j} U_{2\times 2,\alpha j} U^*_{2\times 2,\beta j} \mathrm{e}^{-i(E_k - E_j)t}. \tag{2.2.72}$$

For ultrarelativistic neutrinos, we can approximate the above equation in the form of

$$P_{\nu_\alpha \to \nu_\beta}(L, E) = \sum_{k,j} U^*_{2\times 2,\alpha k} U_{2\times 2,\beta j} U_{2\times 2,\alpha j} U^*_{2\times 2,\beta j} \exp -i \frac{\Delta m^2_{kj} L}{2E}, \tag{2.2.73}$$

where $L = ct$ is the distance between the source and the detector with the speed of light c, $\Delta m^2_{kj} = m^2_k - m^2_j$, and for 2ν mixing case, this is just $\Delta m^2 = m^2_2 - m^2_1$.

To extend Eq. (2.2.73) for three neutrino mixing, we enlarge the mixing matrix to a 3×3 matrix, and need to consider two mass-squared differences, before summing over all mass eigenstates.

In vacuum

In the case that neutrinos travel in vacuum, the states of neutrino are just the eigenstates given in Eq. (2.2.62) during the propagation. From Eq. (2.2.73), it is straightforward to derive the expression for the transition probability $\nu_\alpha \to \nu_\beta$ where $\alpha \neq \beta$

$$P(\nu_\alpha \to \nu_\beta, L, E) = \frac{1}{2} \sin^2 2\theta \sin^2 \left(\frac{\Delta m^2 L}{4E} \right). \tag{2.2.74}$$

For the survival probability $\nu_\alpha \to \nu_\alpha$ is

$$P(\nu_\alpha \to \nu_\alpha, L, E) = 1 - P(\nu_\alpha \to \nu_\beta, L, E) = 1 - \frac{1}{2} \sin^2 2\theta \sin^2 \left(\frac{\Delta m^2 L}{4E} \right). \tag{2.2.75}$$

From the above two equations, we find that the change of neutrino flavour depends on the factor L/E in the way as an oscillation. This is obvious that the amplitude of oscillation is controlled by the mixing angle and the frequency depends on the mass-squared difference. We notice that once $\theta = 0$ (no mixing) or $\Delta m^2 = 0$ (same mass), neutrinos do not oscillate. We finally note that flipping the sign of Δm^2 do not affect to the probability; as a result, we cannot distinguish the ordering of two mass states by reading the oscillation probability in vacuum.

In matter

While neutrinos travel in matter, the eigenstate defined in Eq. (2.2.62) needs to be modified by including the potential for the interaction with matter in the Hamiltonian,

$$\mathcal{H} = \mathcal{H}_0 + \mathcal{H}_I, \text{with } \mathcal{H}|\nu_\alpha\rangle = V_\alpha |\nu_\alpha\rangle, \tag{2.2.76}$$

where $V_\alpha = V_{CC}\delta_{\alpha e} + V_{NC} = \sqrt{2}G_\mathrm{F}\left(N_e\delta_{\alpha e} - \frac{1}{2}N_n\right)$. NC interactions are flavour-blind; this effect can be eliminated by shifting an overall phase. Therefore, in the Schrodinger picture, a neutrino state with the initial flavour α obeys the evolution equation

$$i\frac{\mathrm{d}}{\mathrm{d}t}|\nu_\alpha(t)\rangle = \mathcal{H}|\nu_\alpha(t)\rangle, \tag{2.2.77}$$

where $|\nu_\alpha(0)\rangle = |\nu_\alpha\rangle$. Because the CC interaction with matter is only involved the flavour e, we now assign the initial state and the final state are ν_e and ν_μ respectively.

Similar to Eq. (2.2.71), the amplitude of $\nu_e \to \nu_\mu$ after a time $t = cL$ is therefore

$$A^\mathrm{m}_{e\mu}(t) = \langle\nu_\mu|\nu_e(t)\rangle, \tag{2.2.78}$$

where $A'_{\nu_\alpha\to\nu_\beta}(0) = \delta_{\alpha\beta}$.

$$i\frac{\mathrm{d}}{\mathrm{d}x}\begin{pmatrix} A^\mathrm{m}_{ee} \\ A^\mathrm{m}_{e\mu} \end{pmatrix} = \mathcal{H}_\mathrm{F}\begin{pmatrix} A^\mathrm{m}_{ee} \\ A^\mathrm{m}_{e\mu} \end{pmatrix}, \tag{2.2.79}$$

where

$$\mathcal{H}_\mathrm{F} = \frac{1}{4E}\begin{pmatrix} -\Delta m^2\cos 2\theta + A_\mathrm{CC} & \Delta m^2 \sin 2\theta \\ \Delta m^2 \sin 2\theta & \Delta m^2\cos 2\theta - A_\mathrm{CC} \end{pmatrix}. \tag{2.2.80}$$

This matrix can be diagnoalized by the orthogonal transformation,

$$U^T_\mathrm{M}\mathcal{H}_\mathrm{F}U_\mathrm{M} = \mathcal{H}_\mathrm{M}, \tag{2.2.81}$$

where

$$\mathcal{H}_\mathrm{M} = \frac{1}{4E}\begin{pmatrix} -\Delta m^2_\mathrm{M} & 0 \\ 0 & \Delta m^2_\mathrm{M} \end{pmatrix} \tag{2.2.82}$$

is the effective Hamiltonian matrix in the mass basis in matter. The unitary matrix

$$U_\mathrm{M} = \begin{pmatrix} \cos\theta_\mathrm{M} & \sin\theta_\mathrm{M} \\ -\sin\theta_\mathrm{M} & \cos\theta_\mathrm{M} \end{pmatrix}, \tag{2.2.83}$$

and

$$\Delta m^2_\mathrm{M} = \sqrt{\left(\Delta m^2\cos 2\theta - A_\mathrm{CC}\right)^2 + \left(\Delta m^2 \sin 2\theta\right)^2} \tag{2.2.84}$$

is the effective mass-squared difference. And, the effective mixing angle is

$$\tan 2\theta_\mathrm{M} = \frac{\tan 2\theta}{1 - \frac{A_\mathrm{CC}}{\Delta m^2 \cos 2\theta}}. \tag{2.2.85}$$

Mikheev and Smirnov in 1985 discovered a resonance occurring when $A^R_{\rm CC} = \Delta m^2 \cos 2\theta$, which corresponds to the electron number density $N_e^{\rm R} = \frac{\Delta m^2 \cos 2\theta}{2\sqrt{2} E G_{\rm F}}$. When the resonance occurs, the mixing is maximal, and the effective mixing matrix Eq. (2.2.81) becomes

$$U^R_M = \begin{pmatrix} 0 & 1 \\ 1 & 0 \end{pmatrix}. \tag{2.2.86}$$

And, the effective mass-squared difference Δm^2_M goes to $\Delta m^2 \sin 2\theta$.

With the fixed matter density, the transition probability is given

$$P^{\rm m}(\nu_e \to \nu_\mu, L) = \left|A^{\rm m}_{e\mu}(L)\right|^2 = \sin^2 2\theta_M \sin^2\left(\frac{\Delta m^2_M L}{4E}\right), \tag{2.2.87}$$

and the surviving probability is therefore

$$P^{\rm m}(\nu_e \to \nu_e, L) = 1 - P^{\rm m}(\nu_e \to \nu_\mu, L) = 1 - \sin^2 2\theta_M \sin^2\left(\frac{\Delta m^2_M L}{4E}\right). \tag{2.2.88}$$

From Eq. (2.2.85), we find that flipping the sign of Δm^2 will enhance (suppress) the factor $\sin 2\theta_M$, leading the increase (decrease) of transition probability $P^{\rm m}(\nu_e \to \nu_\mu, L)$. The pattern of this impact is opposite between neutrino and antineutrino modes. And therefore, measuring the transition probability for two modes can be used for determining the mass ordering.

We show the survival and transition probabilities for two neutrino mixing in vacuum and in matter, in Figs. 2.1 and 2.2 respectively. The value of θ we used is 8°, and the oscillation distance is set 1300 km. For the case of oscillations in matter, we assume that the matter density is 3 g/cm^3. The distance and matter density are used according the official design for DUNE experiment. We set the absolute value of Δm^2 to be 2.5×10^{-3} eV^2, and flip the sign of the mass-squared difference for the case in matter, as we have not observed the impact of flipping this sign on the case in vacuum. In these plots, we see the impact of matter effects with the sign of mass-squared difference. As a result, matter effects can be used to break the degeneracy of mass ordering ($\Delta m^2 > 0$ or < 0).

2.2.3 Current understanding of the ν oscillation

The fundamental parameters which describe the oscillation phenomenon are the mixing angles and Dirac phase of the Pontecorvo-Maki-Nakagawa-Sakata (PMNS)

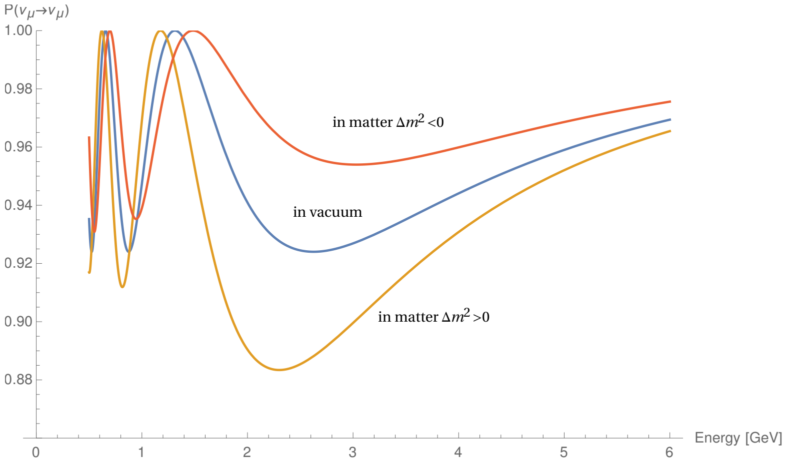

Figure 2.1: The survival probabilities for 2 neutrino mixing with $|\Delta m^2| = 2.5 \times 10^{-3}$ eV^2 and $\theta = 8°$ in vacuum (blue), in matter for $\Delta m^2 > 0$ (yellow), and for $\Delta m^2 < 0$ (red). The matter density is assumed 3 g/cm^3, and the oscillation distance is set 1300 km. The neutrino energy are considered in the range from 0.5 to 6 GeV.

mixing matrix as well as two independent mass-squared splittings *e.g.* Δm^2_{21} and Δm^2_{31}. The PMNS matrix is the mapping between the bases of mass and flavour states (denoted with Latin and Greek indices, respectively), which can be written as

$$\nu_\alpha = U^*_{\alpha i}\nu_i,$$

where U will be expressed by the conventional factorization [40]:

$$\begin{aligned} U_{\text{PMNS}} &= U_{23}U_{13}U_{12}P, \\ &= \begin{pmatrix} 1 & 0 & 0 \\ 0 & c_{23} & s_{23} \\ 0 & -s_{23} & c_{23} \end{pmatrix} \begin{pmatrix} c_{13} & 0 & s_{13}e^{-\mathrm{i}\delta} \\ 0 & 1 & 0 \\ -s_{13}e^{\mathrm{i}\delta} & 0 & c_{13} \end{pmatrix} \begin{pmatrix} c_{12} & s_{12} & 0 \\ -s_{12} & c_{12} & 0 \\ 0 & 0 & 1 \end{pmatrix} \begin{pmatrix} e^{\mathrm{i}\alpha_1} & 0 & 0 \\ 0 & e^{\mathrm{i}\alpha_2} & 0 \\ 0 & 0 & 1 \end{pmatrix}, \\ &= \begin{pmatrix} c_{12}c_{13} & s_{12}c_{13} & s_{13}e^{-\mathrm{i}\delta} \\ -s_{12}c_{23} - c_{12}s_{23}s_{13}e^{\mathrm{i}\delta} & c_{12}c_{23} - s_{12}s_{23}s_{13}e^{\mathrm{i}\delta} & s_{23}c_{13} \\ s_{12}s_{23} - c_{12}c_{23}s_{13}e^{\mathrm{i}\delta} & -c_{12}s_{23} - s_{12}c_{23}s_{13}e^{\mathrm{i}\delta} & c_{23}c_{13} \end{pmatrix} P(\alpha_1, \alpha_2), \end{aligned}$$

where $P(\alpha_1, \alpha_2)$ is a diagonal matrix containing two Majorana phases α_1 and α_2 which play no role in oscillation physics. The mixing angles θ_{12}, θ_{13} and θ_{23} are often referred to as the solar, reactor and atmospheric mixing angles respectively; all of these angles are now known to be non-zero [43].

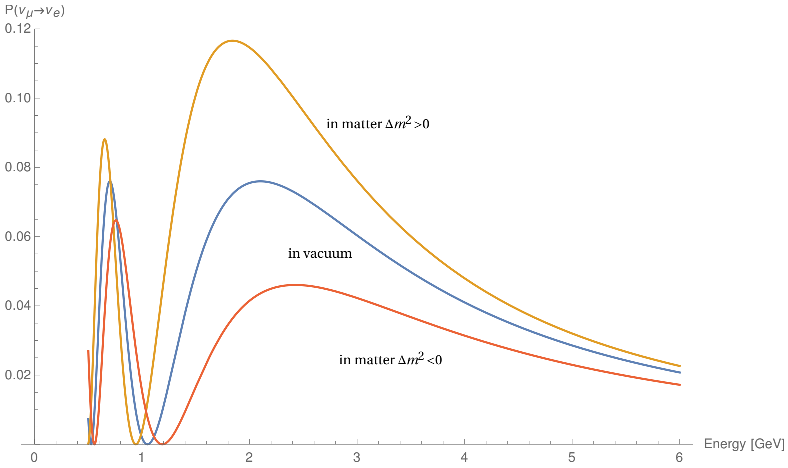

Figure 2.2: The tranisition probabilities for 2 neutrino mixing with $|\Delta m^2| = 2.5 \times 10^{-3}$ eV^2 and $\theta = 8^\circ$ in vacuum (blue), in matter for $\Delta m^2 > 0$ (yellow), and for $\Delta m^2 < 0$ (red). The matter density is assumed 3 g/cm^3, and the oscillation distance is set 1300 km. The neutrino energy are considered in the range from 0.5 to 6 GeV.

The current global fit results are presented in Tab. 2.3. This analysis combines the latest results (as of fall 2016) of solar, atmospheric, long baseline accelerator, and long, medium and short baseline reactor neutrino experiments, to obtain a combined fit to the six standard neutrino oscillation parameters. In Tab. 2.3, we show the results assumed two mass orderings $\Delta m^2_{31} > 0$ and < 0, which prefers the different octant of θ_{23}. The absolute value of Δm^2_{31} is around 2.5×10^{-3} eV^2. Two solutions for the mixing angle θ_{23} locate below and above the maximal value 45° for the normal and inverted ordering respectively. The rest of parameters are not significantly influenced by the assumption of mass ordering. θ_{12} is mainly measured by solar neutrino data, locates around 33°, while the result of the mixing angle θ_{13} is about 8°, encouraging the measurement of the DircaCP phase δ. The mass-squared splitting Δm^2_{21} is about 7.5×10^{-5} eV^2, and its sign is determined by solar data.

We see some hint for CP violation, though the precision still need to be improved. This parameter dictates the size of CP violating effects in vacuum during oscillation. All such effects will be proportional to the Jarlskog invariant of U_{PMNS},

$$J = \frac{1}{8} \sin\delta \sin(2\theta_{23}) \sin(2\theta_{13}) \sin(2\theta_{12}) \cos\theta_{13}.$$

For the theory to manifest CP violating effects, J must be non-zero. Given our

Parameter	Normal ordering	Inverted ordering
θ_{12} [°]	$33.56^{+0.77}_{-0.75}$	$33.56^{+0.77}_{-0.75}$
θ_{13} [°]	$8.46^{+0.15}_{-0.15}$	$8.49^{+0.15}_{-0.15}$
θ_{23} [°]	$41.6^{+1.5}_{-1.2}$	$50.0^{+1.1}_{-1.4}$
Δm^2_{21} [$\times 10^{-5}$ eV^2]	$7.49^{+0.19}_{-0.17}$	$7.49^{+0.19}_{-0.17}$
Δm^2_{3l} [$\times 10^{-3}$ eV^2]	$+2.524^{+0.039}_{-0.040}$	$-2.514^{+0.038}_{-0.041}$
δ [°]	306^{+39}_{-70}	254^{+63}_{-62}

Table 2.3: The true values used in our fit, unless otherwise stated explicitly, with their uncertainties (the 1σ range of the priors we have used in our fit). These are based on NuFit 3.0 (2017) [2], and are similar to the parameters found in other recent global fits (see *e.g.* [41, 42]).

knowledge of the mixing angles, the exclusion of $\delta \notin \{0, \pi\}$ would be sufficient to establish fundamental leptonic CP violation. In addition, the current precision on the oscillation parameters is insufficient to rule out many theoretical models, for example those discussed recently in Refs. [44–47], which offer predictions for δ, the octant, and the mass ordering.

Chapter 3

Details of Oscillation Experiments

In this chapter, we briefly introduce the oscillation experiments that are studied in this thesis. Our intention is one of future long baseline experiments (LBL) — Deep Understand Neutrino Experiment (DUNE). We further extend our interests in LBL to an other experiment — the Tokai to Hyper-Kamiokande (T2HK) experiment, especially for the standard neutrino oscillation. We study reactor experiments for Littlest Seesaw models as well in Ch. 9; these are also introduced in this chapter.

We are using the General Long Baseline Experiment Simulator (GLoBES) libraries [48,49] and in the following sections, we will describe the features of our modelling of these experiments, while the statistical treatment is described in App. A.3. In this chapter we first introduce the experimental and simulation details of DUNE and T2HK in Sec. 3.1, before coming up with the description for the reactor experiments in Sec.3.2.

3.1 Long Baseline Experiments

3.1.1 DUNE

The DUNE experiment consists of a new neutrino source, known as Long Baseline Neutrino Facility (LBNF), a near detector based at Fermilab and a LArTPC detector complex located in SURF a distance of 1300 km away. Several variants of the LBNF beam have been developed. In this work, we study three neutrino fluxes: a 2-horn

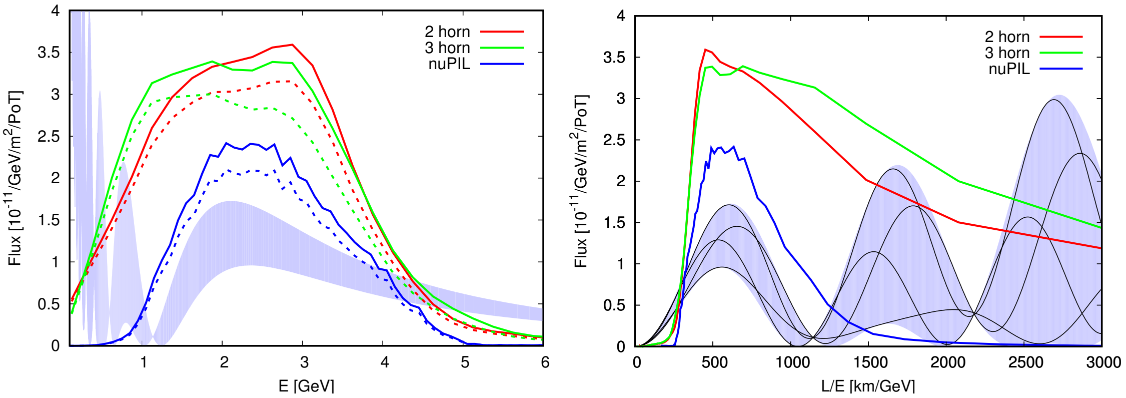

Figure 3.1: Left: ν_μ ($\overline{\nu}_\mu$) flux component in ν-mode ($\bar{\nu}$-mode) shown as solid (dashed) lines for 2-horn optimised, 3-horn optimised, and nuPIL beam designs. Right: the fluxes for ν-mode shown as a function of L/E. In both panels, the shaded region shows the envelope of the oscillation probability as δ is varied over its full range. The black lines in the right panel show the probability for $\delta \in \{0, \frac{\pi}{2}, \pi, \frac{3\pi}{2}\}$.

optimised beam design [12, 52], a 3-horn optimised beam design [50, 51], and the neutrinos from a PIon beam Line (nuPIL) [53–55, 57]. We show all three fluxes used in our simulations in Fig. 3.1.

The 2-horn optimised beam has been designed to maximise the sensitivity to CP violation [12]. In our simulation, we take the proton energy to be 80 GeV, and follow a staged implementation of the beam power in line with the DUNE proposal, which assumes the beam power will double after 6 years [58]. Our simulation assumes a power of 1.07 MW and 1.47×10^{21} protons on target (POT) per year for the first 6 years, and 2.14 MW (2.94×10^{21} POT per year) afterwards. Thanks to constant development work by the DUNE collaboration, an additional optimised beam has also been designed. This 3-horn design has a stronger focus on producing lower energy events, leading to an increase in flux between 0.5 GeV and 1.5 GeV. This leads to a greater number of expected events from around the second oscillation maximum, which is well-known to be particularly sensitive to the phase δ. For this design, the proton energy is assumed to be 62.5 GeV and the POT per year is taken as 1.83×10^{21}, before doubling at the 6th year in line with the expected beam upgrade. At the time of writing this thesis, in the last meeting of DUNE collaboration at CERN in January of 2018, the 3-horn design is officially considered.

We also consider the nuPIL design, which was designed by a working group of the DUNE collaboration as a potential alternative design. Although this design is no longer considered to be an option for the LBNF beam, its novelty leads to interesting phenomenological consequences and we study it alongside the main beam design. nuPIL foresees the collection and sign selection of pions from proton collisions with a target which are then directed though a beam line and ultimately decay to produce neutrinos. This selection and manipulation of the secondary beam forces unwanted parent particles out of the beam resulting in lower intrinsic contamination of the neutrino (antineutrino) flux by antineutrinos (neutrinos). In particular, this would improve the signal to background ratio of the antineutrino mode compared to a conventional neutrino beam. The proton energy for this design is assumed to be 80 GeV, and the corresponding POT per year is 1.47×10^{21} which again doubles after 6 years. Compared to the other two designs, nuPIL offers a lower intrinsic contamination from other flavours and CP states while maintaining low systematic uncertainties. We note that nuPIL also expects a smaller total flux, although this might be avoidable through further design effort. Another characteristic of the nuPIL design is its notably narrower flux. As events from the second oscillation maximum are expected to be highly informative about the true value of δ, this may impact the sensitivity to δ. The coverage of first and second maxima is seen clearly in the right-hand panel of Fig. 3.1, where the fluxes are shown as a function of L/E. The first maximum ($L/E \approx 600$ km/GeV) is covered comparably well for all three flux designs, while the flux at the second maximum ($L/E \approx 1800$ km/GeV) varies significantly. The 2-horn design is seen to be similar to the 3-horn design: the two designs are very similar around the first maximum, but the 2-horn design sees slightly fewer events at higher values of L/E.

Although we consider alternative fluxes, we always assume the same detector configuration of four 10-kiloton LArTPC detectors at 1300 km from the neutrino source. We neglect the possibility of staging, assuming that all four tanks are operational at the same time, and do not account for the expected improvement in performance throughout the lifetime of the detectors. LArTPC technology has a particularly strong particle identification capability as well as good energy resolution which are both crucial in providing high efficiency searches and low backgrounds. We model the LArTPC detector response with migration matrices incorporating the results of parameterized Monte Carlo simulations undertaken by the collaboration [52]. We use fourteen migration matrices — seven each for the disappearance and appearance channels — describing the detection and reconstruction of all three flavours of neutrino and antineutrino, as well as generic flavour blind NC events.

We include both appearance and disappearance searches in our study. The appearance channel signal is taken as the combination of ν_e and $\bar{\nu}_e$ charged-current (CC) events. For the disappearance channel, we study ν_μ and $\bar{\nu}_\mu$ for neutrino and antineutrino modes, respectively. The backgrounds to the appearance channel are taken as neutral-current (NC) events, mis-identified $\nu_\mu + \bar{\nu}_\mu$ CC interactions, intrinsic $\nu_e + \bar{\nu}_e$ CC events, and $\nu_\tau + \bar{\nu}_\tau$ CC events. On the other hand, in ν_μ and $\bar{\nu}_\mu$ disappearance we consider NC events, $\nu_\mu + \bar{\nu}_\mu$ CC events, and $\nu_\tau + \bar{\nu}_\tau$ CC events. These assumptions follow the collaboration's own analysis [12]. The rates of these backgrounds are governed by the migration matrices.

We assume the same systematic errors for all beam designs. The reduction of the systematic errors is an ongoing task in the collaboration, and our values are based on the conservative end of the current estimates of 1–2% [12, 52]. As such, we take an overall normalization error on the signal (2% for appearance and 5% for disappearance) and on the background rates (5% for ν_e, $\bar{\nu}_e$, ν_μ, and $\bar{\nu}_\mu$ CC events, 10% for NC interactions, and 20% for ν_τ and $\bar{\nu}_\tau$ CC events). This accounts for fully correlated uncertainties on the event rates in each bin, and we do not consider uncorrelated uncertainties. We note the nuPILdesign could lower the systematic error with respect to the conventional design, although the extent of this is unknown, and beating 1% systematics will be challenging.

3.1.2 T2HK

The Tokai to Hyper-Kamiokande (T2HK) experiment [59] is the proposed next-generation long-baseline experiment using a neutrino beam produced at the synchrotron at J-PARC in Tokai directed 2.5° off-axis to Hyper-Kamiokande (Hyper-K), a new water Čerenkov detector to be built near Kamioka, 295 km from the beam

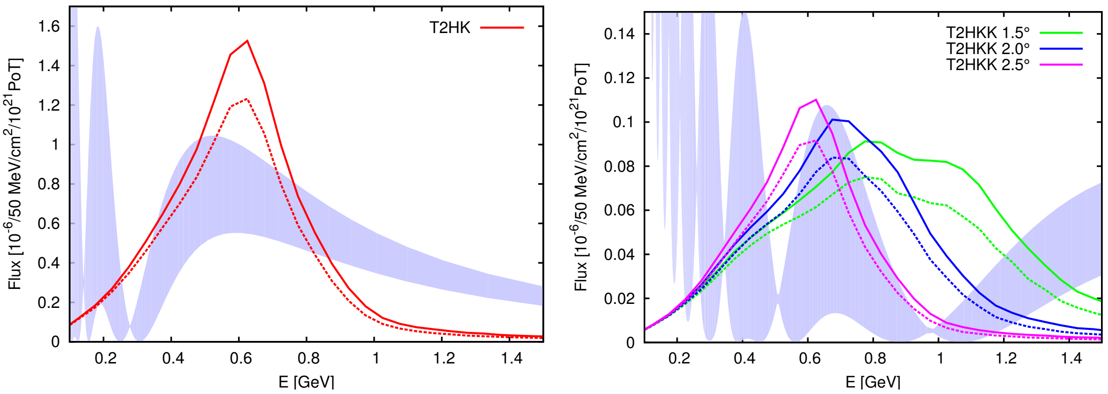

Figure 3.2: Left: T2HK's flux plotted against neutrino energy for ν-mode (solid) and $\overline{\nu}$-mode (dashed). Right: the T2HKK fluxes plotted against energy for ν and $\overline{\nu}$ modes. The shaded region shows the envelope of the probability found by varying the true value of δ. Due to T2HKK's longer baseline but comparable energy range to T2HK, the fluxes on the right sample a very different part of the probability.

source. The narrow-band beam comprises mostly of ν_μ (or $\bar{\nu}_\mu$), with the energy peaked near 600 MeV corresponding to the first oscillation maximum at 295 km. Hyper-K is capable of detecting interactions of ν_μ, $\bar{\nu}_\mu$, ν_e and $\bar{\nu}_e$, allowing measurements of the oscillation probabilities $P(\nu_\mu \to \nu_e)$, $P(\nu_\mu \to \nu_\mu)$, $P(\bar{\nu}_\mu \to \bar{\nu}_e)$, $P(\bar{\nu}_\mu \to \bar{\nu}_\mu)$ with the primary goal of searching for CP violation and measuring δ_{CP}.

The J-PARC neutrino beam will be upgraded from that used for the T2K experiment to provide a beam power of 1.3 MW [60, 61]. The beam is produced from 30 GeV protons colliding with a graphite target. Charged pions produced in these collisions are focused through magnetic horns into a decay volume, where the majority of the neutrinos in the beam are the ν_μ ($\bar{\nu}_\mu$) produced from the π^+ (π^-) decay. The polarity of the 320 kA horn current can be reversed to focus pions of positive or negative charge in order to produce a beam of neutrinos or antineutrinos respectively. A small contamination (less than 1% of the neutrino flux) of ν_e or $\bar{\nu}_e$ in the beam and $\bar{\nu}_\mu$ (ν_μ) in the ν_μ ($\bar{\nu}_\mu$) beam result from the decay of the μ^+ (μ^-) produced in the pion decay, however the majority of the $\mu^\pm$ are stopped after reaching the end of the decay volume before decaying.

The baseline design for the Hyper-Kamiokande detector consists of two water tanks each with a total (fiducial) mass of 258 kt (187 kt) [62]. Each tank is sur-

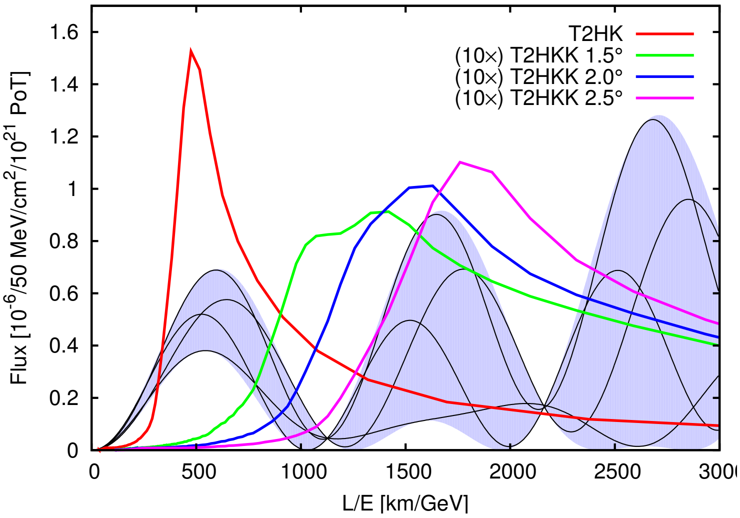

Figure 3.3: The T2HK and T2HKK fluxes shown as a function of L/E. The shaded region shows the envelope of the probability for $L = 1100$ km and the black lines indicate the specific behaviour for $\delta \in \{0, \frac{\pi}{2}, \pi, \frac{3\pi}{2}\}$. Note that the T2HK flux actually samples from the probability with a smaller matter effect corresponding to its shorter baseline $L = 295$ km; however, on this scale the location of the first maximum does not deviate much from what is shown here.

rounded by approximately 40,000 inward facing 50 cm diameter photosensors corresponding to a 40% photocoverage, equivalent to that currently used at Super-Kamiokande. The tanks would be built and commissioned in a staged process with the second tank starting to take data six years after the first. The detectors use the water Čerenkov ring-imaging technique as used at Super-Kamiokande, capable of detecting the charged leptons produced in neutrino interactions on nuclei in water. At these energies, most neutrino–nucleus interactions are quasi-elastic, and the measurement of the outgoing charged lepton allows for an accurate reconstruction of the energy and flavour of the initial neutrino.

We have developed an up-to-date GLoBES implementation of T2HK, incorporating the collaboration's latest estimates for detector performance[1]. Our simulation is based on the GLoBES implementation of T2HK [63] with comprehensive modifi-

---

[1] We thank the Hyper-Kamiokande proto-collaboration for kindly providing us with this information.

cations to match the latest experimental design. The beam power and fiducial mass have been updated to 1.3 MW and 187 kt per tank. For our studies we have used the staged design with one tank operational for 6 years followed by two operational tanks beyond that time. In cases where we show results against the run time of the experiment, we have used additional simulations with just a single tank operational throughout to highlight the discontinuous nature of this design.

The neutrino flux and channel definitions have been updated to match those of [59], with separate channels for four interaction types (charged current quasielastic, charged current with one pion, other charged current and neutral current), for the $\nu_\mu \to \nu_e$ and $\bar{\nu}_\mu \to \bar{\nu}_e$ signals, and unoscillated ν_e, $\bar{\nu}_e$, ν_μ and $\bar{\nu}_\mu$ backgrounds. New tables of pre-smearing efficiencies and migration matrices have been created for each channel based on the full detector simulations used in [59]. New cross-sections for interactions on water for the four interaction types have been generated using the GENIE Monte-Carlo neutrino interaction event generator [64].

The simulation determines the event rates for signal and background components for each of $\nu_\mu/\bar{\nu}_\mu \to \nu_e/\bar{\nu}_e$ appearance and $\nu_\mu/\bar{\nu}_\mu \to \nu_\mu/\bar{\nu}_\mu$ disappearance measurements in neutrino mode and antineutrino mode. The rates are determined for 12 energy bins, given in App. A.2. For the appearance measurements, the energy range is restricted to 0 GeV to 1.25 GeV, so only bins 1 to 8 are included. All bins are included in the disappearance measurements. Separate uncorrelated systematic errors are assumed on the total signal and background rates for each of the four measurements, where the size of the errors assumed, summarised in A.2, are the same as in the official Hyper-K studies after an adjustment to account for correlations between systematics not included in our simulations.

The design of T2HKK [65] and the location of the second detector module are still under development. As such, physics studies are being performed for a number of simulated fluxes with varying off-axis angles, generally ranging from on-axis to 2.5° off-axis, which is aligned with the first detector in Kamioka. The novelty of this design is not only the longer baseline distance, which will enhance the role of matter effects, but also the fact that the energy profile of the flux remains similar to that at the detector at 295 km, meaning that the oscillation probability is sampled at very different values of L/E. This results in the second detector having access to increased spectral information, which can help to break degeneracies and enhance overall sensitivity [66]. This is clearly seen in Fig. 3.2, where the left panel shows how the flux aligns with the first maximum of the probability at Kamioka while the right panel shows that the fluxes align around the second maximum for the Korean detector. When plotted against L/E, as in Fig. 3.3, we see that the T2HK flux has only minor coverage of the second maximum in contrast to T2HKK. The fluxes used in our simulation were provided by the Hyper-Kamiokande proto-collaboration and were produced in the same way as the fluxes used in [59] but with a baseline of 1100 km and off-axis angles of 1.5°, 2.0° and 2.5°.

3.1.3 Total number of events for all configurations

In Table 3.1, we show the expected total rates for events and backgrounds for all configurations, discussed in this work. We adopt the true values according to NuFit 3.0, shown in Tab. 2.3, but assume $\delta = 0$. Two mass orderings are considered. For all cases, cumulative run time is set 10 years. For DUNE, we take events from 0.5 GeV to 8 GeV, while for the other configurations we take from 0.1 GeV to 1.2 GeV.

3.2 Details for the other experiments

For the short and medium baseline reactor experiments, we have included basic constraints on the values of $\sin^2\theta_{13}$, $\sin^2\theta_{12}$ and Δm^2_{21}. Since these measurements are expected to be approximately independent of other parameters we have implemented these constraints as simple Gaussian measurements with a mean of the true simulated value and error as given in Table 3.2.

Short baseline reactor experiments

By observing the oscillations of the $\bar{\nu}_e$ produced in nuclear reactors, short baseline reactor neutrino experiments are able to measure the mixing angle θ_{13} with particularly high accuracy. The Daya Bay experiment [67] currently has the most precise measurement of this parameter with the aim to achieve a precision on $\sin^2\theta_{13}$ of better than 3% [68]. The experiment measures anti-neutrinos produced in six nuclear reactors in south China. A total of eight 20 t liquid scintillator detectors are used; two are located at each of two near detector sites and four at a far detector site L =1.5 to 1.9 km from the reactors near the first atmospheric neutrino oscillation maximum for $\Delta m^2_{31} \sim 2.5 \times 10^{-3}$ eV^2, given the low nuclear energy of the neutrino beam $E \sim$ few MeV. Results of the Double Chooz [69] and RENO [6, 70] short baseline reactor experiments also contribute to the precision obtained on θ_{13} combined with the Daya Bay result. Although DUNE and T2HK will also measure this parameter with high precision, the measurement of the short baseline reactor programme by that time is expected to be at least as precise, and will provide a measurement independent of the other parameters which influence the appearance channel at long-baseline accelerator experiments.

Medium baseline reactor experiments

The Jiangmen Underground Neutrino Observatory [5] (JUNO) and the future plans of the Reactor Experiment for Neutrino Oscillation (RENO-50) [6] are medium baseline reactor neutrino experiments which, like the Daya Bay experiment, will observe the oscillations of electron anti-neutrinos produced in nuclear reactors. The JUNO experiment will use a 20 kt liquid scintillator detector approximately L =53 km from two planned nuclear reactors in southern China, while RENO-50 will use an 18 kt liquid scintillator detector approximately L =50 km from a nuclear reactor in South Korea. Given the low nuclear energy of the neutrino beam $E \sim$ few MeV, these longer baselines correspond to the first solar neutrino oscillation maximum for $\Delta m^2_{21} \sim 7.5 \times 10^{-5}$ eV^2, where the higher frequency atmospheric oscillations appear as wiggles. Thus the longer baseline than at Daya Bay gives greatest sensitivity to a different set of oscillation parameters, in particular θ_{12} and Δm^2_{21}. The precision on the measurements of both $\sin^2\theta_{12}$ and Δm^2_{21} is expected to reach 0.5% [5, 6].

	$\nu_\mu \to \nu_e$		$\nu_\mu \to \nu_\mu$		$\overline{\nu}_\mu \to \overline{\nu}_e$		$\overline{\nu}_\mu \to \overline{\nu}_\mu$	
	NO	IO	NO	IO	NO	IO	NO	IO
2-horn DUNE (total)	2353	1589	13269	13189	667	1210	13180	13095
2-horn DUNE (BG)	486	502	200	203	253	252	111	112
3-horn DUNE (total)	2317	1561	13773	13774	587	1087	5125	5081
3-horn DUNE (BG)	488	504	199	203	228	227	90	92
nuPIL DUNE (total)	1209	721	5756	5801	230	580	2079	2077
nuPIL DUNE (BG)	111	116	84	85	43	42	38	38
staged T2HK (total)	2294	2514	9221	9157	2093	2715	10997	10855
staged T2HK (BG)	522	525	619	619	695	694	805	805
1tank T2HK (total)	1638	1795	6587	6540	1495	1939	7855	7754
1tank T2HK (BG)	373	375	442	442	496	495	575	575
T2HKK1.5° (total)	207	196	3151	3066	288	275	4453	4362
T2HKK1.5° (BG)	96	96	117	117	148	148	176	176
T2HKK2.0° (total)	163	154	1913	1854	198	194	2331	2256
T2HKK2.0° (BG)	51	51	53	53	71	71	63	63
T2HKK2.5° (total)	121	116	1269	1283	135	146	1322	1328
T2HKK2.5° (BG)	29	29	36	36	37	37	41	41

Table 3.1: The total rate of events and backgrounds for all configurations with cumulative run time of 10 years, assuming $\delta = 0$ for normal ordering (NO) and inverted ordering (IO). The true values are adopted according to the best of NuFit 2.2, shown in Tab. 2.3. For all configurations of DUNE, we take events from 0.5 GeV to 8 GeV, while for the others we take from 0.1 GeV to 1.2 GeV.

Experiment	Parameter	Precision
Short baseline reactor	$\sin^2\theta_{13}$	3%
Medium baseline reactor	$\sin^2\theta_{12}$	0.5%
Medium baseline reactor	Δm^2_{21}	0.5%

Table 3.2: Precision of oscillation parameter measurements made by reactor experiments which we have used as constraints in our simulations.

Chapter 4

Standard Neutrino Oscillation

Albeit the high precision for θ_{12}, θ_{13} and Δm^2_{12} is seen in Tab. 2.3, the unknowns remain: the ordering of neutrino masses, the existence and extent of CP violation (CPV) in leptonic mixing, and the precise value, including crucially the octant, of θ_{23}. The remaining parameter in U is the phase δ, which is currently poorly constrained by data. In this chapter, we firstly understand neutrino oscillations at DUNE and T2HK by studying the approximation equations for the probabilities. Then, we see how the oscillation probabilities for DUNE and T2HK depend on the mass ordering, the θ_{23} octant, and the CP violation. In the final section, we learn the phenomenology of δ measurement in DUNE and T2HK in detail.

4.1 Neutrino Oscillations at DUNE and T2HK

Long-baseline experiments such as DUNE and T2HK aim to improve our knowledge of U, as well as the atmospheric mass-squared splitting, by the precision measurement of both the appearance $\nu_\mu \to \nu_e$ and disappearance oscillation channels $\nu_\mu \to \nu_\mu$, as well as their CP conjugates. In this chapter, we will discuss the key aims of the long-baseline program and the important design features of these experiments which lead to their sensitivities. To facilitate this discussion, we introduce an approximation of the appearance channel probability following Ref. [71], which is derived by performing a perturbative expansion in the small parameter

$\epsilon \equiv \Delta m^2_{21}/\Delta m^2_{31} \approx 0.03$ under the assumption that $\sin^2\theta_{13} = \mathcal{O}(\epsilon)$[1]. The expression for the oscillation probability is decomposed into terms of increasing power of ϵ,

$$P(\nu_\mu \to \nu_e; E, L) \equiv P_1 + P_{\frac{3}{2}} + \mathcal{O}\left(\epsilon^2\right), \tag{4.1.1}$$

where E is the neutrino energy, L the oscillation baseline, and the ordered terms $P_n = \mathcal{O}(\epsilon^n)$ are given by

$$P_1 = \frac{4}{(1-r_A)^2}\sin^2\theta_{23}\sin^2\theta_{13}\sin^2\left((1-r_A)\Delta_{31}L\right), \tag{4.1.2}$$

$$P_{\frac{3}{2}} = 8J_r\frac{\epsilon}{r_A(1-r_A)}\cos\left(\delta + \Delta_{31}L\right)\sin\left(r_A\Delta_{31}L\right)\sin\left((1-r_A)\Delta_{31}L\right), \tag{4.1.3}$$

where $J_r = \cos\theta_{12}\sin\theta_{12}\cos\theta_{23}\sin\theta_{23}\sin\theta_{13}$, $r_A = 2\sqrt{2}G_{\mathrm{F}}N_eE/\Delta m^2_{31}$ and $\Delta_{31} = \Delta m^2_{31}/4E$. Using the same scheme, the disappearance channel can be written at leading order as

$$P(\nu_\mu \to \nu_\mu; E, L) = 1 - \sin^2(2\theta_{23})\sin^2\left(\Delta_{31}L\right) + \mathcal{O}(\epsilon). \tag{4.1.4}$$

For both channels, equivalent expressions for antineutrino probabilities can be obtained by the mapping $r_A \to -r_A$ and $\delta \to -\delta$.

We show the transition probability $P(\nu_\mu \to \nu_e)$ ($P(\bar{\nu}_\mu \to \bar{\nu}_e)$) in L/E [km/100 GeV] in E [GeV] in Fig. 4.1 (Fig. 4.2) for $\delta = 0$ (red), 90° (black), 180° (blue), and 270° (green), for DUNE (left) and T2HK (right), because this channel is used to solved the rest unknowns of the neutrino oscillation. The normal mass ordering is assumed. We note that the first maximum is around 500 [km/GeV], while the second one is around 1500 [km/GeV]. We see the larger variation with δ for the second maximum, for both experiments. Further, because of matter effects, the probability for DUNE is generally higher than that for T2HK. In the following sections, we will discuss how this oscillation mode would solve the remaining oscillation problems.

---

[1] For alternative schemes of approximation, see Ref. [72–75]. The resent work Ref. [76], presenting the approximation to oscillation probabilities for LBLs — T2K, NOνA, T2HKK, DUNE with high accuracy, is based on the result in Ref. [75], but is in a more conventional notation.

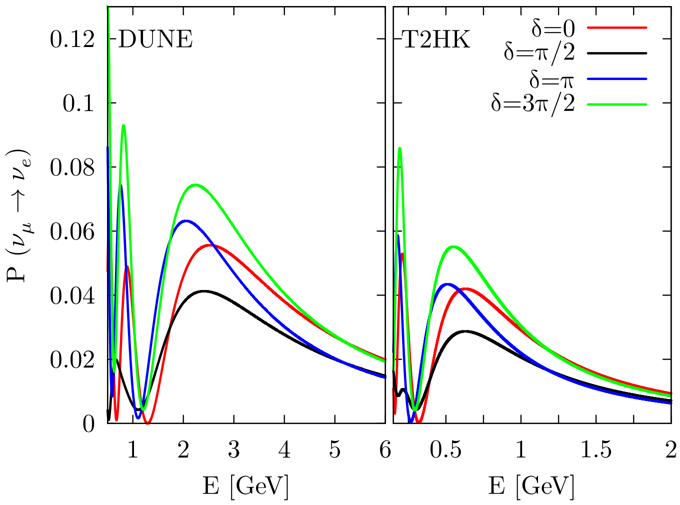

Figure 4.1: The transition probability $P(\nu_\mu \to \nu_e)$ in E [GeV], assumed normal ordering and $\delta = 0$ (red), 90° (black), 180° (blue), and 270° (green), for the neutrino mode, for DUNE (left) and T2HK (right). We note that the first minimum is around 500 [km/100GeV].

4.2 Mass ordering, CPV and the octant of θ_{23}

The sensitivity of long-baseline experiments to the questions of the neutrino mass ordering, the existence of CPV and the octant of θ_{23}, are by now well studied topics (for a recent review see *e.g.* Ref. [84]). To help us clarify the role of the designs of DUNE and T2HK, as well as their possible modifications, we will briefly recap how experiments on these scales derive their sensitivities using the approximate formulae expressed by Eqs. (4.1.2), (4.1.3) and (4.1.4).

The dependence on the sign of Δm^2_{31}, and therefore the mass ordering, arises at long-baseline from the interplay with matter, where forward elastic scattering can significantly enhance or suppress the oscillation probability. This is governed by the parameter r_A in Eq. (4.1.1), which for the experiments of interest is small, and goes to zero in the absence of matter. Changing from Normal Ordering (NO, $\Delta m^2_{31} > 0$) to Inverted Ordering (IO, $\Delta m^2_{31} < 0$) requires the replacements $\Delta_{31} \to -\Delta_{31}$ and $r_A \to -r_A$. However, in vacuum ($r_A = 0$) the leading-order term in Eq. (4.1.1) remains invariant under this mapping. This invariance is broken once a matter term

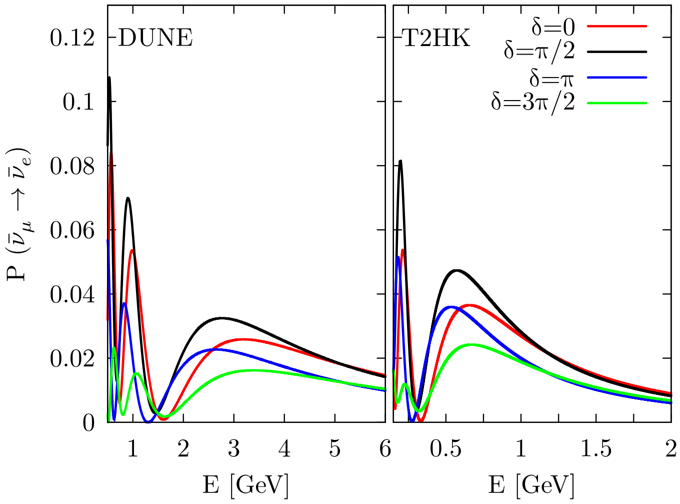

Figure 4.2: The transition probability $P(\bar{\nu}_\mu \to \bar{\nu}_e)$ in E [GeV], assumed normal ordering and $\delta = 0$ (red), 90° (black), 180° (blue), and 270° (green), for the neutrino mode, for DUNE (left) and T2HK (right). We note that the first minimum is around 500 [km/100GeV].

is included ($r_A \neq 0$), and the oscillation probability acquires a measurable enhancement or suppression dependent on the sign of Δm^2_{32}. The size of this enhancement increases with baseline length, and this effect is expected to be very relevant for appearance channels at a long-baseline experiment $\nu_\mu \to \nu_e$ and $\bar{\nu}_\mu \to \bar{\nu}_e$. However, the determination of the mass ordering is further facilitated by the contrasting behaviour of neutrinos and antineutrinos. Due to the dependence on r_A, for NO larger values of the matter density cause an enhancement in the probability for $\nu_\mu \to \nu_e$ oscillation at the first maximum, whilst suppressing the probability for $\bar{\nu}_\mu \to \bar{\nu}_e$. This behaviour is reversed for IO, with neutrinos seeing a suppression and antineutrinos, an enhancement. Moreover, matter effects also affect the energies of the first oscillation maxima for neutrinos and antineutrinos. Through precise measurements around the first maxima, these shifts can be observed allowing long-baseline oscillation experiments to determine the mass ordering.

To detect CPV in neutrino oscillation an experiment requires sensitivity to δ. Unfortunately, the leading order appearance probability is independent of the CP phase

δ in vacuum. CP asymmetries between neutrino and antineutrino channels first appear with the subdominant term $P_{\frac{3}{2}}$. In the presence of a background medium, CP violating effects are instead introduced in P_1; however, these offer no sensitivity to the fundamental CP violating parameter δ, arising instead from the CP asymmetry of the background medium itself via the parameter r_A. As the sensitivity to δ is subdominant and masked by CP asymmetry arising from matter effects, extracting the CP phase is a more challenging measurement, requiring greater experimental sensitivity. Long baseline (LBL) experiments can obtain sensitivity to δ by looking not only at the first maximum but also at the spectral differences between CP conjugate channels. In particular, an important role is played by low-energy events in the sensitive determination of δ [77–80]: around the second maximum, CP dependent terms of the oscillation probability are more significant. Although accessing these events can be a challenging experimental problem, and low statistics or large backgrounds could limit their potential [80], their benefit is clear from recent experimental work [81].

The atmospheric mixing angle is known to be large and close to maximal $\theta_{23} \approx \pi/4$, but it is not currently established if it lies in the first octant $\theta_{23} < \pi/4$ or the second octant $\theta_{23} > \pi/4$. We see in Eq. (4.1.2) that the appearance channel is sensitive to the octant. However, we also see that changing the octant enhances or suppresses the first maximum of the appearance channel in much the same way as the matter enhancement. For this reason, the sensitivity to these questions can be expected to be correlated; however, this correlation will be reduced when data from both neutrino and antineutrino is available as this effect is the same in both CP conjugate channels. The determination of θ_{23} is also known to be beset by issues of degeneracy with δ which can complicate its determination [82–84]. As both of these parameters enter the second-order terms in Eq. (4.1.3), the freedom to vary δ can be used to mask the effects of a wrong octant, making their joint determination more challenging. Fortunately, a precise measurement of $\sin(2\theta_{23})$ is possible through the disappearance channel, helping to break this degeneracy. Also, spectral information is expected to mitigate this problem.

4.3 Precision on δ

Although the question of the *existence* of leptonic CP violation often dominates discussions about δ, the precision measurement of δ could prove to be the most valuable contribution of the long-baseline programme. To determine the existence of fundamental leptonic CP violation it suffices to exclude the CP conserving values $\delta = 0$ and $\delta = \pi$, those values corresponding to a vanishing Jarlskog invariant. Therefore the discovery potential of a facility to CP violation is fundamentally linked to the precision attainable for measurements of δ in the neighbourhood of 0 and π. However, the question of precision on δ goes beyond CP violation discovery. Many models of flavour symmetries, for example, are consistent with the known oscillation data and make predictions for δ.[2] No experiment on comparable time-scales will be able to compete with precision measurements of δ from DUNE and T2HK.

It can be shown that the precision expected on δ worsens significantly around $\delta = \pm\frac{\pi}{2}$, and that this is because of the probability itself [92]. Looking at the CP sensitive term in Eq. (4.1.3) at energies around the first maximum, where $\Delta_{31}L \approx \pi/2$, we can approximate the probability by

$$P_{\frac{3}{2}} \approx -8J_r \frac{\epsilon}{r_A(1-r_A)} \sin\delta \sin\left(r_A\Delta_{31}L\right) \sin\left((1-r_A)\Delta_{31}L\right).$$

The highest sensitivity to δ is found when this function is most sensitive to changes in δ, information naturally encoded in the function's first derivative. Due to the sinusoidal nature of the function, when the CP term has its largest effect ($|\sin\delta| = 1$), it is at a maximum and consequently its gradient is at a minimum. Therefore, we expect the errors on δ to be small around 0 and π, when even though the absolute size of the CP sensitive terms are small, they are most sensitive to parameter shifts. Taking matter effects into account moves the location of the worst sensitivity away from $\delta = \pm\frac{\pi}{2}$. Assuming we are close to the first maximum, and introducing a dimensionless parameter ξ to describe the deviation from this point (where $\xi = 0$ corresponds to the first maximum), the relevant parameter governing the phase of

---

[2] For example, recent studies of mixing sum rules can be seen as predicting δ for long-baseline experiments [85–89]. For a review of the predictions from such models, see *e.g.* Refs. [90] and [91].

the sinusoidal terms can be expressed by

$$2\Delta_{31}L = \pi\frac{1+\xi}{1-r_A}, \tag{4.3.5}$$

we can find the value of δ for which we expect the worst sensitivity by minimising the gradient of Eq. (4.1.3), which occurs for the values

$$\delta \approx -\frac{\pi}{2}\frac{1+\xi}{1-r_A} + \pi n, \tag{4.3.6}$$

for $n \in \mathbb{Z}$. From this formula it is clear that the value of δ with the worst sensitivity shifts away from $\frac{(2n+1)\pi}{2}$ in a direction governed by the signs of r_A and ξ. Specifically, the dependence on r_A means that the neutrino and anti-neutrino mode sensitivities at fixed energy have their worst sensitivity for different true values of δ. Running both CP conjugate channels in a single experiment allows each channel to compensate for the poorer performance of the other at certain values of δ, helping to smooth out the expected precision [92]. In this way, the multichannel nature of LBL experiments allows for a greater physics reach than a single channel experiment.

The argument above assumed that all events came from a fixed energy defined implicitly by ξ in Eq. (4.3.5). Due to the dependence on ξ in Eq. (4.3.6), having information from different energies will also be complementary, acting analogously to the combination of neutrino and antineutrino data by mitigating the poorest performance. Although all LBL experiments aim to include the first maximum, where event rates are highest, none have a purely monochromatic beam and so-called wide-band beams include considerable information from other energies. Therefore such experiments can be expected to avoid the significant loss of sensitivity predicted by the simple analytic formula. We can infer, however, that a narrow beam focused on the first maximum in the presence of small matter effects should have a worse sensitivity at maximal values of δ compared to CP conserving values [92].

With reference to the traditional designs of T2HK and DUNE, from the above discussion we can infer that T2HK can be expected to have a greater range of expected precisions as we vary δ than DUNE. In particular, due to its narrower beam and small matter effects, we expect markedly poorer performance for T2HK at $\delta \in \{-\frac{\pi}{2}, \frac{\pi}{2}\}$. DUNE on the other hand will be less variable as its broad band mitigates the total loss of sensitivity at certain energies, and its large matter effect helps to stabilise performance, but it can be expected to see its worst sensitivity at values of δ slightly displaced from 0 and π, where the sensitivity at the first maximum is worst. This suggests a degree of complementarity of the wide-band and narrow-band beams when it comes to precision measurements of δ: a narrow-band focused on the first maximum is optimal for precision around 0 and π (and by implication, for CPV discovery) while a wide-band beam should perform better for precision measurements around $\delta = \pm\frac{\pi}{2}$. This general behaviour will be relevant not only for the traditional designs of DUNE and T2HK, but also their possible redesigns: nuPIL could lead to a narrowing of the neutrino flux, and T2HKK could see a wider-band component in its flux, or a narrow-band component focused away from the first maximum. The interplay of these factors will be explored in more detail in Ch. 6.

Chapter 5

Sensitivity to mass ordering, CPV, non-maximal CPV, and octant

In this chapter, we present the results of our simulation studying the sensitivity of the standard configurations of DUNE and T2HK. This means we use the 2-horn optimised flux for DUNE with a staged beam upgrade after 6 years, while for the T2HK detector we assume the installation of a second detector module after 6 years. More details of these configurations can be found in Sec. 3.1 . However, for comparison, we also include two unstaged options: where the experiments continue without upgrading at the 6 year mark. We stress that these are not the baseline configurations of the experiments, and that they are interesting for comparison purposes only. The run time and neutrino–antineutrino sharing for these configurations are discussed in more detail in App. A.1. After considering these benchmark configurations and their complementarity, we will return to the potential of alternative designs in Ch. 7.

Through out this chapter, each section focus on different measurement of standard oscillations. From the first to the final section, we study the mass ordering, CP violation sensitivity, the sensitivity to CP violation, the sensitivities to octant degeneracy and θ_{23} measurement. In this chapter, except δ we implement 1-D χ^2 data from NuFit 3.0 for priors, of which the impact is described in App. A.3.

5.1 Mass ordering sensitivity

The mass ordering is one of the central goals of the next generation of LBL experiments; it is also one of the easiest to measure with this technology. We quantify the ability to determine the mass ordering by computing the following test statistic,

$$\Delta\chi^2_{\mathrm{MO}} = \min_{\{\Theta,\xi_s,\xi_b\}} \left[\chi^2(\mathrm{sgn}\Delta m^2_{31} = \mathrm{true}) - \chi^2(\mathrm{sgn}\Delta m^2_{31} = \mathrm{false})\right] . \tag{5.1.1}$$

That is to say, the smallest value of the χ^2 function for any parameter set with the wrong ordering. All parameters are allowed to vary during marginalisation whilst preserving the ordering. Although our composite hypothesis violates the assumptions of Wilks' theorem [93, 94], and therefore invalidates the mapping between $\sqrt{\Delta\chi^2}$ and σ-valued significance for discrimination of the two hypotheses, we stick to convention in this section, reporting the expected sensitivities for the median experiment in terms of $\sqrt{\Delta\chi^2}$ and discussing it in terms of σ. For the reader who is interested in the precise formulation of the statistical interpretation of $\sqrt{\Delta\chi^2}$, see *e.g.* Ref. [95].

The sensitivity we find in Fig. 5.1 is very strong. DUNE, with its large matter effects, can expect a greater than 8.5σ measurement of the mass ordering after 10 years for all values of δ, with an average sensitivity of around 12σ and a maximal sensitivity of around 17σ. T2HK alone has limited access to this measurement due to its shorter baseline, but can still expect a greater than 3σ measurement for around 25% of the possible values of δ after 10 years of data-taking. The combination of DUNE and T2HK running for 10 years each can reach sensitivities of at least 15σ, with an average of around 18σ. Care should be taken when interpreting such large significances; however, it is clear that DUNE, and the combination of DUNE and T2HK, can expect a very strong determination of the mass ordering. We also note the strong complementarity here: for the values of δ where DUNE performs the worst, the information from T2HK helps to raise the global sensitivity by about 7σ. Despite this interesting interplay, the fact that this is such an easy measurement for

---

[0] An updated version of the NuFit global fit (NuFit 3.0) was released after we had concluded this study. We have, however, checked that no significant differences occur if we implement new priors based on its results.

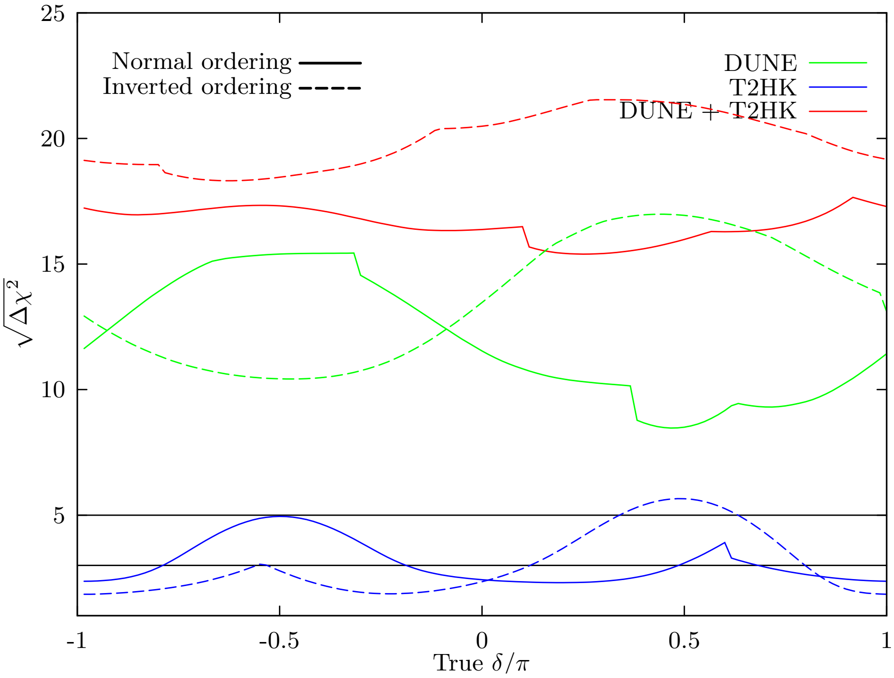

Figure 5.1: The sensitivity to the mass ordering for DUNE and T2HK in isolation and combined for true normal ordering (solid) and inverted ordering (dashed). This plot assumes the "fixed run time" configurations in Table A.1 and the true oscillation parameters given in Table 2.3.

experiments of this type, means that we will not dwell on the question of optimising such a measurement further.

Our sensitivities in Fig. 5.1 deviate from previous published values for DUNE, and we generally report a worse ability for DUNE to exclude the ordering, with lower average sensitivity and visibly discontinuous behaviour in the values of $\Delta\chi^2$. This is due to the priors that we have imposed. Instead of a Gaussian approximation to the global data, we implement the global 1D χ^2 functions, as provided by NuFit [43]. The true global data has strongly non-Gaussian behaviour at high significance, and there exist non-standard parameter sets which are not excluded at greater than 6σ. These parameter sets sometimes become the best-fitting wrong-ordering solution, and must be excluded to rigorously establish the mass ordering. We discuss this in more detail in Appendix B. We point out, however, that our priors do not always significantly affect the point of minimum sensitivity, and DUNE still expects to see a greater than 5σ discovery for all true values of δ. For example, in Fig. 5.1, we have found for the lowest MO sensitivity over δ, in the case of inverted ordering, this degeneracy problem driven by our prior occurs, while for the other ordering, the minimum cannot see those non-standard parameter sets. We find that the complications due to degeneracies are only relevant for the very highest significances.

Another way to understand the complementarity of DUNE and T2HK is in terms of minimal run time necessary to ensure a $\sqrt{\Delta\chi^2} > 5$ measurement regardless of the true value of δ. We plot this quantity in Fig. 5.2, for normal ordering (left) and inverted ordering (right). The shaded bands take into account the variation in sensitivity due to the true value of θ_{23}. DUNE alone takes between 2 and 4 years to reach this sensitivity, while the combination of DUNE and T2HK always takes less than 3 years (which if run in parallel is only 1.5 years). T2HK running alone cannot ensure a measurement of this significance over any plausible run time. We note the small discontinuity along with the upper bound for both orderings after about 4 years run time for DUNE. This marks the appearance of a degenerate solution due to the non-Gaussianity of our priors as discussed before (and in more detail in Appendix B). We also show explicitly the difference in minimal sensitivity for T2HK with (solid lines) and without (dashed lines) a second staged detector module at Kamioka, as well as for DUNE with (solid lines) and without (dashed lines) the upgraded accelerator complex. For T2HK, the increase in performance is negligible, but DUNE as well as the combination of DUNE and T2HK sees a notable performance increase.

5.2 CP violation sensitivity

To fulfil the central aim of the LBL programme, the experiments must be able to rule out CP conservation over a large fraction of the true parameter space. This would imply a non-zero Jarlskog invariant and rigorously establish CP violation in the leptonic sector. Once again, we follow the conventional test statistic and define the quantity

$$\Delta\chi^2_{\mathrm{CP}} = \min_{\delta\in\{0,\pi\}} \Delta\chi^2(\delta), \tag{5.2.2}$$

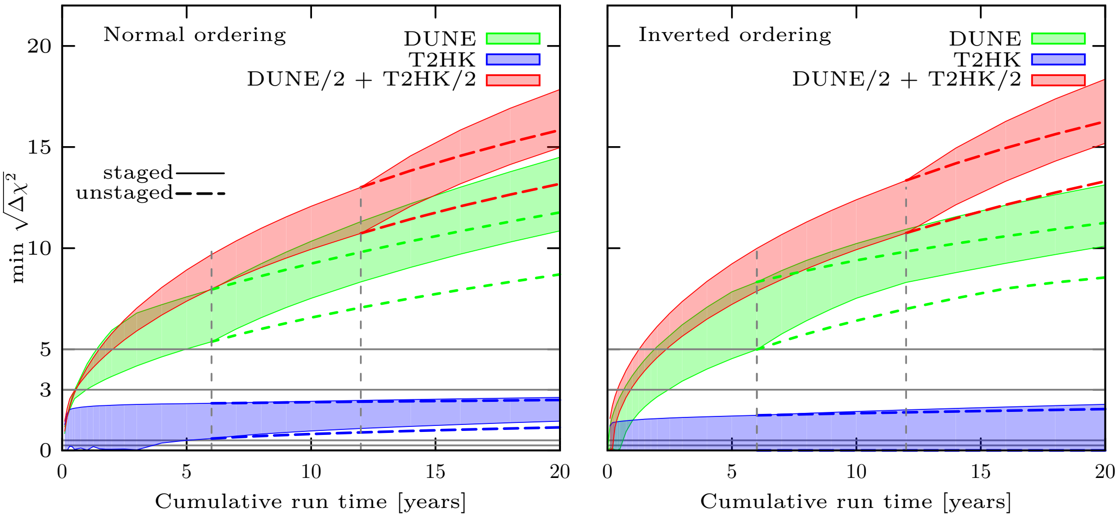

Figure 5.2: The least sensitivity for discovering mass ordering, $\min(\sqrt{\Delta}\chi^2)$, which can be reached by DUNE, T2HK and their combination as a function of cumulative run time. The width of the bands shows the sensitivity for $40^\circ \leq \theta_{23} \leq 50^\circ$. The left (right) panel assumes normal (inverted) ordering. These plots assume the "variable run time" configurations in Table A.1 and the true oscillation parameters, apart from θ_{23}, given in Table 2.3. The vertical lines mark the introduction of a staged second detector for T2HK and/or a increase in the beam power for DUNE. They lead to a notable discontinuity in sensitivity.

which amounts to studying the composite hypothesis of CP conservation ($\delta = 0$ or $\delta = \pi$) [96]. Although at low-significance this test statistic is known to deviate from a χ^2 distribution [97], we expect such effects to be small for the experiments under consideration in this study.

For the discovery of CP violation, the true value of the mass ordering and octant are relevant. We do not specify these values, and have studied the sensitivity for all combinations of values. We show in the left panel of Fig. 5.3 the significance for exclusion of CP conservation for the standard designs of the two facilities, in isolation and combination. We find that both experiments have a high sensitivity to this measurement, with at least a 3σ (5σ) discovery of CPV over 70–75% (46–47%) of the parameter space for DUNE and 73–80% (26–51%) for T2HK. For $0 \leq \delta \leq \pi$, we see a notable difference in behaviour between DUNE and T2HK: the sensitivity for T2HK is limited, and much more dependent on the true value of θ_{23}. This is due to the inability of T2HK to resolve the mass ordering degeneracy, which leads to a degenerate approximately CP conserving solution for these regions of parameter space. We point out that, as DUNE provides high MO sensitivity, the combination of data from DUNE and T2HK does not suffer from this problem, and sees significant improvements in sensitivity for these values of δ. Aside from this limitation, the general shape of these curves can be understood by our discussion in Section 4.3. Discovery potential for CPV is closely related to the precision on δ at the CP conserving values, both rely on distinguishing between *e.g.* $\delta = 0$ and other values. The best sensitivity to CP conserving values of δ is at the first maximum, where the majority of T2HK events are found and consequently it sees a better sensitivity. Our plots have assumed NO, but the qualitative picture remains the same for IO: in this case, the degeneracy occurs for the $-\pi \leq \delta \leq 0$, but otherwise the two regions of δ swap roles and the sensitivites are similar. We note, however, that the current best-fit values of θ_{23} would lead to additional suppression of CPV sensitivity for IO. The global data associates IO with a value of θ_{23} in the higher octant, which predicts poorer sensitivity to δ.

As we mentioned in the last paragraph of Section A.3, our prior correlates the allowed octant to the mass ordering, and this is responsible for differences between our results and previously published work. In Fig 6 of Ref. [98], there is almost no CPV sensitivity for $0 < \delta < \pi$ for T2HK, which has not been found in our results, while their results for DUNE are similar to ours. This feature is explained as being due to the lack of MO sensitivity at T2HK, allowing for degeneracies to limit the sensitivity. In our simulation, however, T2HK alleviates this problem by its strong determination of the octant and the correlation of the global data. This lifts the degeneracy to higher significances, and allows a higher sensitivity to be obtained before the limiting effect becomes relevant.

We find that DUNE performs slightly better in our simulation than is reported in the left panel of Fig 3.13 in Ref. [12]. Around $\delta = \pi/2$ $(-\pi/2)$, their result shows the sensitivity is about 5.8 (4.8).[1] However, our simulation finds a range of between 7.8 to 9.0 (6 to 8σ) for $\delta = -\pi/2$ ($= \pi/2$). There are two sources for this discrepancy. Firstly, we are assuming a longer run time (10 years), for the purposes of comparison between T2HK and DUNE. Secondly, our priors are based on newer data, with updated central values and smaller 1σ intervals. The CPV sensitivity for DUNE does not peak around $\delta = -\pi/2$ in the left panel of Fig 3.13 in Ref. [12] like our results, due to the relatively poor determination of the octant. DUNE does not have as strong octant sensitivity as for the mass ordering, but our prior correlates the two, helping to reduce the impact of this alternative minimum for values of δ around $\delta = -\pi/2$. Finally, we find general agreement between our results and those of Fig. 119 in Ref. [59]. This is because the mass ordering is fixed during fitting in Ref. [59], which mitigates the impact of the mass ordering degeneracy. This leads to superficial agreement between our two sets of results when the degeneracy is not relevant, but discrepancies when it is. Our result shows the sensitivity which is possible assuming only the current global data, whereas assuming the MO is known would require new external data, perhaps from another long-baseline experiment.

In the right panel of Fig. 5.3, we show the fraction of values of δ for which a 5σ exclusion of CP conservation can be made as a function of run time. DUNE requires between 5 and 7 years of data-taking to reach at least a 5σ measurement for 25% of the possible values of δ, while T2HK alone shows a stronger dependence on θ_{23} but expects to be able to make at least a 5σ measurement for more than 25% of the parameter space after 8 years. The combination of DUNE and T2HK is shown as a function of cumulative run time, the sum of the individual run times for each experiment, and as such interpolates the two sensitivities. However, if run in parallel, the combination of the two experiments performs stronger than either in isolation, and expects a greater than 5σ measurement for more than 50% of the parameter space after between 1.5 and 2.5 years of parallel data-taking.

---

[1] The range given in their work is for various beam designs. The result for the design we consider is at the bottom of the range.

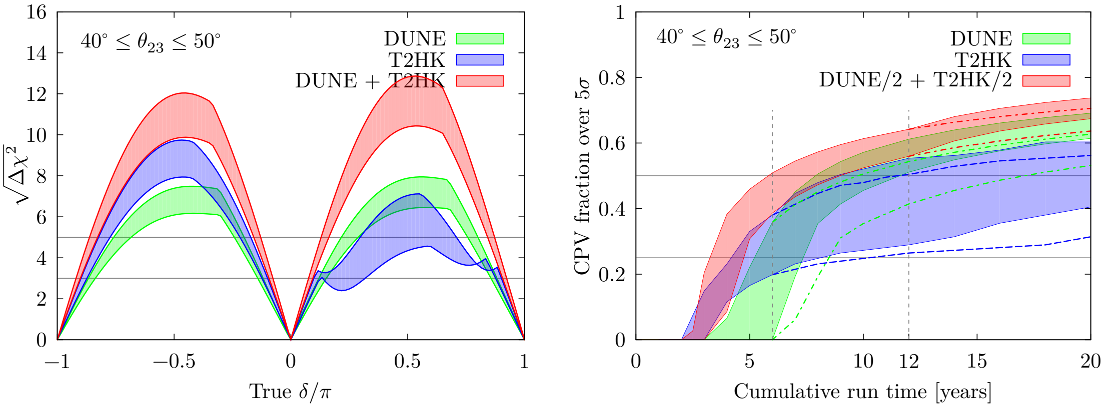

Figure 5.3: The sensitivity to CP violation for DUNE and T2HK in isolation and combined as a function of delta (left) and the fraction of δ parameter space for which greater than 5σ CPV discovery is expected (right). We consider a range of true θ_{23} spanning both octant solutions. The lower edge of the shaded regions corresponds to $\theta_{23} > 45^\circ$ due to a decrease in sensitivity arising from the relative suppression of the CP sensitive terms in Eq. (4.1.1). The left (right) plot assumes the "fixed run time" ("variable run time") configurations in Table A.1 and the true oscillation parameters, apart from θ_{23}, specified in Table 2.3.

5.3 Sensitivity to maximal CP violation

Although the search for any non-zero CPV is the principle goal of the next LBL experiments, understanding the value of δ is also highly relevant. Current global fits [41–43] point towards maximal values of δ, $\delta = \pm\pi/2$. Of course, these should be treated with some scepticism: no single experiment can claim evidence for this at an appreciable level. However, determining if a maximal CP violating phase exists will remain a high priority for the next generation of long-baseline experiments. If established, it could be seen as an "unnatural" value advocated as evidence against anarchic PMNS matrices. Indeed, it is also one of the most common predictions in flavour models with generalised CP symmetries, and is often associated with close to maximal values of θ_{23} in models with residual flavor symmetries. For more discussion, see *e.g.* Ref. [90, 91].

We have studied this question in Fig. 5.4 where we have defined the quantity

$$\Delta\chi^2_{\mathrm{MCP}} = \min_{\delta\in\{-\frac{\pi}{2},\frac{\pi}{2}\}} \Delta\chi^2(\delta). \tag{5.3.3}$$

This is analogous to $\Delta\chi^2_{\mathrm{CP}}$ defined earlier, and gives us a measure of the compatibility of the data with the hypothesis of maximal CP violation. On the left panel, we see the ability to exclude maximal CPV as a function of the true value of δ. There is a similar sensitivity for both facilities. DUNE has the best performance for most cases, but T2HK still achieves the highest significance exclusions while $-3\pi/4 < \delta < -\pi/2$ and $0 < \delta < \pi/2$; although, its sensitivity is more affected by the value of θ_{23} and the mass ordering. In this way, the two experiments once again exhibit a complementarity, and the combination of DUNE and T2HK inherits the best sensitivity of its two component parts, expecting a 3σ exclusion of MCP for over 48–54% of the parameter space.

On the right panel of Fig. 5.4, we show the fraction of true values of δ for which a 5σ exclusion of maximal CP violation can be achieved. By running in parallel for 10 years, DUNE and T2HK can expect a coverage at this significance of around 42–50% of the parameter space. Once again we see T2HK's sensitivity is more dependent on θ_{23} and generally lower than DUNE's.

5.4 Octant degeneracy and the precision on θ_{23}

Although we know that θ_{23} is around 45°, the current global fit data allows for two distinct local minima, one below and one above 45°. This ambiguity is known as the octant degeneracy and arises as the disappearance channel of $\nu_\mu \to \nu_\mu$ is sensitive at leading-order only to $\sin^2 2\theta_{23}$. However, the appearance channel breaks this degeneracy at leading-order, and future long-baseline experiments are expected to significantly improve our knowledge of θ_{23}. In this section, we study how well DUNE and T2HK will be able to measure θ_{23} as well as settling two central questions: is θ_{23} maximal, and which is its correct octant? These questions are also of particular theoretical significance as many models with flavour symmetries exist which predict close to maximal values of θ_{23}, and often the size of its deviation from this point is in correlation to other parameters like δ [90,91]. Therefore, determining the octant (or

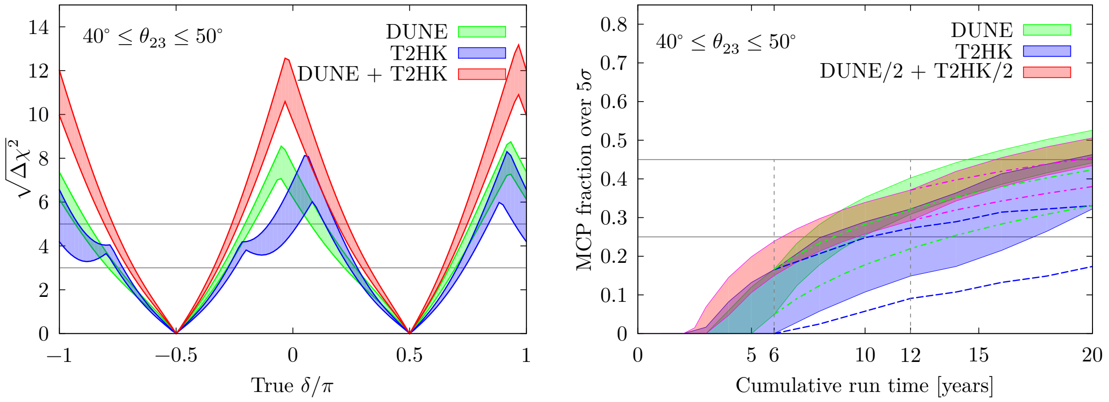

Figure 5.4: Left: the significance at which maximal CP can be excluded for DUNE and T2HK in isolation and combined as a function of true δ. Right: the fraction of δ-parameter space for which maximal CP can be excluded as a function of run time. The left (right) plot assumes the "fixed run time" ("variable run time") configurations in Table A.1 and the true oscillation parameters, apart from θ_{23}, specified in Table 2.3.

maximality) of θ_{23} would be highly instructive in our search to understand leptonic flavour.

The ability to exclude the wrong octant for DUNE, T2HK and their combination is shown in Fig. 5.5. On the left, we show the sensitivity as a function of the true value of θ_{23}. In these plots we assume a fixed value of $\delta = 0$. The impact of varying δ for these measurements is small, as the degeneracy is broken at leading-order in the appearance channel, and the subdominant effects of δ are less relevant. The ability to exclude the wrong octant can reach up to 8σ at the extremes of the current 3σ range of θ_{23}, and we see that 3σ determinations of the upper (lower) octant can be expected for true values of $\sin^2\theta_{23}$ less than 0.47–0.48 (greater than 0.54–0.55). This corresponds to a 3σ determination of the octant for all values of θ_{23} in the ranges $\theta_{23} \lesssim 43.3^\circ$–$43.8^\circ$ or $\theta_{23} \gtrsim 47.3^\circ$–$48.4^\circ$. On the right, we fix the true value of θ_{23} and show how the sensitivity depends on cumulative run time. We see that the sensitivity quickly plateaus, and the staging options make little difference. Overall, the experiments expect to be able to establish the octant for this value of θ_{23} after only 2 to 4 years. Although this plot assumes $\theta_{23} = 40^\circ$, changing the true value of

θ_{23} leads to a predictable change in sensitivity, as indicated in the left panel, but does not qualitatively change the behaviour against run time. We see that overall, T2HK performs better than DUNE for the determination of the octant. However, the difference in performance is marginal, and their combination after 10 years of data for each experiment, outperforms T2HK running alone for 20 years, but preforms slightly worse than DUNE with 20 year of total run time.

In this simulation, we have not imposed a prior on θ_{23}. This process differs from Ref. [12], in which they give a gaussian prior for θ_{23}. It also differs from the fitting method in Ref. [59], where they fit θ_{13}, θ_{23} and the value of Δm^2_{31} without implementing any priors, but fix θ_{12}, Δm^2_{21} and the mass ordering. In Ref. [98], the details of the fitting process are not specified. Despite these differences, we see qualitatively similar behaviour between the three sets of results. We find the regions of θ_{23} where the octant cannot be determined at 5σ to be $\theta_{23} \in [43°, 49.7°]$, $\theta_{23} \in [42°, 48.9°]$, and $\theta_{23} \in [43°, 48.7°]$ for DUNE, T2HK, and their combination, respectively. In Fig. 3.18 of Ref. [12], the equivalent region for DUNE is $\theta_{23} \in [41°, 50°]$, which is comparable to our work. In the middle panels of Fig. 5 in Ref. [98], the authors estimate the region as $42.5° < \theta_{23} < 48.5°$ for T2HK and the combination of DUNE and T2HK, while for DUNE alone the range is slightly smaller than in our simulation at $42° < \theta_{23} < 49°$. Compare to our results, in Fig. 125 of Ref. [59], we find the bigger range at 5σ level is $0.44 < \sin^2\theta_{23} < 0.58$.

In Fig. 5.6, we show the analogous plots for the exclusion of maximal θ_{23}. We see that maximal θ_{23} can generally be excluded at greater significance than the octant. T2HK can reach 5σ sensitivity for $\sin^2\theta_{23} \lesssim 0.47$ as well as for $\sin^2\theta_{23} \gtrsim 0.55$, while DUNE can make an exclusion at the same statistical significance for $\sin^2\theta_{23} \lesssim 0.45$ and $\sin^2\theta_{23} \gtrsim 0.56$. Due to its poorer sensitivity, DUNE plays less of a role in the combination and DUNE + T2HK follows the sensitivity of T2HK. On the right, we show the sensitivity against cumulative run time. Again, the combination of DUNE + T2HK performs similarly to T2HK when the cumulative run time is divided by two, while DUNE performs slightly worse. We see that the staging of T2HK and DUNE plays a notable role, leading to significantly higher sensitivities.

We study the attainable precision on $\sin^2\theta_{23}$ in Fig. 5.7, where we plot $\Delta(\sin^2\theta_{23})$

against the true value of $\sin^2\theta_{23}$ for normal mass ordering. For all configurations, we see the same behaviour: the uncertainty climbs up from about $\sin^2\theta_{23} = 0.48$ and falls down around $\sin^2\theta_{23} = 0.54$, peaking at $\sin^2\theta_{23} \sim 0.51$. This is expected for a measurement dominated by the disappearance channel, where the probability is proportional to $\sin^2(2\theta_{23})$ and a leading-order analytic treatment would imply the relation

$$\Delta(\sin^2\theta_{23}) \propto |\tan(2\theta_{23})|\,,$$

which naively predicts a total loss of sensitivity at maximal mixing, analogous to $\Delta\delta$ at $\delta = \pi/2$. This is mitigated by higher-order effects, as well as the information from the appearance channel, which becomes important around these values. The drop in sensitivity seen in Fig. 5.7 is quite sharp, and for values of $\sin^2\theta_{23}$ away from maximal mixing there is only modest variation in precision. For DUNE, $\Delta(\sin^2\theta_{23})$ is about 0.009 at the boundaries, and peaks up to the value ~ 0.038. T2HK has better performance, with $\Delta(\sin^2\theta_{23}) \sim 0.005$ for $\sin^2\theta_{23} = 0.43$ and 0.585. As with DUNE, the worst performance for T2HK is near the peak at $\sin^2\theta_{23} = 0.5$ with $\Delta(\sin^2\theta_{23}) \sim 0.032$. Largely leaving from $\theta_{23} = 45^\circ$, the combination of DUNE and T2HK performs very similarly to T2HK, as T2HK's high sensitivity drives that of the combination. However, the improvement of including DUNE data is viewable around the peak of $\Delta\sin^2\theta_{23}$. In these plots, we set $\delta = 0$, although qualitatively similar behaviour holds for other choices. There is, however, a correlation between the precision on θ_{23} and δ. We present an estimate of the joint precision on θ_{23} and δ attainable at DUNE and T2HK in Fig. 5.8. In this plot, each ellipse shows the 1σ allowed region for a set of true values inside its boundary taken from the sets $\delta \in \{0^\circ, \pm 90^\circ, \pm 180^\circ\}$ and $\theta_{23} \in \{40^\circ, 45^\circ, 50^\circ\}$. T2HK generally performs slightly better for this measurement; although, at times DUNE achieves a marginally better sensitivity to δ, and the combination of additional data from DUNE helps to reduce the T2HK contours. A minor correlation can be seen due to the reliance on data from both the appearance and disappearance channels. The best measurements will be obtained for large deviations from θ_{23}-maximality and values of δ close to the CP conserving values, where DUNE (T2HK) can expect precisions on θ_{23} of $\Delta\theta_{23} = 0.2^\circ$ ($\Delta\theta_{23} = 0.13^\circ$). Conversely, the worst precision comes from the values of θ_{23} near

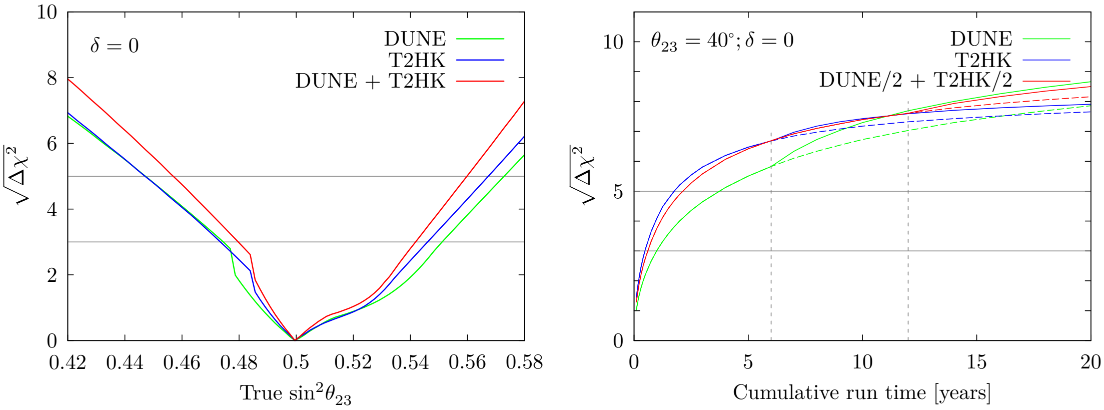

Figure 5.5: The sensitivity to exclude the wrong octant for DUNE, T2HK and their combination, as a function of $\sin^2\theta_{23}$ (left) and the cumulative run time (right). These plots assume $\delta = 0$ and normal mass ordering. The left (right) plot assumes the "fixed run time" ("variable run time") configurations in Table A.1 and the true oscillation parameters, apart from θ_{23}, specified in Table 2.3.

maximal mixing where DUNE (T2HK) can expect larger uncertainties by a factor of around 3 with $\Delta\theta_{23} = 2°$ ($\Delta\theta_{23} = 0.95°$). Comparing our result in Fig. 5.8 to Fig. 123 in [59], we find that our value for $\Delta\sin^2\theta_{23}$ is better than the official result for T2HK, which can be understood by the differences in our treatment of external data mentioned previously.

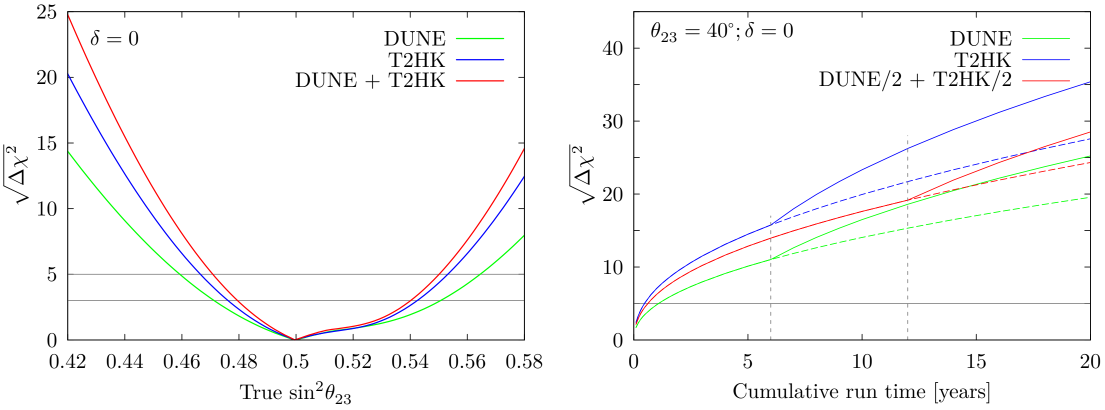

Figure 5.6: The ability to exclude $\theta_{23} = 45°$ for DUNE, T2HK and their combination, against the true value of $\sin^2\theta_{23}$ (left) and the cumulative run time (right). These plots assume $\delta = 0$ and normal mass ordering. The left (right) plot assumes the “fixed run time” (“variable run time”) configurations in Table A.1 and the true oscillation parameters, apart from θ_{23}, specified in Table 2.3.

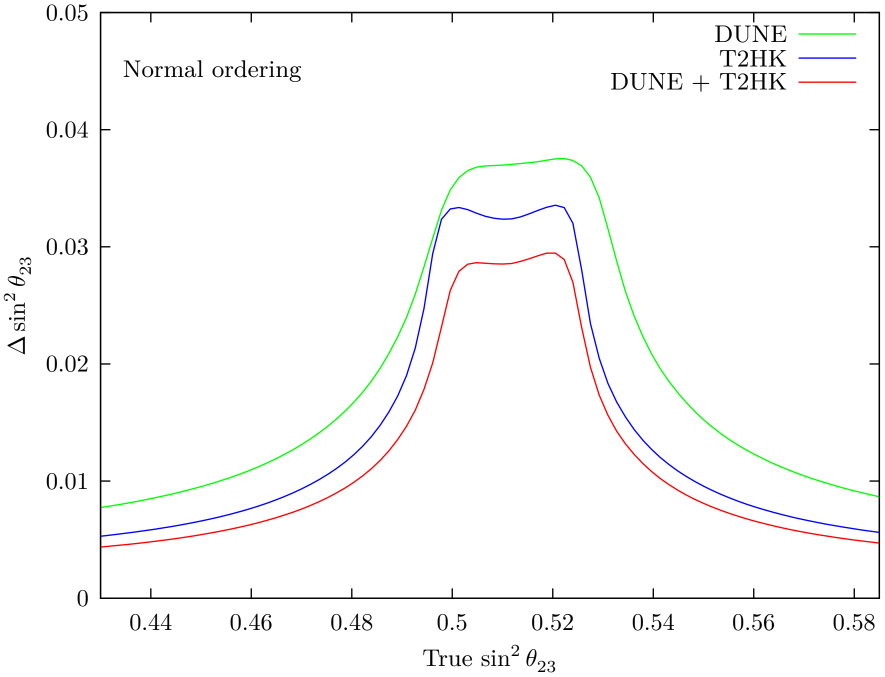

Figure 5.7: The expected 1σ precision on $\sin^2\theta_{23}$ as a function of true value of $\sin^2\theta_{23}$ from 0.43 to 0.585 for DUNE, T2HK, and their combination, under the assumption of normal ordering. This plot assumes the “fixed run time” configurations in Table A.1 and the true oscillation parameters, apart from θ_{23}, specified in Table 2.3.

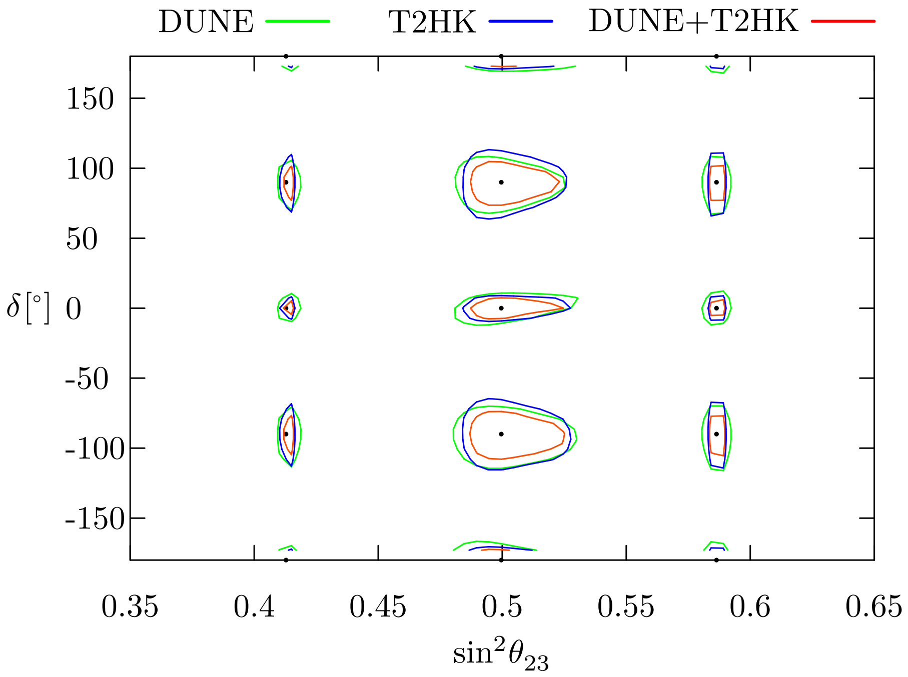

Figure 5.8: The attainable 1σ precision on $\sin^2\theta_{23}$ and δ for DUNE, T2HK, and their combination. In each case, the contours enclose the assumed true values for θ_{23} and δ, marked with a point. This plot assumes the “fixed run time” configurations in Table A.1 and the true oscillation parameters, apart from θ_{23}, specified in Table 2.3.

Chapter 6

Complementarity for precision measurements of δ

For the reasons outlined in Section 4.3, we expect an interesting interplay of sensitivities for a narrow-band and wide-band beam for the determination of δ. In this chapter, we study the complementarity of DUNE and T2HK for precision measurements of δ. In Fig. 6.1, we show the 1σ precision on δ which is attainable by the standard configurations of DUNE and T2HK and their combination. We consider a range of true values of θ_{23} as this significantly affects the ultimate precision. We see that for most of the parameter space T2HK can attain a better precision, with values of δ between 6 and 7° for the CP conserving values of δ compared to between 7.5 and 9° for DUNE. However, DUNE performs better than T2HK for maximally CP violating values of δ up to 5°. This leads to an effective complementarity between the two experiments, and their combined sensitivity reduces $\Delta\delta$ as compared to the two experiments in isolation by between 1 and 6° depending on the value of δ.

We see therefore an improvement when combining the data from the two experiments. This was to be expected for a number of reasons. Firstly, there is a simple statistical benefit of combination — an increase in data reduces the statistical uncertainty and allows for a more precise measurement. On top of this, there is a synergistic benefit, where the two experiments mutually improve the reconstruction of the parameter of interest. To try to understand the synergy between DUNE and

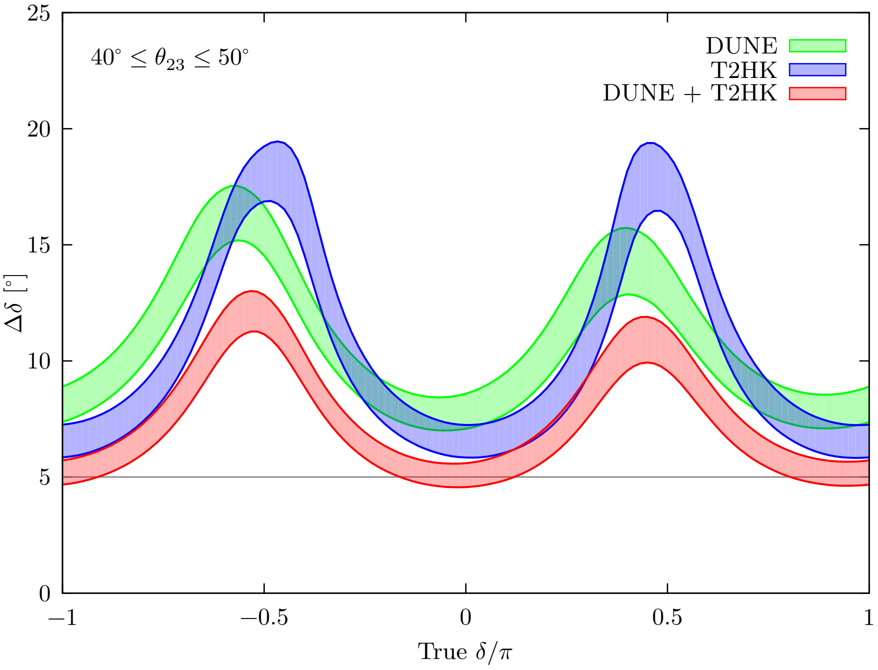

Figure 6.1: The 1σ precision on δ for DUNE and T2HK in isolation and combination. This plot assumes the "fixed run time" configurations in Table A.1 and the true oscillation parameters, apart from θ_{23}, specified in Table 2.3.

T2HK, we have run simulations where we mitigate the statistical advantage through different normalization procedures so as to expose the complementarity shown by the information available in each data set. As the experiments operate under such different assumptions, there is no universal way to do this. There are many factors which influence an experiment's sensitivity: for example, the total flux produced by the accelerator; the effects of baseline distance on the flux; the detector's size, technology and analysis efficiencies; not to mention the purely probabilistic effects of the oscillation itself, which occurs over different baseline distances and at different energies. In the first two sections, we consider different ways to normalise the experiments which reveal different aspects of their sensitivities. Finally, we study the impact of systematics on $\Delta\delta$ for DUNE and T2HK. In this chapter, except δ we implement 1-D χ^2 data from NuFit 3.0 for priors, of which the impact is described in App. A.3.

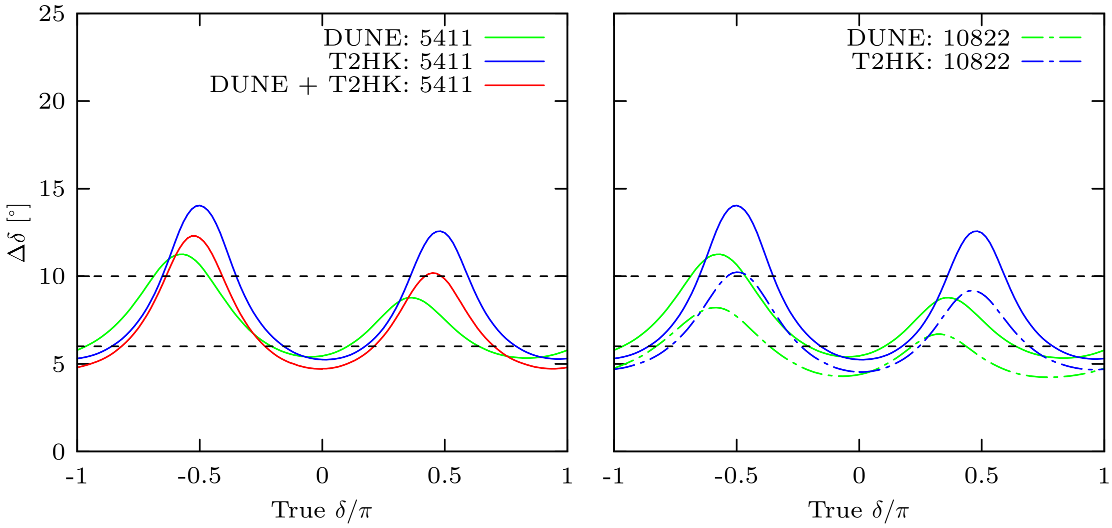

Figure 6.2: Left: the precision attainable by DUNE, T2HK and their combination with a fixed number (5411, the average number expected by DUNE + T2HK) of appearance channel events. On the left, DUNE + T2HK denotes the "fixed run time" configuration in Table A.1, which expects around 5411 events. Right: the performance of DUNE and T2HK with double numbers of appearance events (in brackets) compared to those with 5411 events. In both plots, all unspecified parameters take the true values given in Table 2.3.

6.1 Normalising by number of events

We can remove the statistical advantage of combining two experiments by fixing the number of events. We will consider two ways of doing this, both based on the total number of signal events S, composed of genuine appearance channel events in the detectors. We define S to be the sum of these events across both neutrino and antineutrino mode appearance channels.

Our first normalization method fixes S. This is, of course, an unrealistic goal in practice. However, it answers an interesting hypothetical question: would a fixed number of events be more informative if they came from DUNE or T2HK? We have run the simulation of T2HK and DUNE while fixing the number of events in the appearance channel. This number varies with δ, and so the effective run time has been modified for each value of δ to keep the observed events constant. In the left-hand panel of Fig. 6.2, we have fixed the number of appearance events to be 5411 for each configuration, which is the average number of events expected for the combination of DUNE and T2HK running for 20 years cumulative run time. We see that events at DUNE are more valuable than events at T2HK around maximally CP violating values; however, around CP conserving values, the opposite is true and T2HK has more valuable events. We quantitatively assess this effect in the right-hand panel of Fig. 6.2. This plot compares the performance of DUNE and T2HK with a fixed 5411 events, with the same experiments assuming double the number of events. The figure shows that for DUNE to consistently outperform T2HK, it needs at least twice as many events. The same is true to T2HK: it can only lead to better performance for all values of δ once its has more than twice the exposure.

Our second normalization scheme is designed to include the effect of the probability from the comparison with fixed event rates. The number of appearance channel events, S, is to a good approximation proportional to the oscillation probability,

$$S \propto P(\nu_\mu \to \nu_e; \langle E \rangle),$$

where $\langle E \rangle$ denotes the average energy of the flux, and we introduce a quantity N denoting signal events with the probabilistic effects removed,

$$N(\langle E \rangle) = S / P(\nu_\mu \to \nu_e; \langle E \rangle). \tag{6.1.1}$$

N can be thought of as the constant of proportionality between the number of signal events and the probability, and it is affected by many factors, whose product is often referred to as the *exposure* of the experiment. These factors, such as run time, detector mass and power of the accelerator, describe technical aspects of the experimental design and the exposure is often taken as a proxy for run time in phenomenological studies of neutrino oscillation experiments. However, there are other factors affecting the coefficient N such as the effects of cross-sections and detector efficiencies, which also vary from experiment to experiment. Our definition of N accounts for all of the factors which affect the signal, apart from the fundamental effect of the oscillation probability. Equating N assumes that all technical parameters are identical between the two experiments, and allows us to study the effect of the oscillation probability alone. We find that fixing N^1 leads to little change from fixing S. DUNE still outperforms T2HK for values of δ near maximal mixing, while T2HK performs best at CP conserving values. Even isolating the effect of probability in this way, we arrive at the same conclusion that events at DUNE are more informative about the value of δ than at T2HK around $\delta = \pm\pi/2$, while each event of T2HK has more impact than when δ is CP conserving.

Comparing the expected precision on δ under our different normalization conditions gives us an idea of the role played by the probability. We see that generally, the conclusions are the same: when arranged to have equal normalizations, T2HK does worse than DUNE for maximal CP violation, but performs better at $\delta = 0$ and π. This is true even if probability is included in the normalization, so we infer the difference in performance really does come from the spectrum. We conclude this section by noting that both normalization methods highlight the same aspect of the two experiments: for equal events the two experiments are very complementary, each providing the best measurement of δ for around half of the parameter space. However, in its standard configuration, DUNE expects fewer events than T2HK in the appearance channels. We will study this in more detail in the next section.

6.2 Normalising by run time

Of course, one of the most pragmatic ways to normalise the experiments is by run time. Would a decade of both experiments running in parallel be better than two consecutive decades of DUNE (or T2HK)? To make this comparison, we assume the same cumulative run time for the experiments running alone, and in combination. In Fig. 6.3 we show the results of our simulation. The combination of DUNE and T2HK generally outperforms either experiment running for twice as long. However, there are some small regions of parameter space around maximal CP violating values of δ where 20 years of DUNE outperforms not only T2HK but also the combination

---

[1] In practice, as we are studying neutrino and antineutrino channels and our detector models have binned energy spectra, we define an analogous quantity N_i ($\overline{N}_i$) for each energy E_i ($\overline{E}_i$) in neutrino (antineutrino) mode. We then define N as the sum over $N_i + \overline{N}_i$.

of DUNE and T2HK. At these values of δ, DUNE's wide-band beam performs best by incorporating information from other energies. We also see this benefit in the combination of DUNE and T2HK, which notably outperforms 20 years of T2HK at these values. This result tells us that the combination offers two advantages. First, running the experiments in parallel allows us to collect two decades of data in half the calendar time. This explains a significant part of the sensitivity improvement; however, there is also a complementarity arising from the different sensitivities of the two experiments. This is especially marked for this measurement around the maximally CP violating values of δ.

The behaviour of $\Delta\delta$ for different experimental configurations as a function of run time is shown in Fig. 6.4. We have studied this for the maximum and the minimum values of $\Delta\delta$ (denoted $\Delta\delta_{\mathrm{max}}$ and $\Delta\delta_{\mathrm{min}}$), which describe the extremes of performance for the two experiments. We find that $\Delta\delta_{\mathrm{max}}$ is better at DUNE than T2HK for all run times, whereas the situation is reversed for $\Delta\delta_{\mathrm{min}}$. We note that for both experiments, the staged upgrades lead to a strong improvement in the sensitivity. If run in parallel, the combination of DUNE and T2HK expects $\Delta\delta_{\mathrm{min}} < 5^\circ$ and $\Delta\delta_{\mathrm{max}} \lesssim 11^\circ$ after 10 years.

To end this section, we compare the performance of the two experiments and their combination through the minimal exposures required to obtain certain physics goals. In Table 6.1, we show the value of N, see Eq. (6.1.1), the number of signal events S and the cumulative run time required to reach a precision on δ of 10° for $\Delta\delta_{\mathrm{max}}$ and $\Delta\delta_{\mathrm{min}}$. It is clear from our study in this section that to achieve a precision of 10° for $\Delta\delta_{\mathrm{max}}$ will be a challenging measurement: above 20 years of data is necessary, requiring 12.5 years of both experiments running in parallel. For $\Delta\delta_{\mathrm{min}}$ this is, however, a feasible goal. DUNE expects a similar measurement after a full 5.8 year data-taking period, while T2HK can achieve this goal in 3.3 years. The combination of DUNE and T2HK marginally improves on this, requiring only 1.9 years of parallel running.

	$\Delta\delta_{min}$			$\Delta\delta_{max}$		
	DUNE	T2HK	Both	DUNE	T2HK	Both
δ	354°	0°	0°	255°	270°	264°
N	26837	15868	21900	167497	332532	218995
S	961	1034	739	6811	15653	8124
Cumulative run time [years]	5.8	3.3	3.8	21.1	27.1	25

Table 6.1: Exposures required for $\Delta\delta_{\text{max}}$ and $\Delta\delta_{\text{min}}$ to reach 10°. T2HK has the best precision on reasonable time scales due to its very high event rate especially at $\delta = \pi$. DUNE marginally out performs T2HK for maximally violating values of δ. The year shown in this table, assumes the "variable run time" configurations of Table A.1. The combination "Both" assumes a scaling of the standard configuration of DUNE/2 + T2HK/2.

6.3 Impact of systematic errors

In the previous section, we have looked at the precision on δ under a number of different assumptions. We have seen that T2HK has a larger number of events than DUNE, and for the majority of the parameter space this leads to a better expected precision on δ. This means that the relationship between statistical and systematic uncertainty will be quite different at the different experiments and our assumptions about systematics, always a contentious issue, may be significant. In this section we try to understand these effects and explore the impact on the expected precision on δ under differing systematics assumptions for the combination of DUNE and T2HK.

We can get a feel for the relevance of statistical versus systematic uncertainty by seeing how the sensitivity scales with run time. In our model of the systematics, we only consider effective signal and background normalisation systematics for both DUNE and T2HK. In Fig. 6.5, we show the sensitivity to δ for different run times of the two experiments in isolation, with and without systematic uncertainties. We see that there is little impact from the systematic uncertainty at DUNE, and it continues to further its sensitivity as we increase its run time. This effect is quite different for T2HK where systematics clearly have a more important role; for CP conserving values, there is only modest improvement in sensitivity after extensions of the experiment run time by a factor of 4. This result neatly shows that DUNE is statistically limited while T2HK has more reliance on its systematic assumptions (except for maximally CP violating values of δ). It is interesting to note that in both cases, even after large increases in exposure, neither DUNE nor T2HK taken as a single experiment can significantly improve on the sensitivity at CP conserving values found by the combination of DUNE and T2HK running for only 10 years each.

Due to the limiting effect of systematic uncertainties suspected at T2HK, we can expect that its performance is quite sensitive to our assumptions. To understand how the combination of DUNE and T2HK can help reduce this sensitivity, we have run simulations while varying the value of the normalization systematics in T2HK. We study the case of 2%, 4%, 6% and 8% normalization uncertainty at T2HK for the combination of DUNE and T2HK in comparison to T2HK running for 10 years with the same systematic assumptions. The results are shown in Fig. 6.6. We see that for 2% systematic uncertainty, around $\delta = 0$ and π T2HK dominates the precision on δ and is limited strongly by the systematics, meaning that doubling the run time leads to scant improvement. As the systematic uncertainty on T2HK increases, we see more of an advantage of including DUNE. Although at 4% systematics the lines are almost identical, for 6% systematics the improvement in precision at $\delta = 0$ is around 2° (an improvement of around 10%). We conclude that T2HK is systematically limited around CP conserving values of δ, and including DUNE data can help to mitigate the effect of larger uncertainties. At maximally CP violating value of δ, we see little impact of our systematic assumptions.

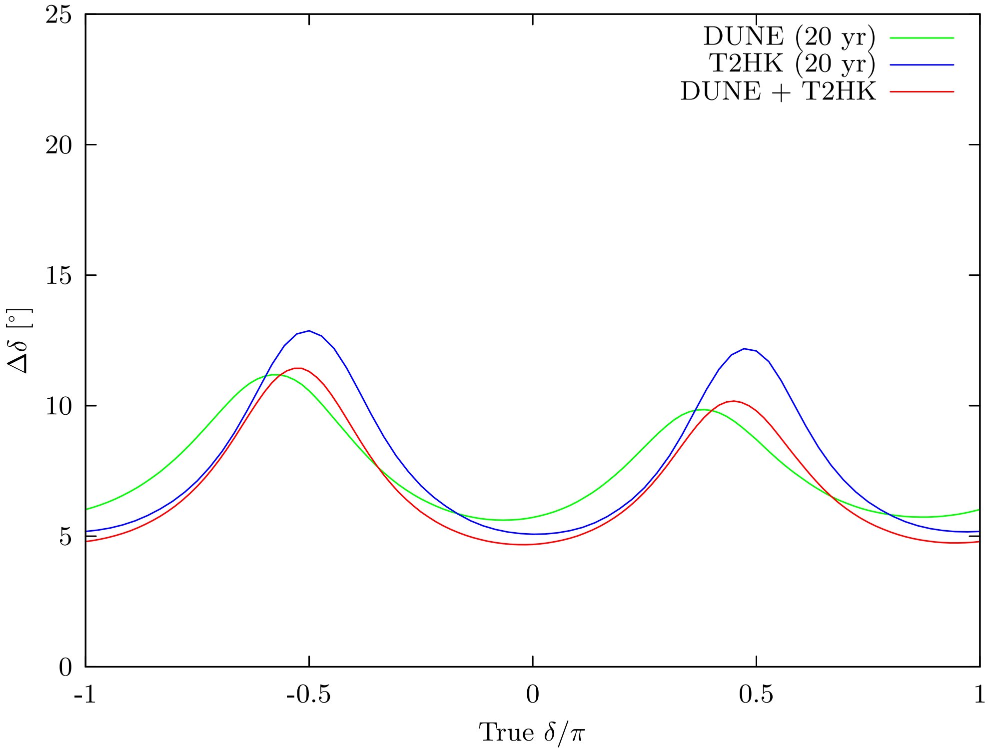

Figure 6.3: The 1σ precision on δ as a function of the true value of δ for DUNE, T2HK and their combination with the same cumulative run time of 20 years. The configuration of DUNE (20 yr) is defined by the "variable run time" entry in Table A.1, with T given in brackets after the experiment's name, whereas DUNE + T2HK is the corresponding "fixed run time" entry. Note that due to the staged upgrades of both designs, DUNE (20 yr) and T2HK (20 yr) correspond to 6 years without the planned upgrades followed by 14 years of upgraded running. This plot assumes normal mass ordering and all other unspecified true parameters are given in Table 2.3.

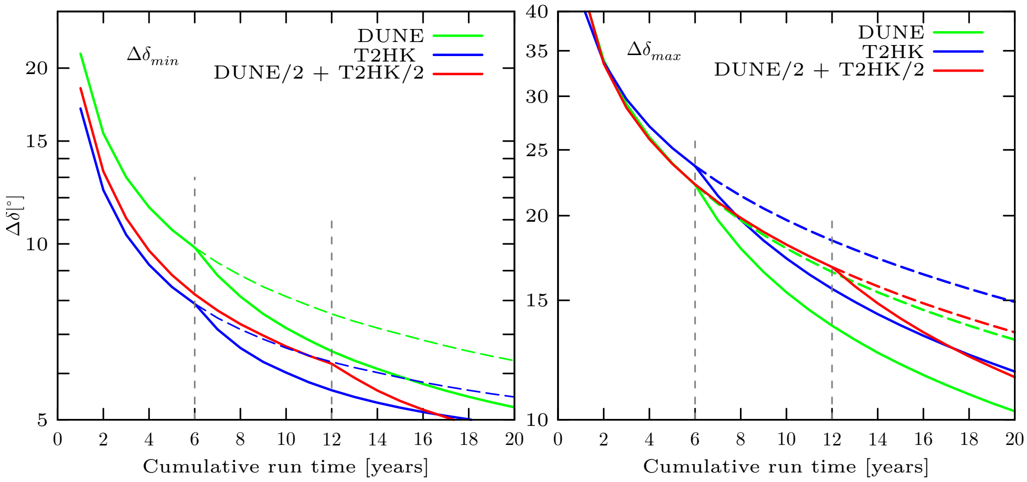

Figure 6.4: $\Delta\delta_{\text{min}}$ (left) and $\Delta\delta_{\text{max}}$ (right) at DUNE, T2HK and their combination as a function of run time. These plots assume the “variable run time” configurations in Table A.1 and the true oscillation parameters appropriate for normal ordering as given in Table 2.3. We have checked that similar behaviour obtains for inverted ordering.

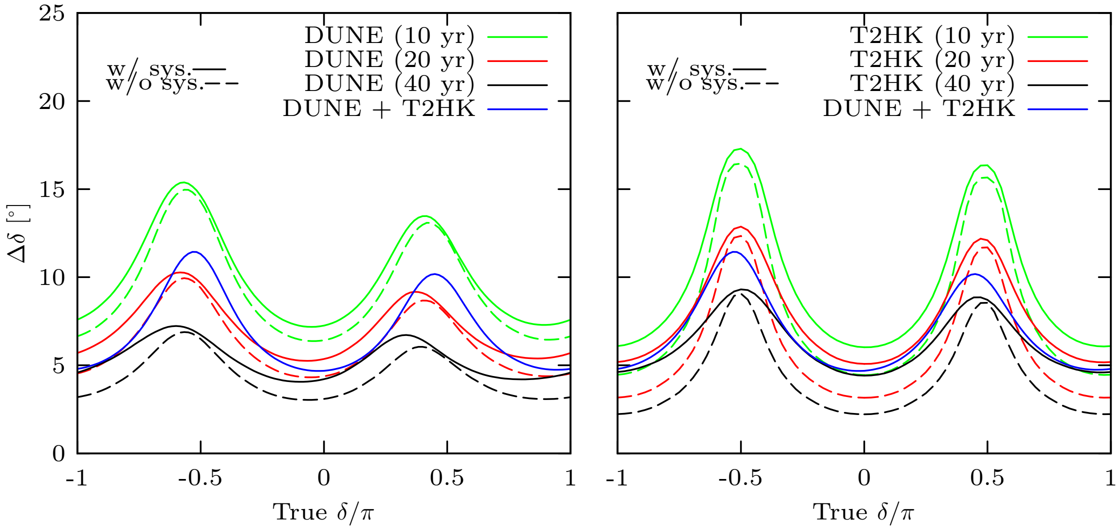

Figure 6.5: Left (right): the expected 1σ precision on δ for DUNE (T2HK) with different run times with and without systematics (solid and dashed, respectively) compared to a reference design of our “fixed run time” configuration of DUNE + T2HK from Table A.1. Note that in all cases, the experiments in isolation have a staged upgrade after 6 years, and so see increasingly long periods of upgraded running.

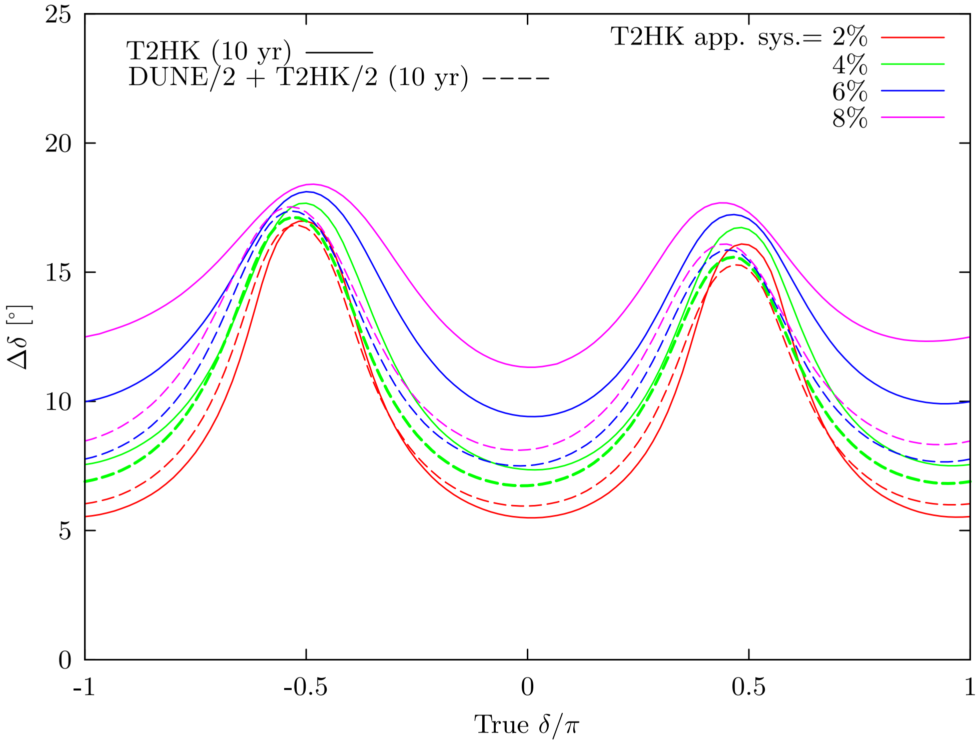

Figure 6.6: $\Delta\delta$ for T2HK and the combination of DUNE/2 + T2HK/2 each with 10 years cumulative run time for different normalization systematic uncertainties on the appearance channel in T2HK (2%, 4%, 6%, and 8%). We hold the normalization systematics at 2% for the appearance channels of DUNE. The configurations in this plot are labelled "variable run time" in Table A.1 with the cumulative run time denoted in brackets after their names. This plot assumes normal ordering, but all other true parameters follow Table 2.3.

Chapter 7

Impacts of Alternative Designs for Standard Oscillations

As part of their continual optimisation work, both the DUNE and T2HK collaborations have considered modifications of their reference designs, aiming to further the physics reach of their experiments. As mentioned in Section 3.1.1, DUNE has considered an optimised beam based on a 3-horn design, and a novel beam concept, nuPIL. For T2HK, the redesign efforts are focused on the location of the second tank. Originally foreseen as being installed at Kamioka 6 years after the experiment started to take data, the possibility of installing the detector in southern Korea has been mooted [66, 99–101]. In this section, we discuss the impact of these redesigns on the physics reach of the experiments, both alone and in combination, via the results of our phenomenological discussion and simulations. We focus on the mass ordering, CPV discovery, MCP and precision measurements of δ. We point out that we do not discuss measurements of θ_{23} further, as we have found that there is little difference between the alternative designs under consideration.

The run time setting is described in Ch. A.1. Then we gradually compare each sensitivity among different experimental designs — mass ordering sensitivity, CPV and MCP sensitivity, and δ measurement, in Secs. 7.1–7.3. In the final section, we show the performance of the optimal configuration, based on the study in the previous studies for the standard design. In this chapter, except δ we implement 1-D χ^2 data from NuFit 3.0 for priors, of which the impact is described in App. A.3.

7.1 Mass ordering

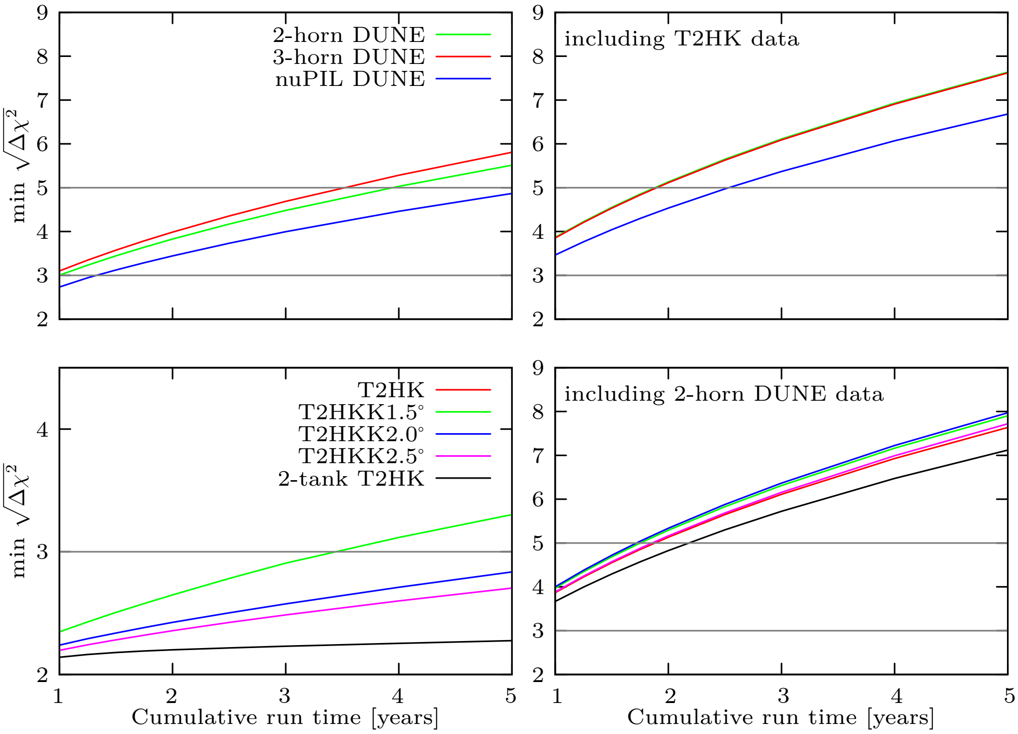

Figure 7.1: Top (bottom) row: The minimum statistical significance of mass ordering discrimination for DUNE (T2HK) with various beam designs. On both rows, the left-hand panels show the performance of the alternative designs in isolation, while the right-hand panels show the impact of an alternative design on the combination of DUNE and T2HK by incorporating the standard T2HK and DUNE designs on the top and bottom rows, respectively. The configurations assumed here are described in Section A.1 and the true oscillation parameters are given in Table 2.3. Note that in the top-right panel, the blue and green lines overlap.

As shown for the standard configurations in Section 5.1, identifying the mass ordering is almost guaranteed for experiments on this scale. However, we see a large difference in performance between DUNE and T2HK due to the difference in baseline distance. The alternative beams of the DUNE collaboration do little to change this picture. The results of our simulation are shown in Fig. 7.1, in which we show the minimum sensitivity to the mass ordering as a function of cumulative run time. The left column of panels shows the performance of the alternative designs for DUNE (top) and T2HK (bottom). We see that for DUNE, the 3-horn and 2-horn designs do better at the minimum sensitivity by about 1σ compared to the nuPIL design. We see that the 3-horn design can reach greater than 5σ significance after around 3.3 years run time, while the 2-horn design achieves the same significance after around 4 years, and nuPIL requires above 5 years. For T2HK and its alternative designs the picture is quite different. The T2HK design cannot achieve sensitivity above 2σ for these run times. However, placing a second tank in Korea will allow T2HKK to see larger matter effects over the 1000–1200 km baseline: the sure-fire way to sensitivity to the mass ordering. Moreover, the possibility of placing the second detector at a different off-axis angle, could produce a wider beam, or a narrow beam whose peak is shifted away from the first maximum. This interplay of factors could qualitatively alter our picture of mass ordering sensitivity at HK(K). We see a greater variation in performance as the fluxes are varied, but as we saw before, lower overall sensitivities. Due to the larger matter effects associated with the Korean detector, we might expect increased sensitivity to the mass ordering over the standard T2HK design; however, we do not see an enhancement of this kind. We understand this effect as due in part to the limited data collected by T2HKK at the longer baseline. Fewer events associated with neutrinos travelling the longer baseline are detected as the beam suffers significant suppression due to dispersion over the longer distance[1]. With WC technology, we know that the advantage comes from scale, and such a limitation on event numbers means that longer baselines will not be competitive unless operated for a longer period of time. Moreover, the matter effect is relatively suppressed compared to the effect at DUNE due to the lower energies of the J-PARC beam. And it has been shown in Ref. [66] that it is not sufficient to allow for a separation of the two degenerate solutions in all cases at fixed energies. However, the most important contribution of a Korean second detector is the very different spectral information it provides from a detector at Kamioka. This helps to provide sensitivity to the ordering, and we see that the T2HKK1.5° option expects to push

---

[1] The flux is dispersed by an inverse square law as baseline increases; subsequently, a Korean detector sees around 11% of the flux seen at Kamioka.

the sensitivity above 3σ after around 3 years. Although we do not show the full MO sensitivity against δ in Fig. 7.1, we can draw a limited comparison between our work and Fig. 18 in Ref. [65]. Our results find slightly lower sensitivities: for T2HKK1.5°, the difference is about 1σ, while for off-axis angles of 2.5° and 2.0° the difference is smaller than 1σ.

The sensitivity is seen to increase as the Korean detector is moved to smaller off-axis angles. This can be explained by the different flux profiles of the T2HKK options. As the detector is moved towards the beam axis, the events sample the oscillation probability increasingly close to the first maximum. This is where the mass ordering is most visible in the presence of matter effects and we see an accordingly stronger discovery potential.

On the right column of Fig. 7.1, we show how the alternative designs impact the combination of the two experiments. Including T2HK data reduces the difference in performance between the three DUNE beam designs, which all expect a minimum sensitivity of 5σ after about 2 years. For T2HK, the inclusion of DUNE data, pushes the overall sensitivity above 5σ for the first time, with an extra Korean detector, DUNE + T2HKK expects a greater than 5σ measurement for all values of δ with around 2 years run time.

7.2 CPV and MCP sensitivity

The sensitivity to CPV is understood to depend upon the energy of the events observed, meaning that modifying the flux spectrum, for example with a narrower beam from nuPIL or a beam located at the second maximum for T2HKK, could lead to significant changes in the physics reach of the design. In the top-left panel of Fig. 7.2 we compare the performance of the standard and alternative DUNE designs. CPV and MCP sensitivities are shown for the three beam options as a function of δ in solid and dashed lines, respectively. We find that the 2-horn and 3-horn designs perform similarly for CPV and MCP measurements, and nuPIL performs slightly worse, by about 1σ. The top-right panel shows how these sensitivities are changed as information from the standard configuration of T2HK is included. We see that due

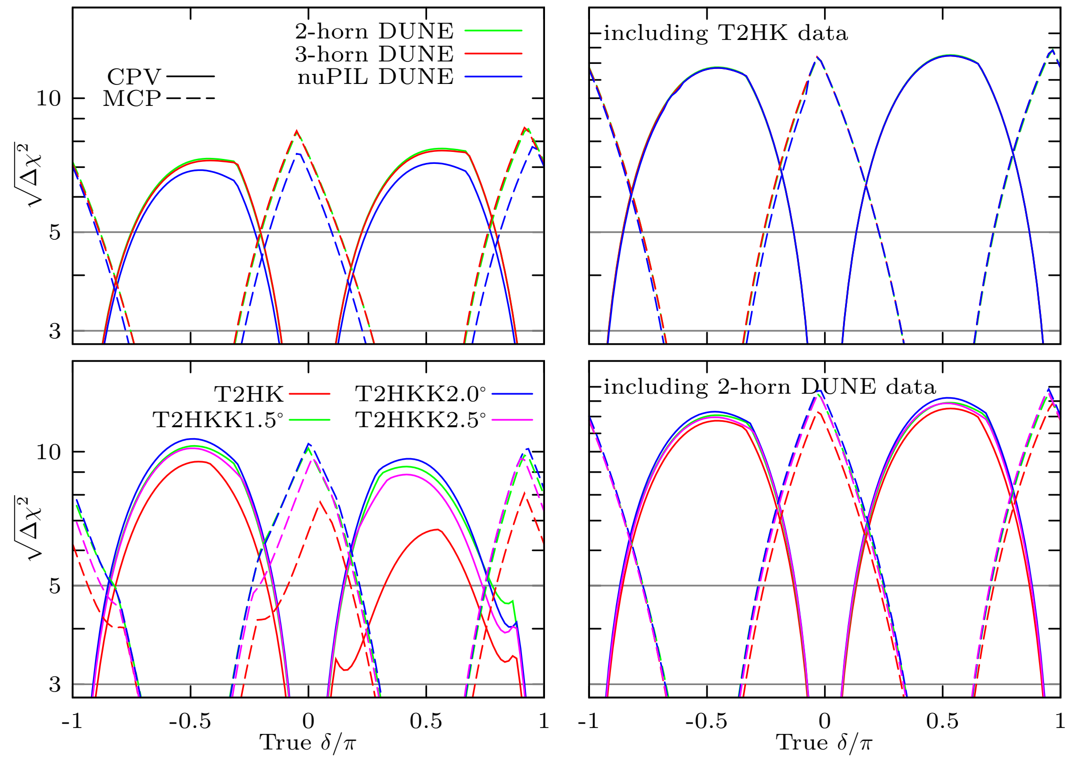

Figure 7.2: The sensitivity to CPV (solid) and MCP (dashed) as a function of δ for various designs of DUNE (top row) and T2HK (bottom row). The configurations assumed here are described in Section A.1 and the true oscillation parameters are given in Table 2.3.

to T2HK's strong sensitivity to the parameter δ, the impact of alternative designs for DUNE is greatly reduced. Maximal sensitivities to CPV (MCO) of above 11σ are found for the maximal values of $\delta \in \{\frac{\pi}{2}, \frac{3\pi}{2}\}$ ($\delta \in \{0, \pi\}$).

For T2HKK we compare three off-axis angles for the Korean detector to the standard configuration in the bottom row of Fig. 7.2. On the left panel, we show the performance of these alternative designs in isolation. We see that the experiments perform comparably, but the best performance comes from the T2HKK2.0° flux. As can be seen in Fig. 3.2, this flux is the best aligned with the second maximum, suggesting that it is the access to events which sample this part of the oscillation spectrum which lead to the increase in sensitivity. The increase in sensitivity for $-\pi \leq \delta \leq 0$ is modest between T2HK and T2HKK. We understand this again due

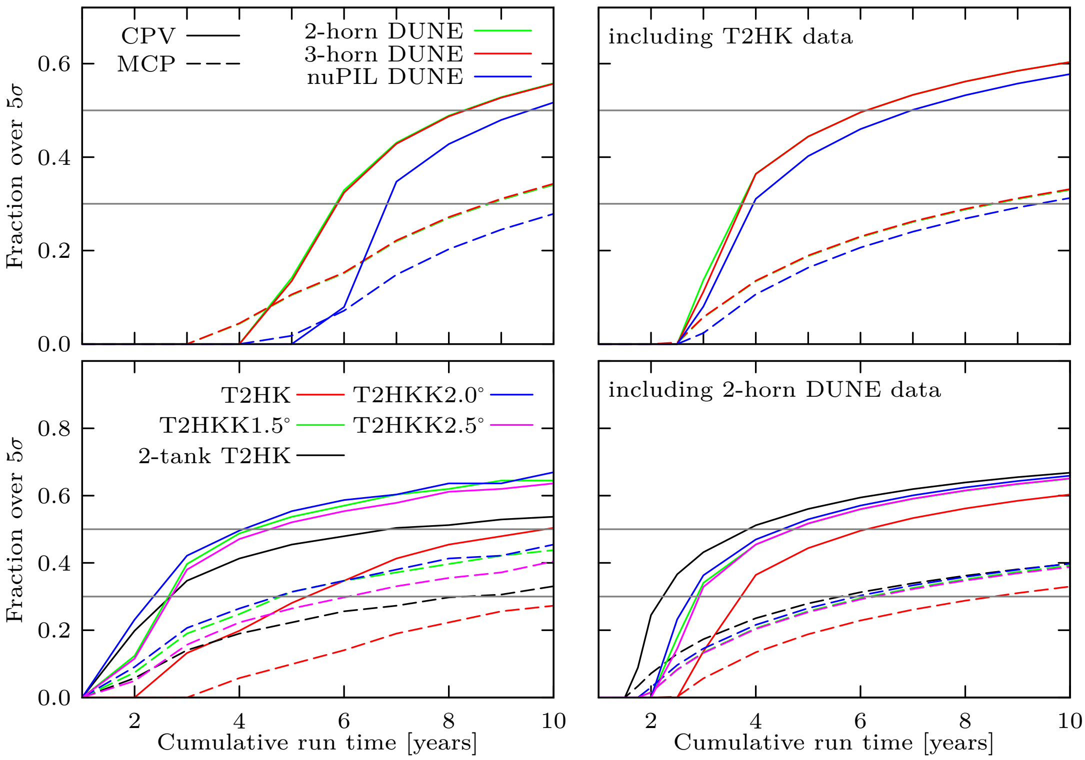

Figure 7.3: The fraction of true δ values for which we expect a CPV sensitivity (solid) and MCP sensitivity (dashed) over 5 σ, against cumulative run time. The configurations assumed here are described in Section A.1 and the true oscillation parameters are given in Table 2.3.

to the suppression in event rates for a Korean detector: although possessing valuable information, they are seen in relatively small numbers, and their impact is limited. However, there is a notable difference for $0 \leq \delta \leq \pi$, as the Korean detector helps to lift the degeneracy which limits the performance of T2HK. In the bottom-right panel of Fig. 7.2, we see the sensitivity to CPV and MCP for combinations of DUNE and T2HKK. In these simulations, the degeneracy is lifted by the inclusion of DUNE data, and there is little difference between the alternative designs for T2HKK aside from an overall improvement in the sensitivities by between 1 and 2σ.

In Fig. 7.3, we have computed the fraction of values of δ for which CP conservation or maximal CP violation can be excluded at greater than 5σ confidence. The top-left panel shows the performance of the alternative DUNE beam designs in isolation. The 3-horn and 2-horn designs have almost identical sensitivities for all run times, with a CPV fraction greater than that of nuPIL by between 10–30% and an MCP fraction higher by around 10%. If we consider 30% to be a benchmark CPV fraction, the 3-horn and 2-horn designs expect to reach this sensitivity after around 5 years, while nuPIL takes around 7 years. Excluding MCP is a harder measurement for all beam designs, and exposures of greater than 10 years would be required to achieve a 30% coverage of δ parameter space at 5σ. The top-right panel shows how the alternative DUNE designs are affected by the inclusion of T2HK data. Thanks to the good CPV and MCP sensitivity of T2HK, we see the improvement for the combination, especially for nuPIL by up to 10%. We also find a relative suppression of the difference between variants — ultimately, DUNE offers less to this configuration and its precise design is less important. These combinations expect to reach a CPV fraction of 30% (50%) after about 4 (6) years. For the exclusion of MCP, a 30% fraction will be approximately reached after 9 cumulative years run time.

The bottom row of Fig. 7.3, shows analogous plots for T2HK and T2HKK. On the left, these alternative designs are considered in isolation, and we have also included a 2-tank T2HK line for comparison which assumes two tanks collecting data at Kamioka from the start of the experiment. There is very little difference between the T2HKK designs, although they all show an increase in CPV and MCP fraction over the T2HK design. T2HKK expects a CPV fraction of over 50% after less than 4 years, while T2HK requires around 10 years for the same sensitivity (and 2-tank T2HK around 7 years). MCP fractions of greater than 30% are possible after 5 and 11 years for T2HKK and T2HK, respectively. Compared with the results shown in the upper panels in Fig. 20 in Ref. [65], we find the same ranking of designs. However, we also find sensitivities around 2σ higher near $\delta = \pm\pi/2$. We suspect this quantitative difference is due to our priors, as in Ref. [65], it is pointed out that priors for δ, θ_{23} and Δm^2_{31} are not implemented. However, we use priors on all variables apart from δ, and our simulation has slightly less leeway to accommodate degenerate solutions, and a correspondingly improved ability to exclude CP conserving parameter sets. It is interesting to point out that, for both DUNE and T2HK, differences in design have a greater impact on the highest sensitivity to CPV and MCP, as seen in Fig. 7.2, than on the long-term average performance encapsulated in the CPV/MCP fraction at 5σ. This can be seen in Fig. 7.2 as the width of the sensitivity curves remaining unchanged, while the peak is raised or lowered. The sensitivity of the peak corresponds to different rising behaviour in Fig. 7.3, but the curves can be seen to quickly plateau for T2HK. For DUNE, this effect is less marked, and suggests increasing run time would still lead to increases in sensitivity.

On the right panel, we show the performance for the combination of DUNE data with the T2HK variants. As in the bottom-left panel, we see that the T2HKK designs perform similarly, with T2HKK2.0 performing marginally better. The inclusion of DUNE data here makes little change to the sensitivities. In fact, as we define cumulative run time as the sum of the individual DUNE and T2HKK run times, we see an apparent decrease in performance. Scaled appropriately for parallel data collection, we find that DUNE + T2HKK expect a 5σ CPV fraction of greater than 50% after around 2 years compared to 4 years for T2HKK alone. We note that there is a notable change in the performance of the T2HK design with two tanks at Kamioka operated for the duration of the experiment. Without DUNE data, this configuration performs more poorly than the T2HKK designs; however, with the inclusion of DUNE data, it becomes the best option. This can be understood as DUNE resolving the degeneracy and T2HK maximising its CPV measurement by a large increase of data at shorter baselines.

To conclude this section, we note that almost all of the experiments, when running in isolation, can expect the exclusion of one of CP conservation or maximal CP violation for all values of δ at 4σ and 5σ for DUNE and T2HK variants, respectively. This can be seen clearly in Fig. 7.2, where the intersections between CPV and MCP lines are above the 3 or 5σ horizontal lines. This is true for all alternative designs, while the combination of DUNE and T2HK ensures that one of these facts would be established with a significance greater than 6σ. The exception is for T2HK alone which, due to the degeneracy, falls short in some some regions of parameter space.

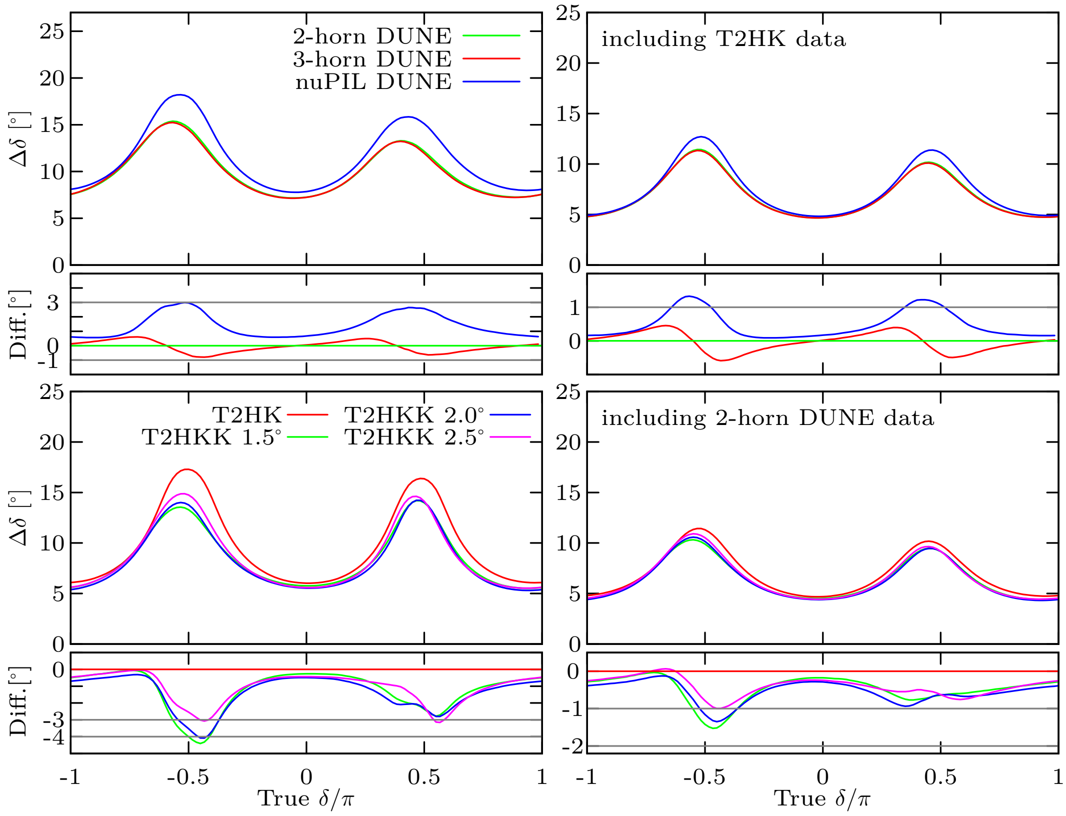

Figure 7.4: The 1σ precision on δ for variants of DUNE (top row) and T2HK (bottom row). In the left column, these designs are considered in isolation while on the right, we combine variant designs of one experiment with the standard configuration of the other. Our configurations are described in Section A.1. These plots assume normal mass ordering and the remaining true parameters are specified in Table 2.3.

7.3 Precision on δ

We show the difference in $\Delta\delta$ for the alternative designs in the left column of Fig. 7.4. We find that for DUNE, the 3-horn design works similarly to 2-horn design; although, the 3-horn design performs slightly better in the 2nd and 4th quadrant and for maximal CP violation, while the 2-horn design expects smaller $\Delta\delta$ in all other cases. These designs expect a precision on δ somewhere between 8 and 18° after their full data taking period. The performance of the nuPIL design depends significantly on the true value of δ. For values near maximal CP violation $\delta = \pm\frac{\pi}{2}$, nuPIL performs worse than the standard design. This can be understood due to the narrowing of the beam, which when focused on first maximum, has insufficient events from other energies to mitigate the poor sensitivity around maximal CP violating phases. On the top-right panel of Fig. 7.4, we show the impact that the DUNE redesigns have on the combination of DUNE and the standard configuration of T2HK. As shown in Ch. 6, data from T2HK improves the resolution on δ for DUNE, and we see a correspondingly small impact of alternative beam designs for DUNE. Notably, we do however see the worsening of performance around maximal CP violating values of δ for the combination of nuPIL and T2HK.

The expected sensitivity of $\Delta\delta$ for the alternative designs for T2HKK are shown on the bottom-left panel of Fig. 7.4. Here we see that all designs with a far detector allow for a significant improvement in the precision on δ, generally seeing the best performance coming from the 1.5° or 2.0° off-axis angle fluxes. We see a slight loss of performance for larger off-axis angles, which may be associated with the peak of the flux falling beyond the second maximum into a region of hard to identify, fast oscillations. Our result for $\Delta\delta$ is very close to that shown in the upper panels of Fig. 23 in Ref. [65], and we agree on the ranking among alternative designs. This is notable, given the differences induced by our priors in other variables of interest, but is explained by the fact that our priors differ in their global structure more than in their local structure. It is this local structure which dictates $\Delta\delta$, as at low significance the Gaussian approximation works well and multiple minima are irrelevant. On the right panel of Fig. 7.4, the combination is shown with different T2HKK fluxes and the standard DUNE configuration. Once again, we see that T2HKK dominates the combination, and therefore the shapes of these curves closely follow those on the left panel.

7.4 Optimal configuration

In the preceding sections, we have studied how the alternative designs of T2HKK and DUNE could impact the physics reach for key measurements, considering both the experiments in isolation and in certain combinations. We have seen that for DUNE, the 2-horn and 3-horn designs perform similarly, with the greatest difference occurring for the measurements of the mass ordering and $\Delta\delta$. Both designs still

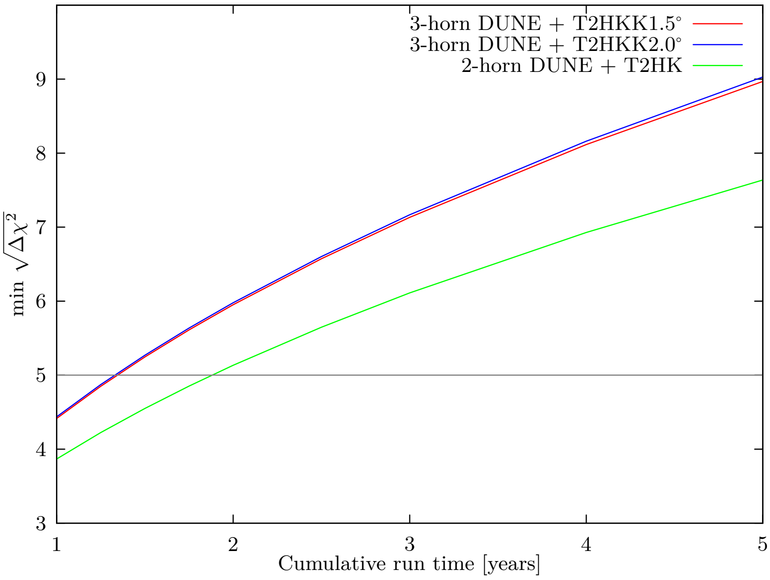

Figure 7.5: The minimum mass ordering sensitivity for the combination of DUNE with the 3 horn flux and T2HKK1.5° (red) and T2HKK2.0° (blue) compared with the standard configurations of DUNE with 2-horn flux and T2HK with a single tank at Kamioka (green). The configurations assumed here are described in Section A.1 and the true oscillation parameters are given in Table 2.3.

expect very high significance measurements of the mass ordering. However, as we see in Fig. 6.1, the 3-horn design can achieve marginally better values of $\Delta\delta$ when δ in the 2nd and 4th quadrants, which is where T2HK performs worse than DUNE. We therefore take the 3-horn design to be the optimal choice for T2HK, with the 2-horn a close second. T2HKK in contrast performs best with a flux positioned between 1.5 and 2.0° degrees off axis. Here it maximizes its sensitivity to CP violation, its ability to exclude maximal CP violation and to make precision measurements of δ around CP conserving values. Whereas so far we have only considered alternative designs for one experiment in combination with the standard design of the other, in this section we report the physics reach of the optimal combination of DUNE 3-horn and T2HKK1.5° (and T2HKK2.0°).

In Fig. 7.5, we show the minimum sensitivity expected for the mass ordering for this optimal configuration of DUNE + T2HKK. A 4σ measurement is expected after less than a cumulative year, which increases to 5σ no more after 1.5 years. In

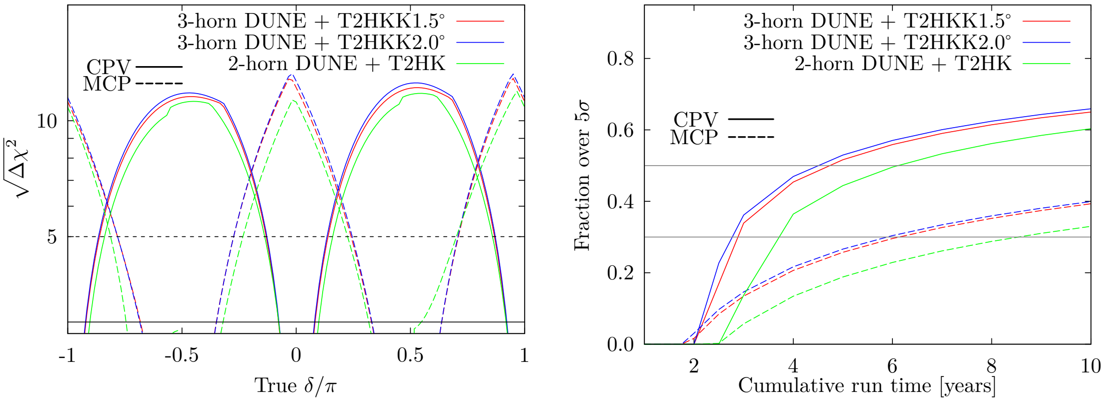

Figure 7.6: Left: the CPV and MCP sensitivity for the combination of DUNE with the 3-horn flux and T2HKK1.5°(2.0°). For reference, we also show the combination of the two standard designs: DUNE with 2 horn beam and T2HK (green). Right: the fraction of δ parameter space for CPV (MCP) sensitivity over 5σ for the same configurations as on the left panel. The configurations assumed here are described in Section A.1 and the true oscillation parameters are given in Table 2.3.

Fig. 7.6, we show the significance at which we can expect to exclude CP conservation (solid) and maximal CP violation (dashed). These are expected to reach a maximal significance of 11σ and 12σ, respectively. The advantage of the combination is clearer when the performance is viewed in terms of the minimal run time required for the exclusions to be made at 5σ. The combination of DUNE + T2HKK expects to have greater than 5σ exclusion of CP conservation for more than 25% (50%) of the parameter space after 2.5 (5) years of cumulative run time. For the exclusion of maximal CP violation, longer run times are required: about 6 years ensures the exclusion for more than 25% of values of δ. For the precision on δ, shown in Fig. 7.7, we see that the optimal combination of DUNE + T2HKK could expect a measurement around a CP conserving value with an uncertainty of only 4.5°. This worsens for maximally CP violating values of δ to around 10°.

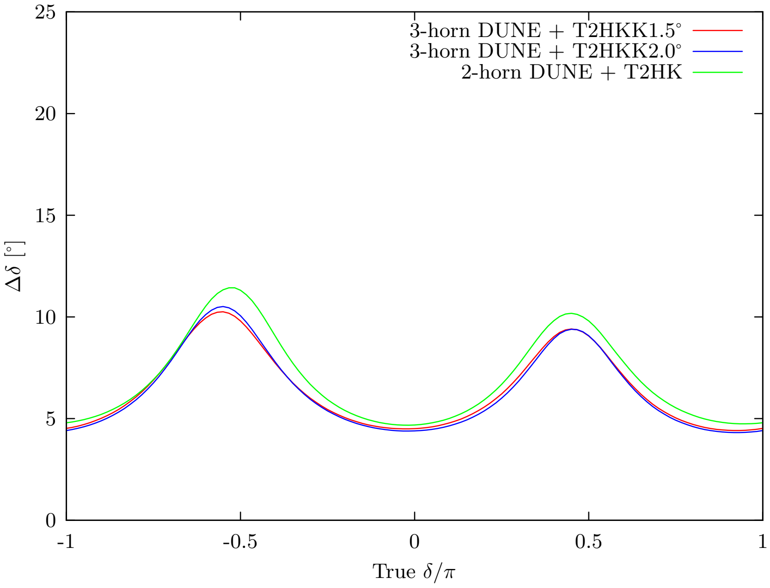

Figure 7.7: The 1σ error on δ for the combination of DUNE with the 3-horn flux and T2HKK1.5°(2.0°) shown in red (blue). For reference, we also show the combination of the two standard designs: DUNE with 2-horn beam and T2HK with one tank (green). The configurations assumed here are described in Section A.1 and the true oscillation parameters are given in Table 2.3.

Chapter 8

Littlest Seesaw

The minimal two right-handed neutrino model with normal hierarchy which can accommodate the known data of neutrino mixing involves a Dirac mass matrix with one texture zero and a characteristic form known as the Littlest Seesaw model (LS) [23]. The Littlest Seesaw model may be embedded in unified models of quarks and leptons in [105]. It leads to successful leptogenesis where the sign of baryon asymmetry is determined by the ordering of the heavy right-handed neutrinos, and the only seesaw phase η is identified as the leptogenesis phase, linking violation of charge parity symmetry (CP) in the laboratory with that in the early universe [106].

The Littlest Seesaw model can be understood as an example of sequential dominance (SD) [107] in which one right-handed neutrino provides the dominant contribution to the atmospheric neutrino mass[1], leading to approximately maximal atmospheric mixing, while the other right-handed neutrino gives the solar neutrino mass and controls the solar and reactor mixing as well as the magnitude of CP violating effects via δ. SD generally leads to normal ordering and a reactor angle which is bounded by $\theta_{13} \lesssim m_2/m_3$ [20], proposed a decade before the reactor angle was measured [1]. Precise predictions for the reactor (and solar) angles result from applying further constraints to the Dirac mass matrix, an approach known as con-

---

[1] With the lightest neutrino massless, $m_1 = 0$, we refer to the two non-zero masses as the *solar neutrino mass* and the *atmospheric neutrino mass*, corresponding to the square roots of the experimentally measured solar and atmospheric neutrino mass splittings $m_2 = \sqrt{\Delta m^2_{21}}$ and $m_3 = \sqrt{\Delta m^2_{31}}$ respectively.

strained sequential dominance (CSD) [108]. For example, keeping the first column of the Dirac mass matrix proportional to $(0,1,1)^T$, a class of CSD(n) models has emerged [23, 102, 103, 108, 109] corresponding to the second column proportional to $(1,n,(n-2))^T$, with a reactor angle approximately given by [104] $\theta_{13} \sim (n-1)\frac{\sqrt{2}}{3}\frac{m_2}{m_3}$. The Littlest Seesaw model corresponds to $n=3$ with a fixed seesaw phase $\eta = 2\pi/3$.

In addition, it was recently realised that the alternative form of the Littlest Seesaw model with second column $(1,1,3)^T$ and seesaw phase $\eta = -2\pi/3$ (also proposed in [23]) may be enforced by an $S_4 \times U(1)$ symmetry, putting this version of the Littlest Seesaw model on a firm theoretical foundation [110] in which the required vacuum alignment emerges from symmetry as a semi-direct model [111]. In general the Littlest Seesaw model is an example of trimaximal TM_1 mixing [112, 113], in which the first column of the tri-bimaximal mixing matrix [114] is preserved, similar to the semi-direct model of trimaximal TM_1 mixing that was developed in [115]. To fix the seesaw phase, one imposes a CP symmetry in the original theory which is spontaneously broken, where, unlike [116], there is no residual CP symmetry in either the charged lepton or neutrino sectors, but instead the phase η in the neutrino mass matrix is fixed to be one of the cube roots of unity due to a Z_3 family symmetry, using the mechanism proposed in [117].

As explained in more detail later on, the Littlest Seesaw model predicts all neutrino masses and mixing parameters in terms of two or three parameters, and it has been shown that the model is in agreement with all existing data, for a suitable range of its internal parameters [103]. The model makes some key predictions about the neutrino mass spectrum, that the lightest neutrino is massless $m_1 = 0$ and that normal ordering obtains $\Delta m^2_{31} > 0$, which offer a means to exclude it via the observation of neutrinoless double beta decay, the measurement of the beta-decay end-point, or from cosmological measurements, as well as any measurement of NO from neutrino oscillation searches. However, it also provides a rich set of predictions and correlations for the mixing angles and phases.

In this chapter, we firstly introduce two models studied — LSA and LSB, before presenting the sum rules predicted by LS. Finally, we see how these models fit with the current global-fit data.

8.1 Littlest Seesaw models of neutrinos

Sequential dominance models of neutrinos arise from the proposal that, via the type-I seesaw mechanism, a dominant heavy right-handed (RH) neutrino is mainly responsible for the atmospheric neutrino mass, a heavier subdominant RH neutrino for the solar neutrino mass, and a possible third largely decoupled RH neutrino for the lightest neutrino mass [107]. This leads to the prediction of normal neutrino mass ordering and, in the minimal case containing just the dominant and subdominant right-handed neutrinos, the lightest neutrino must be massless. Constrained sequential dominance (CSD) constrains these models further through the introduction of flavour symmetry, with the indirect approach used to fix the mass matrix from vacuum alignments of flavon fields [108]. A family of such models, parameterized by n, either integer or real using the flavour symmetry groups S_4 or A_4 respectively, predicts the CSD(n) mass matrix for left-handed neutrinos [23, 104]. This model is also known as the Littlest Seesaw (LS) model since it provides a physically viable seesaw model with the fewest number of free parameters. After integrating out the heavy neutrinos, the resulting left-handed light effective Majorana neutrino mass matrix[2] in the charged-lepton flavour basis is given by

$$m^{\nu} = m_a \begin{pmatrix} 0 & 0 & 0 \\ 0 & 1 & 1 \\ 0 & 1 & 1 \end{pmatrix} + m_b e^{i\eta} \begin{pmatrix} 1 & n & (n-2) \\ n & n^2 & n(n-2) \\ (n-2) & n(n-2) & (n-2)^2 \end{pmatrix}, \tag{8.1.1}$$

where in addition to n there are three free real parameters: two parameters with the dimension of mass m_a and m_b which are proportional to the reciprocal of the masses of the dominant and subdominant right-handed neutrinos, and a relative phase η. A second version of this model has also been proposed, based on an $S_4 \times U(1)$ symmetry, where the second and third rows and columns of the mass matrix are swapped [110]. In this paper, we discuss both these versions for the case where

---

[2] We follow the Majorana mass Lagrangian convention $-\frac{1}{2}\overline{\nu_L} m^{\nu} \nu_L^c$.

$n = 3$, with the two versions of the model denoted as LSA and LSB;

$$m^{\nu}_{\mathrm{LSA}} = m_a \begin{pmatrix} 0 & 0 & 0 \\ 0 & 1 & 1 \\ 0 & 1 & 1 \end{pmatrix} + m_b e^{i\eta} \begin{pmatrix} 1 & 3 & 1 \\ 3 & 9 & 3 \\ 1 & 3 & 1 \end{pmatrix}, \tag{8.1.2}$$

$$m^{\nu}_{\mathrm{LSB}} = m_a \begin{pmatrix} 0 & 0 & 0 \\ 0 & 1 & 1 \\ 0 & 1 & 1 \end{pmatrix} + m_b e^{i\eta} \begin{pmatrix} 1 & 1 & 3 \\ 1 & 1 & 3 \\ 3 & 3 & 9 \end{pmatrix}. \tag{8.1.3}$$

Although, in the most minimal set-up, the relative phase η is a free parameter, it has been shown that in some models the presence of additional Z_3 symmetries can fix the phase $e^{i\eta}$ to a cube root of unity [116], with $\eta = 2\pi/3$ the preferred value for LSA and $\eta = -2\pi/3$ for LSB as determined by current data [103]. This restriction gives the model greater predictivity by reducing the number of free parameters to two, and we will give these cases special attention while also showing some results for the case with η left free.

Diagonalizing the mass matrices above leads to predictions for the neutrino masses as well as the angles and phases of the unitary PMNS matrix, U_{PMNS}, which describes the mixing between the three left-handed neutrinos

$$U^T_{\mathrm{PMNS}} m^{\nu} U_{\mathrm{PMNS}} = \begin{pmatrix} m_1 & 0 & 0 \\ 0 & m_2 & 0 \\ 0 & 0 & m_3 \end{pmatrix}, \tag{8.1.4}$$

where U_{PMNS} has been defined in Sec. 2.2.3. All of the parameters in this decomposition are therefore predicted in terms of the 2 (or 3) real parameters in Eqs. (8.1.2) and (8.1.3). Due to the minimal assumption of only two right-handed neutrinos, the lightest neutrino is massless $m_1 = 0$ and the mass-squared differences, which are the only combinations of masses accessible to neutrino oscillation experiments, are predicted to be $\Delta m^2_{21} = m^2_2$ and $\Delta m^2_{31} = m^2_3$. Of the remaining mixing parameters, θ_{12}, θ_{13}, θ_{23} and δ, are also experimentally accessible via neutrino oscillation, while the Majorana phases β_1 and β_2 are not.

As will be seen in more detail in the next section, due to their similar forms, LSA and LSB make similar predictions. However, the process of diagonalization reveals that the octant of θ_{23} is reversed, along with the sign of δ, while all other parameters are unchanged. Changing the sign of η, however, also reverses the sign of δ with no other effect, and so with the sign of η not fixed by the model the only physical difference between LSA and LSB is the octant of θ_{23}.

8.2 Sum rules of LS

It has already been shown that, since the first column of the LS mixing matrix U_{PMNS} is equal to that of the tri-bimaximal mixing matrix, LS (both LSA and LSB for all values of η) obeys the TM1 sum rules [104, 110]

$$\tan\theta_{12} = \frac{1}{\sqrt{2}}\sqrt{1-3s_{13}^2}, \qquad \sin\theta_{12} = \frac{1}{\sqrt{3}}\frac{\sqrt{1-3s_{13}^2}}{c_{13}}, \qquad \cos\theta_{12} = \sqrt{\frac{2}{3}}\frac{1}{c_{13}}, \tag{8.2.5}$$

$$\cos\delta = -\frac{\cot 2\theta_{23}(1-5s_{13}^2)}{2\sqrt{2}s_{13}\sqrt{1-3s_{13}^2}}, \tag{8.2.6}$$

where $s_{ij} = \sin\theta_{ij}$ and $c_{ij} = \cos\theta_{ij}$, and the forms in Eq. (8.2.5) are equivalent.

For LSA with $\eta = \frac{2\pi}{3}$ or LSB with $\eta = -\frac{2\pi}{3}$, there are several additional sum rules. A set of these additional sum rules can be derived using the fact that the only two remaining input parameters m_a and m_b have dimensions of mass, so all the mixing angles and phases must depend only on the ratio $r \equiv \frac{m_b}{m_a}$. Exact expressions for the mixing angles and Dirac phase as a function of r can be found in Appendix C, along with new exact sum rules derived using these expressions. These results make clear the difference between predictions of LSA and LSB; while θ_{13} and θ_{12} remain unchanged, $\cos 2\theta_{23}$ and $\cos\delta$ differ by a change of sign.

An exact expression for the Jarlskog invariant J was given as [104, 110]

$$J = s_{12}c_{12}s_{13}c_{13}^2 s_{23}c_{23}\sin\delta = \mp\frac{24m_a^3 m_b^3(n-1)\sin\eta}{m_3^2 m_2^2 \Delta m_{32}^2}. \tag{8.2.7}$$

with negative sign taken for LSA and positive for LSB. For both LSA with $\eta = \frac{2\pi}{3}$, and LSB with $\eta = -\frac{2\pi}{3}$ we find the new relation

$$m_2 m_3 = 6m_a m_b. \tag{8.2.8}$$

Using this relation and inserting $n = 3$ into Eq. (8.2.7) leads to the new relation for the Jarlskog invariant J

$$J = -\frac{\sqrt{\Delta m^2_{21}\Delta m^2_{31}}}{3\sqrt{3}\Delta m^2_{32}} \tag{8.2.9}$$

and hence the sum rule,

$$\sin\delta = -\frac{\sqrt{\Delta m^2_{21}\Delta m^2_{31}}}{3\sqrt{3}\Delta m^2_{32} s_{12} c_{12} s_{13} c^2_{13} s_{23} c_{23}}, \tag{8.2.10}$$

which is valid for both LSA with $\eta = \frac{2\pi}{3}$ and LSB with $\eta = -\frac{2\pi}{3}$.

8.3 Probing LS with existing data

Existing measurements of the neutrino mixing parameters have been shown to be in good agreement for CSD(n) for the $n = 3$ case [103]. The best-fit value of η is found to be close to $\pm\frac{2\pi}{3}$, with the positive sign for LSA and the negative sign for LSB, which has been theoretically motivated as one of the cube roots of unity required due to an additional Z_3 symmetry as part of a larger GUT model [104]. In this section, we study both the case where η is fixed by symmetry and the case where it is left as a free parameter of the theory.

8.3.1 Predictions of oscillation parameters with fixed $\eta = \pm 2\pi/3$

In the $n = 3$ case of LSA with $\eta = \frac{2\pi}{3}$ (or LSB with $\eta = -\frac{2\pi}{3}$), all neutrino masses, mixing angles and phases are fully determined from the two remaining parameters m_a and m_b and the three most precisely measured of these parameters, θ_{13}, Δm^2_{31} and Δm^2_{21}, currently provide the strongest test of the LS model. Figure 8.1 shows how these parameters vary in the $m_a - m_b$ plane, along with the regions corresponding to the 1σ and 3σ ranges for these parameters from the NuFit 3.0 (2016) global fit [2], assuming normal mass ordering and a lightest neutrino mass of $m_1 = 0$. The SD proposal requires m_a to be significantly larger than m_b and for this portion of the parameter space the approximate proportionality relations of $m_2 \sim m_b$ and $m_3 \sim m_a$ can be seen, verifying the approximations previously derived in [104].

Even at 1σ the three allowed regions coincide at a single point, as can be seen in Fig. 8.2, and so this benchmark point can be used to make predictions of the remaining angles θ_{12} and θ_{23} and the Dirac phase δ. As described in Section 8.2 these parameters, along with θ_{13}, depend only on the ratio $r = m_b/m_a$; this dependence, given by the relations in Eq. (C.0.1), is shown in Fig. 8.3, with the 1σ and 3σ NuFIT 3.0 ranges and reference point at $m_b/m_a = 0.1$. For θ_{23} and δ, the predictions of both LSA and LSB are shown. At this point it can be seen that while both θ_{13} and θ_{12} lie within their 1σ ranges, θ_{23} lies just outside its 1σ range, and a prediction on the value of the Dirac phase is made of $\delta \simeq -90°$.

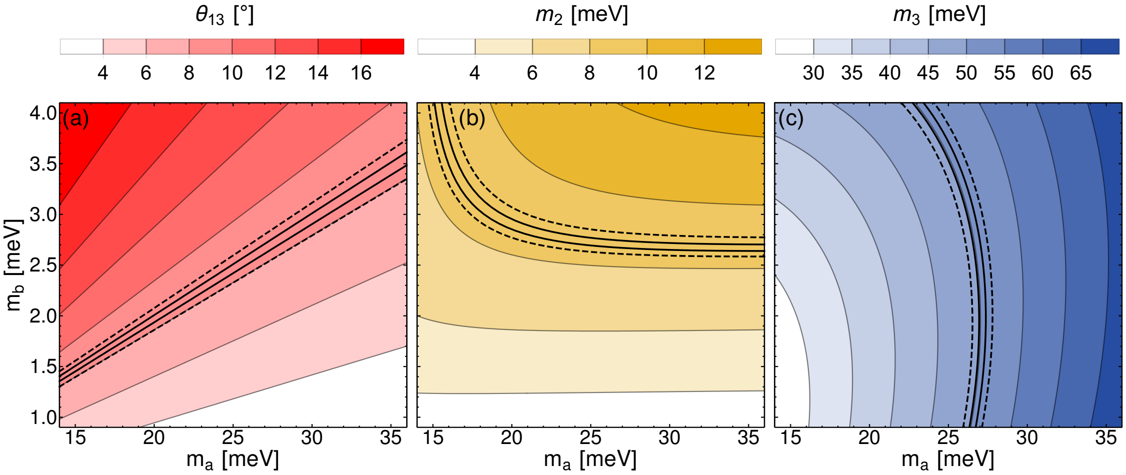

Figure 8.1: Predicted values from LSA with $\eta = \frac{2\pi}{3}$ (or LSB with $\eta = -\frac{2\pi}{3}$) of oscillation parameters depending on the input parameters m_a and m_b. Regions corresponding to the experimentally determined 1σ (solid lines) and 3σ (dashed lines) ranges for each parameter are also shown.

Combining these results for all parameters which have been experimentally measured, displayed together in Fig. 8.4, it is seen that the prediction for θ_{12} lies just within current bounds. However, there is tension at the 1σ level for θ_{23}, due to the allowed regions of LS parameter space requiring values close to maximal, while current data points towards larger deviations from the maximal value. The experimental measurements of θ_{23} do not yet give consistent indications of its value; while the latest results from NOνA disfavour maximal mixing at 2.5σ [118], results from T2K remain fully compatible with maximal θ_{23} [119]. As a result, while the com-

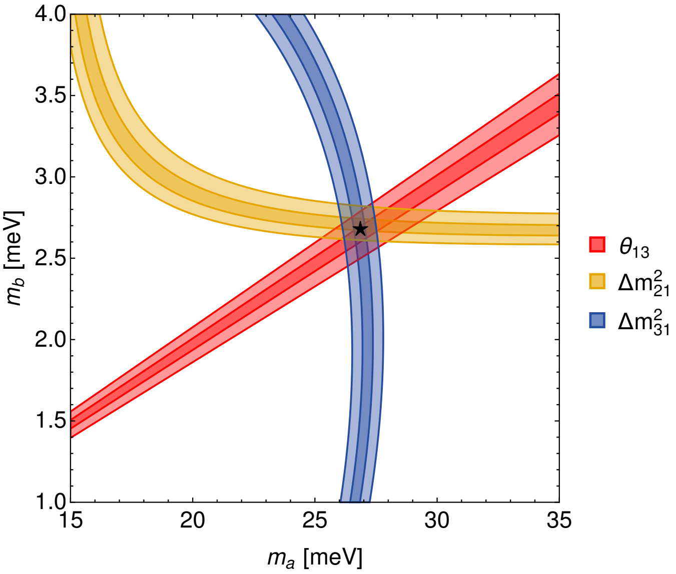

Figure 8.2: Regions in the m_a-m_b plane with fixed $\eta = 2\pi/3$ ($\eta = -2\pi/3$) for LSA (LSB) corresponding to the experimentally determined 1σ and 3σ ranges for θ_{13}, Δm^2_{21} and Δm^2_{31}.

bined fit for θ_{23} is in tension with the LS models at 1σ, the allowed range at 2σ is far wider, crossing both octants and the maximal value of 45°, including the values preferred by the LS model[3].

8.3.2 Predictions of oscillation parameters with η as a free parameter

In the versions of the LS models with η as an additional free parameter, the mixing angles and phases now depend on both the ratio $r = m_b/m_a$ and η. The masses m_3 and m_2 depend on all three input parameters; however, their ratio m_2/m_3 (and therefore the ratio $\Delta m^2_{21}/\Delta m^2_{31}$) will depend only on r and η. As previously, the strongest contraints come from the very precise measurements of θ_{13} and the mass-squared differences Δm^2_{21} and Δm^2_{31}. Figure 8.5 shows the regions corresponding to the 1σ ranges for all the mixing angles, δ and m_2/m_3, where we see that all the five regions come close to overlapping around $\eta = \pm 2\pi/3$ for LSA and LSB,

---

[3] For a more detailed discussion of the current status of experimental measurements of θ_{23}, see [2]

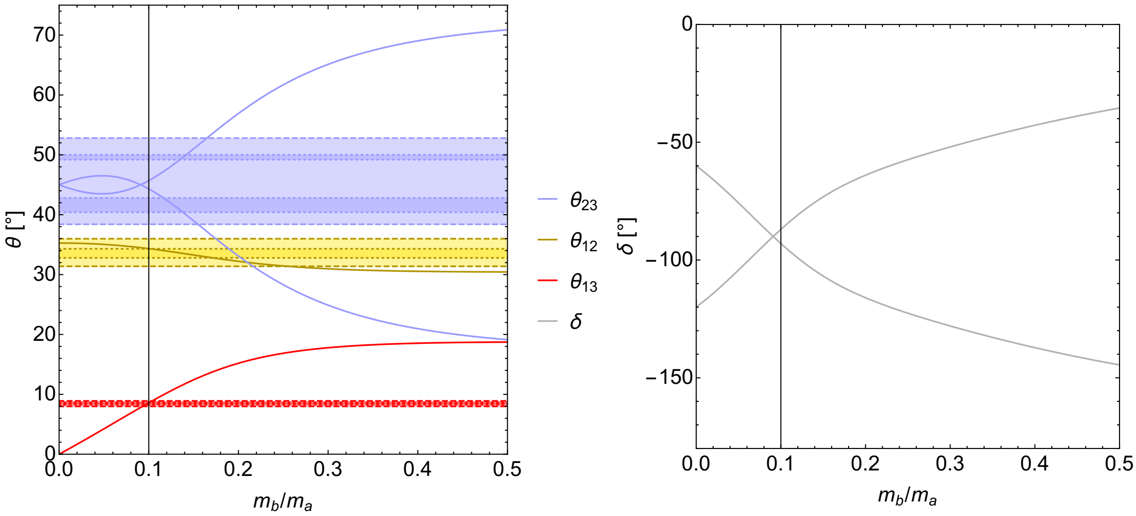

Figure 8.3: Predicted values from LS with fixed $\eta = 2\pi/3$ ($\eta = -2\pi/3$) for LSA (LSB) of the mixing angles and delta as a function of the ratio m_b/m_a. Horizontal bands show the experimentally determined 1σ and 3σ ranges for each parameter. A reference point giving a good prediction for all parameters is shown at $r = m_b/m_a = 0.1$.

respectively. That two input parameters should give a good description of five observables, within their one sigma errors, is ostensibly a remarkable achievement, indeed perhaps better than might be expected on statistical grounds. However, due to the very tight constraints on η from θ_{13} and m_2/m_3, we still find some tension with the value of θ_{23} even when allowing η to vary. As with the case with η fixed, this tension exists only at the 1σ level, where close to maximal θ_{23} is excluded.

8.3.3 Fitting LS models to global fit data

In order to provide a more concrete measure of the agreement between the predictions of the model and existing data, as well as to make further predictions of the less well measured parameters, we have performed a χ^2 fit to the four cases discussed above: LSA and LSB with η fixed and free. As a proxy for the full data sets of previous experiments, our fits use the results of the NuFIT 3.0 global analysis [2]. We use the χ^2 data provided by NuFIT, for the case where normal mass ordering is assumed, combining both the 1D χ^2 data for each mixing parameter with the 2D

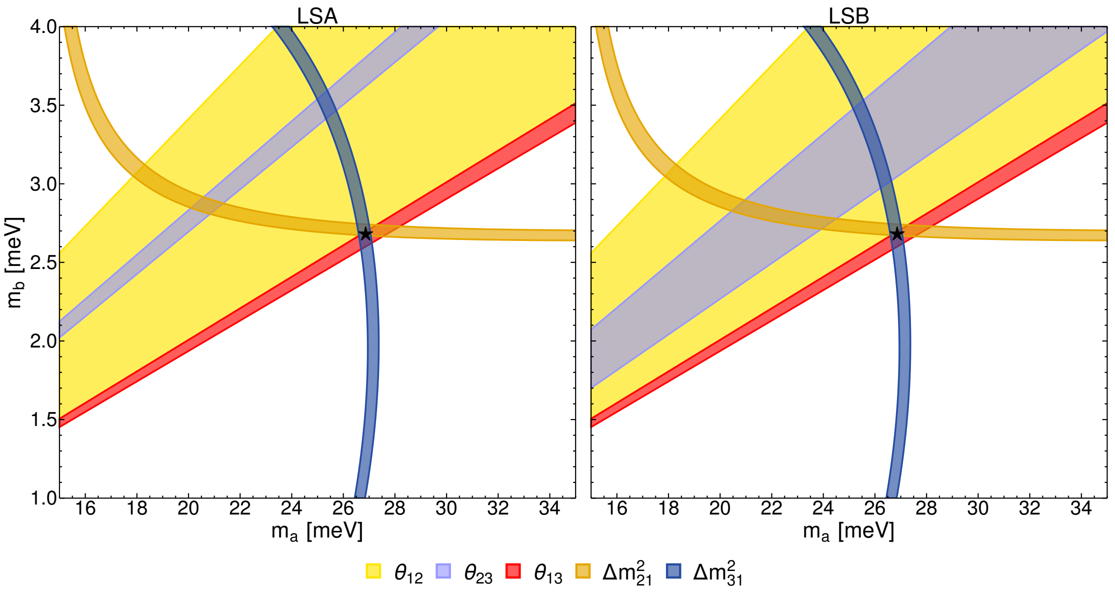

Figure 8.4: Regions in the m_a-m_b plane with fixed $\eta = 2\pi/3$ ($\eta = -2\pi/3$) for LSA (LSB) corresponding to the experimentally determined 1σ ranges for solar and reactor mixing angles and mass-squared differences. The θ_{23} regions shown are in tension with other measurements, however, extending to 2σ these regions become far larger, covering the entire parameter space shown in these plots.

χ^2 data to include correlations between parameter measurements

$$\chi^2_{\mathrm{Fit}}(\Theta) = \sum_{\theta_i \in \Theta} \chi^2_{\mathrm{1D}}(\theta_i) + \sum_{\theta_i \neq \theta_j \in \Theta} \left(\chi^2_{\mathrm{2D}}(\theta_i, \theta_j) - \chi^2_{\mathrm{1D}}(\theta_i) - \chi^2_{\mathrm{1D}}(\theta_j)\right), \tag{8.3.11}$$

where the first sum in this expression combines each of the 1D χ^2 data into a first approximation of the full 6D χ^2 while the second sum provides corrections to this coming from the 2D correlations between each pair of parameters.

We then apply this result first to the standard mixing case, then to the LS model case as follows:

- For the case of standard mixing $\Theta = \Theta_{\mathrm{PMNS}} \equiv \{\theta_{12}, \theta_{13}, \theta_{23}, \Delta m^2_{21}, \Delta m^2_{31}, \delta\}$ and we simply combine the NuFIT 3.0 results as shown above, in order to include correlations, and use it to calculate $\chi^2(\Theta_{\mathrm{PMNS}}) \equiv \chi^2_{\mathrm{Fit}}(\Theta)$ for this case.

- For the LS model we use instead $\Theta = \Theta_{\mathrm{LS}} \equiv \{m_a, m_b, \eta\}$ (or $\Theta_{\mathrm{LS}} = \{m_a, m_b\}$ when fitting with η fixed), which is then minimised over the LS parameter

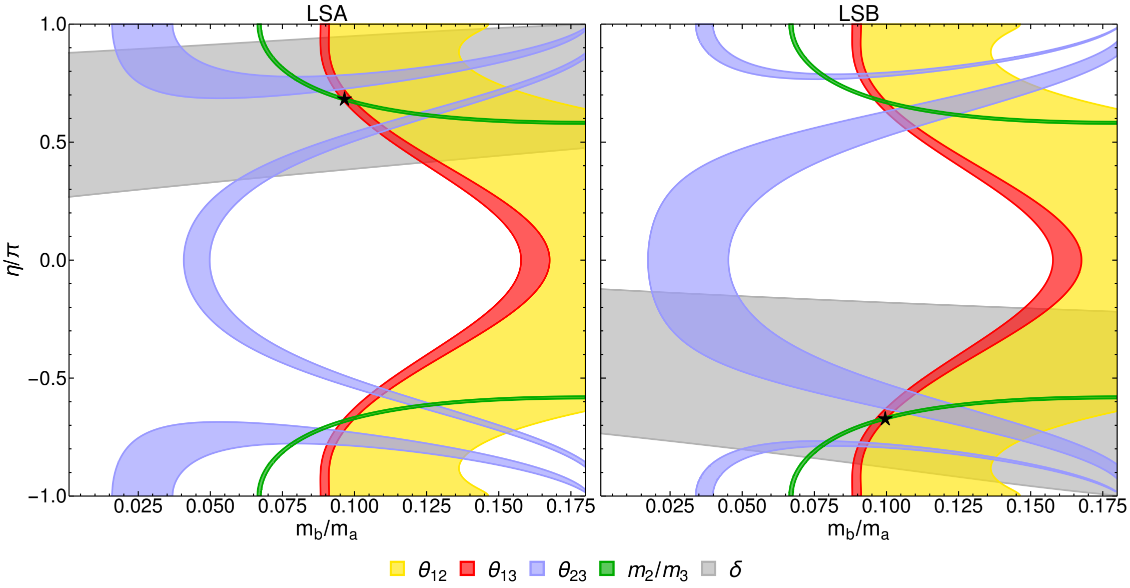

Figure 8.5: Regions in the m_b/m_a-η plane corresponding to the experimentally determined 1σ ranges for all mixing angles, δ and the ratio of neutrino masses m_2/m_3 for LSA (left panel) and LSB (right panel).

space using the analytic relations to calculate standard mixing parameters from LS parameters, and hence calculate $\chi^2\left(\Theta_{\text{LS}}\right) \equiv \chi^2_{\text{Fit}}(\Theta)$ for this case.

Our test statistic for a particular LS model is then given by:

$$\sqrt{\Delta\chi^2} = \sqrt{\min_{\Theta_{\text{LS}}}\left[\chi^2\left(\Theta_{\text{LS}}\right)\right] - \min_{\Theta_{\text{PMNS}}}\left[\chi^2\left(\Theta_{\text{PMNS}}\right)\right]}. \tag{8.3.12}$$

The best fit LSA and LSB points for fits with η left free or with η fixed at $\frac{2\pi}{3}$ are given in Table 8.1. The number of degrees of freedom (d.o.f.) is either 3 or 4, which is just the difference between the number of observables (which we take to be the parameters in Θ_{PMNS}) and the number of LS parameters (namely the parameters in Θ_{LS}, which is either 3 or 2, depending on whether η is free or fixed). For LSA we find a best fit with $\Delta\chi^2 = 4.1$ (3 degrees of freedom) with η free and $\Delta\chi^2 = 5.6$ (4 degrees of freedom) fixing $\eta = \frac{2\pi}{3}$, while for LSB we find better fits, with $\Delta\chi^2 = 3.9$ (3 degrees of freedom) and $\Delta\chi^2 = 4.5$ (4 degrees of freedom) for η free and $\eta = -\frac{2\pi}{3}$ respectively.

Figure 8.6 shows the best fit points with 1σ and 3σ contours of the fits in the $m_a - m_b$ plane for fixed η and in the $r - \eta$ plane for free η. The significance at

	LSA		LSB		NuFIT 3.0
	η free	η fixed	η free	η fixed	global fit
m_a [meV]	27.19	26.74	26.95	26.75	
m_b [meV]	2.654	2.682	2.668	2.684	—
η [rad]	0.680π	$2\pi/3$	-0.673π	$-2\pi/3$	
θ_{12} [°]	34.36	34.33	34.35	34.33	$33.56^{+0.77}_{-0.75}$
θ_{13} [°]	8.46	8.60	8.54	8.60	$8.46^{+0.15}_{-0.15}$
θ_{23} [°]	45.03	45.71	44.64	44.28	$41.6^{+1.5}_{-1.2}$
δ [°]	-89.9	-86.9	-91.6	-93.1	-261^{+51}_{-59}
Δm^2_{21} [10^{-5}eV^2]	7.499	7.379	7.447	7.390	$7.49^{+0.19}_{-0.17}$
Δm^2_{31} [10^{-3}eV^2]	2.500	2.510	2.500	2.512	$2.524^{+0.039}_{-0.040}$
$\Delta\chi^2$ / d.o.f	4.1 / 3	5.6 / 4	3.9 / 3	4.5 / 4	—

Table 8.1: Results of our fit of existing data to LSA and LSB with η left free and for $\eta = \frac{2\pi}{3}$ for LSA and $\eta = -\frac{2\pi}{3}$ for LSB. The results of the NuFIT 3.0 (2016) global fit to standard neutrino mixing are shown for the normal ordering case for comparison.

which a LS model is allowed is determined from the distribution of the $\Delta\chi^2$ test statistic, where $N\sigma$ has been calculated assuming the that Wilks' theorem applies. Note that despite LSA predicting values of θ_{23} which lie outside its individual 1σ range reported by NuFIT 3.0, there are still regions not excluded at 1σ. This is due to the high predictivity of the model; by predicting many parameters from few input parameters there is a greater chance that one of these may lie outside its experimentally determined range. Statistically, this comes from the increased number of degrees of freedom of the χ^2-distribution which approximates our test statistic $\Delta\chi^2$.

Our fit can also be used to identify the regions of standard neutrino mixing parameter space predicted by LS, once existing data has been taken into account. This corresponds to mapping the regions of LS input parameter space allowed by our fit onto the standard mixing parameter space. Figure 8.7 shows the predictions of LS (for the fixed η case) in the planes made from each pair of mixing angles and δ.

Since these values all depend only on the single parameter r, the predictions of LS form lines of allowed solutions in each plane, corresponding to sum-rules between the oscillation parameters. For example, Fig. 8.7a corresponds to the TM1 sum rule in Eq. (8.2.5), while Figs. 8.7b to 8.7f correspond to those in Eq. (C.0.6) or to combinations of these sum rules. It can be seen that very strong restrictions are placed on the allowed values of the less well measured parameters, θ_{12}, θ_{23} and δ. For the remaining angle, θ_{13}, around two thirds of the NuFIT 3.0 range remains viable in LS.

Figure 8.8 shows the allowed regions of parameter space for pairs of variables including the mass-squared differences. In these plots, as the mass-squared differences can depend on both m_a and m_b independently, we see regions of allowed values instead of lines. For each of these planes, any point will fully determine both input parameters m_a and m_b, and so these contours correspond exactly to the equivalent regions shown in Fig. 8.6. In addition to the tight constraints on θ_{12}, θ_{23} and δ already mentioned, in Figs. 8.8b and 8.8e it can be seen that the allowed range of θ_{13} is correlated with that of both Δm^2_{21} and Δm^2_{31}, suggesting that combining future measurements of these parameters could provide a better probe of LS than the individual parameter measurements alone. The ability of future experiment to exclude the model then depends on both the predictions of the model seen here, combined with the sensitivity of experiments to measurements of the parameters in the region of interest predicted by LS, which is the focus of the next chapter.

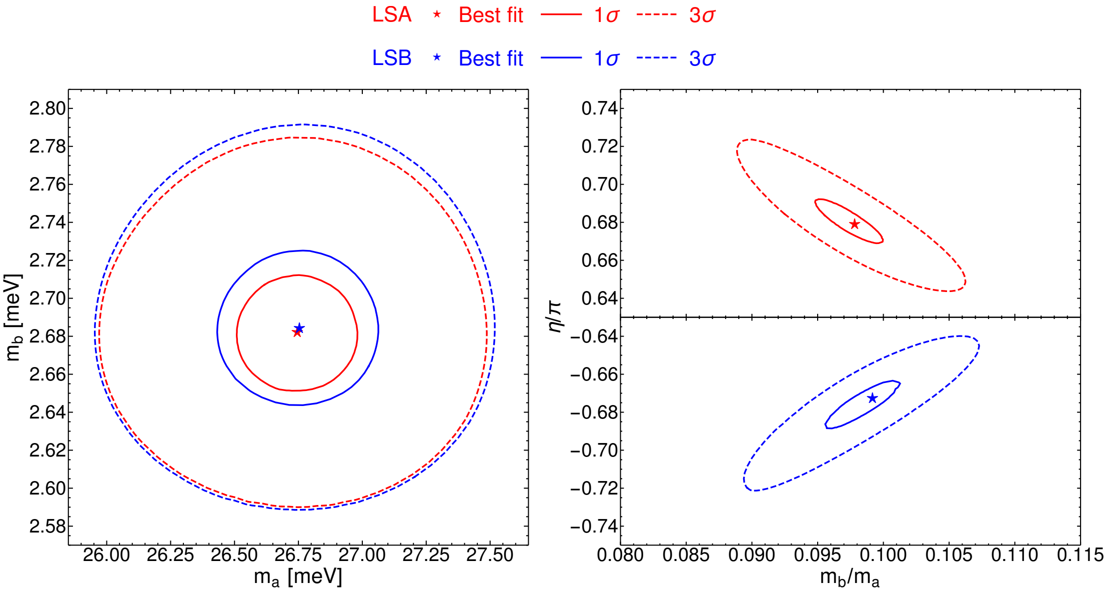

Figure 8.6: Results of the fits to LS of the NuFIT 3.0 (2016) global neutrino oscillation data. Left: LS fit with fixed $\eta = 2\pi/3$ ($\eta = -2\pi/3$) for LSA (LSB). Right: LS fit with η as a free parameter.

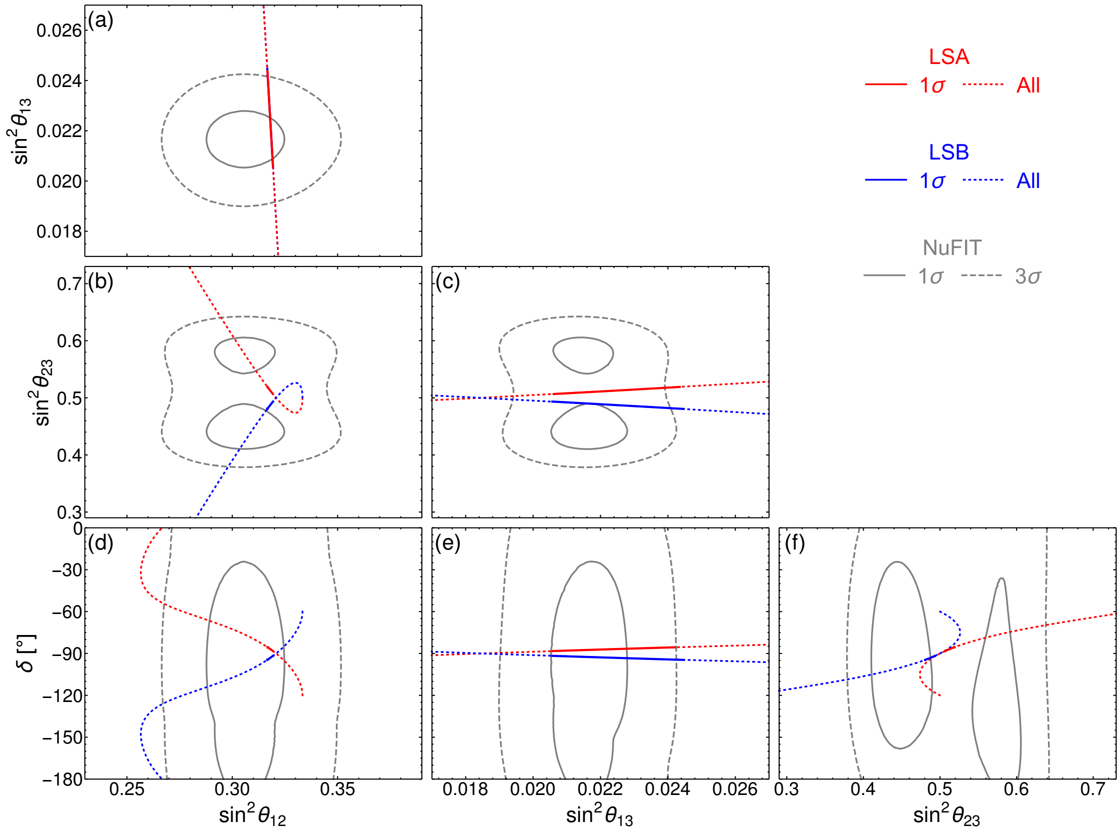

Figure 8.7: Allowed values for LSA (red) and LSB (blue) with $\eta = 2\pi/3$ and $\eta = -2\pi/3$ respectively, showing all possible values (dotted) and the 1σ range (solid). These lines of allowed solutions correspond to the sum rules in Eqs. (8.2.5) and (C.0.6), or combinations thereof. Also shown are the 1σ (solid) and 3σ (dashed) regions from the NuFIT 3.0 2016 global fit (grey).

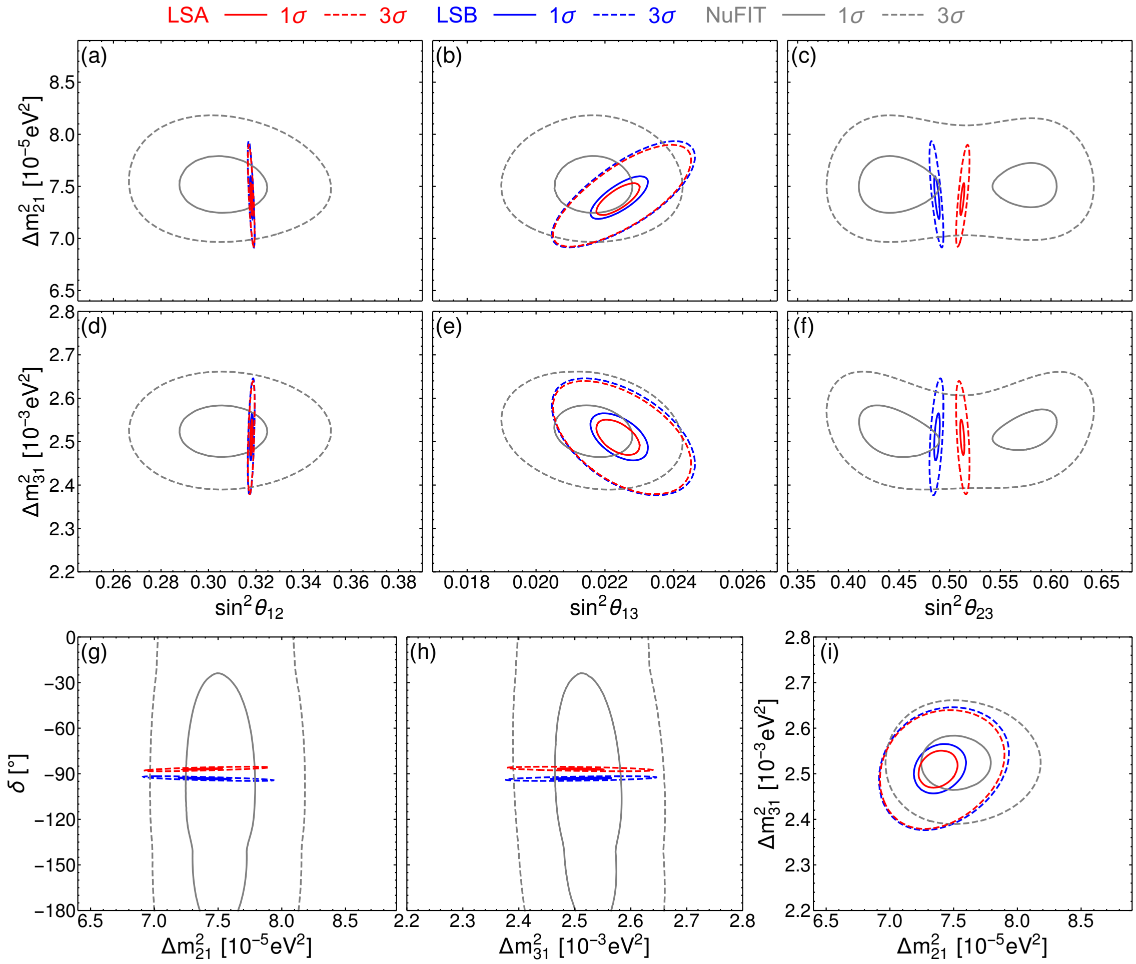

Figure 8.8: Allowed 1σ (solid) and 3σ (dashed) regions for LSA (red) and LSB (blue) with $\eta = 2\pi/3$ and $\eta = -2\pi/3$ respectively. Also shown are the current allowed regions from the NuFIT 3.0 2016 global fit (grey).

Chapter 9

Littlest Seesaw in future experiments

In order to understand the potential for future experiments to exclude the LS models, we have performed simulations of a combination of accelerator and reactor experiments, modelling the experimental data expected over the next two decades. In all our simulations we assume that the mass ordering is known to be normal ordering, as this is a requirement of the LS models; a measurement of inverted ordering would immediately exclude the models.

Our combination of experiments include detailed simulations of the T2HK and DUNE long-baseline accelerator experiments, which aim to provide precision measurements of Δm^2_{31}, θ_{23} and δ, together with basic constraints on θ_{13} from the Daya Bay short baseline reactor experiment and on θ_{12} and Δm^2_{21} from the JUNO and RENO-50 medium baseline reactor experiments. The studied experiments have been introduced in Chp. 3. We have used complete simulations of the latest designs for both DUNE and T2HK where we have assumed both experiments run for 10 years.

9.1 Statistical Method

To determine the statistical significance with which the LS model could be excluded based on simulated data, we perform a minimum-χ^2 fit to both standard three neutrino mixing and to the LS model. As in section 8.3.3, for the case of standard mixing we use $\Theta = \Theta_{\text{PMNS}} \equiv \{\theta_{12}, \theta_{13}, \theta_{23}, \Delta m^2_{21}, \Delta m^2_{31}, \delta\}$, while for LS we use $\Theta = \Theta_{LS} \equiv \{m_a, m_b, \eta\}$ (or $\Theta_{\text{LS}} = \{m_a, m_b\}$ when fitting with η fixed). Our test statistic for the significance to exclude the LS model is then given by

$$\sqrt{\Delta\chi^2} = \sqrt{\min_{\Theta_{\text{LS}}} \left[\chi^2\left(\Theta_{\text{LS}}\right)\right] - \min_{\Theta_{\text{PMNS}}} \left[\chi^2\left(\Theta_{\text{PMNS}}\right)\right]}. \tag{9.1.1}$$

The significance at which LS is excluded is then determined from the distribution of the $\Delta\chi^2$ test statistic; where we give sensitivities in terms of $N\sigma$, this quantity has been calculated assuming the that Wilks' theorem applies. Wilks' theorem states that when comparing nested models, the $\Delta\chi^2$ test statistic is a random variable asymptotically distributed according to the χ^2-distribution with the number of degrees of freedom equal to the difference in number of free parameters in the models. In this case we treat the LS models, with two or three free parameters, as sub-models of standard neutrino mixing with six free parameters, leading to a χ^2-distribution with 4 degrees of freedom when η is kept fixed or 3 degrees of freedom when η is left as a free parameter. We have verified via Monte-Carlo simulations that the distribution of our $\Delta\chi^2$ test statistic is well approximated by these distributions.

In applying the above formula, the $\chi^2(\Theta)$ is minimised over the parameters Θ in our fits and is built from three parts;

$$\chi^2(\Theta) = \chi^2_{\text{LB}}(\Theta) + \chi^2_{\text{R}}(\Theta) + P(\Theta), \tag{9.1.2}$$

with $\chi^2_{\text{LB}}(\Theta)$ for the full simulations of the long-baseline experiments DUNE and T2HK, for which more details are given in App. A.3. And $\chi^2_{\text{R}}(\Theta)$ for the constraints from reactor experiments Daya Bay and JUNO, and $P(\Theta)$ for a prior intended to include information from the results of existing experimental measurements.

For the reactor experiments we simply assume independent Gaussian measurements such that

$$\chi^2_{\text{R}} = \frac{\left(\sin^2\theta_{13} - \sin^2\overline{\theta_{13}}\right)^2}{\sigma^2_{\theta_{13}}} + \frac{\left(\sin^2\theta_{12} - \sin^2\overline{\theta_{12}}\right)^2}{\sigma^2_{\theta_{12}}} + \frac{\left(\Delta m^2_{21} - \overline{\Delta m^2_{21}}\right)^2}{\sigma^2_{\Delta m^2_{21}}}, \tag{9.1.3}$$

where $\overline{\theta_{13}}$, $\overline{\theta_{12}}$ and $\overline{\Delta m^2_{21}}$ are the true parameter values and $\sigma_{\theta_{13}}$, $\sigma_{\theta_{12}}$ and $\sigma_{\Delta m^2_{21}}$ the corresponding experimental measurement uncertainties.

The prior $P(\Theta)$ provides information from existing experimental measurements and is calculated using the results of the NuFIT 3.0 global fit in the same way as our fit in Section 8.3.3, so that $P(\Theta) = \chi^2_{\text{Fit}}(\Theta)$ as defined in Eq. (8.3.11).

In all our simulations, the true parameters are taken to be the best-fit values from the appropriate LS fit results given in Table 8.1, except where stated otherwise.

9.2 Results

The sensitivity to exclude either version of the LS model is shown as a function of the true value of each parameter in Fig. 9.1, for true values, with the range selected along the horizontal axes to be that given by the currently allowed at 3σ by the latest NuFIT 3.0 global fit. In each case, the parameters not shown are assumed to take their best-fit values from the fit to LS described in Section 8.3.3.

From the upper panels in Fig. 9.1, we see that θ_{12}, θ_{23} and δ provide the strongest tests of the model, with there only being a relatively small portion of the presently allowed true parameter space where the model would not be excluded. This is due to the strong predictions of these parameters by the LS models, as discussed in Section 8.3.1. Note that these parameters are those that will be measured most precisely by the three next-generation experiments used in our simulations, JUNO, DUNE and T2HK. For these three parameters, the effect of allowing η to vary does not much change the sensitivity, other than the additional solution (currently disfavoured by experiment) with $\delta = +90°$ which occurs when changing the sign of η. For θ_{12} in particular there is no effect of allowing η to vary. This is due to the sum rule in Eq. (8.2.5) which relates θ_{12} with θ_{13} independently from the value of η; the precise measurement of θ_{13} then fixes the value of θ_{12} to a narrow range such that a measurement of θ_{12} outside of this would exclude the LS model regardless of the LS parameter values. Similarly the precise measurements of θ_{13}, Δm^2_{21} and Δm^2_{31} strongly constrain the magnitude (but not sign) of η, so that the LS allowed regions of the other variables are not significantly changed when η is allowed to vary, with the noted exception that changing the sign of η allows the sign of δ to also change.

From the lower panels in Fig. 9.1, we see that the sensitivity to exclude LS from measurements of θ_{13}, Δm^2_{21} or Δm^2_{31} is much less than for the other three parameters and the sensitivity is also significantly reduced when allowing η to vary. By the converse argument to that used above, this is due to these three parameter measurements driving the fit to m_a and m_b (and η), and so a measurement of these parameters will tend to move the fitted LS parameter values rather than exclude the model, particularly when fitting the extra free parameter η. However, a particularly small measurement of θ_{13} or particularly large measurement of Δm^2_{21}, relative to their current allowed range of values, may still exclude the fixed η version of the models.

The results shown in Fig. 9.1 show only the dependence of the significance to exclude LS on the true value of each variable individually. However, the sensitivity will generally have a strong dependence on the true values of the other parameters. The significance to exclude the LS models depending on the true values of each pair of variables, for the cases where η is kept fixed, is shown in Figures 9.2 and 9.4 for LSA and in Figs. 9.3 and 9.5 for LSB.

Each panel of Figs. 9.2 and 9.3 includes two dimensionless variables (i.e. angle or phase) which both depend only on the ratio of LS input parameters $r = m_b/m_a$, and so, in a LS model, a measurement of any one of these parameters corresponds to a measurement of $r = m_b/m_a$ (see Fig. 8.3). Combining two of these parameter measurement therefore give two measurements of $r = m_b/m_a$, with any conflict between them providing strong evidence to exclude the model. For this reason the significance to exclude the models is close to being simply the combined significance from individual measurements implied by Fig. 9.1.

By contrast, each panel of Figures 9.4 and 9.5 shows the results for the pairs of variables including at least one dimensionful mass-squared difference. Here we can see in Figs. 9.4b, 9.4e and 9.4i for LSA, and in Figs. 9.5b, 9.5e and 9.5i for LSB, there is a strong correlation between the measurements of θ_{13}, Δm^2_{21} and Δm^2_{31}. This shows clearly that, although individual measurements of these parameters cannot exclude a LS model (since the parameters of the LS model could be adjusted to accommodate any of them individually) a *combined* measurement of two of them could serve to exclude the model. This is the reason for presenting these combined sensitivity plots. Of the three parameters for which such *combined* measurements provide the strongest test of the model, each pair includes measurements from different experiments, with θ_{13} coming mainly from the short-baseline reactor measurement such as Daya Bay, Δm^2_{21} from the medium-baseline reactor measurement such as JUNO, and Δm^2_{31} from the long-baseline accelerator measurement such as DUNE and T2HK. This demonstrates a strong synergy between all these experiments in attempts to exclude the LS models.

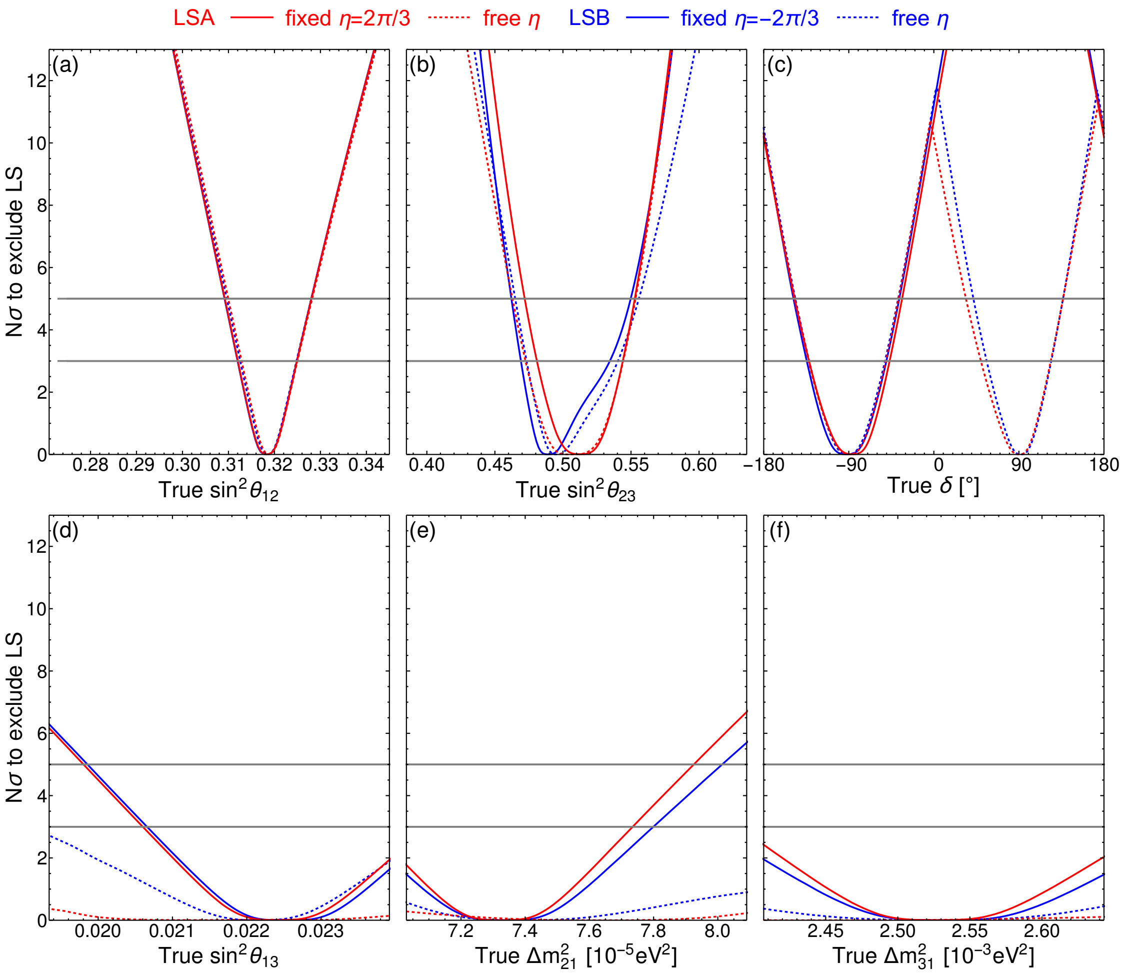

Figure 9.1: The predicted sensitivity of future experiments to excluding LSA (red) and LSB (blue), shown as a function of the true value of each parameter. Solid curves correspond to the case with η fixed at $\eta = \frac{2\pi}{3}$ for LSA or $\eta = -\frac{2\pi}{3}$ for LSB, while dashed curves correspond to the case with η left free. The ranges of true parameters shown in the plots corresponds to the current three sigma allowed NuFIT 3.0 regions.

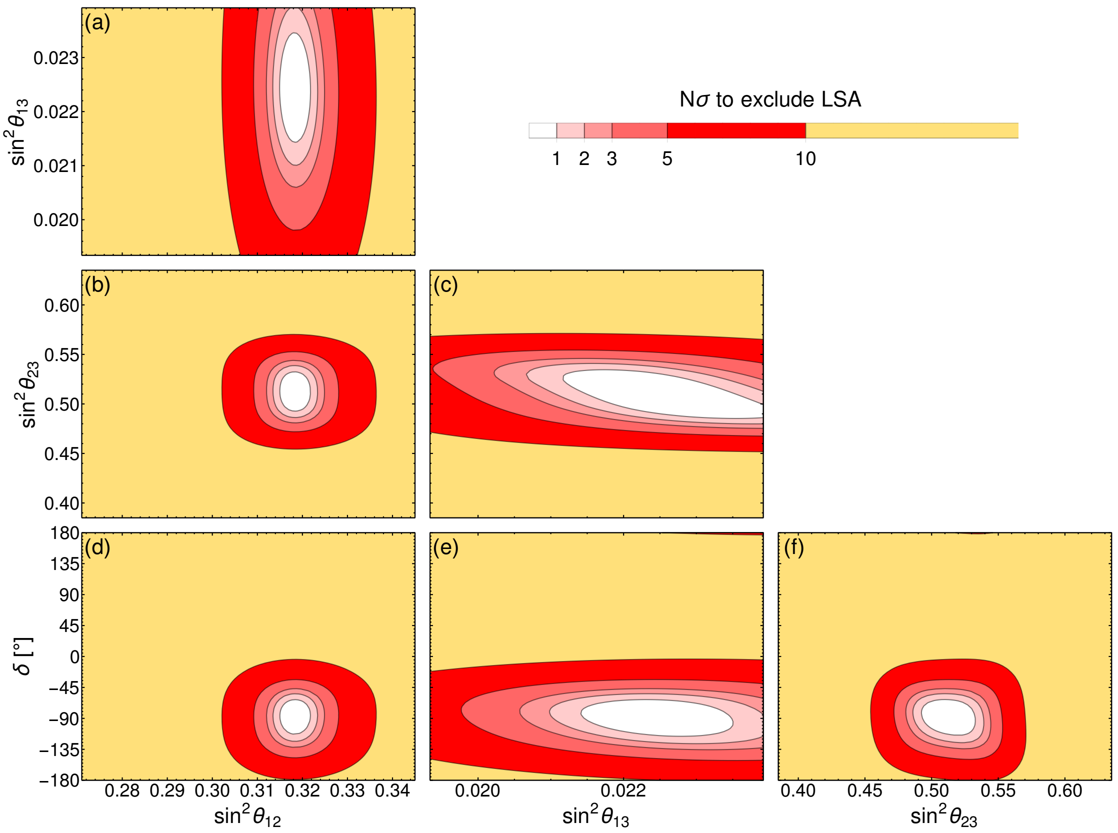

Figure 9.2: The predicted sensitivity of future experiments to excluding LSA, with η fixed at $\eta = \frac{2\pi}{3}$, shown as a function of each pair of true parameters. The ranges of true parameters shown in the plots corresponds to the current three sigma allowed NuFIT 3.0 regions.

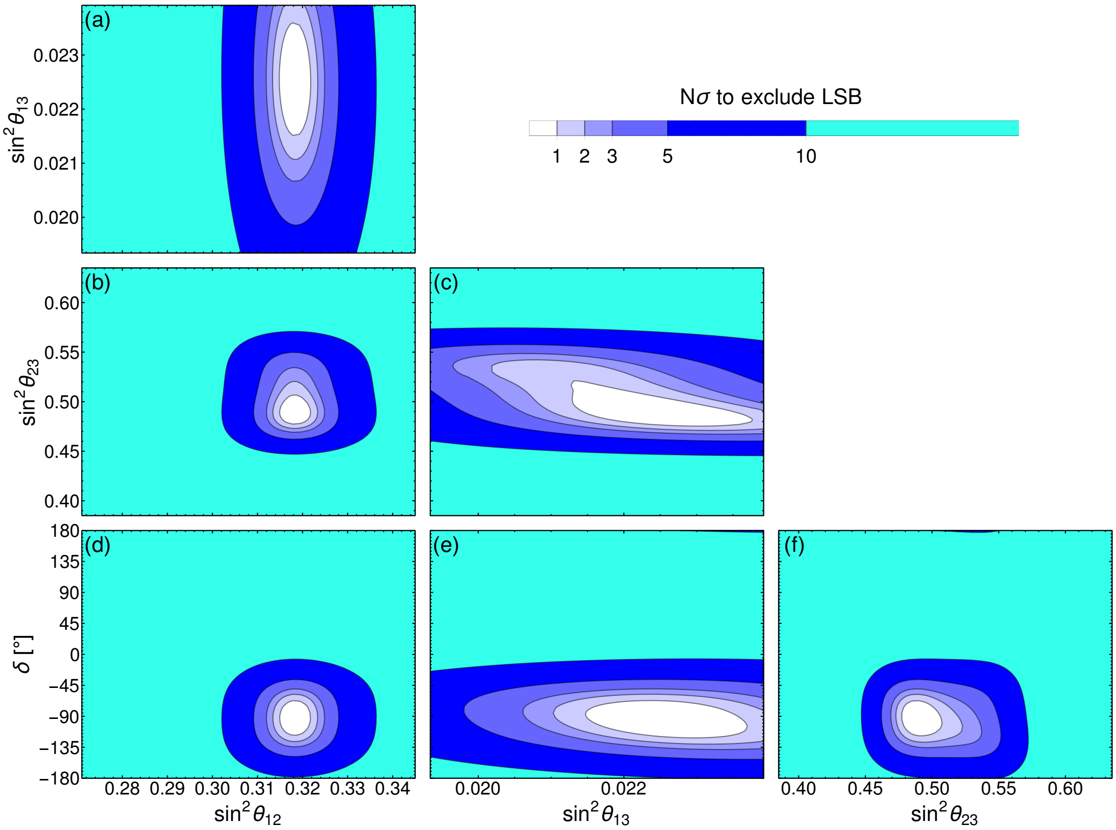

Figure 9.3: The predicted sensitivity of future experiments to excluding LSB, with η fixed at $\eta = -\frac{2\pi}{3}$, shown as a function of each pair of true parameters. The ranges of true parameters shown in the plots corresponds to the current three sigma allowed NuFIT 3.0 regions.

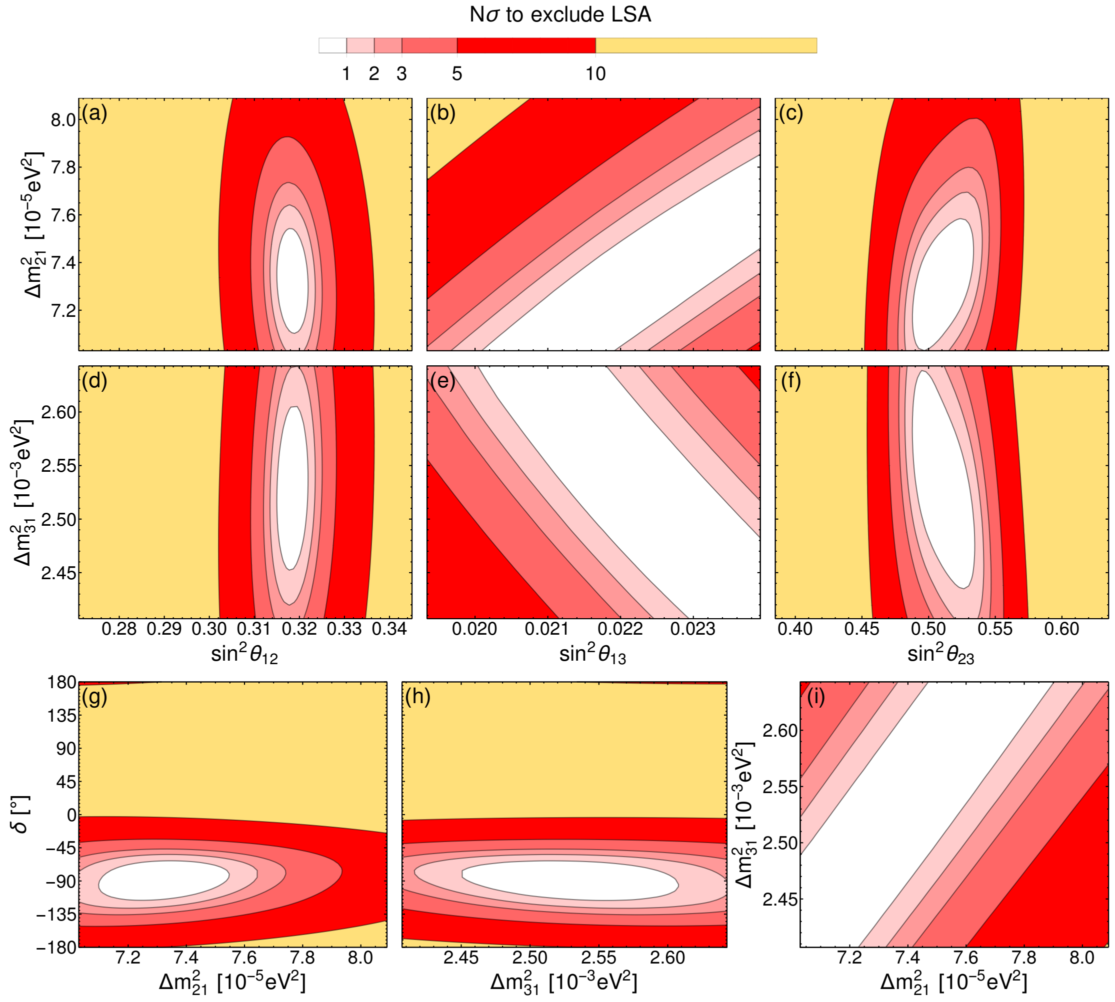

Figure 9.4: The predicted sensitivity of future experiments to excluding LSA, with η fixed at $\eta = \frac{2\pi}{3}$, shown as a function of each pair of true parameters. The ranges of true parameters shown in the plots corresponds to the current three sigma allowed NuFIT 3.0 regions.

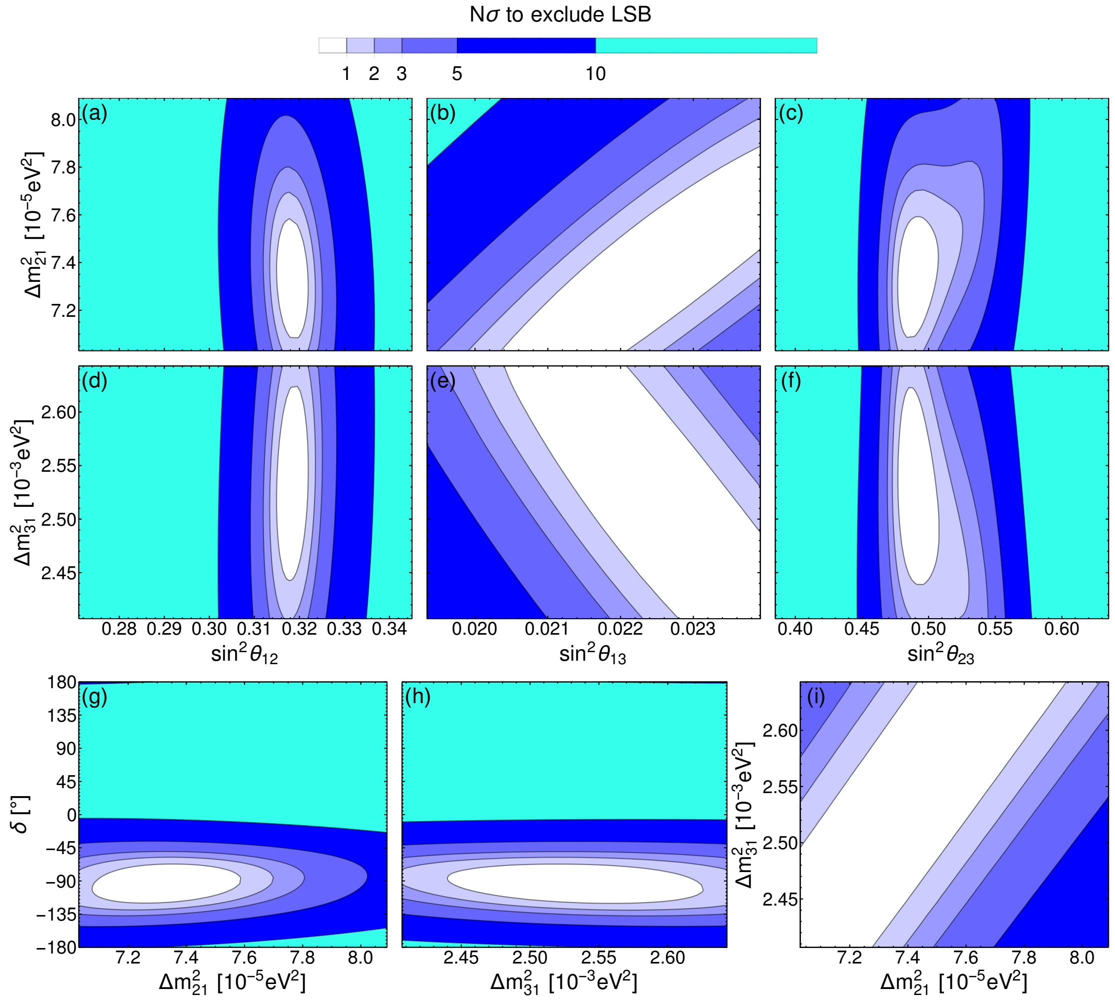

Figure 9.5: The predicted sensitivity of future experiments to excluding LSB, with η fixed at $\eta = -\frac{2\pi}{3}$, shown as a function of each pair of true parameters. The ranges of true parameters shown in the plots corresponds to the current three sigma allowed NuFIT 3.0 regions.

Chapter 10

Nonstandard Interactions (NSIs) in Matter

Nonstandard interactions (NSIs) are the four-fermion interactions involving neutrinos that cannot be explained by the standard model (SM) [31]. NSIs can occur at the source, detector of neutrinos and in matter during the propagation, and are therefore taken as NSIs at the source and detector and in matter respectively. We have not yet discovered hints for NSIs at the source and the detector with high precision [31,36]. However, the weaker bounds for parameters on matter effect NSIs are found in the current global fit results [39].

NSIs in matter are customarily described by a 3×3 Hermitian matrix $\epsilon^{\rm m}$ added to an effective Hamiltonian H in the flavour basis,

$$H = \frac{1}{2E} \left\{ U \begin{pmatrix} 0 & 0 & 0 \\ 0 & \Delta m^2_{21} & 0 \\ 0 & 0 & \Delta m^2_{31} \end{pmatrix} U^\dagger + A \begin{pmatrix} 1+\epsilon^{\rm m}_{ee} & \epsilon^{\rm m}_{e\mu} & \epsilon^{\rm m}_{e\tau} \\ \epsilon^{\rm m}_{\mu e} & \epsilon^{\rm m}_{\mu\mu} & \epsilon^{\rm m}_{\mu\tau} \\ \epsilon^{\rm m}_{\tau e} & \epsilon^{\rm m}_{\tau\mu} & \epsilon^{\rm m}_{\tau\tau} \end{pmatrix} \right\}, \qquad (10.0.1)$$

where $\epsilon^{\rm m}_{\alpha\beta} = \epsilon^{\rm m^*}_{\beta\alpha}$, and $A = 2\sqrt{2} G_F N_e E$ is the usual matter effect with N_e the electron number density in the Earth and E the neutrino beam energy. Because of the fact that we cannot distinguish which particles (electrons, protons, or neutrons) in the Earth participate in NSIs by observing oscillation probabilities, we obtain

$$\epsilon^{\rm m}_{\alpha\beta} = \Sigma_P \left[\epsilon^{e,P}_{\alpha\beta} + \frac{N_u}{N_e} \epsilon^{u,P}_{\alpha\beta} + \frac{N_d}{N_e} \epsilon^{d,P}_{\alpha\beta} \right], \qquad (10.0.2)$$

with N_u (N_d) is the number density of u (d) quarks in the Earth.

On the other hand, NSIs at source and detector are expressed as 3×3 complex matrices ϵ^{s}, ϵ^{d}, respectively, contributing to superpositions of flavour states,

$$|\nu_\alpha^{\mathrm{s}}\rangle = \frac{1}{n_\alpha^{\mathrm{s}}}\Big(|\nu_\alpha\rangle + \sum_\beta \epsilon^{\mathrm{s}}_{\alpha\beta}|\nu_\beta\rangle\Big)\,, \quad \langle\nu_\beta^{\mathrm{d}}| = \frac{1}{n_\beta^{\mathrm{d}}}\Big(\langle\nu_\beta| + \sum_\alpha \epsilon^{\mathrm{d}}_{\alpha\beta}\langle\nu_\alpha|\Big)\,, \qquad (10.0.3)$$

where $n_\alpha^{\mathrm{s}} = \sqrt{\sum_\beta |\delta_{\alpha\beta} + \epsilon^{\mathrm{s}}_{\alpha\beta}|^2}$, $n_\beta^{\mathrm{d}} = \sqrt{\sum_\alpha |\delta_{\alpha\beta} + \epsilon^{\mathrm{d}}_{\alpha\beta}|^2}$ (for $\alpha \neq \beta \neq \gamma \neq \alpha$) are normalisation factors. Replacing A with $-A$ and $\epsilon^{\mathrm{m,d,s}}$ with $\epsilon^{\mathrm{m,d,s}*}$, we obtain those for antineutrinos.

Under the symmetry of $\mathrm{SU}(2)_L$, in principle the tight constraint from SM charge leptons propagates to NSIs. This is true while we only consider dimension-6 operators for new interactions. In this chapter, we argue the allowance of sizeable NSIs in matter, without breaking any symmetry of the SM. After this chapter, we will not specify the super-script $^{\mathrm{m}}$ on $\epsilon_{\alpha\beta}$ to denote the NSIs taking place in matter, but simply use $\epsilon_{\alpha\beta}$. In the first section of this chapter, we adopt the approach of effective field theory, obtaining the operators of the dimension $\leqslant 8$ for NSIs. We will see that in the framework of EFT, after the breaking of electroweak symmetry, NSIs in matter can be independent of the constrain from the charged lepton sector and NSIs at the source and the detector. In the next section, we review the current global-fit results for matter-effect NSIs.

10.1 NSIs in the EFT approach

In this work, we assume that NSIs arise from effective higher-dimensional operators and these operators satisfy the following conditions.

- Lorentz invariance and the SM gauge symmetry $SU(2)_{\mathrm{L}} \times U(1)_{\mathrm{Y}}$ are required around and above the electroweak scale.
- Since neutrino oscillation experiments cannot test lepton-number-violating (LNV) or baryon-number-violating (BNV) processes, we require lepton and baryon number conservation in the effective operator [1].

---

[1] This does not mean that the lepton number or baryon number cannot be broken in the UV-complete scale, as will be discussed in Sec. 12.2.

- We will only focus on operators involving four fermions. The simplest operators have the dimension $d = 6$, and the operators with $d > 6$ are formed by 4 fermions and $d - 6$ Higgs[2]. The SM fermion contents are denoted as

$$E_{\rm R} = (e_{\rm R}, \mu_{\rm R}, \tau_{\rm R})^T \, , \; U_{\rm R} = (u_{\rm R}, c_{\rm R}, t_{\rm R})^T \, , \; D_{\rm R} = (d_{\rm R}, s_{\rm R}, b_{\rm R})^T \, ,$$
$$L = (L_1, L_2, L_3)^T \, , \; Q = (Q_1, Q_2, Q_3)^T \, , \tag{10.1.4}$$

  where $L_1 = (\nu_{e\rm L}, e_{\rm L})$, $L_2 = (\nu_{\mu\rm L}, \mu_{\rm L})$, $L_3 = (\nu_{\tau\rm L}, \tau_{\rm L})$, $Q_1 = (u_{\rm L}, d_{\rm L})$, $Q_2 = (c_{\rm L}, s_{\rm L})$, $Q_3 = (t_{\rm L}, b_{\rm L})$.

- In processes of neutrino production and detection, at least one L must be involved in the relevant operators, while in the neutrino propagation, at least two Ls must be involved in the relevant operators.

- Furthermore, we will impose one more requirement: we only consider NSIs which avoid the strong constraints from 4-charged-fermion interactions, e.g., rare lepton-flavour-violating decays of leptons and hadrons. Since left-handed charged leptons and neutrinos belong to the same electroweak doublet in the SM, any NSI effects from higher-dimensional operators are related to an interaction involving at least one charged lepton. Once all final and initial states of the latter interaction are electrically charged fermions, i.e., charged leptons and quarks, the operator and the relevant NSI parameters should have been strongly constrained by these "visible" processes. For example, the operator $(\overline{L_1}\mu_{\rm R})(\overline{Q_1}u_{\rm R}) = (\overline{\nu_{e\rm L}}\mu_{\rm R})(\overline{d_{\rm L}}u_{\rm R}) - (\overline{e_{\rm L}}\mu_{\rm R})(\overline{u_{\rm L}}u_{\rm R})$ and its conjugate can lead to NSI processes $\pi^+ \to \mu^+\nu_e$ and $\nu_e + (A, Z) \to \mu^- + (A, Z+1)$ over the standard neutrino production process $\pi^+ \to \mu^+\nu_\mu$ and detection process $\nu_\mu + (A, Z) \to \mu^- + (A, Z+1)$, respectively, where (A, Z) is a nucleus with atomic mass number A and proton number Z. But this operator also results in the rare decay $\pi^0 \to \mu^+ e^-$, which gives strong constraints to the coefficient of $(\overline{L_1}\mu_{\rm R})(\overline{Q_1}u_{\rm R})$. Another example is that the non-standard

---

[2] Operators modifying neutrino kinetic terms may also contribute to the NSIs through the non-diagonal Z mediation. These effects are small, $\lesssim 10^{-3}$, from the constraints of the PMNS non-unitarity [38, 120], and will not be our case here.

$\nu_\mu + (e,u,d) \to \nu_e + (e,u,d)$ propagation in matter may be constrained by $\mu + (e,u,d) \to e + (e,u,d)$ in the μ-e conversion measurement. In order to find possible sizeable NSIs, we should not focus on interactions which have the correspondence with "visible" processes.

The following classes of operators and their conjugates are allowed by the first four requirements,

$$\overline{L}E_{\rm R}\overline{D_{\rm R}}Q,\ \overline{L}E_{\rm R}\overline{Q}U_{\rm R},\ \overline{L}L\overline{F}F \text{ with } F = L, E_{\rm R}, Q, U_{\rm R}, D_{\rm R} \tag{10.1.5}$$

for $d = 6$ and

$$\begin{aligned}&\overline{L}L\overline{D_{\rm R}}U_{\rm R}H^*H^*,\ \overline{L}E_{\rm R}\overline{U_{\rm R}}QHH,\ \overline{L}E_{\rm R}\overline{Q}D_{\rm R}HH,\ \overline{L}E_{\rm R}\overline{L}E_{\rm R}HH,\\ &\overline{L}E_{\rm R}\overline{D_{\rm R}}QH^*H,\ \overline{L}E_{\rm R}\overline{Q}U_{\rm R}H^*H,\ \overline{L}L\overline{F}FH^*H\end{aligned} \tag{10.1.6}$$

for $d = 8$. Here we have not written out the necessary Γ matrices, gauge indices and flavour indices. The lepton and baryon number conservations forbid any dimension-7 operators involving 4 fermions. After the Higgs gets the VEV $\langle H\rangle = (0,1)^T(2\sqrt{2}G_F)^{-1/2}$, these operators are classified into two types, those preserving electroweak symmetry and those not. Taking the last requirement into account, we extract the following operators:

- The first class are

$$\begin{aligned}&\varepsilon_{ac}\varepsilon_{bd}(\overline{L_{a\alpha}}\gamma^\mu L_{b\beta})(\overline{L_{c\gamma}}\gamma_\mu L_{d\delta})\,,\\ &\varepsilon_{ac}\varepsilon_{bd}(\overline{L_{a\alpha}}\gamma^\mu L_{b\beta})(\overline{L_{c\gamma}}\gamma_\mu L_{d\delta})H^\dagger H\,,\end{aligned} \tag{10.1.7}$$

  where $\alpha,\beta,\gamma,\delta = 1,2,3$ are flavour indices, $a,b,c,d = 1,2$ are $SU(2)_{\rm L}$ doublet indices, and non-vanishing entries of ε_{ab} are given by $\varepsilon_{12} = -\varepsilon_{21} = 1$. Specifically, we denote the flavour indices in the lepton sector as $(1,2,3) = (e,\mu,\tau)$. Using the relation $\varepsilon_{ac}\varepsilon_{cd} = \delta_{ab}\delta_{cd} - \delta_{ad}\delta_{bc}$ and the Fierz identity, we expand the first term of the above equation and obtain $(\overline{L_{a\alpha}}\gamma^\mu L_{a\beta})(\overline{L_{c\gamma}}\gamma_\mu L_{c\delta}) - (\overline{L_{a\alpha}}\gamma^\mu L_{a\delta})(\overline{L_{c\gamma}}\gamma_\mu L_{c\beta})$, i.e.,

$$\begin{aligned}&(\overline{\nu_{\alpha{\rm L}}}\gamma^\mu\nu_{\beta{\rm L}})(\overline{E_{\gamma{\rm L}}}\gamma_\mu E_{\delta{\rm L}}) + (\overline{\nu_{\gamma{\rm L}}}\gamma^\mu\nu_{\delta{\rm L}})(\overline{E_{\alpha{\rm L}}}\gamma_\mu E_{\beta{\rm L}})\\ -&(\overline{\nu_{\alpha{\rm L}}}\gamma^\mu\nu_{\delta{\rm L}})(\overline{E_{\gamma{\rm L}}}\gamma_\mu E_{\beta{\rm L}}) - (\overline{\nu_{\gamma{\rm L}}}\gamma^\mu\nu_{\beta{\rm L}})(\overline{E_{\alpha{\rm L}}}\gamma_\mu E_{\delta{\rm L}}),\end{aligned} \tag{10.1.8}$$

which we denote as $\mathcal{O}^1_{\alpha\beta\gamma\delta}$. Note that $\mathcal{O}^1_{\alpha\beta\gamma\delta} = -\mathcal{O}^1_{\gamma\beta\alpha\delta} = -\mathcal{O}^1_{\alpha\delta\gamma\beta} = \mathcal{O}^1_{\gamma\delta\alpha\beta}$ is satisfied. This term can lead to NSIs of neutrino interacting with the electron $\nu_\alpha e \to \nu_\beta e$ during the neutrino propagation, but have no influence on 4-charged-lepton interactions such as the scattering $\mu e \to ee$ or the rare decay $\mu \to eee$, and thus are not directly constrained by the latter. The second term in Eq. (10.1.7) gives no more information than $\mathcal{O}^1_{\alpha\beta\gamma\delta}$, which is not necessary to be considered separately.

- The second class of operators are:

$$\begin{gathered}
(\overline{L_\alpha}\tilde{H}\gamma^\mu\tilde{H}^\dagger L_\beta)(\overline{U_{\gamma\mathrm{R}}}\gamma_\mu U_{\delta\mathrm{R}}),\ (\overline{L_\alpha}\tilde{H}\gamma^\mu\tilde{H}^\dagger L_\beta)(\overline{D_{\gamma\mathrm{R}}}\gamma_\mu D_{\delta\mathrm{R}}),\ (\overline{L_\alpha}\tilde{H}\gamma^\mu\tilde{H}^\dagger L_\beta)(\overline{E_{\gamma\mathrm{R}}}\gamma_\mu E_{\delta\mathrm{R}}),\\
(\overline{L_\alpha}\tilde{H}\gamma^\mu\tilde{H}^\dagger L_\beta)(\overline{Q_\gamma}\gamma_\mu Q_\delta),\ (\overline{L_\alpha}\tilde{H}\gamma^\mu\tilde{H}^\dagger L_\beta)(\overline{L_\gamma}\gamma_\mu L_\delta),\\
(\overline{L_\alpha}\tilde{H}\gamma^\mu L_{b\beta})(\overline{Q_{b\gamma}}\gamma_\mu\tilde{H}^\dagger Q_\delta),\ \varepsilon_{bc}(\overline{L_\alpha}\tilde{H}\gamma^\mu L_{b\beta})(\overline{Q_\gamma}H\gamma_\mu Q_{c\delta}),\\
(\overline{L_\alpha}\tilde{H}\gamma^\mu H^\dagger L_\beta)(\overline{D_{\gamma\mathrm{R}}}\gamma_\mu U_{\delta\mathrm{R}}),\ (\overline{L_\alpha}\tilde{H}\sigma^{\mu\nu}E_{\beta\mathrm{R}})(\overline{Q_\gamma}H\sigma_{\mu\nu}U_{\delta\mathrm{R}}),\\
(\overline{L_\alpha}\tilde{H}E_{\beta\mathrm{R}})(\overline{D_{\gamma\mathrm{R}}}\tilde{H}^\dagger Q_\delta),\ (\overline{L_\alpha}\tilde{H}E_{\beta\mathrm{R}})(\overline{Q_\gamma}HU_{\delta\mathrm{R}}). \qquad (10.1.9)
\end{gathered}$$

After the Higgs gets the VEV, the above operators are effectively reduced to 11 4-fermi interactions,

$$\begin{gathered}
(\overline{\nu_{\alpha\mathrm{L}}}\gamma^\mu\nu_{\beta\mathrm{L}})(\overline{U_{\gamma\mathrm{R}}}\gamma_\mu U_{\delta\mathrm{R}}),\ (\overline{\nu_{\alpha\mathrm{L}}}\gamma^\mu\nu_{\beta\mathrm{L}})(\overline{D_{\gamma\mathrm{R}}}\gamma_\mu D_{\delta\mathrm{R}}),\ (\overline{\nu_{\alpha\mathrm{L}}}\gamma^\mu\nu_{\beta\mathrm{L}})(\overline{E_{\gamma\mathrm{R}}}\gamma_\mu E_{\delta\mathrm{R}}),\\
(\overline{\nu_{\alpha\mathrm{L}}}\gamma^\mu\nu_{\beta\mathrm{L}})(\overline{U_{\gamma\mathrm{L}}}\gamma_\mu U_{\delta\mathrm{L}} + \overline{D_{\gamma\mathrm{L}}}\gamma_\mu D_{\delta\mathrm{L}}),\ (\overline{\nu_{\alpha\mathrm{L}}}\gamma^\mu\nu_{\beta\mathrm{L}})(\overline{\nu_{\gamma\mathrm{L}}}\gamma_\mu\nu_{\delta\mathrm{L}} + \overline{E_{\gamma\mathrm{L}}}\gamma_\mu E_{\delta\mathrm{L}}),\\
(\overline{\nu_{\alpha\mathrm{L}}}\gamma^\mu\nu_{\beta\mathrm{L}})(\overline{U_{\gamma\mathrm{L}}}\gamma_\mu U_{\delta\mathrm{L}}) + (\overline{\nu_{\alpha\mathrm{L}}}\gamma^\mu E_{\beta\mathrm{L}})(\overline{D_{\gamma\mathrm{L}}}\gamma_\mu U_{\delta\mathrm{L}}),\\
(\overline{\nu_{\alpha\mathrm{L}}}\gamma^\mu\nu_{\beta\mathrm{L}})(\overline{D_{\gamma\mathrm{L}}}\gamma_\mu D_{\delta\mathrm{L}}) - (\overline{\nu_{\alpha\mathrm{L}}}\gamma^\mu E_{\beta\mathrm{L}})(\overline{D_{\gamma\mathrm{L}}}\gamma_\mu U_{\delta\mathrm{L}}),\\
(\overline{\nu_{\alpha\mathrm{L}}}\gamma^\mu E_{\beta\mathrm{L}})(\overline{D_{\gamma\mathrm{R}}}\gamma_\mu U_{\delta\mathrm{R}}),\ (\overline{\nu_{\alpha\mathrm{L}}}\sigma^{\mu\nu}E_{\beta\mathrm{R}})(\overline{D_{\gamma\mathrm{L}}}\sigma_{\mu\nu}U_{\delta\mathrm{R}}),\\
(\overline{\nu_{\alpha\mathrm{L}}}E_{\beta\mathrm{R}})(\overline{D_{\gamma\mathrm{R}}}U_{\delta\mathrm{L}}),\ (\overline{\nu_{\alpha\mathrm{L}}}E_{\beta\mathrm{R}})(\overline{D_{\gamma\mathrm{L}}}U_{\delta\mathrm{R}}). \qquad (10.1.10)
\end{gathered}$$

In the above operators, the first 5 terms, denoted by $\mathcal{O}^{2,3,4,5,6}_{\alpha\beta\gamma\delta}$, respectively, contribute to NSIs in matter during neutrino propagation. The next 2 terms, denoted by $\mathcal{O}^{7,8}_{\alpha\beta\gamma\delta}$, contribute to both NSIs at the neutrino source and detector, and NSIs for neutrino mediation in matter, and correlate them together. And the final 4 terms, denoted by $\mathcal{O}^{9,10,11,12}_{\alpha\beta\gamma\delta}$, respectively, contribute to NSIs at the source and the detector.

Label	Before EW breaking	After EW breaking	observation
$\mathcal{O}^1$	$\varepsilon_{ac}\varepsilon_{bd}(\overline{L_{a\alpha}}\gamma^\mu L_{b\beta})(\overline{L_{c\gamma}}\gamma_\mu L_{d\delta})$, $\varepsilon_{ac}\varepsilon_{bd}(\overline{L_{a\alpha}}\gamma^\mu L_{b\beta})(\overline{L_{c\gamma}}\gamma_\mu L_{d\delta})H^\dagger H$	$(\overline{\nu_{\alpha\mathrm{L}}}\gamma^\mu \nu_{\beta\mathrm{L}})(\overline{E_{\gamma\mathrm{L}}}\gamma_\mu E_{\delta\mathrm{L}})$ $+(\overline{\nu_{\gamma\mathrm{L}}}\gamma^\mu \nu_{\delta\mathrm{L}})(\overline{E_{\alpha\mathrm{L}}}\gamma_\mu E_{\beta\mathrm{L}})$ $-(\overline{\nu_{\alpha\mathrm{L}}}\gamma^\mu \nu_{\delta\mathrm{L}})(\overline{E_{\gamma\mathrm{L}}}\gamma_\mu E_{\beta\mathrm{L}})$ $-(\overline{\nu_{\gamma\mathrm{L}}}\gamma^\mu \nu_{\beta\mathrm{L}})(\overline{E_{\alpha\mathrm{L}}}\gamma_\mu E_{\delta\mathrm{L}})$	M
$\mathcal{O}^2$	$(\overline{L_\alpha}\tilde{H}\gamma^\mu \tilde{H}^\dagger L_\beta)(\overline{U_{\gamma\mathrm{R}}}\gamma_\mu U_{\delta\mathrm{R}})$	$(\overline{\nu_{\alpha\mathrm{L}}}\gamma^\mu \nu_{\beta\mathrm{L}})(\overline{U_{\gamma\mathrm{R}}}\gamma_\mu U_{\delta\mathrm{R}})$	M
$\mathcal{O}^3$	$(\overline{L_\alpha}\tilde{H}\gamma^\mu \tilde{H}^\dagger L_\beta)(\overline{D_{\gamma\mathrm{R}}}\gamma_\mu D_{\delta\mathrm{R}})$	$(\overline{\nu_{\alpha\mathrm{L}}}\gamma^\mu \nu_{\beta\mathrm{L}})(\overline{D_{\gamma\mathrm{R}}}\gamma_\mu D_{\delta\mathrm{R}})$	M
$\mathcal{O}^4$	$(\overline{L_\alpha}\tilde{H}\gamma^\mu \tilde{H}^\dagger L_\beta)(\overline{E_{\gamma\mathrm{R}}}\gamma_\mu E_{\delta\mathrm{R}})$	$(\overline{\nu_{\alpha\mathrm{L}}}\gamma^\mu \nu_{\beta\mathrm{L}})(\overline{E_{\gamma\mathrm{R}}}\gamma_\mu E_{\delta\mathrm{R}})$	M
$\mathcal{O}^5$	$(\overline{L_\alpha}\tilde{H}\gamma^\mu \tilde{H}^\dagger L_\beta)(\overline{Q_\gamma}\gamma_\mu Q_\delta)$	$(\overline{\nu_{\alpha\mathrm{L}}}\gamma^\mu \nu_{\beta\mathrm{L}})(\overline{U_{\gamma\mathrm{L}}}\gamma_\mu U_{\delta\mathrm{L}} + \overline{D_{\gamma\mathrm{L}}}\gamma_\mu D_{\delta\mathrm{L}})$	M
$\mathcal{O}^6$	$(\overline{L_\alpha}\tilde{H}\gamma^\mu \tilde{H}^\dagger L_\beta)(\overline{L_\gamma}\gamma_\mu L_\delta)$	$(\overline{\nu_{\alpha\mathrm{L}}}\gamma^\mu \nu_{\beta\mathrm{L}})(\overline{\nu_{\gamma\mathrm{L}}}\gamma_\mu \nu_{\delta\mathrm{L}} + \overline{E_{\gamma\mathrm{L}}}\gamma_\mu E_{\delta\mathrm{L}})$	M
$\mathcal{O}^7$	$(\overline{L_\alpha}\tilde{H}\gamma^\mu L_{b\beta})(\overline{Q_{b\gamma}}\gamma_\mu \tilde{H}^\dagger Q_\delta)$	$(\overline{\nu_{\alpha\mathrm{L}}}\gamma^\mu \nu_{\beta\mathrm{L}})(\overline{U_{\gamma\mathrm{L}}}\gamma_\mu U_{\delta\mathrm{L}})$ $+(\overline{\nu_{\alpha\mathrm{L}}}\gamma^\mu E_{\beta\mathrm{L}})(\overline{D_{\gamma\mathrm{L}}}\gamma_\mu U_{\delta\mathrm{L}})$	S,M,D
$\mathcal{O}^8$	$\varepsilon_{bc}(\overline{L_\alpha}\tilde{H}\gamma^\mu L_{b\beta})(\overline{Q_\gamma}H\gamma_\mu Q_{c\delta})$	$(\overline{\nu_{\alpha\mathrm{L}}}\gamma^\mu \nu_{\beta\mathrm{L}})(\overline{D_{\gamma\mathrm{L}}}\gamma_\mu D_{\delta\mathrm{L}})$ $-(\overline{\nu_{\alpha\mathrm{L}}}\gamma^\mu E_{\beta\mathrm{L}})(\overline{D_{\gamma\mathrm{L}}}\gamma_\mu U_{\delta\mathrm{L}})$	S,M,D
$\mathcal{O}^9$	$\varepsilon_{bc}(\overline{L_\alpha}\tilde{H}\gamma^\mu L_{b\beta})(\overline{Q_\gamma}H\gamma_\mu Q_{c\delta})$	$(\overline{\nu_{\alpha\mathrm{L}}}\gamma^\mu E_{\beta\mathrm{L}})(\overline{D_{\gamma\mathrm{R}}}\gamma_\mu U_{\delta\mathrm{R}})$	S,D
$\mathcal{O}^{10}$	$(\overline{L_\alpha}\tilde{H}\sigma^{\mu\nu} E_{\beta\mathrm{R}})(\overline{Q_\gamma}H\sigma_{\mu\nu} U_{\delta\mathrm{R}})$	$(\overline{\nu_{\alpha\mathrm{L}}}\sigma^{\mu\nu} E_{\beta\mathrm{R}})(\overline{D_{\gamma\mathrm{L}}}\sigma_{\mu\nu} U_{\delta\mathrm{R}})$	S,D
$\mathcal{O}^{11}$	$(\overline{L_\alpha}\tilde{H}E_{\beta\mathrm{R}})(\overline{D_{\gamma\mathrm{R}}}\tilde{H}^\dagger Q_\delta)$	$(\overline{\nu_{\alpha\mathrm{L}}}E_{\beta\mathrm{R}})(\overline{D_{\gamma\mathrm{R}}}U_{\delta\mathrm{L}})$	S,D
$\mathcal{O}^{12}$	$(\overline{L_\alpha}\tilde{H}E_{\beta\mathrm{R}})(\overline{Q_\gamma}HU_{\delta\mathrm{R}})$	$(\overline{\nu_{\alpha\mathrm{L}}}E_{\beta\mathrm{R}})(\overline{D_{\gamma\mathrm{L}}}U_{\delta\mathrm{R}})$	S,D

Table 10.1: Higher-dimensional operators ($d \leqslant 8$) which may contribute to NSIs in neutrino oscillation experiments. S, M, and D represent NSIs at a source, in matter and at a detector, respectively.

The effective Lagrangian describing neutrino NSIs for neutrino propagation in matter, produced at the source and measured at the detector can be expressed as

$$\mathcal{L}_{\mathrm{NSI}} = 2\sqrt{2}G_F \sum_{p=1}^{12} c^p_{\alpha\beta\gamma\delta}\mathcal{O}^p_{\alpha\beta\gamma\delta} + \mathrm{h.c.}\,, \tag{10.1.11}$$

where two same flavour indices should be summed. Operators in Eqs. (10.1.8) and (10.1.10) form a full list of NSI operators from $d \leqslant 8$ operators before electroweak symmetry breaking. We have checked that all the other NSIs from $d \leqslant 8$ operators can be represented as a linear combination of these $\mathcal{O}^p_{\alpha\beta\gamma\delta}$. Matching with the effective NSI matrix $\epsilon^{\rm m}$ in Eq. (10.0.1), we obtain

$$\epsilon^{\rm m}_{\alpha\beta} = \epsilon^{e}_{\alpha\beta} + \Big(2 + \frac{N_n}{N_e}\Big)\epsilon^{u}_{\alpha\beta} + \Big(1 + 2\frac{N_n}{N_e}\Big)\epsilon^{d}_{\alpha\beta} \tag{10.1.12}$$

with N_n the neutron number density and

$$\begin{aligned} \epsilon^{e}_{\alpha\beta} &= c^{1}_{\alpha\beta 11} + c^{4}_{\alpha\beta 11} + c^{6}_{\alpha\beta 11}\,, \\ \epsilon^{u}_{\alpha\beta} &= c^{2}_{\alpha\beta 11} + c^{5}_{\alpha\beta 11} + c^{7}_{\alpha\beta 11}\,, \\ \epsilon^{d}_{\alpha\beta} &= c^{3}_{\alpha\beta 11} + c^{5}_{\alpha\beta 11} + c^{8}_{\alpha\beta 11}\,. \end{aligned} \tag{10.1.13}$$

Here in the leptonic flavour space, we have identified the generation indices $\alpha, \beta = 1, 2, 3$ with the leptonic flavour indices e, μ, τ. For $\mathcal{O}^{1}_{\alpha\beta\gamma\delta}$, it is easy to confirm $c^{1}_{\alpha\beta\gamma\delta} = -c^{1}_{\gamma\beta\alpha\delta} = c^{1}_{\alpha\delta\gamma\beta}$, and thus $c^{1}_{e\beta 11}$ and $c^{1}_{\alpha e 11}$ always vanish. In other words, $\mathcal{O}^{1}_{\alpha\beta\gamma\delta}$ will not contribute to the first column and first row in $\epsilon^{\rm m}$. The relation between the NSI parameters at the source and the detector $\epsilon^{\rm s}_{\alpha\beta}$, $\epsilon^{\rm d}_{\alpha\beta}$ and the higher-dimensional operators is given by

$$\epsilon^{\rm s}_{\alpha\beta} = \sum_{p=7}^{12} N^{{\rm s},p} c^{p}_{\alpha\beta 11}\,, \quad \epsilon^{\rm d}_{\alpha\beta} = \sum_{p=7}^{12} N^{{\rm d},p} c^{p}_{\alpha\beta 11}\,, \tag{10.1.14}$$

where $N^{{\rm s},p}$ and $N^{{\rm d},p}$ are order-one coefficients, related to the number densities of electron and neutron. In this work, as we focus on matter-effect NSIs, textures of NSIs in the neutrino production and detection based on the the flavour symmetry and residual symmetries will not be shown in the main text but in the appendix.

10.2 Current Status of NSIs

Current global fit [39] for conventional parameters includes solar, reactor, atmospheric, and LBL neutrino data. The authors point out that they focus on the results for matter-effect NSI constraint; while the NSI effects during the production and detection need included for fitting, they do not fit for NSI with electrons. With the assumption of real off-diagonal NSI terms, the current global fit to standard NSI parameters $\epsilon^{u}_{\alpha\beta}$, which is for matter-effect NSI with u and d quarks, gives the bounds at 90% C.L. in Tab. 13.2. Found are two solutions– Large-mixing-angle (LMA) and Large-mixing-angle-dark (LMA-dark) solutions. **LMA** solution is the solution that is compatible with the SM prediction. **LMA-dark** solution contains a nonzero NSI parameter $\tilde{\epsilon}_{ee}^{u,d} \sim 1$ with $\Delta m_{21}^2 \to -\Delta m_{21}^2 \bigwedge \theta_{12} \to \theta_{12} + \pi/2$. In this chapter and the next chapter, we will only consider the LMA solution.

We estimate the combination of matter NSI effects with electrons, and u, d quarks in earth, by simply timing a factor 3. In Tab. 10.3, we use the results for $\epsilon_{\alpha\beta}^u$, as the results for $\epsilon_{\alpha\beta}^d$ are similar. We find wider spaces for ee, $e\mu$, and $e\tau$ components. For $\tilde{\epsilon}_{ee}$, the precision at 90% C.L. is of the level about 75% of weak interactions, while those are about $\sim$ 20% and $\sim$ 40% for $e\mu$ and $e\tau$ components respectively. A few percentage is also seen for the other two parameters.

Following with the previous section, we conclude that while matter effect NSIs can be disentangled from the limits for NSIs at the source and detector of neutrinos and for the charge lepton sector by including dimension-8 operators, the sizeable matter effect NSIs are allowed by current global fit results. This expects the detection of matter NSI effects for DUNE. In the next section, we will discuss how matter NSI effects can affect to the probabilities, the precision on $\epsilon_{\alpha\beta}^{\mathrm{m}}$ and the exclusion level to the SM prediction for DUNE.

	best fit	LMA	LMA$\bigoplus$LMA-Dark
$\tilde{\epsilon}^u_{ee} \equiv \epsilon^u_{ee} - \epsilon^u_{\mu\mu}$	0.298	$[0, 0.51]$	$[-1.19, -0.81]$
$\tilde{\epsilon}^u_{\tau\tau} \equiv \epsilon^u_{\tau\tau} - \epsilon^u_{\mu\mu}$	0.001	$[-0.01, 0.03]$	$[-0.03, 0.03]$
$\epsilon^u_{e\mu}$	-0.021	$[-0.09, 0.04]$	$[-0.09, 0.1]$
$\epsilon^u_{e\tau}$	0.021	$[-0.14, 0.14]$	$[-0.15, 0.14]$
$\epsilon^u_{\mu\tau}$	-0.001	$[-0.01, 0.01]$	$[-0.01, 0.01]$
$\tilde{\epsilon}^d_{ee} \equiv \epsilon^d_{ee} - \epsilon^d_{\mu\mu}$	0.31	$[0.02, 0.51]$	$[-1.17, -1.03]$
$\tilde{\epsilon}^d_{\tau\tau} \equiv \epsilon^d_{\tau\tau} - \epsilon^d_{\mu\mu}$	0.001	$[-0.01, 0.03]$	$[-0.01, 0.03]$
$\epsilon^d_{e\mu}$	-0.023	$[-0.09, 0.04]$	$[-0.09, 0.08]$
$\epsilon^d_{e\tau}$	0.023	$[-0.13, 0.14]$	$[-0.13, 0.14]$
$\epsilon^d_{\mu\tau}$	-0.001	$[-0.01, 0.01]$	$[-0.01, 0.01]$

Table 10.2: Current global fit results [39] for $\epsilon^{u,d}_{\alpha\beta}$. The first second column gives the best-fit value, while the third and the fourth ones show the bounds at 90% C.L.. In these results, the authors assume off-diagonal elements $\epsilon_{\alpha\neq\beta}$ are real, and only consider matter effect NSIs.

	best fit	LMA	LMA$\bigoplus$LMA-Dark
$\tilde{\epsilon}^{\rm m}_{ee} \equiv \epsilon^{\rm m}_{ee} - \epsilon^{\rm m}_{\mu\mu}$	0.894	$[0, 1.53]$	$[-3.57, -2.43]$
$\tilde{\epsilon}^{\rm m}_{\tau\tau} \equiv \epsilon^{\rm m}_{\tau\tau} - \epsilon^{\rm m}_{\mu\mu}$	0.003	$[-0.03, 0.09]$	$[-0.09, 0.03]$
$\epsilon^{\rm m}_{e\mu}$	-0.063	$[-0.27, 0.12]$	$[-0.27, 0.3]$
$\epsilon^{\rm m}_{e\tau}$	0.063	$[-0.42, 0.42]$	$[-0.45, 0.42]$
$\epsilon^{\rm m}_{\mu\tau}$	-0.003	$[-0.03, 0.03]$	$[-0.03, 0.09]$

Table 10.3: Current global fit results for $\epsilon^{\rm m}_{\alpha\beta}$, by using the result for $\epsilon^u_{\alpha\beta}$ Ref. [39]. The first second column gives the best-fit value, while the third and the fourth ones show the bounds at 90% C.L.. In these results, the authors assume off-diagonal elements $\epsilon_{\alpha\neq\beta}$ are real, and only consider matter effect NSIs.

Chapter 11

Matter effect NSIs in DUNE

Sizeable NSI in matter are thought to be detectable or measurable in DUNE. That is greatly because of sizeable matter effects, in addition to the benefit of the controllable systematics and its high statistics. The reason why T2HK is not focused for measuring NSI effects in matter is as we see in Ch. 3 its shorter baseline and the lower neutrino energy lead matter effects negligible. The phenomenology of matter NSI effects has been well developed. We present our approximation equations for the neutrino oscillation probabilities with nonzero $\epsilon^{\mathrm{m}}_{\alpha\beta}$ in App. D. From these approximation equations, we know which NSI effect is dominating the whole impact on the oscillation proability by comparing the size of their coefficients. We find that $\epsilon_{e\mu}$ $\epsilon_{e\tau}$ ($\epsilon_{\mu\tau}$) are (is) the most influential to (dis)appearance channel for DUNE experiment. From this chapter we explore the physics chance for DUNE to reach beyond the standard oscillation in neutrino oscillations. In this chapter, we are interested in the exclusion level for DUNE to the SM prediction — no NSI occurs. This refers to the signal beyond the SM. It is worthy to point that an analogy of the relation between this quantity to the precision of matter-effect NSI parameter is that of CPV or MCP sensitivity to $\Delta\delta$. We firstly numerically demonstrate impact of matter NSIs for DUNE — the difference of the probabilities between with and without matter NSIs. In the following section, we review the current studies on the precision of NSI matter effects measuring for DUNE. In the final section, we extend our discussion to ask how DUNE can exclude the SM prediction — no NSIs occur.

11.1 Probabilities at DUNE

We define ν oscillation probabilities with matter NSI effects $\epsilon^{\rm m} = \xi^{\rm m}$ for the $\nu_\alpha \to \nu_\beta$ channel in the way,

$$P_{\rm NSI}(\nu_\alpha \to \nu_\beta)|_{\epsilon^{\rm m}=\xi} = P_{\rm NSI}(\nu_\alpha \to \nu_\beta)|_{\epsilon^{\rm m}=0} + \delta P_{\rm NSI}(\nu_\alpha \to \nu_\beta)|_{\epsilon^{\rm m}=\xi}, \tag{11.1.1}$$

where $P_{\rm NSI}(\nu_\alpha \to \nu_\beta)|_{\epsilon^{\rm m}=0}$ is the probability for the standard oscillation, and $\delta P_{\rm NSI}(\nu_\alpha \to \nu_\beta)|_{\epsilon^{\rm m}=\xi^{\rm m}}$ is the difference between the probabilities with $\epsilon^m = \xi$ and without any NSI effects.[1] In the other word, $\delta P_{\rm NSI}(\nu_\alpha \to \nu_\beta)|_{\epsilon^{\rm m}=\xi^{\rm m}}$ is the collection of the whole influence of all matter NSI effects on the probability $\nu_\alpha \to \nu_\beta$. In the following, we study the effect of each element of $\epsilon^{\rm m}$ on the probability through this difference. Therefore, the subscript in the follow is $\epsilon^{\rm m}_{\alpha\beta} = \xi^{\rm m}_{\alpha\beta}$, instead of $\epsilon^{\rm m} = \xi^{\rm m}$, in order to denote which element is studied. How $\delta P_{\rm NSI}(\nu_\alpha(\bar{\nu}_\alpha) \to \nu_\beta(\bar{\nu}_\beta))|_{\epsilon^{\rm m}_{\alpha\beta}=0.05}$ behaves in energy for DUNE are shown in Figs. 11.1 and 11.2. For each line, we set one of NSI parameters to be 0.05, and also compare $\delta P_{\rm NSI}$ with the 2-horn optimised fluxes of DUNE, which roughly emphasis (anti)neutrino energy around $2-3$ GeV. In these figures, the normal mass ordering, $\delta = 270^\circ$, and $\phi_{\alpha\neq\beta} = 0$ are assumed. We find that for the disappearance (appearance) channel, the largest value of $\delta P_{\rm NSI}$ is (are) for non-zero $\epsilon_{\mu\tau}$ ($\epsilon_{e\mu}$ and $\epsilon_{e\tau}$). Among these elements, $\epsilon_{\mu\tau}$, causing the maximum $\delta P_{\rm NSI}(\nu_\mu(\bar{\nu}_\mu) \to \nu_\mu(\bar{\nu}_\mu))|_{\epsilon_{\mu\tau}=0.05} \lesssim 0.03$ at some (anti)neutrino energies, is most influential, while for $\epsilon_{e\mu}$ and $\epsilon_{e\tau}$ $\delta P_{\rm NSI}(\nu_\mu(\bar{\nu}_\mu) \to \nu_e(\bar{\nu}_e))|_{\epsilon_{e\mu(e\tau)}=0.05}$ can reach 0.01 (0.005) for the (anti)neutrino model. These elements are expected to be easier to be detected or measured; this implies that these off-diagonal elements are easier to be detected. It is interesting point out that $\delta P|_{\epsilon_{e\mu}=0.05} \sim -\delta P|_{\epsilon_{e\tau}=0.05}$ for these four channels, which implies the correlation between these two parameters; however, though it is not shown here, this correlation is vanished for $\delta = 0$. Further, there is a wide window in the higher energy > 4 GeV to optimise the sensitivity for flavour-transition NSI effects in matter.

---

[1] The same definition applies to the antineutrino mode.

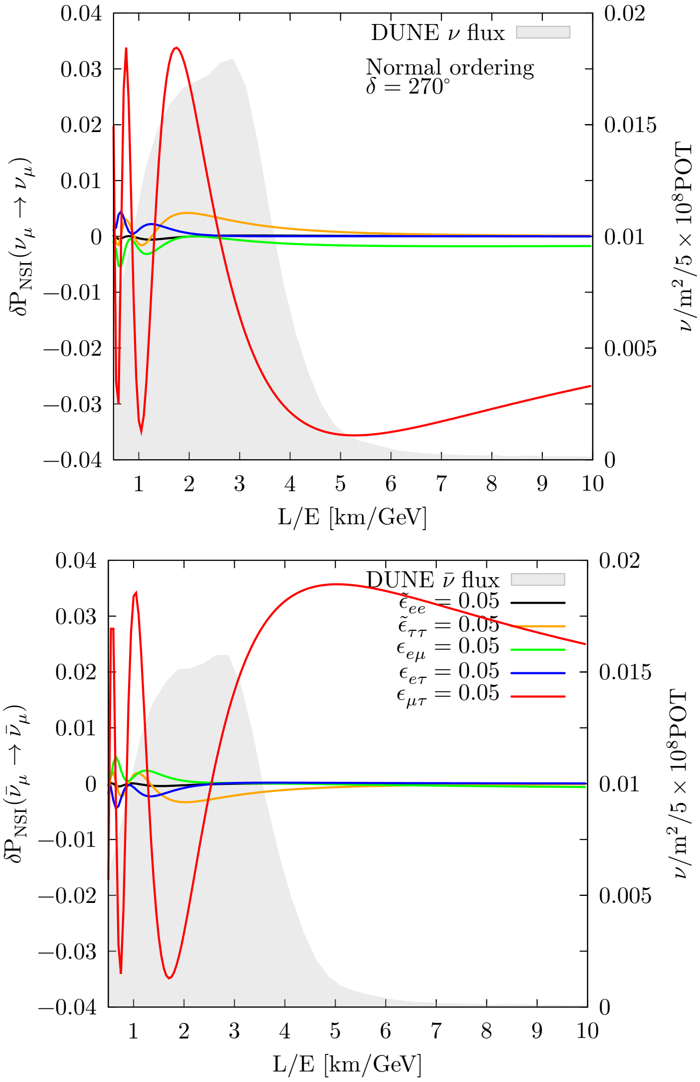

Figure 11.1: The difference of probabilities in the energy between with and without NSI effects for the neutrino (upper) and antineutrino (lower) modes in the disappearance channel, assumed normal mass ordering, $\delta = 270^\circ$, and $\phi_{\alpha\neq\beta} = 0$. For each line, only one of NSI parameters is set to be 0.05, while the other are null. The grey shadow refers to the ν ($\bar{\nu}$) model of the 2-horn optimised flux of DUNE in the left (right) panel.

11.2 The Precision of DUNE on Matter Effect NSIs

The precision on the measurement of $\epsilon^{m}_{\alpha\beta}$ is widely studied for DUNE. These works can be taken as answering if there is no detectable matter NSI effects, how many

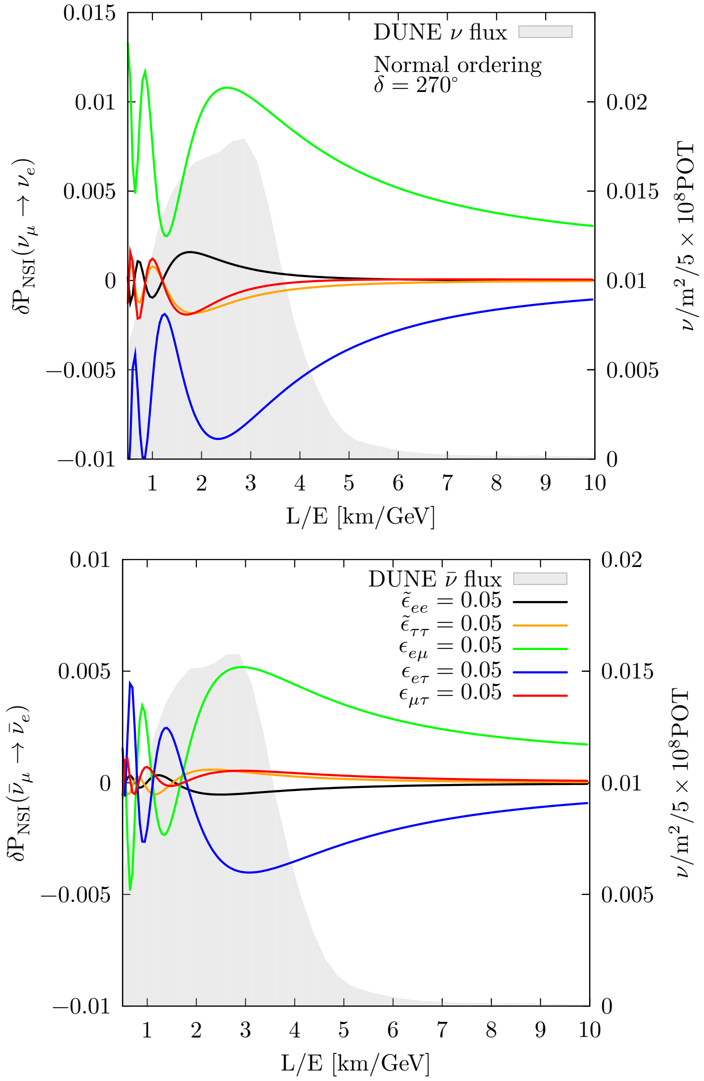

Figure 11.2: The difference of probabilities in the energy between with and without NSI effects for the neutrino (upper) and antineutrino (lower) modes in the appearance channel, assumed normal mass ordering, $\delta = 270^\circ$, and $\phi_{\alpha \neq \beta} = 0$. For each line, only one of NSI parameters is set to be 0.05, while the other are null. The grey shadow refers to the ν ($\bar{\nu}$) model of the 2-horn optimised flux of DUNE in the left (right) panel.

models can be excluded. This is interesting as including the effects of $\epsilon^{m}_{\alpha\beta}$ in neutrino oscillations is equilibrium we enlarge the number of parameters and may open new correlations. Of course, the performance of DUNE does not only depend on the experimental design, but also the impact of parameters on the oscillation probabilities. In this section, we will review the current works on this issue.

In Ref. [121], the author performs the precision on $\epsilon^{\rm m}_{\alpha\beta}$, and the exclusion contour for any two of parameters. We take the results and show in Fig. 11.3. Although the author does not extract $\epsilon^{\rm m}_{\mu\mu}$ from all three diagonal elements like we do in this thesis, the ee and $\mu\mu$ components in Ref. [121] share the same properties to ee and $\tau\tau$ in parameterization used in this thesis respectively. In this paragraph, we summarise the conclusions in the parameterization used in Ref. [121]. As mentioned by the author, we see two important degeneracies between two NSI parameters: the first one is observed in the projection on $\mu\mu$ elements; the other one is seen on the $\epsilon^{\rm m}_{e\tau}$–$\tilde{\epsilon}_{ee}$ plane. These correlations have been also seen in Ref. [122]. In addition, two more correlations are seen between or among the standard oscillation and NSI parameters. The first is between $\tilde{\epsilon}_{\mu\mu}$ and θ_{23} shown in Fig. 3 in Ref. [121], while the other one is among the CP phase δ, $\tilde{\epsilon}_{ee}$ and $\epsilon_{\tau e}$ in Figs. 4 and 5. Although lots of correlation have been seen, the author also points out that the LMA-dark solution can be excluded by DUNE. Finally, the author emphasises the precision on off-diagonal NSI parameters at the level of $\mathcal{O}(0.05 - 0.5)$.

In addition, the impacts on oscillation probabilities of all possible NSI effects– at the source and the detector, and in matter, have been studied in Ref. [123]. From their results, we find that with the previous results as priors, the influence of NSI effects at the source and detector are smaller on that in matter, except for $\epsilon^{\rm m}_{\mu e}$, for which the difference is by $\sim 50\%$.

11.3 NSI signal sensitivity

We study the NSI sensitivity $\Delta\chi^2_{NSI}$ — how much an experiment can exclude the standard model prediction (the matrix $\epsilon^{\rm m} = 0$). In other words, this definition implies the statistics significance of finding any matter effect NSIs which cannot be described by the standard model.

$$\sigma^2_{\rm NSI} \equiv \Delta\chi^2_{\rm NSI} \equiv \min_{\{\Theta_{\rm PMNS}\}} \left\{ \chi^2|_{\text{All } \epsilon_{\alpha\beta}=0} - \chi^2_{\rm b.f.} \right\}, \tag{11.3.2}$$

where $\min_{\{\Theta_{\rm PMNS}\}} \{\chi^2\,(\text{All } \epsilon_{\alpha\beta} = 0)\}$ is the minimum value of χ^2 value for the SM prediction over all oscillation parameters $\Theta_{\rm PMNS}$, and $\chi^2_{\rm b.f.}$ is the χ^2 value for the best

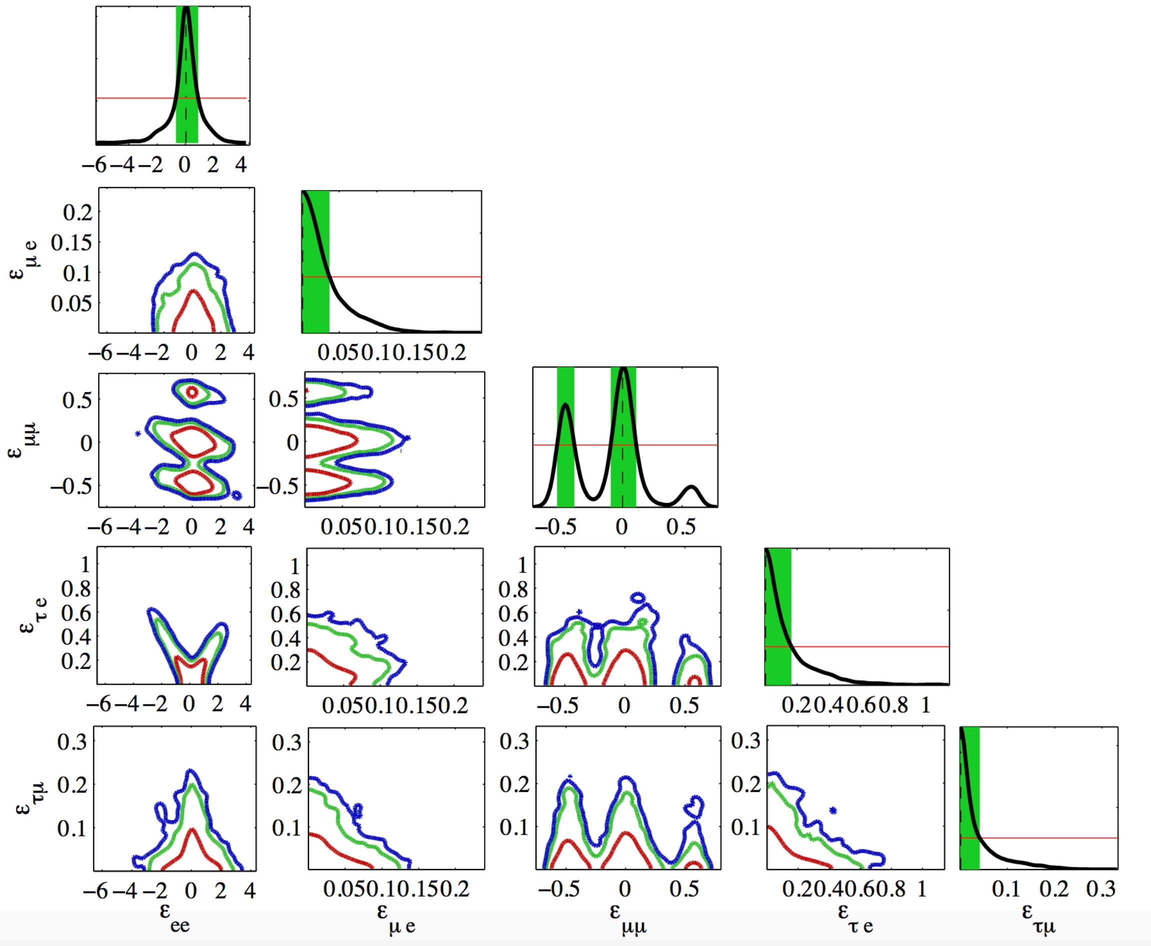

Figure 11.3: Taken from Ref. [121], the precision and correlations of measurement of the parameters for NSIs in matter.

fit. In this chapter, $\chi^2_{\text{b.f.}} = 0$. We let all mixing angles and mass square splittings vary with Gaussian priors, which are adopting the current version of global fit results, and provides the precision of a-few-percentage level. δ is free to vary. However, we fix the matter density at the true value, as its uncertainty does not have any significant influence to the results.

Finally, we are interested in the statistical significance $\sqrt{\Delta\chi^2_{NSI}} \leq 3$ (1) for off-diagonal (diagonal) elements. Therefore, for the flavour-changing elements, we define the width $\delta\epsilon_{\alpha\neq\beta}(A\sigma) \equiv \frac{\epsilon^+_{\alpha\beta}(\sigma_{\text{NSI}}=A)-\epsilon^-_{\alpha\beta}(\sigma_{\text{NSI}}=A)}{2}$, where $\epsilon^{+(-)}_{\alpha\beta}(\sigma_{\text{NSI}} = A)$ is the positive (negative) value of $\epsilon_{\alpha\beta}$ at $\sigma_{\text{NSI}} = A$.

Results

Fig. 11.4 demonstrates the NSI signal sensitivity for DUNE, varying one true value of $\epsilon_{\alpha\beta}$ within $[-0.1, 0.1]$, with $\delta = 270°$ and $\phi_{\alpha\neq\beta} = 0$; we show for both mass orderings — the normal (solid) and inverted (dashed) mass orderings. Obviously, DUNE has the higher sensitivity to detect the flavour-transition NSI effects in matter. The sensitivity at 3σ can be reached around for $\epsilon_{e\mu} \sim 0.05$ and $\epsilon_{e\tau} \sim 0.05$; moreover, for $\epsilon_{\mu\tau}$ it can achieve this significance easier around $\epsilon_{\mu\tau} \sim 0.03$. When diagonal element are at ± 0.1, the σ_{NSI} are 0.6 (1) and 1.6 (1.7) for ee and $\tau\tau$ components for normal (inverted) mass ordering, respectively. This result implies that DUNE has a better sensitivity to flavour-transition NSI effects. In [122], the authors study the same quantities for three special cases, in different scenarios, and demonstrate their results in Tab. II in their paper. By our simulation with the same prior for oscillation parameters, we find the same rank of the exclusion level among these three cases as theirs with the $\sim 2\sigma$ difference, which is because that in our simulation the detector is set heavier and the flux, which is more peaky at the first maximum than that in their work, leads more events.

We have not seen any interesting correlations between two elements of ϵ^{m}, except for $e\mu$ and $e\tau$ components Fig. 11.5. This correlation depends on the value of δ. The Fig. 11.5 shows the contour of 3σ significance on $\epsilon_{e\mu}$ and $\epsilon_{e\tau}$ plane, for $\delta = 270°$ and $\delta = 0$. We see the correlation along with $\epsilon_{e\mu} = \epsilon_{e\tau}$ for the CP-viloation case, but this correlation does not appear for $\delta = 0$. The correlation can be explained by the conclusion $\delta P(\epsilon_{e\mu} = 0.05) \sim -\delta P(\epsilon_{e\tau} = 0.05)$ for Figs. 11.1 and 11.2, which is not seen for $\delta = 0$. This implies that with $\delta = 270°$ for increasing values of $\epsilon_{e\mu}$ and $\epsilon_{e\tau}$ simultaneously, the sensitivity climb slower than the case that one increases but the other decreases.

We study the variation of NSI signal sensitivities against the phase of off-diagonal element $\phi_{\alpha\neq\beta}$ in Fig. 11.6. We find the periodic behaviour for all three elements with the frequency of $1/\pi$. Changing the value of δ shifts the peaks in $\phi_{\alpha\beta}$ for $\delta\epsilon_{e\mu}(3\sigma)$ and $\delta\epsilon_{e\tau}(3\sigma)$.[2] However, the location of peaks of $\delta\epsilon_{\mu\tau}(3\sigma)$ is independent of δ. The

---

[2] The peaks also depend on the value θ_{23}, Δm^2_{31}. Because these two parameters are measured

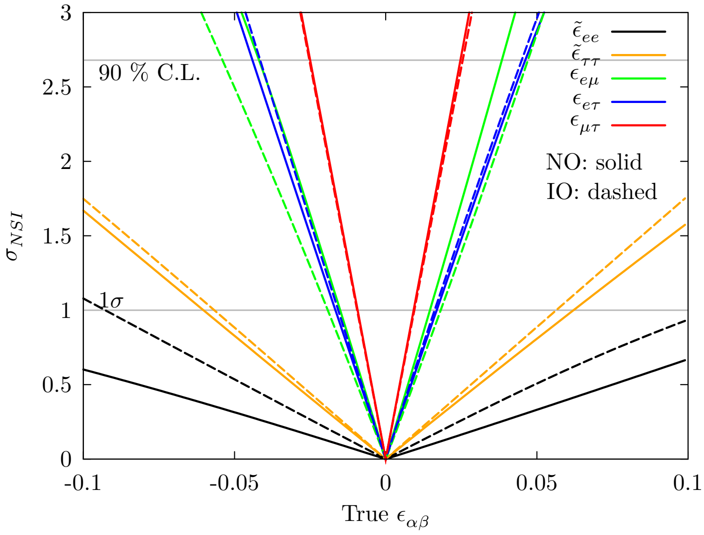

Figure 11.4: This figure shows the square root of the NSI signal sensitivity σ_{NSI} for DUNE with varying every $\epsilon_{\alpha\beta}$ within $[-0.1, 0.1]$.

variation of $\delta\epsilon_{\mu\tau}(3\sigma)$ is the larger than the other two, and is between ~ 0.03 (at $\phi_{\mu\tau} = \pm 0.5\pi$) and 0.2 (at $\phi_{\mu\tau} = 0$ and $\pm\pi$). The smallest one is $\delta\epsilon_{e\mu}(3\sigma)$; $\delta\epsilon_{e\mu}(3\sigma)$ is peaking around 0.1 for $\phi_{e\mu} \sim -0.4\pi$ and $\sim 0.6\pi$, while between these two peaks, it sits at the bottom $\delta\epsilon_{e\mu}(3\sigma) \sim 0.04$. Finally, $\delta\epsilon_{e\tau}(3\sigma)$ climbs from the value, slightly above 0.04 at $\phi_{e\tau} = -0.2\pi$ and 0.8π, to the height ~ 0.2 where $\phi_{e\tau} \sim \pm 0.5\pi$.

Fig. 11.7, we present $\delta\tilde{\epsilon}_{\alpha\alpha}(1\sigma)$ and $\delta\epsilon_{\alpha\neq\beta}(3\sigma)$ against δ over $[-\pi, \pi]$. The largest variation is seen for $\tilde{\epsilon}_{ee}(1\sigma)$ roughly between 0.15 (around $\pm 0.5\pi$) and 0.35 (around 0, $\pm\pi$). In the following, $\delta\epsilon_{e\tau}(3\sigma)$, ranging from 0.55 to 0.15, behaves the same against δ. The similar behaviour is also seen for $\delta\tilde{\epsilon}_{\tau\tau}(1\sigma)$, varying within 0.06 and 0.07. $\delta\epsilon_{e\mu}(3\sigma)$ climbs up to 0.06 around -0.8π and 0.2π, and down to 0.05 around -0.3π and 0.7π. However, $\delta\tilde{\epsilon}_{\tau\tau}(1\sigma)$ is a constant around 0.03 to δ.

In Tab. 11.1, we show the sizes of $\delta\epsilon_{\alpha\neq\beta}(3\sigma)$ and $\delta\tilde{\epsilon}_{\alpha\alpha}(1\sigma)$. We include T2HK and T2HKK1.5° data during fitting, and observe the improvement about $\sim 10\%$ improvement on the size for all components. We find that a bigger improvement is by doubling DUNE exposure by about 10% ($e\mu$ and $e\tau$) to 30% (ee, $\tau\tau$, and $\mu\tau$). This implies us that the statistic error is still largely dominating in the NSI signal detection performance. Though it is not shown here, for the phenomenological interest,

---

in a high precision, their impacts are not relevant.

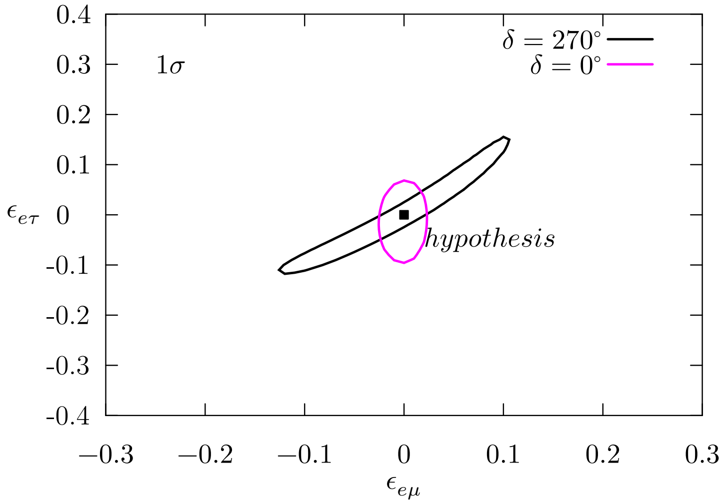

Figure 11.5: The contour presents the NSI sensitivity Eq. 11.3.2 for DUNE in the area $-0.3 < \epsilon_{e\mu} < 0.3$ and $-0.4 < \epsilon_{e\tau} < 0.4$ at $\sigma_{\text{NSI}} = 1$ significant level for $\delta = 270°$ and $\delta = 0$.

we have further inspected the change with reducing the uncertainty of oscillation parameter to 0.1%, i.e. we downsize the width of the priors to 0.1%. We have not found any significant changes to NSI sensitivity, but some minor improvements to some NSI effects by reducing the uncertainty of θ_{13}, θ_{23}, and Δm^2_{31}. This indicates us that the current understanding on oscillation parameters is precise enough to detect NSI effects for DUNE. We also give the prior for δ with width of 1°, we still see bare changes for all elements, except for *ee* component with very minor change.

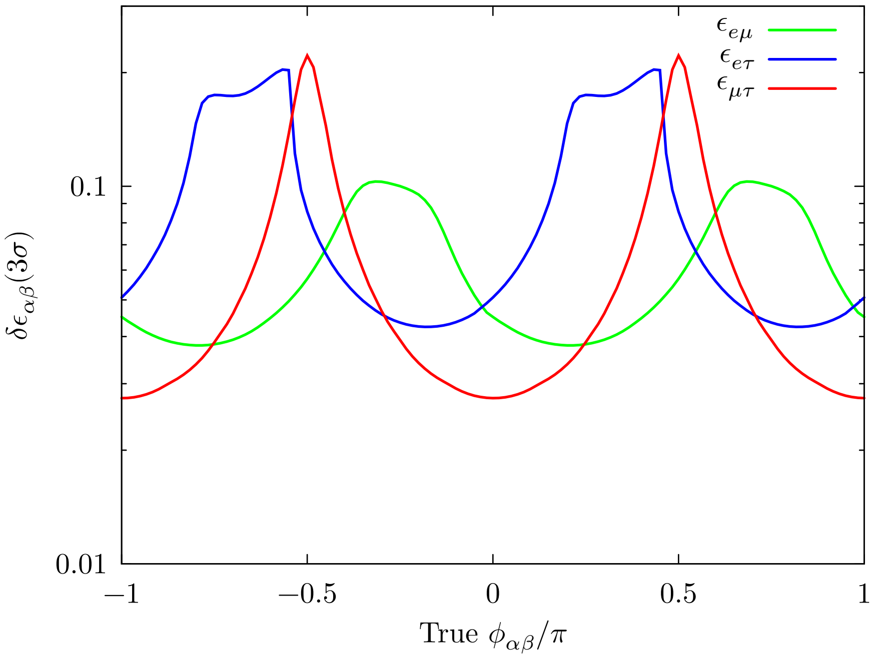

Figure 11.6: The variation of the half size of $\epsilon_{\alpha\neq\beta}$ at the NSI signal sensitivity $\sigma_{\rm NSI} = 3$ over $-\pi \leq \phi_{\alpha\neq\beta} \leq \pi$. The parameter $\delta\epsilon_{\alpha\beta} \equiv \frac{\epsilon^+_{\alpha\beta}(\sigma_{\rm NSI}=3)-\epsilon^-_{\alpha\beta}(\sigma_{\rm NSI}=3)}{2}$ is defined, where $\epsilon^{+(-)}_{\alpha\beta}(\sigma_{\rm NSI} = 3)$ is the positive (negative) value of $\epsilon_{\alpha\beta}$ at $\sigma_{\rm NSI} = 3$. Normal mass ordering and $\delta = 270°$ are assumed.

	$\delta\epsilon_{e\mu}(3\sigma)$	$\delta\epsilon_{e\tau}(3\sigma)$	$\delta\epsilon_{\mu\tau}(3\sigma)$	$\delta\epsilon_{ee}(1\sigma)$	$\delta\epsilon_{\tau\tau}(1\sigma)$
NO, b.f.	0.045	0.051	0.028	0.164	0.061
+T2HK	0.042	0.047	0.025	0.137	0.051
+T2HKK	0.041	0.046	0.025	0.131	0.051
exposure×2	0.039	0.044	0.020	0.125	0.044

Table 11.1: Size of NSI sensitivity $\leq 3\sigma$ ($\leq 1\sigma$) for off-diagonal (diagonal) elements for different scenarios. 'NO, b.f.' is the size for DUNE with 3.5+3.5 years run time, with the true value Tab. 2.3, assumed normal mass ordering. The improvement by including T2HK or T2HKK1.5°, and by doubling the exposure of DUNE are also present.

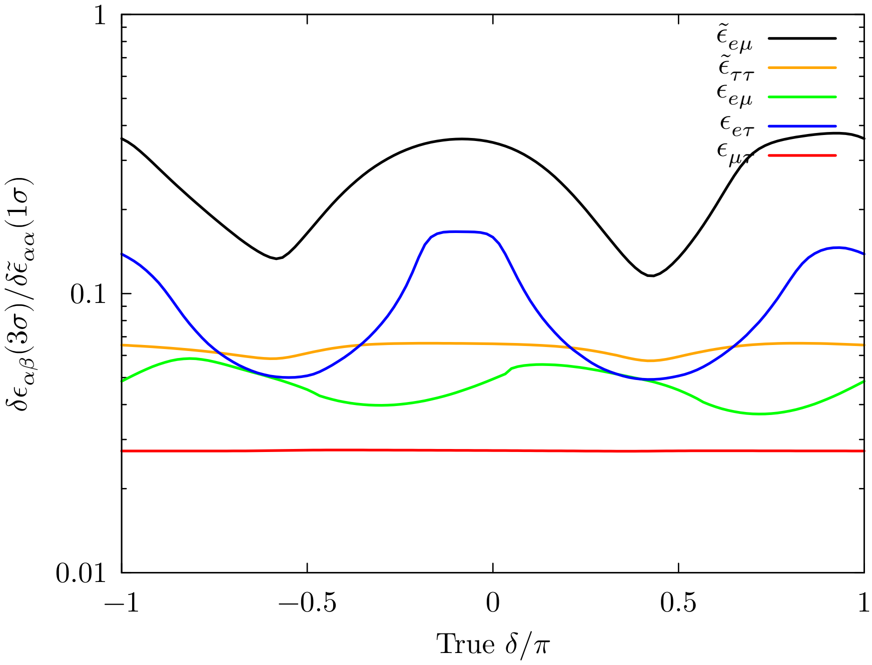

Figure 11.7: The variation of the half size of $\epsilon_{\alpha\neq\beta}$ ($\tilde{\epsilon}_{\alpha\alpha}$) at the NSI signal sensitivities $\sigma_{\rm NSI} = 3$ (1) over $-\pi \leq \delta \leq \pi$. The parameter $\delta\epsilon_{\alpha\beta} = \frac{\epsilon^{+}_{\alpha\beta}(\sigma_{\rm NSI}=3)-\epsilon^{-}_{\alpha\beta}(\sigma_{\rm NSI}=3)}{2}$ is defined, where $\epsilon^{+(-)}_{\alpha\beta}(\sigma_{\rm NSI} = 3)$ is the positive (negative) value of $\epsilon_{\alpha\beta}$ at $\sigma_{\rm NSI} = 3$. This definition is also applied for $\delta\tilde{\epsilon}_{\alpha\alpha}$, but the NSI signal sensitivity is at $\sigma_{\rm NSI} = 1$. Normal mass ordering and $\phi_{\alpha\neq\beta} = 0$ are assumed.

Chapter 12

NSI Textures under Flavour Symmetries

In this chapter, we discuss the flavour dependence of matter-effect NSIs under the flavour symmetry A_4 or $Z-2$. If flavour symmetry is a true symmetry behind, it will automatically constrain NSIs. As a consequence, interesting relations of NSI parameters $\epsilon^{\rm m}_{\alpha\beta}$ are obtained, which may be helpful for solving the parameter degeneracy problem in the studies of NSIs. In Sec. 12.1, we follow the general set-up that NSIs are resulted from heavy mediators. Both higher-dimensional operators in the EFT approach with respecting to the electroweak symmetry and ultraviolet (UV) completions will be discussed in Sec. 12.2.

12.1 Predicting Textures by Flavour Symmetries

12.1.1 NSI textures predicted by A_4

We consider how neutrino NSIs from the higher-dimensional operators are constrained by flavour symmetries. For definiteness, we only focus on textures realised in the tetrahedral group A_4. A_4 is generated by two generators $\mathcal{S}$ and $\mathcal{T}$ with the requirements $\mathcal{S}^2 = \mathcal{T}^3 = (\mathcal{S}\mathcal{T})^3 = 1$ and contains 12 elements. It has 4 irreducible representations: three singlet representations $\mathbf{1}$, $\mathbf{1}'$, $\mathbf{1}''$ and one triplet representation $\mathbf{3}$. Kronecker products of two irreducible representations are reduced in the following way:

$$\begin{aligned}\mathbf{1}\times\mathbf{1}^{(\prime,\prime\prime)}=\mathbf{1}^{(\prime,\prime\prime)}\,,\ \mathbf{1}^{\prime}\times\mathbf{1}^{\prime}=\mathbf{1}^{\prime\prime}\,,\ \mathbf{1}^{\prime\prime}\times\mathbf{1}^{\prime\prime}=\mathbf{1}^{\prime}\,,\ \mathbf{1}^{\prime}\times\mathbf{1}^{\prime\prime}=\mathbf{1}\,,\\ \mathbf{3}\times\mathbf{1}^{(\prime,\prime\prime)}=\mathbf{3}\,,\ \mathbf{3}\times\mathbf{3}=\mathbf{1}+\mathbf{1}^{\prime}+\mathbf{1}^{\prime\prime}+\mathbf{3}_{\mathrm{S}}+\mathbf{3}_{\mathrm{A}}\,,\end{aligned} \tag{12.1.1}$$

where the subscripts $_{\mathrm{S}}$ and $_{\mathrm{A}}$ stand for the symmetric and anti-symmetric components, respectively. We work in the Altarelli-Feruglio (AF) basis [27], where $\mathcal{T}$ and $\mathcal{S}$ are respectively given by

$$\mathcal{T}=\begin{pmatrix}1&0&0\\0&\omega^2&0\\0&0&\omega\end{pmatrix}\,,\qquad \mathcal{S}=\frac{1}{3}\begin{pmatrix}-1&2&2\\2&-1&2\\2&2&-1\end{pmatrix}\,. \tag{12.1.2}$$

This basis is widely used in the literature since the charged lepton mass matrix invariant under $\mathcal{T}$ is diagonal in this basis. The products of each two triplet representations $a=(a_1,a_2,a_3)^T$ and $b=(b_1,b_2,b_3)^T$ can be expressed as

$$\begin{aligned}&(ab)_{\mathbf{1}}\ \ =a_1b_1+a_2b_3+a_3b_2\,,\\ &(ab)_{\mathbf{1}^\prime}\ =a_3b_3+a_1b_2+a_2b_1\,,\quad (ab)_{\mathbf{3}_{\mathrm{S}}}=\frac{1}{2}\begin{pmatrix}2a_1b_1-a_2b_3-a_3b_2\\2a_3b_3-a_1b_2-a_2b_1\\2a_2b_2-a_3b_1-a_1b_3\end{pmatrix}\,,\\ &(ab)_{\mathbf{1}^{\prime\prime}}=a_2b_2+a_1b_3+a_3b_1\,,\\ &(ab)_{\mathbf{3}_{\mathrm{A}}}=\frac{1}{2}\begin{pmatrix}a_2b_3-a_3b_2\\a_1b_2-a_2b_1\\a_3b_1-a_1b_3\end{pmatrix}\,.\end{aligned} \tag{12.1.3}$$

We require that the higher-dimensional operators are invariant under the symmetry A_4 and consider what kinds of NSI textures we could gain from the symmetry. As we only care about matter-effect NSI textures, we limit our discussion on the operators $\mathcal{O}^{1-8}$[1].

The results also depend on how the representations of the fermions could be arranged under A_4. In order to get large mixing angles, in most flavour models, the lepton doublets $L=(L_1,L_2,L_3)^T$ are often arranged as a triplet $\mathbf{3}$ of A_4[2]. We follow the same arrangement. Besides, we do not specify the representations for

---

[1] In the appendix **B** of [133], one can find the NSI textures at the source and detector from the operators $\mathcal{O}^{7-12}$.

[2] In the AF basis, the conjugate of L should be arranged as $\overline{L}=(\overline{L_1},\overline{L_3},\overline{L_2})^T$.

the other fermions in the flavour space. In other words, the right-handed charged leptons, left-handed quarks and right-handed quarks could be any irreducible representations of A_4, $\mathbf{1}, \mathbf{1}', \mathbf{1}''$ or $\mathbf{3}$. It is worth noting that we do not specify if A_4 can be responsible for the quark mixing in this work. If all quarks are arranged as the singlet representation $\mathbf{1}$, quark flavour mixing is totally independent of A_4. We scan for all these possibilities, and find the following NSI textures:

$$\mathbb{T}_{11} \equiv \mathbb{1} = \begin{pmatrix} 1 & 0 & 0 \\ 0 & 1 & 0 \\ 0 & 0 & 1 \end{pmatrix}, \qquad \mathbb{T}_{12} = \begin{pmatrix} 2 & 0 & 0 \\ 0 & -1 & 0 \\ 0 & 0 & -1 \end{pmatrix},$$
$$\mathbb{T}_{13} = \begin{pmatrix} 0 & 0 & 0 \\ 0 & 1 & 0 \\ 0 & 0 & -1 \end{pmatrix}. \tag{12.1.4}$$

In the following, we explain how to get these textures.

The first operator $c^1_{\alpha\beta\gamma\delta}\mathcal{O}^1_{\alpha\beta\gamma\delta}$, i.e., the dimension-6 $\varepsilon_{ac}\varepsilon_{bd}c^1_{\alpha\beta\gamma\delta}(\overline{L_{a\alpha}}\gamma^\mu L_{b\beta})(\overline{L_{c\gamma}}\gamma_\mu L_{d\delta})$, satisfy the anti-permutation property of two leptons and two antileptons, as shown in Eq. (10.1.8), which results in $c^1_{e\beta 11} = c^1_{\alpha e 11} = 0$. There are 5 independent A_4-invariant operators:

$$(\overline{L}L)_{\mathbf{1}}(\overline{L}L)_{\mathbf{1}}\,,\ (\overline{L}L)_{\mathbf{1}'}(\overline{L}L)_{\mathbf{1}''}\,,\ (\overline{L}L)_{\mathbf{3}_{\rm S}}(\overline{L}L)_{\mathbf{3}_{\rm S}}\,,$$
$$(\overline{L}L)_{\mathbf{3}_{\rm A}}(\overline{L}L)_{\mathbf{3}_{\rm A}}\,,\ (\overline{L}L)_{\mathbf{3}_{\rm S}}(\overline{L}L)_{\mathbf{3}_{\rm A}}\,. \tag{12.1.5}$$

Here, we have ignored the unnecessary flavour-independent notations, including the $SU(2)_{\rm L}$ indices, Γ matrices and the Higgs field. The representations in the subscripts are understood as in Eq. (12.1.3). Taking account of the CG coefficients in Eq. (12.1.3), we obtain

$$c^1_{\mu\mu 11} = c^1_{\tau\tau 11}\,,\ c^1_{ee11} = c^1_{\alpha\beta 11} = 0 \text{ for } \alpha \neq \beta, \tag{12.1.6}$$

for the first 4 operators which lead to the NSI texture

$$\mathbb{T}'_{12} \equiv \begin{pmatrix} 0 & 0 & 0 \\ 0 & 1 & 0 \\ 0 & 0 & 1 \end{pmatrix} \propto 2\mathbb{T}_{11} - \mathbb{T}_{12}\,. \tag{12.1.7}$$

The last operator gives vanishing $c^1_{\alpha\beta 11}$ and thus does not contribute to NSIs.

For the second one in Table 10.1, $c^2_{\alpha\beta\gamma\delta}\mathcal{O}^2_{\alpha\beta\gamma\delta}$, i.e., the dimension-8 $(\overline{L_\alpha}\tilde{H}\gamma^\mu\tilde{H}^\dagger L_\beta)(\overline{U_{\gamma\mathrm{R}}}\gamma_\mu U_{\delta\mathrm{R}})$, the A_4-invariant operators depend on the flavour representation of U_R:

- If $U_{1\mathrm{R}}$ is arranged to be a singlet $\mathbf{1}^{(\prime,\prime\prime)}$ of A_4, there is only one A_4-invariant operator

  $$(\overline{L}L)_\mathbf{1}(\overline{U_{1\mathrm{R}}}U_{1\mathrm{R}})_\mathbf{1}\,. \tag{12.1.8}$$

  It leads to the relation of the coefficients

  $$c^2_{ee11} = c^2_{\mu\mu 11} = c^2_{\tau\tau 11}\,,\; c^2_{\alpha\beta 11} = 0 \text{ for } \alpha \neq \beta\,. \tag{12.1.9}$$

  Representations of $U_{2\mathrm{R}}$ and $U_{3\mathrm{R}}$ are irrelevant for our discussion since $U_{2\mathrm{R}}$ and $U_{3\mathrm{R}}$ do not attend to the low energy NSIs.

- If $U_\mathrm{R} = (U_{1\mathrm{R}}, U_{2\mathrm{R}}, U_{3\mathrm{R}})^T$ is a triplet $\mathbf{3}$ of A_4, there are 7 independent A_4-invariant operators

  $$\begin{aligned}&(\overline{L}L)_\mathbf{1}(\overline{U_\mathrm{R}}U_\mathrm{R})_\mathbf{1}\,,\; (\overline{L}L)_{\mathbf{1}'}(\overline{U_\mathrm{R}}U_\mathrm{R})_{\mathbf{1}''}\,,\; (\overline{L}L)_{\mathbf{1}''}(\overline{U_\mathrm{R}}U_\mathrm{R})_{\mathbf{1}'}\,,\; (\overline{L}L)_{\mathbf{3}_\mathrm{S}}(\overline{U_\mathrm{R}}U_\mathrm{R})_{\mathbf{3}_\mathrm{S}}\,,\\ &(\overline{L}L)_{\mathbf{3}_\mathrm{A}}(\overline{U_\mathrm{R}}U_\mathrm{R})_{\mathbf{3}_\mathrm{S}}\,,\; (\overline{L}L)_{\mathbf{3}_\mathrm{S}}(\overline{U_\mathrm{R}}U_\mathrm{R})_{\mathbf{3}_\mathrm{A}}\,,\; (\overline{L}L)_{\mathbf{3}_\mathrm{A}}(\overline{U_\mathrm{R}}U_\mathrm{R})_{\mathbf{3}_\mathrm{A}}\,.\end{aligned} \tag{12.1.10}$$

  The first operator gives the same correlation as in Eq. (12.1.9), $(\overline{L}L)_{\mathbf{3}_\mathrm{S}}(\overline{U_\mathrm{R}}U_\mathrm{R})_{\mathbf{3}_\mathrm{S}}$ and $(\overline{L}L)_{\mathbf{3}_\mathrm{A}}(\overline{U_\mathrm{R}}U_\mathrm{R})_{\mathbf{3}_\mathrm{S}}$ give rise to

  $$\begin{aligned}&c^2_{ee11} = -2c^2_{\mu\mu 11} = -2c^2_{\tau\tau 11}\,,\; c^2_{\alpha\beta 11} = 0 \text{ for } \alpha \neq \beta\,;\\ &c^2_{\mu\mu 11} = -c^2_{\tau\tau 11}\,,\; c^2_{ee11} = c^2_{\alpha\beta 11} = 0 \text{ for } \alpha \neq \beta\,,\end{aligned} \tag{12.1.11}$$

  respectively, where all non-vanishing values are real. The rest, $(\overline{L}L)_{\mathbf{1}'}(\overline{U_\mathrm{R}}U_\mathrm{R})_{\mathbf{1}''}$, $(\overline{L}L)_{\mathbf{1}''}(\overline{U_\mathrm{R}}U_\mathrm{R})_{\mathbf{1}'}$, $(\overline{L}L)_{\mathbf{3}_\mathrm{S}}(\overline{U_\mathrm{R}}U_\mathrm{R})_{\mathbf{3}_\mathrm{A}}$, and $(\overline{L}L)_{\mathbf{3}_\mathrm{A}}(\overline{U_\mathrm{R}}U_\mathrm{R})_{\mathbf{3}_\mathrm{A}}$ have no contribution to $c^2_{\alpha\beta 11}$.

The correlations of the coefficients $c^2_{\alpha\beta 11}$ directly determine the flavour structure of matter-effect NSIs. In detail, Eq. (12.1.9) directly gives rise to $\mathbb{T}_{11}$, and Eq. (12.1.11) leads to $\mathbb{T}_{12}$ and $\mathbb{T}_{13}$. The discussion of $\mathcal{O}^2_{\alpha\beta\gamma\delta}$ applies to $\mathcal{O}^{3-8}_{\alpha\beta\gamma\delta}$. In other words, the NSI textures $\mathbb{T}_{11}$, $\mathbb{T}_{12}$ and $\mathbb{T}_{13}$ can be derived from

$$(\overline{L}L)_\mathbf{1}(\overline{F}F)_\mathbf{1}\,,\; (\overline{L}L)_{\mathbf{3}_\mathrm{S}}(\overline{F}F)_{\mathbf{3}_\mathrm{S}}\,,\; (\overline{L}L)_{\mathbf{3}_\mathrm{A}}(\overline{F}F)_{\mathbf{3}_\mathrm{S}}\,, \tag{12.1.12}$$

respectively, where F represents any fermions in the SM.

12.1.2 NSI textures predicted by the residual symmetry of A_4

In most A_4 flavour models, the full A_4 symmetry is not preserved at low energy. Instead, there are some residual symmetries roughly preserved, Z_3 in the charged lepton sector and Z_2 in the neutrino sector. They are often realised by two flavons getting the following VEVs

$$\varphi = (1,0,0)^T v_\varphi\,, \qquad \chi = (1,1,1)^T v_\chi\,, \tag{12.1.13}$$

respectively [26, 27, 30]. Additional interactions, e.g., higher-dimensional operators, may lead to small deviations from the above directions, which are usually regarded as subleading corrections and will be ignored in this thesis. Note that the conjugates of φ and χ are identical with φ and χ, respectively, and thus are not necessary to be mentioned in the rest of this thesis. We consider that the operators $c^p_{\alpha\beta\gamma\delta}\mathcal{O}^p_{\alpha\beta\gamma\delta}$ are effectively realised from

$$c^{\varphi,p}_{\alpha'\alpha\beta\gamma\delta}\frac{\varphi_{\alpha'}}{v_\varphi}\mathcal{O}^p_{\alpha\beta\gamma\delta}\,, \quad c^{\chi,p}_{\alpha'\alpha\beta\gamma\delta}\frac{\chi_{\alpha'}}{v_\chi}\mathcal{O}^p_{\alpha\beta\gamma\delta}\,. \tag{12.1.14}$$

These operators are A_4-invariant before flavons get VEVs. Taking the VEVs in Eq. (12.1.13), we obtain $c^p_{\alpha\beta\gamma\delta}\mathcal{O}^p_{\alpha\beta\gamma\delta}$ with

$$c^p_{\alpha\beta\gamma\delta} = c^{\varphi,p}_{1\alpha\beta\gamma\delta} \;\text{ or }\; c^{\chi,p}_{1\alpha\beta\gamma\delta} + c^{\chi,p}_{2\alpha\beta\gamma\delta} + c^{\chi,p}_{3\alpha\beta\gamma\delta} \tag{12.1.15}$$

is not A_4-invariant any more, but preserves only a Z_3 or Z_2 symmetry, since φ and χ preserve Z_3 and Z_2 symmetries, respectively. The Z_3-invariant operators $\varphi\mathcal{O}$ will not give as anything new, but Eq. (12.1.4). The reason is that the generator of Z_3, T, is diagonal, and the predicted NSI textures must be also diagonal. In the following, we only consider the Z_2-invariant operator $\varphi\mathcal{O}$ anymore.

Now we focus on the A_4-breaking Z_2-invariant operators $\chi\mathcal{O}$. We first define the following non-diagonal textures:

$$\mathbb{T}_{21} = \begin{pmatrix} 0 & 1 & 1 \\ 1 & 0 & 1 \\ 1 & 1 & 0 \end{pmatrix}, \qquad \mathbb{T}_{22} = \begin{pmatrix} 0 & -1 & -1 \\ -1 & 0 & 2 \\ -1 & 2 & 0 \end{pmatrix},$$
$$\mathbb{T}_{23} = \begin{pmatrix} 0 & -1 & 1 \\ -1 & 0 & 0 \\ 1 & 0 & 0 \end{pmatrix}, \qquad \mathbb{T}_{31} = \begin{pmatrix} 0 & -i & i \\ i & 0 & -i \\ -i & i & 0 \end{pmatrix},$$
$$\mathbb{T}_{32} = \begin{pmatrix} 0 & i & -i \\ -i & 0 & -2i \\ i & 2i & 0 \end{pmatrix}, \qquad \mathbb{T}_{33} = \begin{pmatrix} 0 & i & i \\ -i & 0 & 0 \\ -i & 0 & 0 \end{pmatrix}. \tag{12.1.16}$$

$\mathbb{T}_{2n}$ represent non-diagonal real NSI textures, while $\mathbb{T}_{3n}$ represent pure imaginary NSI textures.

For $c^{\chi,1}_{\alpha'\alpha\beta\gamma\delta}\chi_{\alpha'}\mathcal{O}^1_{\alpha\beta\gamma\delta}$, there are 9 Z_2-invariant operators that can contribute to NSIs:

$$\begin{gathered}
\chi(\overline{L}L)_{\mathbf{3}_\mathrm{S}}(\overline{L}L)_{\mathbf{1}},\ \chi(\overline{L}L)_{\mathbf{3}_\mathrm{S}}(\overline{L}L)_{\mathbf{1}'},\ \chi(\overline{L}L)_{\mathbf{3}_\mathrm{S}}(\overline{L}L)_{\mathbf{1}''},\\
\chi(\overline{L}L)_{\mathbf{3}_\mathrm{A}}(\overline{L}L)_{\mathbf{1}},\ \chi(\overline{L}L)_{\mathbf{3}_\mathrm{A}}(\overline{L}L)_{\mathbf{1}'},\ \chi(\overline{L}L)_{\mathbf{3}_\mathrm{A}}(\overline{L}L)_{\mathbf{1}''},\\
\chi\big((\overline{L}L)_{\mathbf{3}_\mathrm{S}}(\overline{L}L)_{\mathbf{3}_\mathrm{S}}\big)_{\mathbf{3}_\mathrm{S}},\ \chi\big((\overline{L}L)_{\mathbf{3}_\mathrm{A}}(\overline{L}L)_{\mathbf{3}_\mathrm{A}}\big)_{\mathbf{3}_\mathrm{S}},\\
\chi\big((\overline{L}L)_{\mathbf{3}_\mathrm{S}}(\overline{L}L)_{\mathbf{3}_\mathrm{A}}\big)_{\mathbf{3}_\mathrm{S}},\ \chi\big((\overline{L}L)_{\mathbf{3}_\mathrm{S}}(\overline{L}L)_{\mathbf{3}_\mathrm{A}}\big)_{\mathbf{3}_\mathrm{A}}.
\end{gathered} \tag{12.1.17}$$

Due to the antisymmetric property between α and γ and that between β and δ, $c^1_{e\beta11} = c^1_{\alpha e11} = 0$ for all cases. The other coefficients satisfy the following relations, respectively. Taking the CG coefficients in Eq. (12.1.3) into account, we obtain

$$2c^1_{\mu\mu11} = 2c^1_{\tau\tau11} = c^1_{\mu\tau11} = c^1_{\tau\mu11} \tag{12.1.18}$$

for $\chi\big((\overline{L}L)_{\mathbf{3}_\mathrm{S}}(\overline{L}L)_{\mathbf{1},\mathbf{1}',\mathbf{1}''}\big)_{\mathbf{3}}$, $\chi\big((\overline{L}L)_{\mathbf{3}_\mathrm{S}}(\overline{L}L)_{\mathbf{3}_\mathrm{S}}\big)_{\mathbf{3}_\mathrm{S}}$, $\chi\big((\overline{L}L)_{\mathbf{3}_\mathrm{A}}(\overline{L}L)_{\mathbf{3}_\mathrm{A}}\big)_{\mathbf{3}_\mathrm{S}}$ and

$$c^1_{\mu\mu11} = -c^1_{\tau\tau11}\,,\ c^1_{\mu\tau11} = c^1_{\tau\mu11} = 0 \tag{12.1.19}$$

for $\chi\big((\overline{L}L)_{\mathbf{3}_\mathrm{A}}(\overline{L}L)_{\mathbf{1},\mathbf{1}',\mathbf{1}''}\big)_{\mathbf{3}}$, $\chi\big((\overline{L}L)_{\mathbf{3}_\mathrm{S}}(\overline{L}L)_{\mathbf{3}_\mathrm{A}}\big)_{\mathbf{3}_\mathrm{S}}$, $\chi\big((\overline{L}L)_{\mathbf{3}_\mathrm{S}}(\overline{L}L)_{\mathbf{3}_\mathrm{A}}\big)_{\mathbf{3}_\mathrm{A}}$. The first two relations give

$$\frac{1}{3}(2\mathbb{T}_{11} - \mathbb{T}_{12} + 2\mathbb{T}_{21} + 2\mathbb{T}_{23}) = \begin{pmatrix} 0 & 0 & 0 \\ 0 & 1 & 2 \\ 0 & 2 & 1 \end{pmatrix} \tag{12.1.20}$$

and $\mathbb{T}_{13}$, respectively.

For $c^{\chi,2}_{\alpha'\alpha\beta\gamma\delta}\chi_{\alpha'}\mathcal{O}^2_{\alpha\beta\gamma\delta}$, i.e., the first dimension-8 operator $(\overline{L_\alpha}\tilde{H}\gamma^\mu\tilde{H}^\dagger L_\beta)(\overline{U_{\gamma\mathrm{R}}}\gamma_\mu U_{\delta\mathrm{R}})$, depending on the representation of U_R, there are several Z_2-invariant operators:

- If $U_{1\mathrm{R}}$ is a trivial singlet $\mathbf{1}$, $\mathbf{1}'$, or $\mathbf{1}''$ of A_4, there are two Z_2-invariant operators

  $$\chi(\overline{L}L)_{\mathbf{3}_\mathrm{S}}(\overline{U_{1\mathrm{R}}}U_{1\mathrm{R}})_{\mathbf{1}}\,,\chi(\overline{L}L)_{\mathbf{3}_\mathrm{A}}(\overline{U_{1\mathrm{R}}}U_{1\mathrm{R}})_{\mathbf{1}}\,. \tag{12.1.21}$$

  They lead to the correlations of the coefficients

  $$\begin{gathered} c^2_{ee11}=c^2_{\mu\tau11}=c^2_{\tau\mu11}=-2c^2_{\mu\mu11}=-2c^2_{\tau\tau11}=-2c^2_{e\mu11}=-2c^2_{\mu e11}=-2c^2_{e\tau11}=-2c^2_{\tau e11}\,; \\ -c^2_{\mu\mu11}=c^2_{\tau\tau11}=c^2_{e\mu11}=c^2_{\mu e11}=-c^2_{e\tau11}=-c^2_{\tau e11}\,, \\ c^2_{ee11}=c^2_{e\tau11}=c^2_{\tau e11}=0\,, \end{gathered} \tag{12.1.22}$$

  respectively. They give rise to two textures $\mathbb{T}_2\equiv\mathbb{T}_{12}+\mathbb{T}_{22}$ and $\mathbb{T}_3\equiv\mathbb{T}_{13}+\mathbb{T}_{23}$, respectively.

- If $U_{1\mathrm{R}}$ is arranged as one component of a triplet $U_\mathrm{R}=(U_{1\mathrm{R}},U_{2\mathrm{R}},U_{3\mathrm{R}})^T\sim\mathbf{3}$ of A_4, there are 6 independent Z_2-invariant operators contributing to NSIs,

  $$\begin{gathered} \chi(\overline{L}L)_{\mathbf{3}_\mathrm{S}}(\overline{U_\mathrm{R}}U_\mathrm{R})_{\mathbf{1}}\,,\ \chi(\overline{L}L)_{\mathbf{3}_\mathrm{A}}(\overline{U_\mathrm{R}}U_\mathrm{R})_{\mathbf{1}}\,,\ \chi\big((\overline{L}L)_{\mathbf{3}_\mathrm{S}}(\overline{U_\mathrm{R}}U_\mathrm{R})_{\mathbf{3}_\mathrm{S}}\big)_{\mathbf{3}_\mathrm{S}}\,, \\ \chi\big((\overline{L}L)_{\mathbf{3}_\mathrm{S}}(\overline{U_\mathrm{R}}U_\mathrm{R})_{\mathbf{3}_\mathrm{S}}\big)_{\mathbf{3}_\mathrm{A}}\,,\ \chi\big((\overline{L}L)_{\mathbf{3}_\mathrm{A}}(\overline{U_\mathrm{R}}U_\mathrm{R})_{\mathbf{3}_\mathrm{S}}\big)_{\mathbf{3}_\mathrm{S}}\,, \\ \chi\big((\overline{L}L)_{\mathbf{3}_\mathrm{A}}(\overline{U_\mathrm{R}}U_\mathrm{R})_{\mathbf{3}_\mathrm{S}}\big)_{\mathbf{3}_\mathrm{A}}\,. \end{gathered} \tag{12.1.23}$$

  The first two give the two correlations as in Eq. (12.1.22). The rest four give rise to

  $$\begin{gathered} c^2_{ee11}=-2c^2_{\mu\mu11}=-2c^2_{\tau\tau11}=-2c^2_{\mu\tau11}=-2c^2_{\tau\mu11}=4c^2_{e\mu11}=4c^2_{\mu e11}=c^2_{e\tau11}=4c^2_{\tau e11}\,; \\ c^2_{\mu\mu11}=-c^2_{\tau\tau11}=2c^2_{e\mu11}=2c^2_{\mu e11}=-2c^2_{e\tau11}=2c^2_{\tau e11}\,,\ c^2_{ee11}=c^2_{e\tau11}=c^2_{\tau e11}=0\,; \\ ic^2_{\mu\tau11}=-ic^2_{\tau\mu11}=-2ic^2_{e\mu11}=2ic^2_{\mu e11}=2ic^2_{e\tau11}=-2ic^2_{\tau e11}\,,\ c^2_{ee11}=c^2_{\mu\mu11}=c^2_{\tau\tau11}=0\,; \\ ic^2_{e\mu11}=-ic^2_{\mu e11}=ic^2_{e\tau11}=-ic^2_{\tau e11}\,, \\ c^2_{ee11}=c^2_{\mu\mu11}=c^2_{\tau\tau e11}=c^2_{\mu\tau e11}=c^2_{\tau\mu11}=0\,, \end{gathered} \tag{12.1.24}$$

  respectively, where all non-vanishing values are real, required by the Hermitean of the Lagrangian. They give rise to

$$2\mathbb{T}_{12}-\mathbb{T}_{22}=\begin{pmatrix}4 & 1 & 1\\ 1 & -2 & -2\\ 1 & -2 & -2\end{pmatrix},$$
$$2\mathbb{T}_{13}-\mathbb{T}_{23}=\begin{pmatrix}0 & 1 & -1\\ 1 & 2 & 0\\ -1 & 0 & -2\end{pmatrix}, \tag{12.1.25}$$

and $\mathbb{T}_{32}$ and $\mathbb{T}_{33}$, respectively.

The similiar discussion applies to $\mathcal{O}^{3-8}$ and the same textures as predicted by $\mathcal{O}^2$ are obtained from these operators.

Nine textures $\mathbb{T}_{mn}$ in Eqs. (12.1.4) and (12.1.16) form a complete basis for a Hermitian 3×3 matrix. Any two of these textures are orthogonal in the Hilbert-Schmidt inner product, $\mathrm{tr}(\mathbb{T}^\dagger_{mn}\mathbb{T}_{m'n'})\propto\delta_{mm'}\delta_{nn'}$. Matter-effect NSIs contribute to the effective Hamiltonian term via the matrix

$$\epsilon=\sum_{m,n=1,2,3}\alpha_{mn}\mathbb{T}_{mn}/N_{mn}, \tag{12.1.26}$$

where N_{mn} are normalization factor $N_{11}=\sqrt{3}$, $N_{12}=\sqrt{6}$, $N_{13}=\sqrt{2}$, $N_{21}=N_{31}=\sqrt{6}$, $N_{22}=N_{32}=2\sqrt{3}$ and $N_{23}=N_{33}=2$. The relations between $\epsilon_{\alpha\beta}$ and α_{mn} are shown in Table 13.1, andthe following properties are satisfied

$$\mathrm{tr}(\epsilon\epsilon^{\mathrm{m}\dagger})=\sum_{\alpha,\beta=e,\mu,\tau}|\epsilon^{\mathrm{m}}_{\alpha\beta}|^2=\sum_{m,n=1,2,3}\alpha^2_{mn}\,. \tag{12.1.27}$$

Note that $\mathbb{T}_{11}\equiv\mathbb{1}$ is unobservable in neutrino oscillations experiments.

We list all A_4- and Z_2-motivated matter-effect NSI textures predicted by $\mathcal{O}^p$- and Z_2-invariant operators $\chi\mathcal{O}^p$ in Table 12.1, where χ is the flavon VEV inducing A_4 to be broken to Z_2. As can be seen from the table, a NSI texture predicted by an A_4-invariant (Z_2-invariant) operator usually does not preserve A_4 (Z_2). This is because the matter-effect NSIs have specified the first-generation charged fermions. These charged fermions, if not be arranged as a A_4-invariant **1**, is not invariant in A_4 or Z_2, and thus the NSI texture does not respect A_4 or Z_2. In a specific A_4 model, the NSI matrix ϵ could be a linear combinations of $\mathbb{T}_{mn}$. However, it is notable that $\mathbb{T}_{31}$ cannot be obtained directly from the above analysis. The analysis based on higher-dimensional operators cannot determine which texture is more important and dominant in oscillation experiments. However, as what we will discuss in the next section, once we consider these textures resulted from UV-complete models and include experimental constriants, some of them are suppressed and cannot be measured in neutrino experiments.

12.2 NSI textures realised in renormalisable flavour models

In this section, we consider how to realise higher-dimensional operators in UV-complete models. New particles in the UV sector lead to correlations of the NSI textures $\mathbb{T}_{mn}$. These particles may also contribute to some processes beyond the 4-charged-fermion interactions. Experimental constraints from these processes may forbid some of the textures. These issues will be discussed in the following.

12.2.1 UV completion of the dimension-6 operator

We first consider the UV completion of $\mathcal{O}^1$, $\varepsilon_{ac}\varepsilon_{bd}(\overline{L_{a\alpha}}\gamma^\mu L_{b\beta})(\overline{L_{c\gamma}}\gamma_\mu L_{d\delta})$. The only way is to introduce a singly charged scalar S which is a $SU(2)_{\rm L}$ singlet with $Y=+1$ and assume that it couples to L in an "antisymmetric" form [34]. Together with the kinetic and mass term of S, we write out the renormalisable Lagrangian terms as

$$\mathcal{L} \;=\; (D_\mu S)^\dagger (D^\mu S) - (M_S^2)_{\alpha\beta} S^*_\alpha S_\beta + \lambda_{\alpha\beta\gamma}\varepsilon_{ab}\overline{L^{\rm C}_{a\alpha}} L_{b\beta} S_\gamma + \text{h.c.}\,, \quad (12.2.28)$$

where $\lambda_{\alpha\beta\gamma} = -\lambda_{\beta\alpha\gamma}$. In the framework of A_4, S cannot be arranged as a singlet representation $\mathbf{1}, \mathbf{1}'$ or $\mathbf{1}''$ of A_4 since the symmetric CG coefficients of A_4 and the anti-symmetric property of λ lead to $S(\overline{L^{\rm C}}L)_{\mathbf{1}^{('','')}} \equiv 0$. Similarly by arranging $S\sim\mathbf{3}$, we obtain $S(\overline{L^{\rm C}}L)_{\mathbf{3}_{\rm S}} = 0$. The only term that can contribute to the operator in Eq. (12.2.28) is $S(\overline{L^{\rm C}}L)_{\mathbf{3}_{\rm A}}$ for $S\sim\mathbf{3}$. All non-vanishing coefficients satisfy

$$\lambda_{123} = \lambda_{231} = \lambda_{312} = -\lambda_{132} = -\lambda_{213} = -\lambda_{321} \equiv \lambda_0\,. \quad (12.2.29)$$

After S decouples and by using the Fierz identity, we obtain $\mathcal{O}^1$ and the resulted NSI parameters are obtained as

$$\epsilon^e_{\alpha\beta} = \frac{1}{\sqrt{2}G_F}\lambda_{\beta e}(M_S^2)^{-1}\lambda^\dagger_{\alpha e}\,, \tag{12.2.30}$$

where each $\lambda_{\alpha\beta}$ is the 1×3 matrix given by $\lambda_{\alpha\beta} = (\lambda_{\alpha\beta 1}, \lambda_{\alpha\beta 2}, \lambda_{\alpha\beta 3})$.

The structures of $\epsilon^e_{\alpha\beta}$ are fully determined by the flavour structure of M_S^2. We will see how to constrain the M_S^2 structure.

- An A_4-invariant mass term for the charged scalar can only take the form $\mu_S^2(S^*S)_{\mathbf{1}} = \mu_S^2\sum_\alpha S^*_\alpha S_\alpha$ with $\mu_S^2 > 0$, leading to the charged scalar mass matrix $M_S^2 = \mu_S^2\mathbb{1}$. From this mass matrix, we obtain the texture $\epsilon^e = \alpha_0\mathbb{T}'_{12}$ with $\alpha_0 = \frac{\mu_S^2}{\sqrt{2}G_F}$.

- In order to obtain non-vanishing off-diagonal NSI entries, A_4 has to be broken. As shown in the last section, the key is to introduce a flavon with the Z_2-preserving VEV χ. We add the following renormalisable couplings to the Lagrangian,

  $$\frac{\mu_S^2}{v_\chi}\left[\frac{2}{3}h_{\rm S}\Big(\chi(S^*S)_{\mathbf{3}_{\rm S}}\Big)_{\mathbf{1}} - \frac{2}{\sqrt{3}}h_{\rm A}\Big(\chi(S^*S)_{\mathbf{3}_{\rm A}}\Big)_{\mathbf{1}}\right]\,, \tag{12.2.31}$$

  where $h_{\rm S}$ and $h_{\rm A}$ are real dimensionless coefficients as required by the Hermiticity of the Lagrangian. Then, the S mass matrix is modified to

  $$M_S^2/\mu_S^2 = \mathbb{1} + h_{\rm S}\mathbb{T}_2 + h_{\rm A}\mathbb{T}_3\,. \tag{12.2.32}$$

  And the resulted NSI matrix becomes

  $$\epsilon^e = \alpha_0\left[\mathbb{T}'_{12} + \frac{1}{3}\begin{pmatrix} 0 & 0 & 0 \\ 0 & h_{\rm S} - h_{\rm S}^2 & 2h_{\rm S} + h_{\rm S}^2 \\ 0 & 2h_{\rm S} + h_{\rm S}^2 & h_{\rm S} - h_{\rm S}^2 \end{pmatrix} + \frac{1}{3}\begin{pmatrix} 0 & 0 & 0 \\ 0 & \sqrt{3}h_{\rm A} - h_{\rm A}^2 & h_{\rm A}^2 \\ 0 & h_{\rm A}^2 & -\sqrt{3}h_{\rm A} - h_{\rm A}^2 \end{pmatrix}\right]\,, \tag{12.2.33}$$

  where $\alpha_0 = |\lambda_0|^2/[\sqrt{2}G_F\mu_S^2(1 - h_{\rm S}^2 - h_{\rm A}^2)]$. ϵ^e contains three real parameters $\epsilon_{\mu\mu}$, $\epsilon_{\tau\tau}$ and $|\epsilon_{\mu\tau}|$. The renormalisable quartic terms $\Big((\chi\chi)_{\mathbf{3}_{\rm S}}(S^*S)_{\mathbf{3}_{\rm S}}\Big)_{\mathbf{1}}$ and

$\Big((\chi\chi)_{\mathbf{3}_{\rm S}}(S^*S)_{\mathbf{3}_{\rm A}}\Big)_{\mathbf{1}}$ are also allowed by the symmetry, such terms do not modify the flavour structures of M_S^2 and ϵ^e except redefinitions of $h_{\rm S}$ and $h_{\rm A}$.

However, sizeable NSI textures are hard to be realised in this approach due to the strong constraint from the radiative charged LFV measurements. Although the tree-level 4-charged-fermion interactions have been avoided, radiative decays $E_\alpha \to E_\beta\gamma$ involving S and neutrinos in the loop could be triggered by the interaction $\overline{L^{\rm C}}LS$, and the relative branching ratios are $\propto |G_F^{-1}\lambda_{\alpha\gamma}(M_S^2)^{-1}\lambda^\dagger_{\beta\gamma}|^2$, where $\gamma \neq \alpha, \beta$. General upper bounds of $\tau \to e\gamma$ and $\tau \to \mu\gamma$ branching ratios are around 10^{-8} [124] and [125], and that of $\mu \to e\gamma$ is 4.2×10^{-13} [126]. Without flavour symmetries, the coefficients $\lambda_{\alpha\beta\gamma}$ and mass terms $(M_S^2)_{\alpha\beta}$ are free parameters, and $\tau \to e\gamma$ and $\mu \to e\gamma$ do not provide direct constraints to NSIs [34]. Once the flavour symmetry is included, relations such as Eqs. (12.2.29) and (12.2.31) are satisfied. In the limit $h_{\rm S}, h_{\rm A} \to 0$, all radiative decays are forbidden. However, off-diagonal NSIs are also forbidden in this case, which are less interesting in oscillation experiments. On the other hand, by assuming $h_{\rm S}$ or $h_{\rm A} \sim \mathcal{O}(1)$, very strong constraint, $|\epsilon^e_{\alpha\beta}| < 7 \times 10^{-5}$, is obtained from the upper limit of $\mu \to e\gamma$.

12.2.2 UV completions of dimension-8 operators

In the following, we will only consider NSIs from UV completions of dimension-8 operators. Before performing a detailed analysis, we directly point out our main result that, in UV-complete models with the Z_2 residual symmetry, only linear combinations of the following NSI textures with coefficients at the percent level are still allowed by experimental data,

$$\mathbb{T}_1 = \frac{1}{3}\begin{pmatrix} 2 & -1 & -1 \\ -1 & 2 & -1 \\ -1 & -1 & 2 \end{pmatrix}, \mathbb{T}_2 = \frac{1}{3}\begin{pmatrix} 2 & -1 & -1 \\ -1 & -1 & 2 \\ -1 & 2 & -1 \end{pmatrix},$$
$$\mathbb{T}_3 = \frac{1}{\sqrt{3}}\begin{pmatrix} 0 & -1 & 1 \\ -1 & 1 & 0 \\ 1 & 0 & -1 \end{pmatrix}, \mathbb{T}_4 = \frac{1}{\sqrt{3}}\begin{pmatrix} 0 & -i & i \\ i & 0 & -i \\ -i & i & 0 \end{pmatrix}. \qquad (12.2.34)$$

We refer them to major NSI textures. They are combinations of some $\mathbb{T}_{mn}$, $\mathbb{T}_1 = \frac{1}{3}(2\mathbb{T}_{11} - \mathbb{T}_{21})$, $\mathbb{T}_2 = \frac{1}{3}(\mathbb{T}_{12} + \mathbb{T}_{22})$, $\mathbb{T}_3 = \frac{1}{\sqrt{3}}(\mathbb{T}_{13} + \mathbb{T}_{23})$, and $\mathbb{T}_4 = \frac{1}{\sqrt{3}}\mathbb{T}_{31}$. The rest NSI textures $\mathbb{T}_{12}$, $\mathbb{T}_{13}$, $\mathbb{T}_{32}$, $\mathbb{T}_{33}$ and their combinations are strongly constrained by current data. We do not expect that they have any detectable effects in the future neutrino oscillation experiments and regard them as minor NSI textures.

Major NSI textures realised in UV-complete A_4 models

We consider how to realise the major NSI textures in the renormalisable A_4 models and consider their experimental constraints. The following mathematical features of $\mathbb{T}_i$ will be helpful for our later discussion.

- $\mathbb{T}_i$ (for $i = 1, 2, 3, 4$) form the following "closed" algebras,

$$\begin{aligned} &\mathbb{T}_i^2 = \mathbb{T}_1\,, \quad \mathbb{T}_1\mathbb{T}_i = \mathbb{T}_i\,, \quad \mathbb{T}_2\mathbb{T}_3 = -i\mathbb{T}_4\,, \\ &\mathbb{T}_2\mathbb{T}_4 = i\mathbb{T}_3\,, \quad \mathbb{T}_3\mathbb{T}_4 = -i\mathbb{T}_2\,. \end{aligned} \tag{12.2.35}$$

- Given two 3×3 coupling matrices or mass matrices $M_1 = \alpha_0\mathbb{1} + \sum_{i=1}^4 \alpha_i\mathbb{T}_i$ and $M_2 = \beta_0\mathbb{1} + \sum_{i=1}^4 \beta_i\mathbb{T}_i$, their product M_1M_2 is a linear combination of $\mathbb{1}$ and $\mathbb{T}_i$,

$$\begin{aligned} M_1M_2 = \;& \alpha_0\beta_0\mathbb{1} + (\alpha_0\beta_1 + \alpha_1\beta_0 + \alpha_1\beta_1 + \alpha_2\beta_2 + \alpha_3\beta_3 + \alpha_4\beta_4)\mathbb{T}_1 \\ & +(\alpha_0\beta_2 + \alpha_2\beta_0 + \alpha_1\beta_2 + \alpha_2\beta_1 + i\alpha_4\beta_3 - i\alpha_3\beta_4)\mathbb{T}_2 \\ & +(\alpha_0\beta_3 + \alpha_3\beta_0 + \alpha_1\beta_3 + \alpha_3\beta_1 + i\alpha_2\beta_4 - i\alpha_4\beta_2)\mathbb{T}_3 \\ & +(\alpha_0\beta_4 + \alpha_4\beta_0 + \alpha_1\beta_4 + \alpha_4\beta_1 + i\alpha_3\beta_2 - i\alpha_2\beta_3)\mathbb{T}_4\,. \end{aligned} \tag{12.2.36}$$

- If M_1 is reversible, the inverse matrix M_1^{-1}

$$\begin{aligned} M_1^{-1} \;=\; & \frac{\alpha_0}{\det A}\left[\frac{\det A}{\alpha_0^2}\mathbb{1} + \left(\alpha_0 + \alpha_1 - \frac{\det A}{\alpha_0^2}\right)\mathbb{T}_1 \right. \\ & \left. -\alpha_2\mathbb{T}_2 - \alpha_3\mathbb{T}_3 - \alpha_4\mathbb{T}_4\right], \end{aligned} \tag{12.2.37}$$

  where $\det M_1 = \alpha_0(\alpha_0^2 + 2\alpha_0\alpha_1 + \alpha_1^2 - \alpha_2^2 - \alpha_3^2 - \alpha_4^2)$, is also a linear combination of $\mathbb{1}$ and $\mathbb{T}_i$.

By setting some of α_i or β_i to zero, the following corollaries are obtained:

- $\mathbb{1}$ and $\mathbb{T}_1$ form a closed algebra, if M_1, M_2 are linear combinations of $\mathbb{1}$ and $\mathbb{T}_1$, their product and inverse matrices (if reversible) are also linear combination of $\mathbb{1}$ and $\mathbb{T}_1$.

- $\mathbb{1}$, $\mathbb{T}_1$ and $\mathbb{T}_2$ form a closed algebra, if M_1, M_2 are linear combinations of $\mathbb{1}$, $\mathbb{T}_1$ and $\mathbb{T}_2$, their product and inverse matrices (if reversible) are also linear combination of $\mathbb{1}$, $\mathbb{T}_1$ and $\mathbb{T}_2$.

- $\mathbb{1}$, $\mathbb{T}_1$ and $\mathbb{T}_3$ form a closed algebra, if M_1, M_2 are linear combinations of $\mathbb{1}$, $\mathbb{T}_1$ and $\mathbb{T}_2$, their product and inverse matrices (if reversible) are also linear combination of $\mathbb{1}$, $\mathbb{T}_1$ and $\mathbb{T}_3$.

Before electroweak symmetry breaking, the operators $\mathcal{O}^{2-6}$ take the form as dimension-8 operator $(\overline{L}\tilde{H}\gamma^\mu\tilde{H}^\dagger L)(\overline{F}\gamma_\mu F)$. A popular way to realise large NSIs is introducing a vector boson Z'. Then, the 4-charged-fermion interaction $(\overline{F}\gamma^\mu F)(\overline{F}\gamma_\mu F)$ is unavoidable. In order to be consistent with experimental data, the coupling must be very small. Here, we will carefully avoid the 4-charged-fermion interactions newly introduced after the decouple of the new particles in the UV sector. Thus, interactions mediated by Z' will not be considered.

We focus on $\mathcal{O}^4$ by using a singly charged scalar ϕ and a neutral fermion N to realise major NSI textures. The renormalisable interactions are given by

$$\begin{aligned}\mathcal{L} &= (D_\mu\phi)^\dagger(D^\mu\phi) - (M_\phi^2)_{\alpha\beta}\phi_\alpha^*\phi_\beta + \overline{N}i\partial\!\!\!/ N - M_{N\alpha\beta}\overline{N_{\alpha\mathrm{R}}}N_{\beta\mathrm{L}} \\ &\quad -\kappa_{\alpha\beta\gamma}\overline{E_{\alpha\mathrm{R}}}N_{\beta\mathrm{L}}\phi_\gamma^* - y_{\alpha\beta}\overline{L_\alpha}\tilde{H}N_{\beta\mathrm{R}} + \mathrm{h.c.}\,, \qquad (12.2.38)\end{aligned}$$

where $D_\mu = \partial_\mu + ieA_\mu$. The charged scalar is a $SU(2)_\mathrm{L}$ singlet with $Y = -1$. In order to distinguish it from S in the last subsection, we denote it as ϕ. There is no lepton-number-violating (LNV) coupling in the above interactions. For the neutral fermion N, we require a vector-like mass term $M_N\overline{N_\mathrm{R}}N_\mathrm{L}$ as shown in the above. If there is an additional small LNV mass term $\mu\overline{N_\mathrm{L}^\mathrm{C}}N_\mathrm{L}$ and hierarchical masses $y/\sqrt{G_F} \ll M_N$, we recover the inverse seesaw model [127]. But here we do not specify if N is related to the origin of active neutrino masses. No matter whether there is a small LNV mass term, we can always arrive at a dimension-8 operator $\sim \frac{\kappa^2y^2}{M_\phi^2M_N^2}(\overline{L}\tilde{H}E_\mathrm{R})(\overline{E_\mathrm{R}}\tilde{H}^\dagger L)$ after the decouple of the charged scalar and

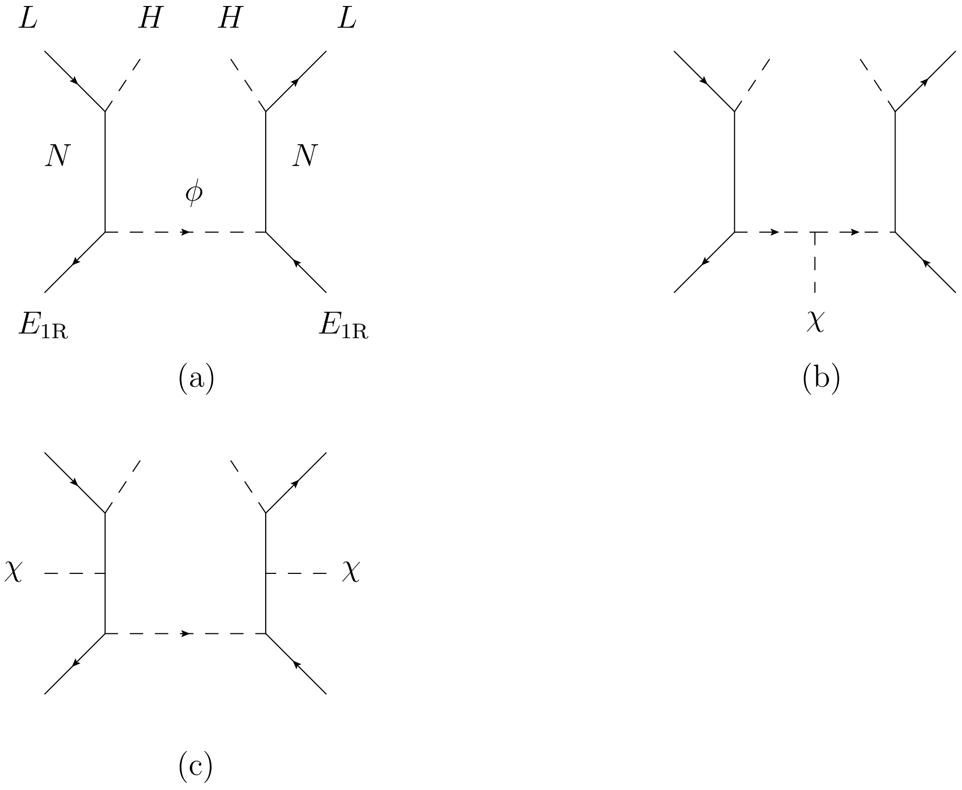

(a) (b) (c)

Figure 12.1: Diagrams to realise sizeable NSI textures corresponding to dimension-8 operator $\mathcal{O}^4$ in leptonic A_4 models.

sterile neutrinos, from which we obtain $\mathcal{O}^4$. Once the flavour structure is included, the 3×3 NSI parameter matrix ϵ^e is expressed as

$$\epsilon^e = \frac{1}{8G_F^2}(yM_N^{-1}\kappa_e)(M_\phi^2)^{-1}(yM_N^{-1}\kappa_e)^\dagger \,, \tag{12.2.39}$$

where κ_e is a 3×3 matrix defined via $(\kappa_\alpha)_{\beta\gamma} = \kappa_{\alpha\beta\gamma}$ for $\alpha = e, \mu, \tau$.

We will discuss how the A_4 symmetry can constrain NSIs in this renormalisable model. We first consider A_4-invariant NSI textures without the involvement of flavons. In the flavour space, since we have arranged $L \sim \mathbf{3}$, the fields N_L, N_R and ϕ must be triplets to ensure the invariance of Lagrangian in A_4. We follow the setup of most A_4 models that $E_{1\mathrm{R}}$ is fixed as a singlet $\mathbf{1}$ of A_4. An invariant mass term for the charged scalar can only take the form $\mu_\phi^2(\phi^*\phi)_\mathbf{1} = \mu_\phi^2 \sum_i \phi_i^*\phi_i$ with $\mu_\phi^2 > 0$, i.e., the charged scalar mass matrix $M_\phi^2 = \mu_\phi^2 \mathbb{1}$. Similarly, to be invariant under transformations of A_4, the Dirac mass matrix of the sterile neutrinos M_N and the Yukawa coupling between L and N_R, y is also proportional to an identity matrix, $M_N = \mu_N \mathbb{1}$, $y = y_0 \mathbb{1}$. The structures of the couplings y and κ depend on representations of $E_{\rm R}$. The interaction between involving ϕ and N are given by

$$\kappa_0 \overline{E_{1\rm R}} (N_{\rm L}\phi^*)_{\mathbf{1}} + y_0 (\overline{L}\tilde{H} N_{\rm R})_{\mathbf{1}} + \text{h.c.}\,. \tag{12.2.40}$$

Thus, both coupling matrices κ and y appear to be proportional to the identity matrix, $\kappa = \kappa_0 \mathbb{1}$, $y = y_0 \mathbb{1}$. After ϕ and N are integrated out from the Lagrangian, we obtain that the $\mathcal{O}^4$ takes the $(\overline{L}L)_{\mathbf{1}}(\overline{F}F)_{\mathbf{1}}$ form as listed in Table 12.1 for $F = E_{\rm R}$. Finally, we obtain the NSI texture is $\epsilon^e = \alpha_0 \mathbb{1}$, where

$$\alpha_0 = \frac{|y_0 \kappa_0|^2}{8 G_F^2 \mu_N^2 \mu_\phi^2}\,. \tag{12.2.41}$$

Since $\mathbb{1}$ is an identity matrix, ϵ^e in this special case has no observable signatures in neutrino oscillation experiments.

The involvement of χ breaks A_4 to Z_2 and modifies the correlation relations of NSI parameters. In order to realise relatively large and measurable NSI effects, we only consider the contribution of renormalisable couplings of χ. There are cases, as shown in Figure 12.1 (b) and (c), where χ couples to ϕ and N, modifying their mass matrices, respectively.

- The charged scalar ϕ mass matrix modified by the coupling between χ and ϕ. We add the following renormalisable coupling to the Lagrangian,

  $$\frac{\mu_\phi^2}{v_\chi}\left[\frac{2}{3} f_{\rm S} \Big(\chi (\phi^*\phi)_{\mathbf{3}_{\rm S}}\Big)_{\mathbf{1}} - \frac{2}{\sqrt{3}} f_{\rm A} \Big(\chi (\phi^*\phi)_{\mathbf{3}_{\rm A}}\Big)_{\mathbf{1}}\right], \tag{12.2.42}$$

  where $f_{\rm S}$ and $f_{\rm A}$ are real dimensionless coefficients as required by the Hermiticity of the Lagrangian. The relevant higher-dimensional operators after ϕ and N integrated out take the forms as $\chi(\overline{L}L)_{\mathbf{3}_{\rm S}}(\overline{F}F)_{\mathbf{1}}$ and $\chi(\overline{L}L)_{\mathbf{3}_{\rm A}}(\overline{F}F)_{\mathbf{1}}$, respectively. The modified ϕ mass matrix turns out to be

  $$M_\phi^2 / \mu_\phi^2 = \mathbb{1} + f_{\rm S} \mathbb{T}_2 + f_{\rm A} \mathbb{T}_3\,. \tag{12.2.43}$$

  Terms such as $\big((\chi\chi)_{\mathbf{3}_{\rm S}} (\phi^*\phi)_{\mathbf{3}_{\rm S}}\big)_{\mathbf{1}}$, $\big((\chi\chi)_{\mathbf{3}_{\rm S}} (\phi^*\phi)_{\mathbf{3}_{\rm A}}\big)_{\mathbf{1}}$ are also renormalisable and should be considered for completeness. These terms will not induce new structures different from Eq. (12.2.43).

- The Dirac mass matrix of N is modified by couplings between χ and N. The related renormalisable Lagrangian term is given by

$$\frac{\mu_N}{v_\chi}\left[\frac{2}{3}g_{\rm S}\big(\chi(\overline{N_{\rm L}}N_{\rm R})_{\mathbf{3}_{\rm S}}\big)_{\mathbf{1}} - \frac{2}{\sqrt{3}}g_{\rm A}\big(\chi(\overline{N_{\rm L}}N_{\rm R})_{\mathbf{3}_{\rm A}}\big)_{\mathbf{1}}\right] + {\rm h.c.}\,, \qquad (12.2.44)$$

  where $g_{\rm S}$ and $g_{\rm A}$ are in general complex parameters. Dirac mass matrix M_N is modified to

$$M_N/\mu_N = \mathbb{1} + g_{\rm S}\mathbb{T}_2 + g_{\rm A}\mathbb{T}_3\,. \qquad (12.2.45)$$

Taking the flavon-modified mass matrices of ϕ and N into account, we state that the final detectable (i.e., ignoring the undetectable $\mathbb{1}$) NSI matrix ϵ^e in Eq. (12.2.39) is always a linear combination of $\mathbb{T}_i$ for $i = 1, 2, 3, 4$. This is guaranteed by the algebra of $\mathbb{T}_i$ and can be straightforwardly proven by implying Eqs. (12.2.36) and (12.2.37). From Table 12.1, one can expect that the textures $\mathbb{T}_2 \propto \mathbb{T}_{12} + \mathbb{T}_{22}$ and $\mathbb{T}_3 \propto \mathbb{T}_{13}+\mathbb{T}_{23}$ will be predicted. The other two textures, $\mathbb{T}_1 \propto 2\mathbb{1}-\mathbb{T}_{21}$ and $\mathbb{T}_4 \propto \mathbb{T}_{31}$, which are not predicted from higher-dimensional operators, are obtained from the inverse transformations of M_ϕ^2 and M_N, and matrix product $\mathbb{T}_2\mathbb{T}_3 = -i\mathbb{T}_4$. $\mathbb{T}_1$ and $\mathbb{T}_4$ appear at the second order of $f_{\rm S}, f_{\rm A}$ and $g_{\rm S}, g_{\rm A}$. If $f_{\rm S}, f_{\rm A}, g_{\rm S}, g_{\rm A} \ll 1$ is satisfied, the $\mathbb{T}_1$ and $\mathbb{T}_4$ parts are negligible compared with the $\mathbb{T}_2$ and $\mathbb{T}_3$ parts. However, these coefficients, as coefficients of renormalisable terms, may take $\mathcal{O}(1)$ values, and thus in this case, $\mathbb{T}_1$ and $\mathbb{T}_4$ may have comparable NSI effects to $\mathbb{T}_2$ and $\mathbb{T}_3$.

Taken the $A_4 \to Z_2$ effect into account, the flavour structures of NSIs can be further simplified in the following scenarios:

- With the assumption of additional symmetries, χ may only couples to χ, not to N, i.e., $g_{\rm A}, g_{\rm S} = 0$. The resulted detectable NSI matrix is explicitly expressed as

$$\epsilon^e = \alpha_0\left[(f_{\rm S}^2 + f_{\rm A}^2)\mathbb{T}_1 - f_{\rm S}\mathbb{T}_2 - f_{\rm A}\mathbb{T}_3\right]\,. \qquad (12.2.46)$$

  Here, only $\mathbb{T}_1$, $\mathbb{T}_2$ and $\mathbb{T}_3$ appear, and α_0 has been redefined.

- On the other hand, if χ only couple to N, we obtain the following NSI matrix

$$\begin{aligned}\epsilon^e \;=\; \alpha_0\big\{\big[& -(2+|g_{\rm S}|^2+|g_{\rm A}|^2)(|g_{\rm S}|^2+|g_{\rm A}|^2) + 4{\rm Re}(g_{\rm S}^2+g_{\rm A}^2) + 4[{\rm Im}(g_{\rm S}^* g_{\rm A})]^2\big]\mathbb{T}_1 \\ & -2{\rm Re}(g_{\rm S})\mathbb{T}_2 - 2{\rm Re}(g_{\rm A})\mathbb{T}_3 - 2{\rm Im}(g_{\rm S}^* g_{\rm A})\mathbb{T}_4\big\}\,. \qquad (12.2.47)\end{aligned}$$

where α_0 has been redefined. It is a linear combination of all four $\mathbb{T}_i$, but $\mathbb{T}_4$ is important only if both $|g_\mathrm{S}|$ and $|g_\mathrm{A}|$ are sizeable and there is a relative phase between g_S and g_A.

- If the anti-symmetric couplings f_A and g_A are forbidden, the NSI matrix can be simplified to a linear combination of $\mathbb{T}_1$ and $\mathbb{T}_2$. On the contrary, if the symmetric couplings f_S and g_S are forbidden, the NSI matrix is a linear combination of $\mathbb{T}_1$ and $\mathbb{T}_3$. These two cases are valid if the flavour symmetry A_4 is replaced by S_4. In S_4, there are two triplet irreducible representations, and the symmetric and anti-symmetric products $\mathbf{3}_\mathrm{S}$ and $\mathbf{3}_\mathrm{A}$ corresponds to two different representations. By arranging χ to be one of the triplets, the anti-symmetric (or symmetric) products can be forbidden, and thus only the symmetric (or anti-symmetric) couplings are left.

Naively, one may expect that NSIs from the UV completion of the dimension-8 operator is more constrained than that of the dimension-6 operator, but this is not the case in the framework of the flavour symmetry. As required, no tree-level 4-charged-fermion interactions have been introduced from the Lagrangian in Eq. (12.2.38). The coupling $\overline{E_\mathrm{R}} N_\mathrm{L} \phi$ can directly contribute to some radiative CLFV processes via involving the sterile neutrino and charged scalar in the loop. Besides, the coupling $\overline{E_\mathrm{R}} \nu_\mathrm{L} \phi$ resulted from neutrino kinetic mixing can also induce the radiative decays and 3-body decays at one loop level. All these contributions rely on the coupling with the second or third charged lepton $E_{2\mathrm{R}}$ or $E_{3\mathrm{R}}$. Since $E_{1\mathrm{R}}$, $E_{2\mathrm{R}}$ and $E_{3\mathrm{R}}$ are arranged as different singlets of A_4, the relevant coefficients are theoretically independent of those involving in matter NSIs [128, 129]. As a result, this model does not transport the tight constraint from CLFV results to NSIs, by simply turning off the couplings for the second and third generations with the sterile neutrino, $\kappa_{2\beta\gamma} = \kappa_{3\beta\gamma} = 0$. At colliders, the charged scalar ϕ can be produced through the electroweak associated pair production $e^+e^- \to \gamma^*/Z^* \to \phi\bar{\phi}$, and ϕ decays to a charged lepton and an active neutrino, where the active neutrino is generated via the Yukawa coupling with N and appears as the missing energy. LEP shows that a charged scalar with mass < 80 GeV has been excluded, based on a combined analysis with ϕ decaying to lepton pair and quark pair included [130]. At LHC, the search strategy is similar to studies of direct pair production of sleptons and the mass range between 90 GeV to 325 GeV has been excluded at 95% CL [131]. Fortunately, these constraints can be safely avoided since the charged scalar required in the UV completion here specifies the coupling with the first generation of charged lepton. With a careful treatment of ϕ decaying e plus missing transverse momentum or τ plus missing transverse momentum, the authors in [132] demonstrate that the existing LEP and LHC constraints do not exclude a singlet charged scalar as light as 65 GeV.

The main constraint in this model is the bound of the non-unitarity of the lepton mixing. The decouple of sterile neutrinos contributes to the active neutrino kinetic mixing as $\frac{y^2}{M_N^2}(\overline{L}\tilde{H})\partial\!\!\!/(\tilde{H}^\dagger L)$. After rescaling the kinetic terms of active neutrinos, non-unitarity of the PMNS matrix is

$$\eta \equiv V^\dagger_{\rm PMNS} V_{\rm PMNS} - \mathbf{1} = \frac{1}{2\sqrt{2}G_F}(yM_N^{-1})(yM_N^{-1})^\dagger \,. \tag{12.2.48}$$

The non-unitarity bound from a global analysis of LFV decays, probes of the universality of weak interactions, CKM unitarity bounds and electroweak precision data is around $\eta \sim 10^{-3}$ [120]. Combining with the above constraints, we see that it is still possible to achieve the major NSI textures with coefficients $\sim \eta/(G_F M_\phi^2)$ at 10^{-2} or 10^{-3} level. These values may be potentially measured by the next-generation accelerator neutrino oscillation experiments.

In the above, we have constructed UV-complete models for $\mathcal{O}^4$ and $\chi\mathcal{O}^4$. A similar discussion can be directly extended to the $\mathcal{O}^{2,3,5}$ and $\chi\mathcal{O}^{2,3,5}$ series by replacing the singly-charged scalar ϕ by $\phi_{U_{\rm R},D_{\rm R},Q}$ which are $SU(2)_{\rm L}$ gauge singlet, single and doublet with hypercharge $Y = -2/3, +1/3$ and $-1/6$, respectively, and replacing the singlet $F = E_{1\rm R}$ with $F = U_{1\rm R}$, $D_{1\rm R}$ and Q_1, respectively. The resulted NSI matrix is also a linear combination of the textures $\mathbb{T}_1$, $\mathbb{T}_2$, $\mathbb{T}_3$ and $\mathbb{T}_4$. The textures $\mathbb{T}_1$, $\mathbb{T}_2$, $\mathbb{T}_3$ and $\mathbb{T}_4$ are obtained by assuming the charged fermion as singlets of A_4. This treatment can avoid strong constraints from the second- and third-generation charged fermions. These textures are less constrained than the other textures discussed below and thus, we call them major NSI textures.

Minor NSI textures realised in UV-complete A_4 models

The minor NSI textures $\mathbb{T}_{12}$, $\mathbb{T}_{13}$, $\mathbb{T}_{32}$, $\mathbb{T}_{33}$ and their combinations cannot be realised in the above arrangements. This is compatible with Table 12.1, where the minor textures are obtained by setting $F \sim \mathbf{3}$. To achieve these textures, as shown in Table 12.1, F has to be assumed to be a triplet of A_4. Then F cannot be chosen as right-handed charged leptons and cannot be realised in the $\mathcal{O}^4$ and $\chi\mathcal{O}^4$ series. We will discuss how to realise them in UV-complete A_4 models as a complement.

To realise the A_4-invariant $\mathbb{T}_{12}$ and $\mathbb{T}_{13}$, we choose $F = U_{\rm R} \equiv (U_{1{\rm R}}, U_{2{\rm R}}, U_{3{\rm R}})^T \sim \mathbf{3}$ of A_4 and consider the UV completion of $\mathcal{O}^2$. The latter is obtained by replacing the singly charged scalar ϕ with a fractionally charged scalar $\phi_{U_{\rm R}}$, i.e., a scalar leptoquark, with the hypercharge $Y = -2/3$, and coupling to $N_{\rm L}$ and $U_{\rm R}$. The renormalisable couplings are given by

$$\kappa_{\rm S}^{U_{\rm R}}((\overline{U_{\rm R}}N_{\rm L})_{\mathbf{3}_{\rm S}}\phi_{U_{\rm R}}^*)_{\mathbf{1}} + \kappa_{\rm A}^{U_{\rm R}}((\overline{U_{\rm R}}N_{\rm L})_{\mathbf{3}_{\rm A}}\phi_{U_{\rm R}}^*)_{\mathbf{1}} + \text{h.c.}\,. \tag{12.2.49}$$

Then, coupling matrix κ is modified to $\kappa_{U_{\rm R}} = \kappa_{\rm S}^{U_{\rm R}}\mathbb{T}_{12} + \kappa_{\rm A}^{U_{\rm R}}\mathbb{T}_{13}$ and the A_4-preserved NSI texture

$$\epsilon^u \equiv \frac{1}{8G_F^2}(yM_N^{-1}\kappa_{U_{\rm R}})(M_{\phi_{U_{\rm R}}}^2)^{-1}(yM_N^{-1}\kappa_{U_{\rm R}})^\dagger \tag{12.2.50}$$

is obtained as a linear combination of $\mathbb{T}_{12}$ and $\mathbb{T}_{13}$. Finally, we include the A_4-breaking effect in the $\phi_{U_{\rm R}}$ and N mass matrices, as in Eqs. (12.2.43) and (12.2.45). Non-zero $\mathbb{T}_{32}$ and $\mathbb{T}_{33}$ can be extracted out in principle.

The minor textures $\mathbb{T}_{12}$, $\mathbb{T}_{13}$, $\mathbb{T}_{32}$ and $\mathbb{T}_{33}$ are expected to receive stronger constraints. The main reason is that $U_{\rm R} = (U_{1{\rm R}}, U_{2{\rm R}}, U_{3{\rm R}})$ is arranged as a triplet of A_4 and constraints from the second- and third- generation charged fermions should be included. The neutrino kinetic mixing leads to coupling $\overline{U_{\rm R}}\nu_{\rm L}\phi_{U_{\rm R}}^*$. It further modifies processes, e.g., (semi-)leptonic decays $U_\alpha \to U_\beta\nu\overline{\nu}$ at tree level, radiative decays $U_\alpha \to U_\beta\gamma\gamma$ at loop level and FCNC processes $U_\alpha \to U_\beta\overline{U_\gamma}U_\delta$ at loop level, from their SM predictions. As a consequence, precision measurements of charm mesons and baryons can give strong constraints to ϵ^u. A detailed discussion of these constraints is not our subject in this paper. Realisations of sizeable NSI textures $\mathbb{T}_{12}$, $\mathbb{T}_{13}$, $\mathbb{T}_{32}$ and $\mathbb{T}_{33}$ via UV completions of the other dimension-8 operators are also hard. Those via $\mathcal{O}^{3,5,7,8}$ gain strong constraints from K and B decays, and those via $\mathcal{O}^{6}$ gain constraints from $E_\alpha \to E_\beta\gamma$ decays again. Since it is hard to generate sizeable NSI for textures $\mathbb{T}_{12}$, $\mathbb{T}_{13}$, $\mathbb{T}_{32}$, $\mathbb{T}_{33}$ or their combinations, we refer them to minor NSI textures.

	Representations	A_4-invariant operators	NSI textures
$\mathcal{O}^1$	$L \sim \mathbf{3}$	$(\overline{L}L)_{\mathbf{1}}(\overline{L}L)_{\mathbf{1}}$, $(\overline{L}L)_{\mathbf{1'}}(\overline{L}L)_{\mathbf{1''}}$, $(\overline{L}L)_{\mathbf{3}_\mathrm{S}}(\overline{L}L)_{\mathbf{3}_\mathrm{S}}$, $(\overline{L}L)_{\mathbf{3}_\mathrm{A}}(\overline{L}L)_{\mathbf{3}_\mathrm{A}}$	$2\mathbb{T}_{11} - \mathbb{T}_{12}$
$\mathcal{O}^{2-8}$	$L \sim \mathbf{3}, F \sim \mathbf{1}, \mathbf{1'}, \mathbf{1''}, \mathbf{3}$	$(\overline{L}L)_{\mathbf{1}}(\overline{F}F)_{\mathbf{1}}$	$\mathbb{T}_{11}$
	$L \sim \mathbf{3}, F \sim \mathbf{3}$	$(\overline{L}L)_{\mathbf{3}_\mathrm{S}}(\overline{F}F)_{\mathbf{3}_\mathrm{S}}$	$\mathbb{T}_{12}$
		$(\overline{L}L)_{\mathbf{3}_\mathrm{A}}(\overline{F}F)_{\mathbf{3}_\mathrm{S}}$	$\mathbb{T}_{13}$

	Representations	Z_2-invariant operators	NSI textures
$\chi\mathcal{O}^1$	$\chi \sim \mathbf{3}, L \sim \mathbf{3}$	$\chi\big((\overline{L}L)_{\mathbf{3}_\mathrm{S}}(\overline{L}L)_{\mathbf{1},\mathbf{1'},\mathbf{1''}}\big)_{\mathbf{3}}$, $\chi\big((\overline{L}L)_{\mathbf{3}_\mathrm{S}}(\overline{L}L)_{\mathbf{3}_\mathrm{S}}\big)_{\mathbf{3}_\mathrm{S}}$, $\chi\big((\overline{L}L)_{\mathbf{3}_\mathrm{A}}(\overline{L}L)_{\mathbf{3}_\mathrm{A}}\big)_{\mathbf{3}_\mathrm{S}}$	$\frac{1}{3}(2\mathbb{T}_{11}-\mathbb{T}_{12}$ $+2\mathbb{T}_{21}+2\mathbb{T}_{23})$
		$\chi\big((\overline{L}L)_{\mathbf{3}_\mathrm{A}}(\overline{L}L)_{\mathbf{1},\mathbf{1'},\mathbf{1''}}\big)_{\mathbf{3}}$, $\chi\big((\overline{L}L)_{\mathbf{3}_\mathrm{S}}(\overline{L}L)_{\mathbf{3}_\mathrm{A}}\big)_{\mathbf{3}_\mathrm{S}}$	$\mathbb{T}_{13}$
$\chi\mathcal{O}^{2-8}$	$\chi \sim \mathbf{3}, L \sim \mathbf{3}, F \sim \mathbf{1}, \mathbf{1'}, \mathbf{1''}, \mathbf{3}$	$\chi(\overline{L}L)_{\mathbf{3}_\mathrm{S}}(\overline{F}F)_{\mathbf{1}}$	$\mathbb{T}_{12} + \mathbb{T}_{22}$
		$\chi(\overline{L}L)_{\mathbf{3}_\mathrm{A}}(\overline{F}F)_{\mathbf{1}}$	$\mathbb{T}_{13} + \mathbb{T}_{23}$
	$\chi \sim \mathbf{3}, L \sim \mathbf{3}, F \sim \mathbf{3}$	$\chi\big((\overline{L}L)_{\mathbf{3}_\mathrm{S}}(\overline{F}F)_{\mathbf{3}_\mathrm{S}}\big)_{\mathbf{3}_\mathrm{S}}$	$2\mathbb{T}_{12} - \mathbb{T}_{22}$
		$\chi\big((\overline{L}L)_{\mathbf{3}_\mathrm{A}}(\overline{F}F)_{\mathbf{3}_\mathrm{S}}\big)_{\mathbf{3}_\mathrm{S}}$	$2\mathbb{T}_{13} - \mathbb{T}_{23}$
		$\chi\big((\overline{L}L)_{\mathbf{3}_\mathrm{S}}(\overline{F}F)_{\mathbf{3}_\mathrm{S}}\big)_{\mathbf{3}_\mathrm{A}}$	$\mathbb{T}_{32}$
		$\chi\big((\overline{L}L)_{\mathbf{3}_\mathrm{A}}(\overline{F}F)_{\mathbf{3}_\mathrm{S}}\big)_{\mathbf{3}_\mathrm{A}}$	$\mathbb{T}_{33}$

Table 12.1: NSI Textures in matter predicted by A_4 and the residual symmetry Z_2, where F represents any SM fermions. The textures $\mathbb{T}_{1n}$ are defined in Eq. (12.1.4), $\mathbb{T}_{2n}$ and $\mathbb{T}_{3n}$ are defined in Eq. (12.1.16), and χ is defined in Eq. (12.1.13).

Chapter 13

Testing NSI textures at LBL experiments

The long baseline experiment with the wide-band beam and sizeable matter effects is expected to measure more than one $\epsilon_{\alpha\beta}$, which implies that the flavour dependence of NSIs ϵ^{m} can be inspected. As a result, an experiment of this kind is possible to study the flavour symmetry model through the operators $\mathcal{O}^{1-8}$. In this section we will study the matter NSI effects for DUNE experiment under the flavour symmetry A_4 or Z_2. NSI textures $\mathbb{T}_{mn}$ can be tested in future LBL experiments. From Sec. 12.2, we summarise the connection of texture parameters α_{mn} to the conventional parameters $\epsilon_{\alpha\beta}$ in Table 13.1. In App. D, we do not just only show the approximation equations to oscillation probabilities with NSI matter effects, but also demonstrate the leading-order coefficients of each α_{mn}, presenting in oscillation approximation equations, according to this table.

The current global fit for matter-effect NSIs [39] includes solar, atmospherical, reactor and LBL neutrino data. With the assumption that all NSIs coming entirely from up or down quarks to avoid NSIs at the source and the detector, the current global fit to standard NSI parameters $\epsilon^{u}_{\alpha\beta}$ and $\epsilon^{d}_{\alpha\beta}$ has been performed in [39], respectively. We adopt these results to estimate the bounds for $\alpha^{u,d}_{mn}$. We only take the bound for each $\epsilon^{u,d}_{\alpha\beta}$, i.e., the results of 1-D projection. Furthermore, we neglect underlying corrections among any two or more than two parameters, which are $\epsilon_{\alpha\beta}$, or mixing angles, mass square splittings. Assuming Gaussian distributions, taken

$\tilde{\epsilon}_{ee}(\equiv \epsilon_{ee} - \epsilon_{\mu\mu})$	$3\alpha_{12}/\sqrt{6} - \alpha_{13}/\sqrt{2}$
$\tilde{\epsilon}_{\tau\tau}(\equiv \epsilon_{\tau\tau} - \epsilon_{\mu\mu})$	$-2\alpha_{13}/\sqrt{2}$
$\epsilon_{e\mu}$	$\alpha_{21}/\sqrt{6} - \alpha_{22}/\sqrt{12} - \alpha_{23}/2 + i\left(-\alpha_{31}/\sqrt{6} + \alpha_{32}/\sqrt{12} + \alpha_{33}/2\right)$
$\epsilon_{e\tau}$	$\alpha_{21}/\sqrt{6} - \alpha_{22}/\sqrt{12} + \alpha_{23}/2 + i\left(\alpha_{31}/\sqrt{6} - \alpha_{32}/\sqrt{12} + \alpha_{33}/2\right)$
$\epsilon_{\mu\tau}$	$\alpha_{21}/\sqrt{6} + 2\alpha_{22}/\sqrt{12} + i\left(-\alpha_{31}/\sqrt{6} - \alpha_{32}/\sqrt{12}\right)$

Table 13.1: Expressions of conventional parameters $\epsilon_{\alpha\beta}$ in terms of texture parameters α_{mn} according to Eqs. (12.1.4), (12.1.16), (12.1.26).

90% C.L. limits from [39], bounds on $\epsilon^{u,d}_{\alpha\beta}$ at 1σ are shown in Table 13.2. Since in their analysis the imaginary part is assumed to be 0 or π, we directly translate their bounds for $\alpha^{u,d}_{1n}$ and $\alpha^{u,d}_{2n}$ by setting the imaginary $\alpha^{u,d}_{3n} = 0$, and the results are shown in Table 13.3. NSIs with down quarks $\epsilon^{u,d}_{\alpha\beta}$ have very similar constraints as those for $\epsilon^{u}_{\alpha\beta}$. As we neglect some correlations among parameters, our results can be viewed to be optimal. In Table 13.3, we see that most parameters are constrained around or below the a-few-percent level of weak interactions, except for $\alpha^{u,d}_{12}$, for which 1σ bounds are around 15%.

1σ bounds of global fit results			
$\tilde{\epsilon}^u_{ee}$	$[0.188, 0.376]$	$\tilde{\epsilon}^d_{ee}$	$[0.203, 0.384]$
$\tilde{\epsilon}^u_{\tau\tau}$	$[-0.003, 0.012]$	$\tilde{\epsilon}^d_{\tau\tau}$	$[-0.003, 0.012]$
$\epsilon^u_{e\mu}$	$[-0.046, 0.002]$	$\epsilon^d_{e\mu}$	$[-0.048, 0]$
$\epsilon^u_{e\tau}$	$[-0.038, 0.065]$	$\epsilon^d_{e\tau}$	$[-0.036, 0.066]$
$\epsilon^u_{\mu\tau}$	$[-0.004, 0.003]$	$\epsilon^d_{\mu\tau}$	$[-0.004, 0.003]$

Table 13.2: Taken from the current global fit results [39] for $\epsilon^u_{\alpha\beta}$ and $\epsilon^d_{\alpha\beta}$. In these results, the authors assume that off-diagonal elements $\epsilon_{\alpha\neq\beta}$ are real, consider that NSIs is only contributed by u (d) quarks for $\epsilon^u_{\alpha\beta}$ ($\epsilon^d_{\alpha\beta}$), but do not include NSIs at the source and the detector.

In this chapter, we firstly discuss how matter-effect NSIs α_{mn} affect neutrino oscillations in DUNE and then, study the physics capacity for DUNE to test A_4 symmetry and Z_2 residual symmetry via the NSI measurement.

1σ bounds by global fit results			
α^u_{12}	$[0.089, 0.247]$	α^d_{12}	$[0.099, 0.26]$
α^u_{13}	$[-0.003, 0.007]$	α^d_{13}	$[-0.003, 0.007]$
α^u_{21}	$[-0.045, 0.049]$	α^d_{21}	$[-0.045, 0.047]$
α^u_{22}	$[-0.037, 0.03]$	α^d_{22}	$[-0.035, 0.0302]$
α^u_{23}	$[-0.019, 0.096]$	α^d_{23}	$[-0.0154, 0.096]$

Table 13.3: The 1σ bounds for α^u_{12} (α^d_{12}), α^u_{13} (α^d_{13}) and α^u_{2i} (α^d_{2i}), with fixed $\alpha^u_{3i} = 0$ ($\alpha^d_{3i} = 0$), by global fit results [39] shown in Table 13.2. More details can be seen in the text.

13.1 Oscillation probabilities in DUNE

As mentioned in the introduction, matter-effect NSIs in DUNE have been widely discussed. Because of the propagation in such long distance of neutrino in the earth, and also due to the high-energy neutrino beam, matter effects play a substantial role. Before discussing its physics potential for any flavour symmetries, we firstly study the impact of α_{mn} on the oscillation probability for DUNE.

We show oscillation probabilities with one nonzero α_{mn}, $P(\nu_\alpha \to \nu_\beta)$, and the differences from those without NSIs, $\delta P_{\mathrm{NSI}}(\nu_\alpha \to \nu_\beta) \equiv P(\nu_\alpha \to \nu_\beta) - P_0(\nu_\alpha \to \nu_\beta)$ in Figs. 13.1–13.3. While the curve labeled by “w/o NSI” corresponds to oscillation probabilities without NSI effects, those labeled by $\mathbb{T}_{mn}$ corresponds to the coefficient α_{mn} fixed at 0.1 and all the other NSI parameters are fixed at zeros. In Figs. 13.1 and 13.2, the Dirac phase $\delta = 270^\circ$ and the normal mass ordering are assumed, while in Fig. 13.3 δ is set to be 0. Changing the δ value does not significantly affect the result for disappearance channels, so we do not show disappearance channels for $\delta = 0$.

In Fig. 13.1, we observe the oscillation behaviour of δP_{NSI} in L/E in disappearance channels, and except for α_{13} it goes to 0 at the 1st and 2nd minimums. The wide-band beam feature of DUNE provides more information about how α_{mn} affects on the disappearance channels. Further, it is obvious that the disappearance channels can be sensitive to α_{21} and α_{22} as their impacts δP_{NSI} are significantly larger

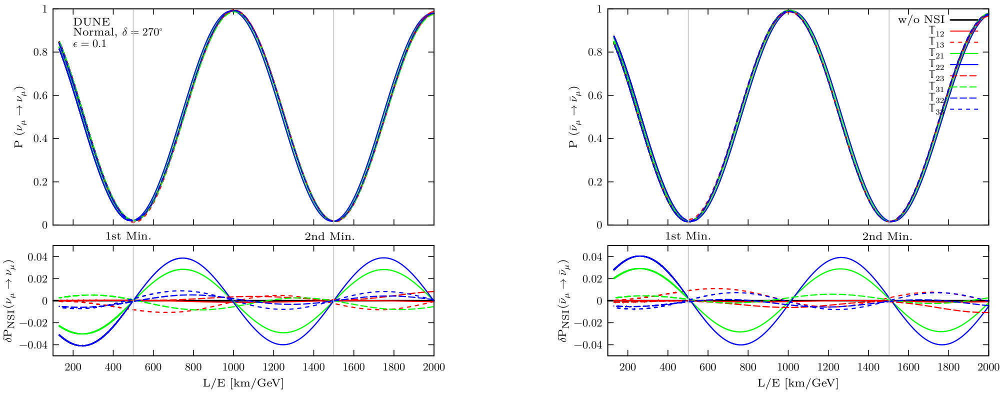

Figure 13.1: Oscillation probabilities $P(\nu_\mu(\bar{\nu}_\mu) \to \nu_\mu(\bar{\nu}_\mu))$ (left) and $\delta P_{\rm NSI}(\nu_\mu(\bar{\nu}_\mu) \to \nu_\mu(\bar{\nu}_\mu))$ (right) against L/E [km/GeV] for the case without NSIs and those with one nonzero α_{mn}. The left and right panels show ν and $\bar{\nu}$ modes, respectively. The oscillation parameters are used the current global fit results [2] (shown in Table 2.3) for the normal ordering with $\delta = 0$, and the oscillation baseline is considered 1300 km.

than the others. An interesting feature is that disappearance channels for neutrino and antineutrino modes look similar, but $\delta P_{\rm NSI}$ behaves oppositely, i.e. $\delta P_{\rm NSI}(\nu_\mu \to \nu_\mu) = -\delta P_{\rm NSI}(\bar{\nu}_\mu \to \bar{\nu}_\mu)$. This is because $P(\nu_\mu \to \nu_\mu; \delta, A) = P(\bar{\nu}_\mu \to \bar{\nu}_\mu; -\delta, -A)$, and also due to the fact that the contribution of α_{mn} is proportional to A in the disappearance channel.

For appearance channels in Figs. 13.2 and 13.3, we see that the NSI parameters non-trivially modify the oscillation probability for $\delta = 270°$ and $\delta = 0$ respectively. They both change the amplitude of oscillation probability and distort the oscillation behaviour against L/E. α_{22}, α_{31} and α_{32} (α_{21}, α_{22}, α_{31} and α_{32}) have larger imparts on $\delta P_{\rm NSI}$ than the other NSI parameters, and $\delta P_{\rm NSI}$ around the 1st maximum reaches up to or over 0.01 for the neutrino mode, for $\delta = 270°$ ($\delta = 0$). Besides, these impacts are slightly larger in the neutrino mode than the antineutrino mode, and this is due to our assumption of the normal mass ordering. DUNE with the wide-band beam reads the variation of $\delta P_{\rm NSI}$ over the 1st maximum. As a result, the sophisticated behaviour in the appearance channel over the 1st maximum plays a role of distinguishing different textures. Furthermore, we cannot ignore the influence of δ in the appearance channel due to the dependence of $\delta P_{\rm NSI}$ on δ, as analytically

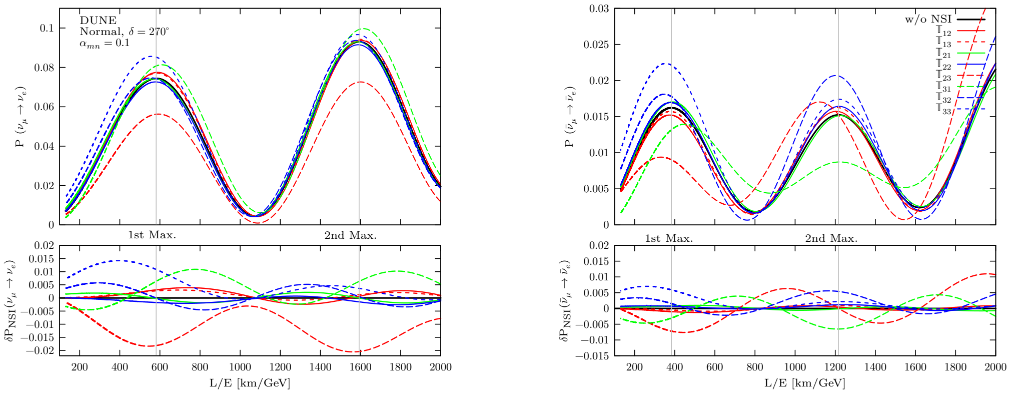

Figure 13.2: Oscillation probabilities $P(\nu_\mu(\bar{\nu}_\mu) \to \nu_e(\bar{\nu}_e))$ (upper) and $\delta P_{\rm NSI}(\nu_\mu(\bar{\nu}_\mu) \to \nu_e(\bar{\nu}_e))$ (lower) against L/E [km/GeV] for the case without NSIs and those with one nonzero α_{mn}. The left and right panels show ν and $\overline{\nu}$ modes, respectively. The oscillation parameters are used the current global fit results [2] (shown in Table 2.3) for the normal ordering with $\delta = 270^\circ$, and the oscillation baseline is considered 1300 km.

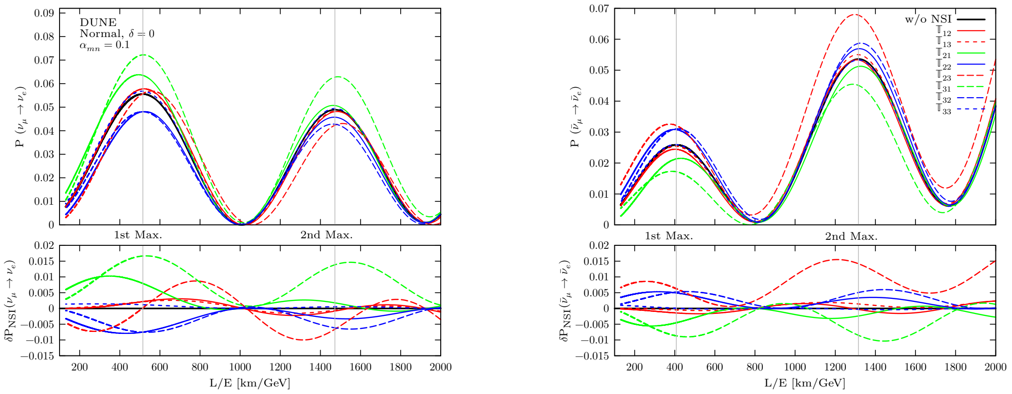

Figure 13.3: Oscillation probabilities $P(\nu_\mu(\bar{\nu}_\mu) \to \nu_e(\bar{\nu}_e))$ (upper) and $\delta P_{\rm NSI}(\nu_\mu(\bar{\nu}_\mu) \to \nu_e(\bar{\nu}_e))$ (lower) against L/E [km/GeV] for the case without NSIs and those with one nonzero α_{mn}. The left and right panels show ν and $\overline{\nu}$ modes, respectively. The oscillation parameters are used the current global fit results [2] (shown in Table 2.3) for the normal ordering with $\delta = 0$, and the oscillation baseline is considered 1300 km.

shown in Eq. (D.0.2) in Appendix D. It implies that the precise measurement of δ plays an important role of distinguishing textures.

We conclude that the wide-band-beam feature of DUNE is an advantage to detect NSI textures. Different NSI textures result in different distortions of the probabilities in the disappearance channel. Therefore, we can distinguish different textures by reading out the variation of $P(\nu_\mu \to \nu_e)$ along energy.

13.2 Testing “A_4 symmetry” in DUNE

NSIs from A_4 invariant operators only allow diagonal entries. After the breaking of A_4 by the Z_2-preserving flavon VEV χ, textures $\mathbb{T}_{2n}$, $\mathbb{T}_{3n}$, or their linear combinations is involved in the NSI matrix $\epsilon^{\rm m}$. Eqs. (D.0.1) and (D.0.2) indicate us that accelerator LBL experiments can be sensitive to off-diagonal terms in $\epsilon^{\rm m}$, as $\epsilon_{\mu\tau}$ and $\epsilon_{e\mu}$, $\epsilon_{e\tau}$ are the leading terms in the disappearance and appearance channels, respectively. As a result, experiments of this kind can test the conservation of A_4 symmetry. Reversely, A_4-symmetry conservation could provide an explain for undiscover of flavour-transition NSIs in matter.

Through out the study in this section, we adopt General Long Baseline Experiment Simulator (GLoBES) library [48, 49]. To simulate probabilities with matter-effect NSIs, we modify the default probability engine of GLoBES, by simply adding the matrix $A\epsilon^{\rm m}$ in the Hamiltonian. For the simulation for DUNE, we implement the simulation package in Ref. [52], with run time fixed by 7 years total (corresponding to 300 MW×kton×years) and 2-horn optimised beam design with 80 GeV protons. The other sets for oscillation parameters are described in Tab. 2.3.

We study the capacity for DUNE to rule out the “A_4 symmetry” hypothesis. The statistics quantity that we study is

$$\Delta\chi^2_{A_4} \equiv \chi^2\big|_{\alpha_{2n}=\alpha_{3n}=0} - \chi^2_{b.f.}, \tag{13.2.1}$$

where $\chi^2|_{\alpha_{2n}=\alpha_{3n}=0}$ is the χ^2 value with the assumption of $\alpha_{2n} = \alpha_{3n} = 0$ ($n = 1, 2, 3$), and $\chi^2_{b.f.}$ is the χ^2 value for the best fit. The central values and widths of the priors for the standard oscillation parameters, which are assumed Gaussian, are respectively used the best fit and 1σ width of NuFit results, and are given in Tab. 2.3. The value of $\chi^2_{b.f.}$ is always 0, as the best fit is exactly the true value. In the following results, we allow α_{12} and α_{13} to be free to vary. While varying the true value for one of $\{\alpha_{21}, \alpha_{22}, \alpha_{23}, \alpha_{31}, \alpha_{32}, \alpha_{33}\}$, we set true values of α_{12} and α_{13} to be 0.

We scan all possible true values for the targeted parameter to test the "A_4 symmetry" hypothesis, i.e. $\alpha_{2n} = \alpha_{3n} = 0$ (for $n = 1, 2, 3$) in Fig. 13.4. The solid curves and dashed curves correspond to oscillation parameters fixed at their best-fit values and values varying in 1σ ranges as given in Tab. 2.3. For any flavour model consistent with oscillation data, the χ^2 value is located between these two curves. We summarise the above setting in Table 13.4. In the upper panel of Fig. 13.4, we see a better performance to test "A_4 symmetry" for α_{21}, α_{22}, α_{23} and α_{33}; within $[-0.1,\ 0.1]$, which is roughly 1σ bounds constrained by global fit results shown in Tab. 13.3 [1], this hypothesis can be excluded with the significance more than $\Delta\chi^2_{A_4} = 9$. For the other two parameters α_{31} and α_{32}, with a worse performance, a minor asymmetry feature is seen. $\alpha_{31} < 0$ has the slightly higher significance than $\alpha_{31} > 0$. At $\alpha_{31} = 0.1$, the exclusion level can reach $1 \leqslant \Delta\chi^2_{A_4} \leqslant 6$; however, at $\alpha_{31} = -0.1$, $\Delta\chi^2_{A_4}$ ranges from 2.5 to 9.5. The asymmetry is in the opposite way for α_{32}, as $1.6 \leqslant \Delta\chi^2_{A_4} \leqslant 6.3$ ($0.4 \leqslant \Delta\chi^2_{A_4} \leqslant 4.8$) at $\alpha_{32} = 0.1$ (-0.1).

In the lower panel of Fig. 13.4, we fix oscillation parameters and study the impact of δ by comparing two cases with $\delta = 0$ and $\delta = 270°$. In general, DUNE performs worse with $\delta = 0$, especially for α_{3n}. However, this is not true for α_{21}. Strikingly, the performance of DUNE for α_{33} depends on δ significantly; at $\alpha_{33} = \pm 0.1$, the exclusion level is $\Delta\chi^2_{A_4} < 0.5$ ($\Delta\chi^2_{A_4} > 9$) for $\delta = 0$ ($270°$). Significant differences for α_{32} are also seen for $\alpha_{32} > 0$; at $\Delta\chi^2_{A_4} = 9$ it shifts from $\alpha_{32} \sim 0.3$ for $\delta = 0$ to $\alpha_{32} \sim 0.1$ for $\delta = 270°$. We see about 50% reduction for the interval between the boundaries at $\Delta\chi^2_{A_4} = 9$ for α_{23} and α_{31} with $\delta = 270°$, rather than those with $\delta = 0$. There is almost no difference for α_{22}. Though the results are not shown here, we find minor changes by flipping θ_{23} octant or mass ordering [2].

We conclude this subsection that DUNE has a high potential to test textures

---

[1] The bounds in Tab. 13.3, are for NSIs with u quarks only. Here, we assume only u quarks contribute NSI effects for neutrinos; therefore, the bounds in this table need to roughly time a factor '3' before comparing the results in Fig. 13.4.

[2] The central value of the prior for θ_{23} or Δm^2_{31} is set to be the new true value.

	Osc. Para.	$\alpha_{12},\ \alpha_{13}$	$\alpha_{2n},\ \alpha_{3n}$
true values	fix them at B.F.	fix them at 0	change one; fix the other at 0
tested values	all fixed or free	allow them varying	fix all at 0

Table 13.4: The summary of the setting for the true and tested values, used for studying $\Delta\chi^2_{A_4}$. The oscillation parameters (Osc. Para.) are fixed at the best fit (B.F.) of the global fit results in Tab. 2.3 for the true values. We study both scenarios with fixed and varying oscillation parameters with priors; giving a specific flavour symmetry model, the result should locate between the results for these two scenarios. The width of priors for oscillation parameters are used the size of 1σ uncertainty of global fit results in Tab. 2.3. The flavour symmetry A_4 only allows $\{\alpha_{12},\ \alpha_{13}\}$, which are fixed at 0 for true values, but allowed to freely vary for tested values. The parameters $\{\alpha_{2n},\ \alpha_{3n}\}$ are not allowed by A_4. For their true values, we study each of them by changing its value from -0.3 to 0.3, but fix the other at 0. For the tested values, we fix all of them at 0.

predicted by the “A_4 symmetry” hypothesis, which predicts only diagonal entries of ϵ^{m}. For the best scenario, DUNE is predicted to have an exclusion level over $\chi^2 = 9$ at $\alpha_{21}, \alpha_{22}, \alpha_{23}, \alpha_{33} = \pm 0.1$.

13.3 Testing “Z_2 symmetry” in DUNE

From the EFT point of view, combining dimension-8 operators with Z_2-preserving flavon VEV can predict plenty of off-diagonal NSI textures. Therefore, testing the “Z_2 symmetry” by using Z_2-motivated NSI textures is more complicated than testing the “A_4 symmetry”. Fortunately, some of them have stronger constraints than the others if UV completions of these operators are accounted, and only $\mathbb{T}_1$, $\mathbb{T}_2$, $\mathbb{T}_3$ and $\mathbb{T}_4$ may reach the percent level, as shown in Section 12.2.2. To simplify our discussion, we will only focus on these textures. We re-parametrise their linear combination as

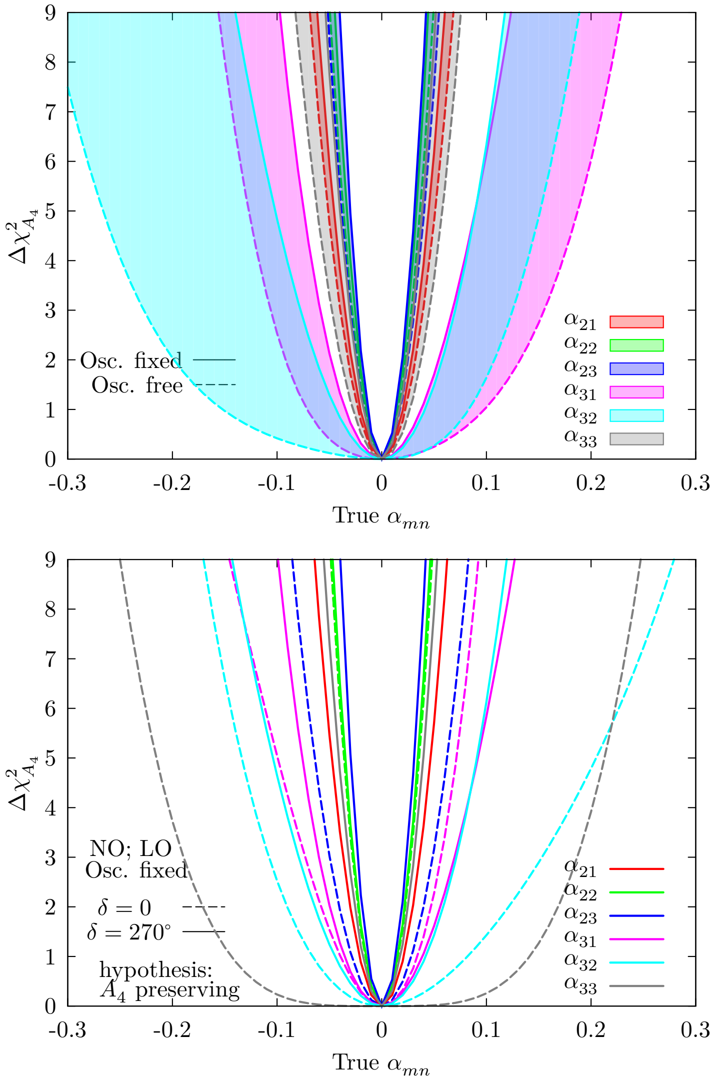

Figure 13.4: $\Delta\chi^2_{A_4}$ to exclude the "A_4 symmetry" hypothesis ($\alpha_{2n} = \alpha_{3n} = 0$) over the true value of α_{2n} or α_{3n} from -0.3 to 0.3. α_{2n} or α_{3n} are forbidden under the flavour symmetry A_4. More details of the setting can be seen in Table 13.4. Normal mass ordering with $\delta = 270°$ is assumed in the left panel. The oscillation parameters are taken from the current global fit results [2] (shown in Table 2.3). In the upper panel we show the exclusion level for all parameters. In this panel, the solid (dashed) curves present as fixed (free) oscillation parameters; with implementing flavour model for oscillation parameter, the results will locate somewhere between solid and dashed curves. The lower panel shows the impact of δ; the solid (dashed) is for $\delta = 270°$ ($\delta = 0$) with fixed oscillation parameters.

follows

$$\begin{pmatrix} y & x-z-iw & x+z+iw \\ x-z+iw & x+z & y-iw \\ x+z-iw & y+iw & x-z \end{pmatrix} \tag{13.3.2}$$

for the phenomenological benefit, where $x \equiv \frac{\alpha_1}{3} - \frac{\alpha_2}{3\sqrt{2}}$, $y \equiv \frac{\alpha_1}{3} + \frac{\alpha_2}{3\sqrt{2}}$, $z \equiv \frac{\alpha_3}{\sqrt{6}}$ and $w \equiv \frac{\alpha_{31}}{\sqrt{6}}$.

Global Fit		Global Fit		DUNE sensitivity	
w^u	–	w^d	–	w	$[-0.013, 0.025]$
x^u	$[-0.034, 0.013]$	x^d	$[-0.035, 0.012]$	x	$[-0.1, 0.1]$
y^u	$[-0.004, 0.003]$	y^d	$[-0.004, 0.003]$	y	$[-0.01, 0.01]$
z^u	$[-0.002, 0.005]$	z^d	$[-0.002, 0.005]$	z	$[-0.007, 0.017]$

Table 13.5: The 1σ bounds for $x^{u,d}$, $y^{u,d}$, and $z^{u,d}$, by global fit [39] shown in Table 13.2, and expected 1σ bounds w, x, y, and z, for DUNE with fixed oscillation parameters, assuming true values $w = x = y = z = 0$. The upper-scripts u, d denote NSIs only with u and d quarks, respectively. For both fitting, we allow the other NSI parameters to vary, except for w in the fit using global fit results. To avoid conflicting to the “real $\epsilon_{\alpha\neq\beta}$” assumption of global fit, we set $w = 0$ in the second and fourth columns.

Table 13.5 shows the 1σ constraint on x, y, z, w in Eq. (13.3.2) from Table 13.2, according to the same process in Section 13.2, and predicted sensitivity for DUNE with fixed oscillation parameters, assuming $w = x = y = z = 0$. For both cases, we test one parameter and allow the others to vary, except for w in the fitting with global fit results. Keeping in mind that a rough factor ‘3’ should be multiplied to $x^{u,d}$, $y^{u,d}$ and $z^{u,d}$ when comparing with x, y and z, we find the precision on x, y, and z for DUNE is competitive to current global fit results. Besides, DUNE is sensitive to the imaginary part w, but this paper is assumed zero in the global fit.

We find the result in Table 13.5 imposes very restricting bounds for y and z around zeros through the elements $\tilde{\epsilon}_{\tau\tau}$ and $\epsilon_{\mu\tau}$, and the possibility of nonzero x.

This result motivates us the structure

$$\begin{pmatrix} 0 & x & x \\ x & x & 0 \\ x & 0 & x \end{pmatrix} . \tag{13.3.3}$$

Two sum rules can be read out from Eq. (13.3.3),

$$\epsilon_{e\mu} = \epsilon_{e\tau} = -\tilde{\epsilon}_{ee} \, , \tag{13.3.4}$$

$$\epsilon_{\mu\tau} = \tilde{\epsilon}_{\tau\tau} = 0 \, . \tag{13.3.5}$$

In the following, we study the exclusion level for DUNE to exclude the matter-effect NSIs in the form of Eq. (13.3.3). The statistics quantity that we study is

$$\Delta\chi^2_{Z_2} \equiv \chi^2\big|_x - \chi^2_{b.f.}, \tag{13.3.6}$$

where $\chi^2|_x$ is the χ^2 value assuming ϵ^{m} satisfies the structure Eq. (13.3.3). We simply adopt Wilks' theorem, that the $\Delta\chi^2$ value for nested hypothesis testing asymptotically follows the χ-distribution with the degrees of freedom equal to the difference in the number of free parameters between two models.

In Fig. 13.5, we show how much DUNE can exclude the hypothesis Eq. (13.3.3) (testing two sum rules together) with fixed and free oscillation parameters. With a given flavour symmetry model, the sensitivity locates between these two curves. We vary only the true value of a certain $\epsilon_{\alpha\beta}$, but fix the others to be zero. We use the same setting for oscillation parameters as those in Section 13.2. For the first sum rule, in Eq. (13.3.4), within $[-0.05, \; +0.05]$, $\epsilon_{e\mu}$ and $\epsilon_{e\tau}$ can reach this significance. The performance for ee component, which is the worst one, is strongly dependent upon oscillation parameters, especially δ. For the second sum rule, in Eq. (13.3.5), “$\Delta\chi^2_{Z_2} < 1$” significance covers roughly $-0.2 < \tilde{\epsilon}_{\tau\tau} < 0.2$ and $-0.03 < \epsilon_{\mu\tau} < 0.03$. In the right panel of Fig. 13.5, this is obvious that $\delta = 0$ has worse sensitivity, especially for the ee component. In Fig. 13.6, we see only $\epsilon_{e\mu}$-$\epsilon_{e\tau}$ contour is along with $\eta = \xi$, because the sensitivity to $\tilde{\epsilon}_{ee}$ is worse. As a result, the $\tilde{\epsilon}_{ee}$-$\epsilon_{e\mu}$ ($\tilde{\epsilon}_{ee}$-$\epsilon_{e\tau}$) contour is restricted by $\epsilon_{e\tau}$ ($\epsilon_{e\mu}$) at $\epsilon_{e\mu} = 0$ ($\epsilon_{e\tau} = 0$), while the $\epsilon_{e\mu}$-$\epsilon_{e\tau}$ contour is not imposed by $\epsilon_{e\mu} = \epsilon_{e\tau} = 0$.

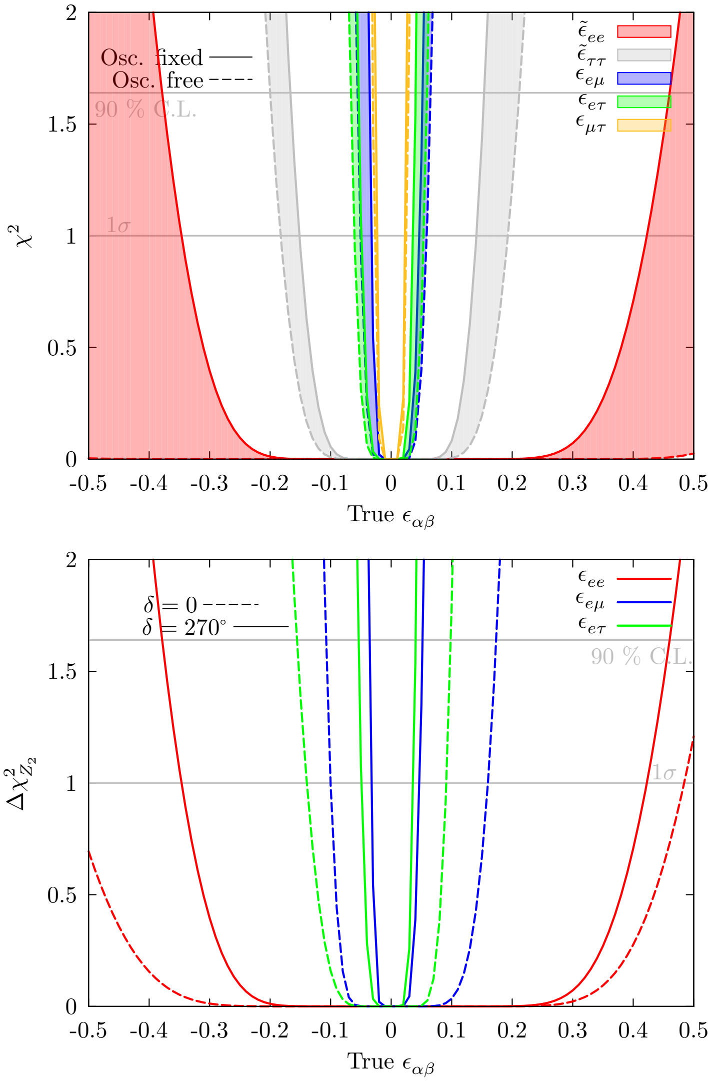

Figure 13.5: χ^2 value to exclude sum rules in Eqs. (13.3.4) and Eq. (13.3.5) over true value of $-0.5 < \epsilon_{\alpha\beta} < 0.5$, for normal mass ordering with $\delta = 270°$, in the upper panel. The solid (dashed) curves present as fixed (free) oscillation parameter; with implementing flavour model for oscillation parameter, the results will locate somewhere between solid and dashed curves. The lower panel shows the impact of δ; the solid (dashed) is for $\delta = 270°$ ($\delta = 0$), with fixed oscillation parameters.

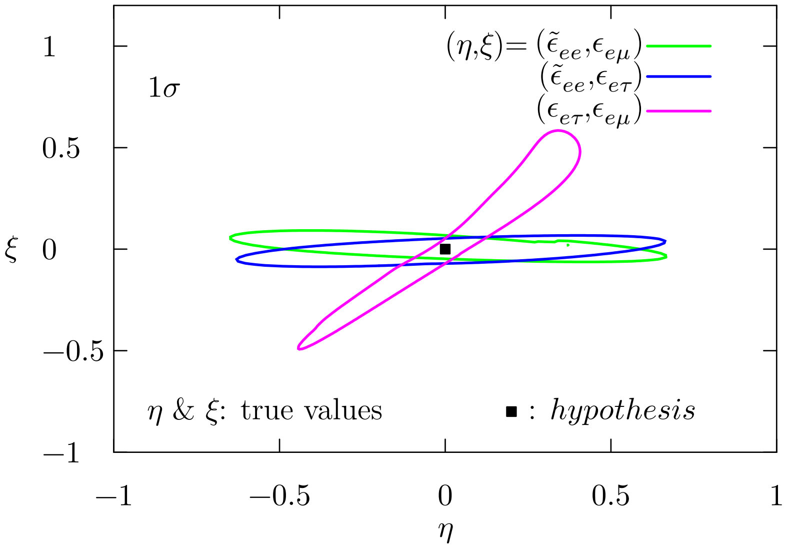

Figure 13.6: This figure shows $\tilde{\epsilon}_{ee}$–$\epsilon_{e\mu}$ (green), $\tilde{\epsilon}_{ee}$–$\epsilon_{e\tau}$ (blue), and $\epsilon_{e\mu}$–$\epsilon_{e\tau}$ (fuchsia) contours to exclude sum rules Eq. (13.3.3) at 1σ over true values from -1 to 1, assumed the normal ordering, with $\delta = 270°$. Eq. (13.3.3) predicts the sum rule $\tilde{\epsilon}_{ee} = \epsilon_{e\mu} = \epsilon_{e\tau} \equiv x$.

Chapter 14

Conclusions

The neutrino oscillation, which implies that neutrinos have mass, is a concrete evidence that the standard model (SM) is not complete. As a result, studying neutrino oscillations is an approach to extend our knowledge of new physics. We are now entering the era of precision measurement of oscillation physics. Most of current problem in neutrino oscillation are expected to be solved with new proposed neutrino oscillation experiments. This thesis is trying to answer how much we can extend our knowledge beyond the SM, especially the symmetry of leptonic flavour, with the future progression of neutrino oscillations; in more detail this thesis focus on the physics potential of future long baseline neutrino oscillation experiments (LBLs), and is separated into two halves, whether the exotic physics is taken into account or not. The main discussion in the first half is within the scheme of the standard oscillation, which can be described by mixing angles and mass-squared differences. These parameters can be further simplified by a flavour symmetry theory. We discuss the standard oscillation for two future LBLs — DUNE and T2HK, which adopt different technologies and aim to catch different neutrino oscillation probability features. In the second half, we focus on nonstandard interactions (NSIs) in matter for DUNE; matter effects are sizeable to the oscillation probabilities for DUNE. These interactions in matter are not measured with high precision, like those for other BSM signals, e.g. CLFV, etc. T2HK is not studied in this half due to its negligible matter effects. In the following, we summarise the conclusions in more detail.

DUNE and T2HK will lead the way in key measurements of the neutrino oscillation parameters. These long-baseline experiments will make high statistics determinations of the mass ordering, have an excellent chance to establish the presence of fundamental CP violation in the leptonic sector, and have the first precision measurements of δ. In Ch. 5 and 6, we study the expected performance of DUNE and T2HK. We conclude that DUNE and T2HK have a natural complementarity. Sensitivity to the mass ordering will come primarily from DUNE, sensitivity to CPV sees a larger contribution from T2HK (although due to the mass ordering degeneracy the sensitivity is notably improved by DUNE data), but precision on δ is a bit more nuanced with wider-band information being preferred for maximally CP violating values of δ, and high statistics first maximum measurements preferred for CP conserving values. For the measurements of the octant and maximal mixing sensitivities, the performance of the combination generally follows the sensitivity of T2HK. The precision on $\sin^2\theta_{23}$ strongly depends on the true value of θ_{23}, with the worst precision close to maximal mixing.

In Ch. 7, we have also considered potential alternative designs for T2HK and DUNE. T2HK may locate its second detector module in southern Korea, while DUNE has been associated with two beam designs beyond its 2-horn design: a 3-horn optimised design and the nuPIL design. Although the nuPIL design is no longer being actively pursued by the collaboration, we have shown that this novel technology leads to interesting phenomenology which highlights the flux dependence of an experiment's sensitivities to key measurements. We have investigated the ability of these designs to determine the mass ordering, to exclude CP conservation and maximal CP violation, and to measure δ. These alternatives are promising extensions of the current physics programme, and lead to modest improvements in these measurements. We have identified the combination of DUNE (3-horn) and T2HKK with a flux between 1.5° and 2.0° off-axis as the optimal choice; although, the difference between the performance of the 2-horn and 3-horn designs is not very significant.

The Littlest Seesaw (LS) models work within the framework of the Type I seesaw mechanism, using two right-handed neutrinos to generate the left-handed neutrino masses. Combined with constraints from flavour symmetries, the neutrino mixing angles and phases can be predicted from a small number of parameters. In Ch. 8, we have studied two versions of this model (LSA and LSB) which use different flavour symmetries to enforce constraints which result in different permutations of the second and third rows and columns of the neutrino mass matrix, leading to different predictions for the octant of θ_{23}. Using the results of a recent global fit of neutrino oscillation experiments, we have found that both versions can well accommodate the parameter values as measured by experiment, with the greatest tension on the value of θ_{23} at the 1σ level. We find that the LSB version, predicting a value of θ_{23} in the lower octant, to be slightly preferred.

In Ch. 9, the result presented shows that the most straightforward way to exclude the LS model is to provide a better *individual* determination of the three currently less precisely measured parameters θ_{12}, θ_{23}, and δ, which requires both medium baseline experiments such as JUNO and RENO-50, and long baseline experiments such as DUNE and T2HK. In addition, the LS model could be constrained by *combined* measurements of the three remaining parameters Δm^2_{21}, Δm^2_{31} and θ_{13}, where an even higher precision of the latter reactor parameter at the short baseline Daya Bay experiment can also play an important role. We remark that, although the above conclusions have been established for the LSA and LSB models, similar arguments can be expected to apply to any highly predictive flavour models which determine the oscillation parameters from a smaller number of input model parameters. We conclude that the need for future reactor and accelerator experiments to measure individually θ_{12}, θ_{23} and δ, plus combinations of θ_{13}, Δm^2_{21} and Δm^2_{31}, may be considered to be general requirements in order to probe predictive flavour symmetry models. Therefore a broad programme of such precision experiments seems to be essential in order to take the next step in understanding neutrino oscillations in the context of the flavour puzzle of the Standard Model.

In Ch. 10, we introduce nonstandard interactions (NSIs), which are the interactions that cannot be explained by the SM, but are thought to be via mediating the beyond-standard-model (BSM) particle. Depending on where it occurs in the neutrino oscillation, NSIs can be classified into NSIs at the source and detector, and in matter during neutrino propagation. With the knowledge of effective field theory (EFT), we present all possible operators for NSI effects with dimension $\leqslant 8$, involving SM fermions and Higgs bosons only. We find that in the framework of EFT, after the electroweak symmetry breaks, NSIs in matter can avoid the tight constraints from CLFVs and NSIs at the source and detector. As a result, the experimental constraint on the parameters for NSIs in matter is in general mainly from their measurement. We finally review the constraints by the current global fit for matter effect NSIs in Tab. 10.3, finding the order $\epsilon^{\rm m}_{\alpha\beta} \sim \mathcal{O}(0.01 - 0.7)$ at 90% C.L., and therefore conclude that large matter effect NSIs are allowed.

Due to the large matter effects and the upgrade of precision, DUNE is expected to detect the sizeable matter NSI effects. Many works discuss the precision of the measurement on matter-effect NSI parameters for DUNE under the SM, which can be understood as if there is no matter NSI effects, how DUNE can exclude a variety of NSI models, and are reviewed in Sec. 11.2. We see the better precision of the off-diagonal elements $\epsilon^{\rm m}_{\alpha\neq\beta}$, though new degeneracies are also discovered. In Sec. 11.3, we take another attitude to ask if there are NSI effects in matter, how DUNE can exclude the SM prediction $\epsilon^{\rm m} = 0$, and define the NSI signal sensitivity σ_{NSI} showing the exclusion ability in Eq. 11.3.2. An analogy of the relation between this quantity to the precision of matter-effect NSI parameter is that of CPV or MCP sensitivity to $\Delta\delta$. We study σ_{NSI}, varying the true value of each $\epsilon^{\rm m}_{\alpha\beta}$. We find that DUNE has high sensitivity for flavour-transition matter NSI effects. In our simulation, σ_{NSI} can reach around 3σ while $\epsilon^{\rm m}_{e\mu}$, $\epsilon^{\rm m}_{e\mu} \sim 0.05$ or $\epsilon^{\rm m}_{\mu\tau} \sim 0.03$. We also see that σ_{NSI} depends on the phases, δ, $\phi_{e\mu}$, $\phi_{e\tau}$, and $\phi_{\mu\tau}$. While $\delta \sim \pm\pi/2$, σ_{NSI} can be the best. This is just opposite for $\phi_{\mu\tau}$, for $\epsilon_{\mu\tau}$ the sensitivity reaches the peak (bottom) while its phase goes to $0,\ \pi$ $(\pm\pi/2)$. The worst sensitivity for $e\mu$ and $e\tau$ components take place where $\phi_{e\mu} \sim -0.4\pi,\ 0.6\pi$ and $\phi_{e\tau} \sim \pm 0.5\pi$ respectively. We also discover the correlation between $\epsilon_{e\mu}$ and $\epsilon_{e\tau}$, which depends on the true value of δ. We see this correlation for $\delta = 3\pi/2$, but do not observe it while $\delta = 0$. We investigate that the improvement by increasing the exposure can be more significant than those by including T2HK or T2HKK1.5° data for most of $\epsilon_{\alpha\beta}$.

NSI effects are flavour-dependent, and therefore can be correlated by the theory of flavour. In Ch. 12, we firstly follow the general approach used in flavour models, the three lepton doublets are arranged as a triplet of A_4. For any other SM fermions, we perform a scan of all possible representations in the flavour space. Including a flavon with a Z_2-preserving VEV, A_4 is broken to Z_2, and we can obtain Z_2-motivated relations of flavour dependence of NSIs. We expand each relation in a basis of matrices, which are called "textures". We focus on textures for matter NSI effects. The matrix $\epsilon^{\rm m}$ is accordingly the combination of textures. Both A_4- and Z_2-motivated textures have been systematically searched in Sec. 10.1, with the main result listed in Table 12.1. Then, we consider how to realise these operators listed in Tab. 10.1 by introducing new particles in renormalisable models. Extra experimental constraints on new particles may suppress the NSI effect. Specifically, those on charged scalars forbid observable NSIs from UV completions of the dimension-6 operator. This is because only SM lepton doublets, which are arranged as a triplet of A_4, are involved in these operators. Thus, couplings for e, μ and τ are correlated with each other and radiative decays of μ and τ lead to strong constraints on the NSI coefficients. This problem can be avoided for UV-complete models based on the dimension-8 operators $\mathcal{O}^{2-5}$ where the fermion F can be arranged as a singlet of A_4. UV completions of the latter are unavoidable to introduce other dimension-6 operators which further lead to non-unitary effects of lepton flavour mixing. This is the main constraint on NSIs from UV completions of the dimension-8 operators. Including the Z_2 breaking effect, we obtain four textures $\mathbb{T}_1$, $\mathbb{T}_2$, $\mathbb{T}_3$ and $\mathbb{T}_4$ in Eq. (12.2.34), which are regarded as major textures.

In Ch. 13, we apply the A_4- and Z_2-motivated NSI textures to analyse how to test the flavour symmetry by measuring NSIs in DUNE. Two applications are studied. The first one is testing "A_4 symmetry". The off-diagonal entries of the NSI matrix are forbidden by A_4 symmetry. Excluding this hypothesis can be used to exclude the "A_4 symmetry". We find that DUNE have high sensitivity to exclude NSI effects predicted by A_4; within 1σ allowed region in global fit results, it can reach the significance over 3σ. The other application is testing "Z_2 symmetry". We also focus on major NSI textures suggested by UV-complete models, predicted in Sec. 12.2.2. DUNE can constrain NSI parameters competitively with current global data. In particular, it can measure the imaginary part, labelled as w, with the percentage precision. We also suggest to text two sum rules of NSI parameters as shown in Eqs. (13.3.4) and (13.3.5). They are weakly constrained by former oscillation data. DUNE can reach the sensetivity at 1σ for off-diagonal NSI parameters around the percent level.

We have been exploring both left and right halves of Fig. 1.1. We summarise two most important conclusions: 1. Solving the remaining problems and making precision measurement of δ in the standard neutrino oscillation by the combination of DUNE and T2HK can be highly expected, and therefore, large numbers of flavour symmetry models can be excluded in the near future; 2. DUNE has better sensitivity for flavour-transition matter-effect NSIs with higher σ_{NSI} and better resolution, which implies the high exclusion ability for excluding the A_4 flavour symmetry in NSIs in matter. Based on the above conclusions, we can expect the great step forward in the leptonic-flavour physics by the precision measurement of oscillation parameters or matter-effect NSI parameters. These effects — the standard oscillation and NSIs — are not necessary to be correlated, if there is no interlock provided by the flavour symmetry. As a result, processing both approaches can be considered as a cross-check for flavour symmetry models. Thus, there is a chance to get the confidence for a model of flavour symmetry by getting the consistent results (as an indirect evidence), before we reach an extremely high energy at a collider and hunt the signal of flavons. Of course, this thesis, generally discussing about how the flavour symmetry theory can be checked by using both measurements, is not the end story of this indirect evidence, but opens a new opportunity.

Bibliography

[1] Special Issue on "Neutrino Oscillations: Celebrating the Nobel Prize in Physics 2015" Edited by Tommy Ohlsson, Nucl. Phys. B **908** (2016) Pages 1-466 (July 2016),
`http://www.sciencedirect.com/science/journal/05503213/908/supp/C`.

[2] I. Esteban, M. C. Gonzalez-Garcia, M. Maltoni, I. Martinez-Soler and T. Schwetz, JHEP **1701**, 087 (2017) doi:10.1007/JHEP01(2017)087 [arXiv:1611.01514 [hep-ph]].

[3] M. Antonello *et al.* [MicroBooNE and LAr1-ND and ICARUS-WA104 Collaborations], arXiv:1503.01520 [physics.ins-det].

[4] F. An *et al.* [JUNO Collaboration], J. Phys. G **43**, no. 3, 030401 (2016) doi:10.1088/0954-3899/43/3/030401 [arXiv:1507.05613 [physics.ins-det]].

[5] Z. Djurcic *et al.* [JUNO Collaboration], arXiv:1508.07166 [physics.ins-det].

[6] S. B. Kim, Nucl. Part. Phys. Proc. **265-266**, 93 (2015) doi:10.1016/j.nuclphysbps.2015.06.024 [arXiv:1412.2199 [hep-ex]].

[7] P. Adamson *et al.* [NOvA Collaboration], Phys. Rev. Lett. **116**, no. 15, 151806 (2016) doi:10.1103/PhysRevLett.116.151806 [arXiv:1601.05022 [hep-ex]].

[8] P. Adamson *et al.* [NOvA Collaboration], Phys. Rev. D **93**, no. 5, 051104 (2016) doi:10.1103/PhysRevD.93.051104 [arXiv:1601.05037 [hep-ex]].

[9] K. Abe *et al.* [T2K Collaboration], Phys. Rev. D **91**, no. 7, 072010 (2015) doi:10.1103/PhysRevD.91.072010 [arXiv:1502.01550 [hep-ex]].

[10] K. Abe *et al.* [Hyper-Kamiokande Working Group], arXiv:1412.4673 [physics.ins-det].

[11] C. Adams *et al.* [LBNE Collaboration], arXiv:1307.7335 [hep-ex].

[12] R. Acciarri *et al.* [DUNE Collaboration], arXiv:1512.06148 [physics.ins-det].

[13] Y. Fukuda *et al.* [Super-Kamiokande Collaboration], Nucl. Instrum. Meth. A **501**, 418 (2003). doi:10.1016/S0168-9002(03)00425-X

[14] M. Ghosh, S. Goswami and S. K. Raut, Eur. Phys. J. C **76**, no. 3, 114 (2016) doi:10.1140/epjc/s10052-016-3962-7 [arXiv:1412.1744 [hep-ph]].

[15] S. F. King and C. Luhn, Rept. Prog. Phys. **76** (2013) 056201 [arXiv:1301.1340].

[16] S. F. King, Rept. Prog. Phys. **67** (2004) 107 [hep-ph/0310204]; H. Ishimori, T. Kobayashi, H. Ohki, Y. Shimizu, H. Okada and M. Tanimoto, Prog. Theor. Phys. Suppl. **183** (2010) 1 [arXiv:1003.3552]; S. F. King, A. Merle, S. Morisi, Y. Shimizu and M. Tanimoto, New J. Phys. **16** (2014) 045018 [arXiv:1402.4271]; S. F. King, J. Phys. G: Nucl. Part. Phys. **42** (2015) 123001 [arXiv:1510.02091].

[17] P. Minkowski, Phys. Lett. B **67** (1977) 421; M. Gell-Mann, P. Ramond and R. Slansky in Sanibel Talk, CALT-68-709, Feb 1979, and in *Supergravity*, North Holland, Amsterdam (1979); T. Yanagida in *Proc. of the Workshop on Unified Theory and Baryon Number of the Universe*, KEK, Japan (1979); S.L.Glashow, Cargese Lectures (1979); R. N. Mohapatra and G. Senjanovic, Phys. Rev. Lett. **44** (1980) 912; J. Schechter and J. W. F. Valle, Phys. Rev. D **22** (1980) 2227.

[18] S. F. King, Nucl. Phys. B **908** (2016) 456 [arXiv:1511.03831], [appearing in [1]], `http://www.sciencedirect.com/science/article/pii/S0550321315004356`.

[19] S. F. King, Nucl. Phys. B **576** (2000) 85 [hep-ph/9912492].

[20] S. F. King, JHEP **0209** (2002) 011 [hep-ph/0204360].

[21] P. H. Frampton, S. L. Glashow and T. Yanagida, Phys. Lett. B **548** (2002) 119 [hep-ph/0208157].

[22] K. Harigaya, M. Ibe and T. T. Yanagida, Phys. Rev. D **86** (2012) 013002 [arXiv:1205.2198].

[23] S. F. King, JHEP **1307** (2013) 137 [arXiv:1304.6264].

[24] E. Ma and G. Rajasekaran, Phys. Rev. D **64** (2001) 113012 [hep-ph/0106291].

[25] R. N. Mohapatra, M. K. Parida and G. Rajasekaran, Phys. Rev. D **69** (2004) 053007 [hep-ph/0301234].

[26] G. Altarelli and F. Feruglio, Nucl. Phys. B **720** (2005) 64 [hep-ph/0504165].

[27] G. Altarelli and F. Feruglio, Nucl. Phys. B **741**, 215 (2006) doi:10.1016/j.nuclphysb.2006.02.015 [hep-ph/0512103].

[28] C. S. Lam, Phys. Rev. D **78**, 073015 (2008) doi:10.1103/PhysRevD.78.073015 [arXiv:0809.1185 [hep-ph]].

[29] P. F. Harrison, D. H. Perkins and W. G. Scott, Phys. Lett. B **530** (2002) 167 [hep-ph/0202074]; Z. Z. Xing, Phys. Lett. B **533** (2002) 85 [hep-ph/0204049]; P. F. Harrison and W. G. Scott, Phys. Lett. B **535** (2002) 163 [hep-ph/0203209]; X. G. He and A. Zee, Phys. Lett. B **560** (2003) 87 [hep-ph/0301092].

[30] For some reviews, see G. Altarelli and F. Feruglio, Rev. Mod. Phys. **82** (2010) 2701 [arXiv:1002.0211 [hep-ph]]; S. F. King and C. Luhn, Rept. Prog. Phys. **76** (2013) 056201 [arXiv:1301.1340 [hep-ph]]; S. F. King, A. Merle, S. Morisi, Y. Shimizu and M. Tanimoto, New J. Phys. **16** (2014) 045018 [arXiv:1402.4271 [hep-ph]].

[31] T. Ohlsson, Rept. Prog. Phys. **76** (2013) 044201 doi:10.1088/0034-4885/76/4/044201 [arXiv:1209.2710 [hep-ph]]; O. G. Miranda and

H. Nunokawa, New J. Phys. **17** (2015) no.9, 095002 doi:10.1088/1367-2630/17/9/095002 [arXiv:1505.06254 [hep-ph]].

[32] M. B. Wise and Y. Zhang, Phys. Rev. D **90** (2014) no.5, 053005 doi:10.1103/PhysRevD.90.053005 [arXiv:1404.4663 [hep-ph]]

[33] D. V. Forero and W. C. Huang, JHEP **1703** (2017) 018 doi:10.1007/JHEP03(2017)018 [arXiv:1608.04719 [hep-ph]].

[34] S. Antusch, J. P. Baumann and E. Fernandez-Martinez, Nucl. Phys. B **810** (2009) 369 [arXiv:0807.1003 [hep-ph]].

[35] Y. Farzan, Phys. Lett. B **748** (2015) 311 doi:10.1016/j.physletb.2015.07.015 [arXiv:1505.06906 [hep-ph]]; Y. Farzan and I. M. Shoemaker, JHEP **1607** (2016) 033 doi:10.1007/JHEP07(2016)033 [arXiv:1512.09147 [hep-ph]]; Y. Farzan and J. Heeck, Phys. Rev. D **94** (2016) no.5, 053010 doi:10.1103/PhysRevD.94.053010 [arXiv:1607.07616 [hep-ph]].

[36] D. Akimov *et al.* [COHERENT Collaboration], Science **357**, no. 6356, 1123 (2017) doi:10.1126/science.aao0990 [arXiv:1708.01294 [nucl-ex]].

[37] M. Masud, A. Chatterjee and P. Mehta, J. Phys. G **43** (2016) no.9, 095005 doi:10.1088/0954-3899/43/9/095005/meta, 10.1088/0954-3899/43/9/095005 [arXiv:1510.08261 [hep-ph]]; A. de Gouva and K. J. Kelly, Nucl. Phys. B **908**, 318 (2016) doi:10.1016/j.nuclphysb.2016.03.013 [arXiv:1511.05562 [hep-ph]]; P. Coloma, JHEP **1603**, 016 (2016) doi:10.1007/JHEP03(2016)016 [arXiv:1511.06357 [hep-ph]]; J. Liao, D. Marfatia and K. Whisnant, Phys. Rev. D **93** (2016) no.9, 093016 doi:10.1103/PhysRevD.93.093016 [arXiv:1601.00927 [hep-ph]]; P. Bakhti and Y. Farzan, JHEP **1607** (2016) 109 doi:10.1007/JHEP07(2016)109 [arXiv:1602.07099 [hep-ph]]; M. Masud and P. Mehta, Phys. Rev. D **94**, 013014 (2016) doi:10.1103/PhysRevD.94.013014 [arXiv:1603.01380 [hep-ph]]; P. Coloma and T. Schwetz, Phys. Rev. D **94**, no. 5, 055005 (2016) Erratum: [Phys. Rev. D **95**, no. 7, 079903 (2017)] doi:10.1103/PhysRevD.95.079903, 10.1103/PhysRevD.94.055005 [arXiv:1604.05772 [hep-ph]; M. Masud and P. Mehta, Phys. Rev. D **94** (2016)

no.5, 053007 doi:10.1103/PhysRevD.94.053007 [arXiv:1606.05662 [hep-ph]]; M. Blennow, S. Choubey, T. Ohlsson, D. Pramanik and S. K. Raut, JHEP **1608**, 090 (2016) doi:10.1007/JHEP08(2016)090 [arXiv:1606.08851 [hep-ph]]; S. K. Agarwalla, S. S. Chatterjee and A. Palazzo, Phys. Lett. B **762** (2016) 64 doi:10.1016/j.physletb.2016.09.020 [arXiv:1607.01745 [hep-ph]]; S. F. Ge and A. Y. Smirnov, JHEP **1610**, 138 (2016) doi:10.1007/JHEP10(2016)138 [arXiv:1607.08513 [hep-ph]]; S. Fukasawa, M. Ghosh and O. Yasuda, Phys. Rev. D **95** (2017) no.5, 055005 doi:10.1103/PhysRevD.95.055005 [arXiv:1611.06141 [hep-ph]]; K. N. Deepthi, S. Goswami and N. Nath, arXiv:1612.00784 [hep-ph]; J. Liao, D. Marfatia and K. Whisnant, JHEP **1701**, 071 (2017) doi:10.1007/JHEP01(2017)071 [arXiv:1612.01443 [hep-ph]]; P. Coloma, P. B. Denton, M. C. Gonzalez-Garcia, M. Maltoni and T. Schwetz, JHEP **1704**, 116 (2017) doi:10.1007/JHEP04(2017)116 [arXiv:1701.04828 [hep-ph]]; M. Masud, M. Bishai and P. Mehta, arXiv:1704.08650 [hep-ph].

[38] M. Blennow, P. Coloma, E. Fernandez-Martinez, J. Hernandez-Garcia and J. Lopez-Pavon, JHEP **1704** (2017) 153 [arXiv:1609.08637 [hep-ph]].

[39] M. C. Gonzalez-Garcia and M. Maltoni, JHEP **1309**, 152 (2013) doi:10.1007/JHEP09(2013)152 [arXiv:1307.3092 [hep-ph]].

[40] J. Beringer *et al.* [Particle Data Group], Phys. Rev. D **86**, 010001 (2012). doi:10.1103/PhysRevD.86.010001

[41] D. V. Forero, M. Tortola and J. W. F. Valle, Phys. Rev. D **90**, no. 9, 093006 (2014) doi:10.1103/PhysRevD.90.093006 [arXiv:1405.7540 [hep-ph]].

[42] F. Capozzi, E. Lisi, A. Marrone, D. Montanino and A. Palazzo, Nucl. Phys. B **908**, 218 (2016) doi:10.1016/j.nuclphysb.2016.02.016 [arXiv:1601.07777 [hep-ph]].

[43] M. C. Gonzalez-Garcia, M. Maltoni and T. Schwetz, JHEP **1411**, 052 (2014) doi:10.1007/JHEP11(2014)052 [arXiv:1409.5439 [hep-ph]].

[44] P. Ballett, S. F. King, S. Pascoli, N. W. Prouse and T. Wang, JHEP **1703**, 110 (2017) doi:10.1007/JHEP03(2017)110 [arXiv:1612.01999 [hep-ph]].

[45] E. Ma, Phys. Lett. B **755**, 348 (2016) doi:10.1016/j.physletb.2016.02.032 [arXiv:1601.00138 [hep-ph]].

[46] J. N. Lu and G. J. Ding, Phys. Rev. D **95**, no. 1, 015012 (2017) doi:10.1103/PhysRevD.95.015012 [arXiv:1610.05682 [hep-ph]].

[47] J. M. Berryman and D. Hernndez, Phys. Rev. D **95**, no. 11, 115007 (2017) doi:10.1103/PhysRevD.95.115007 [arXiv:1611.07033 [hep-ph]].

[48] P. Huber, M. Lindner and W. Winter, Comput. Phys. Commun. **167**, 195 (2005) doi:10.1016/j.cpc.2005.01.003 [hep-ph/0407333].

[49] P. Huber, J. Kopp, M. Lindner, M. Rolinec and W. Winter, Comput. Phys. Commun. **177**, 432 (2007) doi:10.1016/j.cpc.2007.05.004 [hep-ph/0701187].

[50] V. Papadimitriou *et al.*, doi:10.18429/JACoW-IPAC2016-TUPMR025 arXiv:1704.04471 [physics.acc-ph].

[51] DUNE Collaboration, 2016, http://home.fnal.gov/∼ljf26/DUNEFluxes/

[52] T. Alion *et al.* [DUNE Collaboration], arXiv:1606.09550 [physics.ins-det].

[53] J. B. Lagrange, J. Pasternak, A. Bross and A. Liu, NUFACT-2015-124, FERMILAB-CONF-16-160-AD.

[54] A. Liu, A. Bross and J. B. Lagrange, doi:10.18429/JACoW-IPAC2016-THPMB055

[55] J. B. Lagrange, J. Pasternak, A. Bross, A. Liu, R. Appleby and S. Tygier, doi:10.18429/JACoW-IPAC2016-THPMB054

[56] V. Papadimitriou *et al.*, doi:10.18429/JACoW-IPAC2016-TUPMR025 arXiv:1704.04471 [physics.acc-ph].

[57] DUNE Collaboration, 2016, https://indico.fnal.gov/conferenceDisplay.py?confId=12361

[58] R. Acciarri *et al.* [DUNE Collaboration], arXiv:1601.05471 [physics.ins-det].

[59] K. Abe *et al.* [Hyper-Kamiokande Proto-Collaboration], KEK Preprint 2016-21, ICRR-Report-701-2016-1 (2016) `https://lib-extopc.kek.jp/preprints/PDF/2016/1627/1627021.pdf`

[60] Koseki, T., 2015, J-PARC Accelerator: achievement and future upgrade. Talk presented at the Workshop for Neutrino Programs with Facilities in Japan, August 4, 2015 Tokai, Japan

[61] Kobayashi, T., 2015, Potential J-PARC beam power improvement and beam delivery before 2026 Talk presented at the Workshop for Neutrino Programs with Facilities in Japan, August 4, 2015 Tokai, Japan

[62] Shiozawa, M., 2016, Hyper-Kamiokande Talk presented at the Third International Meeting for Large Neutrino Infrastructures, May 30, 2016, Tsukuba, Japan

[63] P. Huber, M. Lindner and W. Winter, Nucl. Phys. B **645**, 3 (2002) doi:10.1016/S0550-3213(02)00825-8 [hep-ph/0204352].

[64] C. Andreopoulos *et al.*, Nucl. Instrum. Meth. A **614**, 87 (2010) doi:10.1016/j.nima.2009.12.009 [arXiv:0905.2517 [hep-ph]].

[65] K. Abe *et al.* [Hyper-Kamiokande proto- Collaboration], arXiv:1611.06118 [hep-ex].

[66] M. Ishitsuka, T. Kajita, H. Minakata and H. Nunokawa, Phys. Rev. D **72**, 033003 (2005) doi:10.1103/PhysRevD.72.033003 [hep-ph/0504026].

[67] X. Guo *et al.* [Daya Bay Collaboration], hep-ex/0701029.

[68] J. Cao and K. B. Luk, Nucl. Phys. B **908** (2016) 62 doi:10.1016/j.nuclphysb.2016.04.034 [arXiv:1605.01502 [hep-ex]].

[69] F. Ardellier *et al.*, hep-ex/0405032.

[70] J. K. Ahn *et al.* [RENO Collaboration], arXiv:1003.1391 [hep-ex].

[71] K. Asano and H. Minakata, JHEP **1106**, 022 (2011) doi:10.1007/JHEP06(2011)022 [arXiv:1103.4387 [hep-ph]].

[72] S. K. Agarwalla, Y. Kao and T. Takeuchi, JHEP **1404**, 047 (2014) doi:10.1007/JHEP04(2014)047 [arXiv:1302.6773 [hep-ph]].

[73] M. B. Johnson, E. M. Henley and L. S. Kisslinger, Phys. Rev. D **91**, no. 7, 076005 (2015) doi:10.1103/PhysRevD.91.076005 [arXiv:1501.04093 [hep-ph]].

[74] H. Minakata and S. J. Parke, JHEP **1601**, 180 (2016) doi:10.1007/JHEP01(2016)180 [arXiv:1505.01826 [hep-ph]].

[75] P. B. Denton, H. Minakata and S. J. Parke, JHEP **1606**, 051 (2016) doi:10.1007/JHEP06(2016)051 [arXiv:1604.08167 [hep-ph]].

[76] P. B. Denton, H. Minakata and S. J. Parke, arXiv:1801.06514 [hep-ph].

[77] M. Bishai, M. V. Diwan, S. Kettell, J. Stewart, B. Viren, E. Worchester and L. Whitehead, arXiv:1203.4090 [hep-ex].

[78] S. Geer, O. Mena and S. Pascoli, Phys. Rev. D **75**, 093001 (2007) doi:10.1103/PhysRevD.75.093001 [hep-ph/0701258 [HEP-PH]].

[79] P. Coloma and E. Fernandez-Martinez, JHEP **1204**, 089 (2012) doi:10.1007/JHEP04(2012)089 [arXiv:1110.4583 [hep-ph]].

[80] P. Huber and J. Kopp, JHEP **1103**, 013 (2011) Erratum: [JHEP **1105**, 024 (2011)] doi:10.1007/JHEP03(2011)013, 10.1007/JHEP05(2011)024 [arXiv:1010.3706 [hep-ph]].

[81] S. K. Agarwalla *et al.* [LAGUNA-LBNO Collaboration], arXiv:1412.0593 [hep-ph].

[82] H. Minakata and S. J. Parke, Phys. Rev. D **87**, no. 11, 113005 (2013) doi:10.1103/PhysRevD.87.113005 [arXiv:1303.6178 [hep-ph]].

[83] P. Coloma, H. Minakata and S. J. Parke, Phys. Rev. D **90**, 093003 (2014) doi:10.1103/PhysRevD.90.093003 [arXiv:1406.2551 [hep-ph]].

[84] S. K. Agarwalla, Adv. High Energy Phys. **2014**, 457803 (2014) doi:10.1155/2014/457803 [arXiv:1401.4705 [hep-ph]].

[85] S. Antusch, P. Huber, S. F. King and T. Schwetz, JHEP **0704**, 060 (2007) doi:10.1088/1126-6708/2007/04/060 [hep-ph/0702286 [HEP-PH]].

[86] P. Ballett, S. F. King, C. Luhn, S. Pascoli and M. A. Schmidt, Phys. Rev. D **89** (2014) 1, 016016 [arXiv:1308.4314]; P. Ballett, S. F. King, C. Luhn, S. Pascoli and M. A. Schmidt, J. Phys. Conf. Ser. **598** (2015) 1, 012014 [arXiv:1406.0308].

[87] I. Girardi, S. T. Petcov and A. V. Titov, Nucl. Phys. B **894**, 733 (2015) doi:10.1016/j.nuclphysb.2015.03.026 [arXiv:1410.8056 [hep-ph]].

[88] P. Ballett, S. F. King, C. Luhn, S. Pascoli and M. A. Schmidt, JHEP **1412**, 122 (2014) doi:10.1007/JHEP12(2014)122 [arXiv:1410.7573 [hep-ph]].

[89] I. Girardi, S. T. Petcov and A. V. Titov, Eur. Phys. J. C **75**, 345 (2015) doi:10.1140/epjc/s10052-015-3559-6 [arXiv:1504.00658 [hep-ph]].

[90] S. F. King, J. Phys. G **42**, 123001 (2015) doi:10.1088/0954-3899/42/12/123001 [arXiv:1510.02091 [hep-ph]].

[91] S. F. King, Prog. Part. Nucl. Phys. **94** (2017) 217 doi:10.1016/j.ppnp.2017.01.003 [arXiv:1701.04413 [hep-ph]].

[92] P. Coloma, A. Donini, E. Fernandez-Martinez and P. Hernandez, JHEP **1206**, 073 (2012) doi:10.1007/JHEP06(2012)073 [arXiv:1203.5651 [hep-ph]].

[93] X. Qian, A. Tan, W. Wang, J. J. Ling, R. D. McKeown and C. Zhang, Phys. Rev. D **86**, 113011 (2012) doi:10.1103/PhysRevD.86.113011 [arXiv:1210.3651 [hep-ph]].

[94] E. Ciuffoli, J. Evslin and X. Zhang, JHEP **1401**, 095 (2014) doi:10.1007/JHEP01(2014)095 [arXiv:1305.5150 [hep-ph]].

[95] M. Blennow, P. Coloma, P. Huber and T. Schwetz, JHEP **1403**, 028 (2014) doi:10.1007/JHEP03(2014)028 [arXiv:1311.1822 [hep-ph]].

[96] J. Elevant and T. Schwetz, JHEP **1509**, 016 (2015) doi:10.1007/JHEP09(2015)016 [arXiv:1506.07685 [hep-ph]].

[97] M. Blennow, P. Coloma and E. Fernandez-Martinez, JHEP **1503**, 005 (2015) doi:10.1007/JHEP03(2015)005 [arXiv:1407.3274 [hep-ph]].

[98] S. Fukasawa, M. Ghosh and O. Yasuda, Nucl. Phys. B **918**, 337 (2017) doi:10.1016/j.nuclphysb.2017.02.008 [arXiv:1607.03758 [hep-ph]].

[99] K. Hagiwara, N. Okamura and K. i. Senda, Phys. Lett. B **637**, 266 (2006) Erratum: [Phys. Lett. B **641**, 491 (2006)] doi:10.1016/j.physletb.2006.09.003, 10.1016/j.physletb.2006.04.041 [hep-ph/0504061].

[100] K. Hagiwara, N. Okamura and K. i. Senda, Phys. Rev. D **76**, 093002 (2007) doi:10.1103/PhysRevD.76.093002 [hep-ph/0607255].

[101] T. Kajita, H. Minakata, S. Nakayama and H. Nunokawa, Phys. Rev. D **75**, 013006 (2007) doi:10.1103/PhysRevD.75.013006 [hep-ph/0609286].

[102] S. F. King, Phys. Lett. B **724** (2013) 92 [arXiv:1305.4846]; S. F. King, JHEP **1401** (2014) 119 [arXiv:1311.3295]; S. F. King, JHEP **1408** (2014) 130 [arXiv:1406.7005].

[103] F. Bjorkeroth and S. F. King, J. Phys. G **42** (2015) no.12, 125002 [arXiv:1412.6996].

[104] S. F. King, JHEP **1602** (2016) 085 [arXiv:1512.07531].

[105] F. Bjorkeroth, F. J. de Anda, I. de Medeiros Varzielas and S. F. King, JHEP **1506** (2015) 141 [arXiv:1503.03306]; F. Bjorkeroth, F. J. de Anda, I. d. M. Varzielas and S. F. King, arXiv:1512.00850.

[106] F. Bjorkeroth, F. J. de Anda, I. de Medeiros Varzielas and S. F. King, JHEP **1510** (2015) 104 [arXiv:1505.05504].

[107] S. F. King, Phys. Lett. B **439** (1998) 350 [hep-ph/9806440]; S. F. King, Nucl. Phys. B **562** (1999) 57 [hep-ph/9904210].

[108] S. F. King, JHEP **0508** (2005) 105 [hep-ph/0506297].

[109] S. Antusch, S. F. King, C. Luhn and M. Spinrath, Nucl. Phys. B **856** (2012) 328 [arXiv:1108.4278].

[110] S. F. King and C. Luhn, JHEP **1609** (2016) 023 doi:10.1007/JHEP09(2016)023 [arXiv:1607.05276 [hep-ph]].

[111] S. F. King and C. Luhn, JHEP **0910** (2009) 093 [arXiv:0908.1897].

[112] Z. Z. Xing and S. Zhou, Phys. Lett. B **653** (2007) 278 [hep-ph/0607302]; C. H. Albright, A. Dueck and W. Rodejohann, Eur. Phys. J. C **70** (2010) 1099 [arXiv:1004.2798]; X. -G. He and A. Zee, Phys. Rev. D **84** (2011) 053004 [arXiv:1106.4359]; W. Rodejohann and H. Zhang, Phys. Rev. D **86** (2012) 093008 [arXiv:1207.1225]; I. de Medeiros Varzielas and L. Lavoura, J. Phys. G **40** (2013) 085002 [arXiv:1212.3247]; W. Grimus, J. Phys. G **40** (2013) 075008 [arXiv:1301.0495].

[113] C. H. Albright and W. Rodejohann, Eur. Phys. J. C **62** (2009) 599 [arXiv:0812.0436].

[114] P. F. Harrison, D. H. Perkins and W. G. Scott, Phys. Lett. B **530** (2002) 167 [hep-ph/0202074].

[115] C. Luhn, Nucl. Phys. B **875** (2013) 80 [arXiv:1306.2358].

[116] G. J. Ding, S. F. King, C. Luhn and A. J. Stuart, JHEP **1305** (2013) 084 [arXiv:1303.6180]; F. Feruglio, C. Hagedorn and R. Ziegler, Eur. Phys. J. C **74** (2014) 2753 [arXiv:1303.7178].

[117] S. Antusch, S. F. King, C. Luhn and M. Spinrath, Nucl. Phys. B **850** (2011) 477 [arXiv:1103.5930].

[118] P. Vahle, "New results from NOvA." Talk given at the *XXVII International Conference on Neutrino Physics and Astrophysics*, London, UK, July 4–9, 2016.

[119] K. Iwamoto, "Recent Results from T2K and Future Prospects." Talk given at the *38th International Conference on High Energy Physics*, Chicago, USA, August 3–10, 2016.

[120] E. Fernandez-Martinez, J. Hernandez-Garcia and J. Lopez-Pavon, JHEP **1608** (2016) 033 [arXiv:1605.08774 [hep-ph]].

[121] P. Coloma, JHEP **1603**, 016 (2016) doi:10.1007/JHEP03(2016)016 [arXiv:1511.06357 [hep-ph]].

[122] A. de Gouva and K. J. Kelly, Nucl. Phys. B **908**, 318 (2016) doi:10.1016/j.nuclphysb.2016.03.013 [arXiv:1511.05562 [hep-ph]].

[123] M. Blennow, S. Choubey, T. Ohlsson, D. Pramanik and S. K. Raut, JHEP **1608**, 090 (2016) doi:10.1007/JHEP08(2016)090 [arXiv:1606.08851 [hep-ph]].

[124] K. Hayasaka *et al.*, Phys. Lett. B **687** (2010) 139 [arXiv:1001.3221 [hep-ex]].

[125] B. Aubert *et al.* [BaBar Collaboration], Phys. Rev. Lett. **104** (2010) 021802 [arXiv:0908.2381 [hep-ex]].

[126] A. M. Baldini *et al.* [MEG Collaboration], Eur. Phys. J. C **76** (2016) 434 doi:10.1140/epjc/s10052-016-4271-x [arXiv:1605.05081 [hep-ex]].

[127] D. Wyler and L. Wolfenstein, Nucl. Phys. B **218** (1983) 205 doi:10.1016/0550-3213(83)90482-0; R. N. Mohapatra, Phys. Rev. Lett. **56** (1986) 561. doi:10.1103/PhysRevLett.56.561; R. N. Mohapatra and J. W. F. Valle, Phys. Rev. D **34** (1986) 1642. doi:10.1103/PhysRevD.34.1642

[128] C. Biggio, M. Blennow and E. Fernandez-Martinez, JHEP **0903** (2009) 139 doi:10.1088/1126-6708/2009/03/139 [arXiv:0902.0607 [hep-ph]].

[129] C. Biggio, M. Blennow and E. Fernandez-Martinez, JHEP **0908**, 090 (2009) doi:10.1088/1126-6708/2009/08/090 [arXiv:0907.0097 [hep-ph]].

[130] G. Abbiendi *et al.* [ALEPH and DELPHI and L3 and OPAL and LEP Collaborations], Eur. Phys. J. C **73**, 2463 (2013) doi:10.1140/epjc/s10052-013-2463-1 [arXiv:1301.6065 [hep-ex]].

[131] G. Aad *et al.* [ATLAS Collaboration], JHEP **1405** (2014) 071 [arXiv:1403.5294 [hep-ex]].

[132] Q. H. Cao, G. Li, K. P. Xie and J. Zhang, arXiv:1711.02113 [hep-ph].

[133] T. Wang and Y. L. Zhou, arXiv:1801.05656 [hep-ph].

[134] T. Kikuchi, H. Minakata and S. Uchinami, JHEP **0903**, 114 (2009) doi:10.1088/1126-6708/2009/03/114 [arXiv:0809.3312 [hep-ph]].

Appendix A

More Simulation Details

A.1 Experimental run times and $\nu : \bar{\nu}$ ratios for alternative designs

The previous sections have discussed our models of the experimental details of DUNE and T2HK. However, in the present study, we consider a number of different exposures for these experiments and their combination. This section is intended to clarify our terminology and explain our choices of run time, neutrino–antineutrino sharing, and staging adopted in the following analyses.

First, we comment that although the ratio of the run time between ν and $\bar{\nu}$ beam modes is also known to affect the sensitivities of long-baseline experiments, we stick to the ratios defined by each experiment's official designs throughout our work. For DUNE and T2HK, the ratio of ν to $\bar{\nu}$ are 1:1 and 1:3, respectively. We have investigated the impact of changing these ratios, but they do not significantly impact the results, and for both experiments the optimal ratio was close to those assumed here. In the study for alternative designs, we stick with the same ratios as the standard configurations of DUNE and T2HK.

Most of our plots deal with three configurations labelled as DUNE, T2HK and DUNE + T2HK, and the sensitivities shown assume the full data taking periods for these experiments have ended. These are our standard configurations, and are defined in terms of run times and neutrino–antineutrino sharing in the rows labelled

	Label	$\nu : \overline{\nu}$ at DUNE	$\nu : \overline{\nu}$ at T2HK
Fixed run time	DUNE	$5 : 5$	$0 : 0$
	T2HK	$0 : 0$	$2.5 : 7.5$
	DUNE + T2HK	$5 : 5$	$2.5 : 7.5$
Variable run time	DUNE	$T/2 : T/2$	$0 : 0$
	T2HK	$0 : 0$	$T/4 : 3T/4$
	DUNE/2 + T2HK/2	$T/4 : T/4$	$T/8 : 3T/8$

Table A.1: The run times in years for each component of DUNE, T2HK, and their combination (DUNE + T2HK) for both the standard full data taking period (top 3 rows) and when considered with variable run times (bottom 3 rows). Plots with cumulative run time T on the x-axis are for the "variable run time" configurations, whilst all other plots are for the "fixed run time" configurations. We specify the details for configurations without staged power or mass increases when relevant in the text. We note here that 10 years of cumulative run time for DUNE and T2HK corresponds to 599.2 and 3403.4 kiloton×MW× years of exposure, respectively.

"fixed run time" in Table A.1. We point out that as we are interested in comparing experimental performance, we take our standard configuration of DUNE to have 10 years runtime, equal to the baseline configuration of T2HK [59]. This does, however, differ from the 7 years considered in Ref. [12], and our sensitivities are correspondingly better.

However, we also plot quantities against run time, and for these figures we define the sharing of run time between components in terms of a quantity we call the cumulative run time T; these are shown in the rows labelled "variable run time" in Table A.1. The cumulative run time for the combination of DUNE and T2HK is defined to be the sum of the individual experiments' run times, *i.e.* if the two experiments were run back to back, with no overlapping period of operation, then our definition of cumulative run time is identical to the calendar time taken for the full data set to be collected[1]. Of course, if the experiments run in parallel, with

---

[1] In the interests of clarity, let us point out that we use the term *calendar time* to denote

identical start and end dates, our definition of cumulative run time would be double the calendar time required to collect the data. To remind readers of our definitions, we label this variable run time configuration as DUNE/2 + T2HK/2, as half of the cumulative run time goes to each experiment. Note also that, as per the official studies of each experiment, we assume 10^7 seconds per year of active beam time for T2HK (2.7×10^{21} POT/year at 1.3 MW with 30 GeV protons) and combined accelerator uptime and efficiency of 56% (1.47×10^{21} POT/year at 1.07 MW with 80 GeV protons up to the 6th year, doubling the POT thereafter) for DUNE.

The possible staging options for the two modules of T2HK and the power of LBNF cause some added complication when plotting sensitivities against run time. In this study, we assume that our standard configurations of T2HK and DUNE follow the staging scenarios suggested by the collaborations: 6 years of 1-tank (187 kt of total volume) running followed by 4 with an additional tank for T2HK (374 kiloton of total volume), and 6 years of 1.07 MW (1.47×10^{21} POT/year) followed by 4 of 2.14 MW (2.54×10^{21} POT/year) for DUNE with 2-horn 80-GeV-proton design. In practice, we implement an effective mass for T2HK which depends on the run time t assigned to T2HK defined by

$$M(t) = M_0 \left[1 + \Theta(t-6) \frac{t-6}{t} \right],$$

where M_0 is the mass of a single tank, defined above as 187 kt, and $\Theta(x)$ is the Heaviside step function. We make an analogous definition for the power of DUNE, again increasing by a factor of two after 6 years. As our definition of cumulative run time T would require 12 years to pass before 6 years of data had been collected by either of the experiments in the combination of DUNE/2 + T2HK/2, we see the discontinuity in sensitivity due to staging appear in two different places in our plots against run time: one for an experiment alone, and one for DUNE/2 + T2HK/2. This can be seen clearly in *e.g.* Fig. 5.2, where we mark the discontinuities with vertical dashed lines. So as to better understand the impact of these upgrades, we

---

the actual time passed on the calendar. This is highly dependent on staging and the relative placements of individual experiment schedules, and is only used later in the text as an informal means of comparison for certain staging options.

also show the sensitivities against run time which would apply were they absent. However, we stress that the full programme of upgrades is an integral part of the collaborations' proposals and should be taken as part of their baseline configurations.

Finally, in Ch. 6 we deviate from these configurations (and the labels in Table A.1) as we consider non-standard exposures for the purpose of better exploring the complementarity of DUNE and T2HK. This be discussed in more detail in Ch. 6.

Experimental run times and $\nu : \overline{\nu}$ ratios

In all plots that follow, we assume that DUNE and its variants run with equal time allocated to neutrino and antineutrino mode, while T2HK and T2HKK always follow the 1:3 ratio of their standard configuration. We also assume that there is no staged implementation of any of the variants of T2HKK, and that both detector modules start collecting data at the same time. For DUNE and the lines labelled T2HK, we assume our standard configurations which implement a staged upgrade at 6 years.

The run time configurations for these alternative designs follow those of the "variable run time" options in Table A.1, albeit with variant fluxes for each experiment. All variants of DUNE, T2HK and T2HKK when run on their own are assumed to have a cumulative run time of 10 years. When a variant of DUNE is run in combination with a variant of T2HK, we assume that the cumulative run time is divided equally between the two experiments in the same way as DUNE/2 + T2HK/2 in Table A.1. This means that when not plotted against T, the combination of DUNE and T2HK have $T = 20$, corresponding to 10 years running time for each of the two experiments.

A.2 Further details of T2HK simulation

Our model of the T2HK detector significantly deviates from previous work. In this appendix, we give some further details of its implementation which where glossed over in the main text and a comparison with the collaboration's simulation.

	$\nu_\mu \to \nu_e$	$\nu_\mu \to \nu_\mu$	$\overline{\nu}_\mu \to \overline{\nu}_e$	$\overline{\nu}_\mu \to \overline{\nu}_\mu$
Signal	2.4%	2.7%	2.925%	2.7%
Background	2.4%	2.7%	2.925%	2.7%

Table A.2: Systematic errors used for T2HK simulation.

Energy bins

Our model of the T2HK detector(s) features 12 energy bins. Bin 1 collects all events below 0.35 GeV. The next 5 bins are 0.1 GeV wide, collecting events from 0.35-0.85 GeV. The next two bins are 0.2 GeV wide, followed by a single bin of 0.25 GeV width. There are then 3 increasingly broad bins, from 1.5 to 3.5, 3.5 to 6 and an overspill bin from 6 to 10 GeV.

Channel systematic uncertainties

Our model of the systematic uncertainty at T2HK uses two general normalisation systematics for the signal and background of each channel. The precise systematic errors used in our simulation are given, channel by channel, in Table A.2.

Comparison with published event rates

In Fig. A.1 we compare the event rates from our simulation to the official rates published by T2HK. The official simulation does not use GLoBES, and our reproduction is a non-trivial check to show that the signal and background modelling in our simulation is faithful. Additional checks have also been made to ensure that our simulations are able to reproduce the final sensitivities of official simulations, once we have modified our simulation to match the priors and chosen fitted parameters of the official simulations.

A.3 Statistical method

Our simulation uses GLoBES [48, 49] to compute the event rates and the statistical significance for the experiments discussed in the previous section. We now briefly

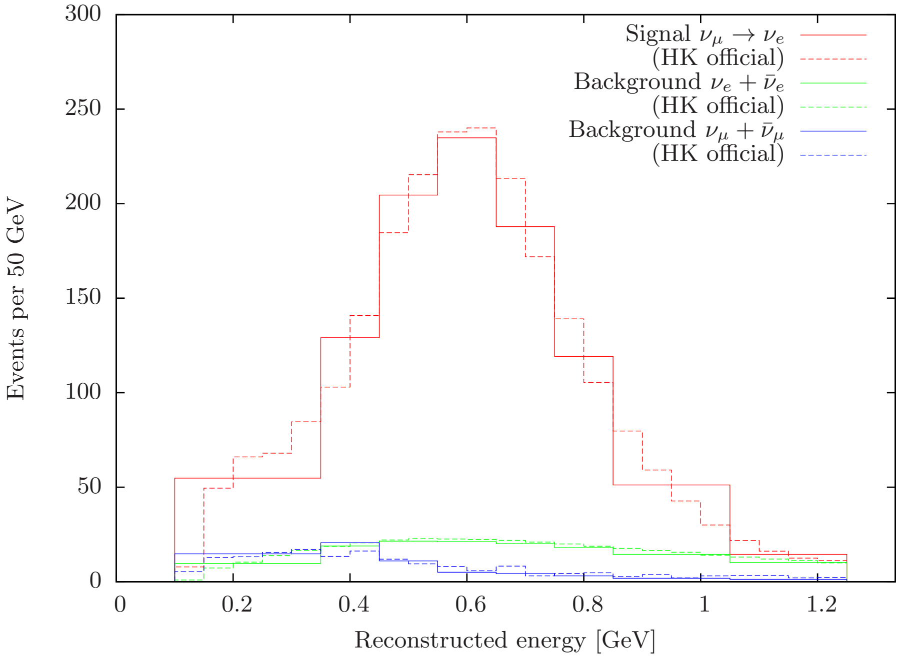

Figure A.1: T2HK appearance spectrum from our simulation compared to official event rates [59]. Note that the finer binning of the rates published by T2HK are shown for reference, but this finer granularity is not used in their oscillation fits; the binning we have used in our own fits has been chosen to match that of the official T2HK studies

recap the salient details of the statistical model underlying the analysis.

Given the true bin-by-bin event rates n_i for a specific experimental configuration, we construct a χ^2 function based on a log-likelihood ratio,

$$\chi^2(\Theta, \xi_s, \xi_b) = 2 \sum_i \left(\eta_i(\Theta, \xi_s, \xi_b) - n_i + n_i \ln \frac{n_i}{\eta_i(\Theta, \xi_s, \xi_b)} \right) + p(\xi_s, \sigma_s) + p(\xi_b, \sigma_b), \tag{A.3.1}$$

where i runs over the number of bins, $\eta_i(\Theta, \xi_s, \xi_b)$ is the hypothesis event rate for bin i and E_i is the central bin energy. The vector Θ has six components, corresponding to each of the three mixing angles, one phase and two mass-squared splittings of the hypothesis. The parameters ξ_s and ξ_b are introduced to account for the systematic uncertainty of normalization for the signal (subscript s) and background (subscript b) components of the event rate, and are allowed to vary in the fit as nuisance parameters. For a given hypothesised set of parameters Θ, the event rate for bin i

is calculated as

$$\eta_i(\Theta, \xi_s, \xi_b) = (1 + \xi_s) \times n_i + (1 + \xi_b) \times b_i,$$

where n_i and b_i are the expected number of signal and background events in bin i, respectively. The nuisance parameters are constrained by terms $p(\xi, \sigma) = \xi^2/\sigma^2$, representing Gaussian priors on ξ_s and ξ_b with corresponding uncertainties σ_s and σ_b. To test a given hypothesis against a data set, we profile out unwanted degrees of freedom. This amounts to minimising the χ^2 function Eq. (A.3.1) over these parameters whilst holding the relevant parameters fixed.

$$\chi^2(\Theta) = \min_{\{\xi_s, \xi_b\}} \left[2 \sum_i \left(\eta_i(\Theta, \xi_s, \xi_b) - n_i + n_i \ln \frac{n_i}{\eta_i(\Theta, \xi_s, \xi_b)} \right) + p(\xi_s, \sigma_s) + p(\xi_b, \sigma_b) \right] \tag{A.3.2}$$

We explain the statistical parameters of interest for each analysis in the following sections, however, as an example we be interested in how well different hypothesised values of δ fit a given data set. In this case, we would compute

$$\chi^2(\delta) = \min_{\{\Theta \neq \delta, \xi_s, \xi_b\}} \left(\chi^2(\Theta, \xi_s, \xi_b) + P(\Theta) \right), \tag{A.3.3}$$

where the notation $\Theta \neq \delta$ means all parameters other than δ. The function $P(\Theta)$ is a prior, introduced to mimic the role of data from existing experiments during fitting. In all fits that we perform, unless explicitly stated otherwise, we use true values from the recent global fit NuFit 3.0 (2016) [2]. To catch the real feature of current neutrino oscillation problems, in Chs. 5-7, $P(\Theta)$ comprises a sum of the 1D χ^2 data provided by NuFit for each parameter, except for δ, and we switch between NO and IO priors depending on the mass ordering of our hypothesis. This includes the correlations which are currently seen in the global data, and our treatment goes beyond the common assumption of Gaussian priors, allowing for both the degenerate solution and its relative poorness of fit to be more accurately taken into account. The values of all parameters are permitted to vary, including the different octants for θ_{23}, the value of δ_{CP} and the mass orderings, subject to the global constraints. Our choice of true values depends on the mass ordering, and are given explicitly in Table 2.3, unless stated otherwise. Note that the current best-fit values correlate the mass ordering and the octant, with NO preferring the lower octant and IO, the higher octant. This affects our simulation, for example leading to poorer CPV sensitivity for IO, and in Ch. 5 and Fig. 6.1 we show results for a band of θ_{23} spanning both solutions to mitigate this asymmetry.

We point out that our treatment of the external data, which attempts to accurately model the global constraints beyond the approximation of independent Gaussians, leads to some differences between our results and those of previous studies [12, 59, 98]. The differences can be traced to two key features: first, we take into account the significantly non-Gaussian behaviour of the global constraints at higher significances. This is particularly relevant for the prior on Δm^2_{21} and we comment on this in more detail in Section 5.1 and Appendix B. The second important feature of our priors is the strong correlation between mass ordering and the octant of θ_{23}. The current global data disfavours the combination of IO and first octant (NO and second octant). This fact is reflected in our priors; although a visible local minimum is always present, it is never degenerate with the true minimum. In previous studies, various treatments of this degeneracy have been employed, some which do not allow the alternative minimum, and some which do not penalise it at all. Our method interpolates between these two extremes, and attempts to faithfully describe the current global picture.

In Ch. 9, we include two dimensional χ^2 data from NuFit 3.0, for catching the feature of correlations between or among standard oscillation parameters. To do this, we implement Eq. 8.3.11. In Chs. 11 and 13, we simply adopt Gaussian priors for oscillation parameters.

Appendix B

Mass ordering sensitivity at high significance

The sensitivity to mass ordering is conventionally reported as the difference between the value of a χ^2 statistic for the true parameter set and the close degenerate set with the atmospheric mass splitting changed by the following mapping,

$$\Delta m^2_{31} \to -\Delta m^2_{31} + \Delta m^2_{21}.$$

This local minimum becomes a worse and worse fit as data is collected, and reaches a $\Delta\chi^2$ value of above 8σ within a few years of running DUNE. This method computes the decreasing quality of a poor fit to the data; however, there are lots of parameter sets which are poor fits to the current data, and many cannot be excluded with a significance greater than 8σ. Statistically speaking, to establish the mass ordering we must exclude all possible parameter sets with that ordering regardless of the other parameter values. In some circumstances, this may mean the local minimum identified above is not the true global wrong-ordering minimum. We find this problem is relevant for DUNE as soon as the local minimum approaches a 5σ exclusion. This is because the global prior for the solar mass-squared splitting, Δm^2_{21} has a second minimum at around this significance. The long-baseline experiments considered in this paper, offer no sensitivity to this parameter themselves, and rely on the priors to help constrain it. We have plotted the prior that we have used in our simulations in Fig. B.1, where the second minimum can be seen just above

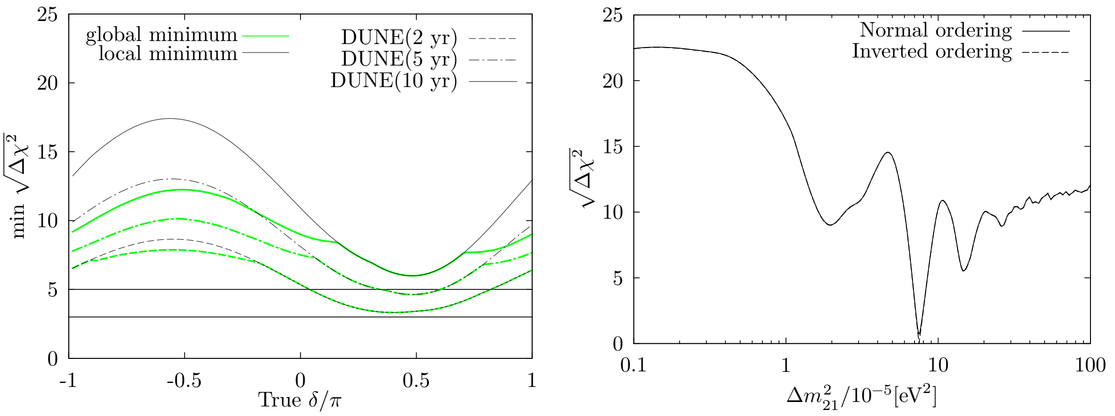

Figure B.1: Left: Comparison of our reported sensitivities based on the global minimum and more common published versions which show only a local minimum. This is due to the presence of additional wrong-ordering minima at high significance in the global data. Right: The prior on Δm^2_{21} provided by the NuFit global fit [43]. The second local minimum with a significance around 5σ ($\Delta m^2_{21} \approx 1.6 \times 10^{-4}$ eV^2) leads to the unusual behaviour in our reported mass ordering sensitivities.

the global minimum. For DUNE to exclude the wrong mass ordering at above 5σ, we must ensure it considers all values of Δm^2_{21} allowed by the global data at this significance. We find that DUNE can often exclude this minimum only at lower significance than the more obvious local minimum corresponding to the expected degeneracy. This causes the lower significances, and discontinuous behaviour, that we have reported in Section 5.1. On average, this reduces the expected significance of the mass ordering measurement by around 5σ.

Of course, predicting any sensitivities at high significance requires good control over all other aspects of the statistical modelling, and we do not pretend that our method correctly models all uncertainties up to very small fluctuations. However, we point out this particular subtlety as a concrete example of how the oft quoted sensitivity is not quite what it seems: it is the confidence at which we can expect to exclude a particular local minimum, not to the best-fitting set of parameters with the wrong ordering. The difference in these quantities starts to become relevant at for DUNE at very modest exposures. In the left panel of Fig. B.1, we show the difference in $\Delta\chi^2$ values for the local minimum (black) and the full set of wrong ordering parameter sets (green), which starts to be visible after only 2 years run time. We hope that this example helps to highlight some of the complexities of making precise statements with high confidence sensitivities.

Appendix C

Exact expressions for LS sum rules

The angles and Dirac phase can then be written as

$$\sin^2\theta_{13} = s(r), \qquad \tan^2\theta_{12} = t(r), \qquad \cos 2\theta_{23} = \pm c(r), \qquad \cos\delta = \pm d(r), \tag{C.0.1}$$

with positive signs taken for LSA and negative for LSB and where

$$s(r) = \frac{1}{6}\left(1 - \frac{55r^2 + 4(1-4r)}{\sqrt{\left((11r)^2 + 4(1-7r)\right)\left((11r)^2 + 4(1-r)\right)}}\right) \tag{C.0.2}$$

$$t(r) = \frac{1}{4}\left(1 + \frac{55r^2 + 4(1-4r)}{\sqrt{\left((11r)^2 + 4(1-7r)\right)\left((11r)^2 + 4(1-r)\right)}}\right) \tag{C.0.3}$$

$$c(r) = \frac{2r(11r-1)\left(55r^2 - 16r + 4 - 5\sqrt{\left((11r)^2 + 4(1-7r)\right)\left((11r)^2 + 4(1-r)\right)}\right)}{\left((11r)^2 + 4(1-7r)\right)\left((11r)^2 + 4(1-r)\right) + 4r^2\left((11r)^2 + 2(2-11r)\right)} \tag{C.0.4}$$

$$d(r) = -\frac{c(r)(1-5s(r))}{2\sqrt{2s(r)(1-c(r)^2)(1-3s(r))}}. \tag{C.0.5}$$

Similar expressions for the Majorana phases also possible. Combining these, expressions relating any two of the angles and/or phases can be found. The first such relation, relating θ_{13} and θ_{12}, is the same as Eq. (8.2.5), which is general for all CSD(n). New exact relations between θ_{13} and θ_{23} or θ_{12} and θ_{23}, as well as the relation between δ and θ_{12}, true for LSA with $\eta = \frac{2\pi}{3}$ or LSB with $\eta = -\frac{2\pi}{3}$, are found of the form

$$f_\pm(\theta_{13}, \theta_{23}) = 0, \qquad g_\pm(\theta_{12}, \theta_{23}) = 0, \qquad h_\pm(\delta, \theta_{12}) = 0, \tag{C.0.6}$$

where again the positive (negative) sign is used in the functions valid for LSA (LSB). Exact expressions are given as

$$f_{\pm}(\theta_{13},\theta_{23}) = \frac{44 s_{13}^2\sqrt{1-3s_{13}^2}}{4(1-6s_{13}^2)\mp 3c_{13}^2\cos 2\theta_{23}} \pm \frac{c_{13}^2\cos 2\theta_{23}}{\sqrt{1-3s_{13}^2}} - \sqrt{\frac{8s_{13}^2}{3}-\frac{c_{13}^4\cos^2 2\theta_{23}}{3(1-3s_{13}^2)}}, \tag{C.0.7}$$

$$g_{\pm}(\theta_{12},\theta_{23}) = \frac{22 s_{12}^2\sqrt{1-3s_{12}^2}}{2(5s_{12}^2-1)\mp \cos 2\theta_{23}} \pm \frac{\cos 2\theta_{23}}{\sqrt{1-3s_{12}^2}} - \sqrt{4s_{12}^2-\frac{\cos^2 2\theta_{23}}{3(1-3s_{12}^2)}}, \tag{C.0.8}$$

$$h_{\pm}(\delta,\theta_{12}) = \frac{5s_{12}^2-1}{s_{12}\sqrt{1-3s_{12}^2}} \pm \frac{\sqrt{3}\cos\delta}{\sqrt{1-12s_{12}^2(1-3s_{12}^2)\sin^2\delta}} + \frac{11\sqrt{1-12s_{12}^2(1-3s_{12}^2)\sin^2\delta}}{2(6s_{12}^2-1)\sin\delta\mp 2\sqrt{3}\cos\delta}. \tag{C.0.9}$$

Appendix D

Oscillation probabilities with matter NSI effects

To understand the impact of α^{m}_{mn} (in the following, we simply use α_{mn}) on neutrino oscillation probabilities, we are based on the knowledge of the probabilities with non-zero $\epsilon^{\mathrm{m}}_{\alpha\beta}$ (in the following, we simply use $\epsilon_{\alpha\beta}$). Therefore we firstly study the probability including the NSI matter effects in terms of $\epsilon_{\alpha\beta}$, and then by using the relations between two parameter sets Table 13.1, we can extend our understanding on how flavour symmetry model realises at oscillation probability through matter-effect NSI.

Assuming $\sqrt{\frac{\Delta m^2_{21}}{\Delta m^2_{31}}} \sim \sqrt{|\epsilon_{\alpha\beta}|} \sim s_{13}$ as the 1st order perturbation terms ξ, we expand the disappearance oscillation probability $P(\nu_\mu \to \nu_\mu)$ and appearance oscillation probability $P(\nu_\mu \to \nu_e)$. These equations are given with the leading-ordering coefficient for each $\epsilon_{\alpha\beta}$ to understand how each elements affect to the probability at the leading order.[1]

---

[1] Our result is consistent with those in Ref. [134].

$$\begin{aligned}
&P(\nu_\mu \to \nu_\mu) = P_0(\nu_\mu \to \nu_\mu) + \delta P_{\rm NSI}(\nu_\mu \to \nu_\mu) \\
&\sim P_0(\nu_\mu \to \nu_\mu) \\
&-A\epsilon_{\mu\tau}\cos\phi_{\mu\tau}\left(\sin^3 2\theta_{23}\tfrac{L}{2E}\sin\Delta_{13}L + 4\sin 2\theta_{23}\cos^2 2\theta_{23}\tfrac{1}{\Delta m^2_{31}}\sin^2\tfrac{\Delta_{13}L}{2}\right) \\
&-A\tilde{\epsilon}_{\tau\tau}c^2_{23}s^2_{23}(c^2_{23}-s^2_{23})\left(\tfrac{L}{8E}\sin\Delta_{13}L - \tfrac{1}{\Delta m^2_{31}}\sin^2\tfrac{\Delta_{13}L}{2}\right) \\
&+\mathcal{C}^1_{\mu\to e;e\mu}|\epsilon_{e\mu}| + \mathcal{C}^1_{\mu\to e;e\tau}|\epsilon_{e\tau}| + \mathcal{C}^2_{\mu\to e;ee}\tilde{\epsilon}_{ee},
\end{aligned} \tag{D.0.1}$$

$$\begin{aligned}
&P(\nu_\mu \to \nu_e) = P_0(\nu_\mu \to \nu_e) + \delta P_{\rm NSI}(\nu_\mu \to \nu_e) \\
&\sim P_0(\nu_\mu \to \nu_e) \\
&+8s_{13}|\epsilon_{e\mu}|s_{23}\tfrac{\Delta m^2_{31}}{\Delta m^2_{31}-A}\sin\tfrac{(\Delta m^2_{13}-A)L}{4E} \\
&\times\left(s^2_{23}\tfrac{A}{\Delta m^2_{31}-A}\cos(\delta+\phi_{e\mu})\sin\frac{\left(\Delta m^2_{31}-A\right)L}{4E} + c^2_{23}\sin\tfrac{AL}{4E}\cos\left(\delta+\phi_{e\mu}-\tfrac{\Delta m^2_{31}L}{4E}\right)\right) \\
&+8s_{13}|\epsilon_{e\tau}|c_{23}s^2_{23}\tfrac{\Delta m^2_{31}}{\Delta m^2_{31}-A}\sin\tfrac{(\Delta m^2_{31}-A)L}{2} \\
&\times\left(\tfrac{A}{\Delta m^2_{31}-A}\cos(\delta+\phi_{e\tau})\sin\frac{\left(\Delta m^2_{31}-A\right)L}{4E} - \sin\tfrac{AL}{4E}\cos\left(\delta+\phi_{e\tau}-\tfrac{\Delta m^2_{31}L}{4E}\right)\right) \\
&+\mathcal{C}^2_{\mu\to e;\mu\tau}|\epsilon_{\mu\tau}| + \mathcal{C}^2_{\mu\to e;ee}\tilde{\epsilon}_{ee} + \mathcal{C}^2_{\mu\to e;\tau\tau}\tilde{\epsilon}_{\tau\tau},
\end{aligned} \tag{D.0.2}$$

where $P_0(\nu_\alpha \to \nu_\beta)$ is the transition probability for $\nu_\alpha \to \nu_\beta$ without NSI matter effects, and
$\Delta_{13} \equiv \frac{\Delta m^2_{31}}{2E}$, and for the cofficient $\mathcal{C}^{\rm order}_{\rm channel,\ element}$, the upper index gives the order of this coefficient, and the lower one gives the channel and the element.

It is worthwhile to note that in Eq. (D.0.1) those with the coefficient starts from zeroth order, for $\epsilon_{\mu\tau}$, $\tilde{\epsilon}_{\tau\tau}$. Nevertheless, the coefficients for $\tilde{\epsilon}_{ee}$, $\epsilon_{e\mu}$, $\epsilon_{e\tau}$ are of the 2nd, 1st and 1st order, respectively. The contribution of $\tilde{\epsilon}_{\tau\tau}$ is suppressed by the factor $(c^2_{23} - s^2_{23})$. This means for the same small value of each $\epsilon_{\alpha\beta}$, the contributions of the others are smaller than that of $\epsilon_{\mu\tau}$. On the other hand, from Eq. (D.0.2), it is obvious that the most contribution on the transition probability is of $\epsilon_{e\mu}$ and of $\epsilon_{e\tau}$, with the coefficient of the 1st order. The others are with the 2nd order coefficient.

We summarise what we get to the coefficient from Eq. (D.0.1) and (D.0.2) and Table 13.1 in Tab D.1. From this table we can see which α_{mn} have the bigger impact to a certain channel due to the larger coefficient. α_{13}, α_{2n}, and α_{3n} are easier to be detected in disappearance channel $\nu_\mu \to \nu_\mu$. On the appearance probability

channel	$\nu_\mu \to \nu_\mu$	$\nu_\mu \to \nu_e$
$\tilde{\epsilon}_{ee}$	$\mathcal{C}^2_{\mu\to\mu;ee}$	$\mathcal{C}^2_{\mu\to e;ee}$
$\tilde{\epsilon}_{\tau\tau}$	$\mathcal{C}^0_{\mu\to\mu;\tau\tau}$	$\mathcal{C}^2_{\mu\to e;\tau\tau}$
$\epsilon_{e\mu}$	$\mathcal{C}^1_{\mu\to\mu;e\mu}$	$\mathcal{C}^1_{\mu\to e;e\mu}$
$\epsilon_{e\tau}$	$\mathcal{C}^1_{\mu\to\mu;e\tau}$	$\mathcal{C}^1_{\mu\to e;e\tau}$
$\epsilon_{\mu\tau}$	$\mathcal{C}^0_{\mu\to\mu;\mu\tau}$	$\mathcal{C}^2_{\mu\to e;\mu\tau}$
α_{12}	$\mathcal{C}^2_{\mu\to\mu;ee}$	$\mathcal{C}^2_{\mu\to e;ee}$
α_{13}	$-\sqrt{2}\mathcal{C}^0_{\mu\to\mu,\tau\tau}$	$\frac{1}{2}\mathcal{C}^2_{\mu\to e;ee} - \sqrt{2}\mathcal{C}^2_{\mu\to e;\tau\tau}$
α_{21}	$\frac{1}{\sqrt{6}}\mathcal{C}^0_{\mu\to\mu;\mu\tau}$	$\frac{1}{\sqrt{6}}\mathcal{R}\mathcal{C}^1_{\mu\to e;e\mu} + \frac{1}{\sqrt{6}}\mathcal{R}\mathcal{C}^1_{\mu\to e;e\tau}$
α_{22}	$\frac{1}{\sqrt{3}}\mathcal{C}^0_{\mu\to\mu;\mu\tau}$	$\frac{1}{\sqrt{12}}\mathcal{R}\mathcal{C}^1_{\mu\to e;e\mu} + \frac{1}{\sqrt{12}}\mathcal{R}\mathcal{C}^1_{\mu\to e;e\tau}$
α_{23}	$-\frac{1}{2}\mathcal{R}\mathcal{C}^1_{\mu\to\mu,e\mu} + \frac{1}{2}\mathcal{R}\mathcal{C}^1_{\mu\to\mu,e\tau}$	$-\frac{1}{2}\mathcal{R}\mathcal{C}^1_{\mu\to e;e\mu} + \frac{1}{2}\mathcal{R}\mathcal{C}^1_{\mu\to e;e\tau}$
α_{31}	$-\frac{1}{\sqrt{6}}\mathcal{I}\mathcal{C}^1_{\mu\to\mu,e\mu} + \frac{1}{\sqrt{6}}\mathcal{I}\mathcal{C}^1_{\mu\to\mu,e\tau}$	$-\frac{1}{\sqrt{6}}\mathcal{I}\mathcal{C}^1_{\mu\to e;e\mu} + \frac{1}{\sqrt{6}}\mathcal{I}\mathcal{C}^1_{\mu\to e;e\tau}$
α_{32}	$\frac{1}{\sqrt{12}}\mathcal{I}\mathcal{C}^1_{\mu\to\mu,e\mu} - \frac{1}{\sqrt{12}}\mathcal{I}\mathcal{C}^1_{\mu\to\mu,e\tau}$	$\frac{1}{\sqrt{12}}\mathcal{I}\mathcal{C}^1_{\mu\to e;e\mu} - \frac{1}{\sqrt{12}}\mathcal{I}\mathcal{C}^1_{\mu\to e;e\tau}$
α_{33}	$\frac{1}{2}\mathcal{I}\mathcal{C}^1_{\mu\to\mu,e\mu} + \frac{1}{2}\mathcal{I}\mathcal{C}^1_{\mu\to\mu,e\tau}$	$\frac{1}{2}\mathcal{I}\mathcal{C}^1_{\mu\to e;e\mu} + \frac{1}{2}\mathcal{I}\mathcal{C}^1_{\mu\to e;e\tau}$

Table D.1: . The leading coefficient of each $\epsilon_{\alpha\beta}$ and α_{ij}, for $\nu_\mu \to \nu_\mu$ and $\nu_\mu \to \nu_e$. $\mathcal{R}\mathcal{C}^x_{\alpha\to\beta;\gamma\delta}$ ($\mathcal{I}\mathcal{C}^x_{\alpha\to\beta;\gamma\delta}$ is the coefficient for real (image) part of $\gamma\delta$ in $\alpha \to \beta$, which is of the order x.

$P(\nu_\mu \to \nu_e)$, α_{2n} and α_{3n} affect more significantly. The order of coefficient in the disappearance channel has larger impact by α, as the order is lower.